Multi-wavelength Studies of Active Galactic Nuclei (AGNs)

A thesis submitted in partial fulfillment of

the requirements for the degree of

Doctor of Philosophy

by

Neeraj Kumari

(Roll No. 17330020)

Under the guidance of

Prof. Sachindranatha Naik

Astronomy and Astrophysics Division
Physical Research Laboratory, Ahmedabad, India.

DEPARTMENT OF PHYSICS
INDIAN INSTITUTE OF TECHNOLOGY GANDHINAGAR
July, 2022

Dedicated to

The Society

DECLARATION

I, Neeraj Kumari, declare that the work reported in this thesis represents my own ideas and words. I have adequately cited and referenced the original sources, wherever others' ideas or content have been included. I further declare that I have adhered to all principles of academic honesty and integrity and have not misrepresented or fabricated or falsified any idea/data/fact/source in this submission. I understand that any violation of the above can cause disciplinary action by the Institute and can also evoke penal action from the sources which have thus not been properly cited or from whom proper permission has not been taken when needed.

Name: Neeraj Kumari

(Roll No: 17330020)

Date:

CERTIFICATE

It is certified that the work contained in the thesis entitled **"Multi-wavelength Studies of Active Galactic Nuclei (AGNs)"** by **Ms. Neeraj Kumari** (Roll number: 17330020), has been carried out under my supervision and this work has not been submitted elsewhere for any degree or diploma.

I have read this dissertation and in my opinion, it is fully adequate in scope and quality as a dissertation for the degree of Doctor of Philosophy.

Prof. Sachindranatha Naik
(Thesis Supervisor)
Professor
Astronomy & Astrophysics Division
Physical Research Laboratory
Unit of Department of Space, Govt. of India
Ahmedabad-380009, Gujarat, India.

Date:

Acknowledgements

The last five years of my PhD in PRL have been more meaningful till now than those spent before that. In PRL, I have met some amazing people who filled my life with great pleasure and contributed to my personal growth. Here, I want to acknowledge all those people who have been directly or indirectly part of this exciting, fulfilling, and, at the same time, a bit frustrating journey.

The foremost person I want to express my heartfelt thank is my PhD supervisor *Prof. Sachindra Naik*, who helped me not only professionally but also personally gave me a different perspective of viewing certain things. He always encouraged me to do well in life and cared for me like a family member. Due to his constant push, I could gain more confidence in public speaking, for which I will always be grateful to him. His punctuality and commitment to work are appreciable, which I want to inculcate in my life. I also want to thank *Manorama ma'am* for her love and care whenever I visited Sir's place. Being an Indian woman, I silently got inspired by her commitment to work and family.

Further, I convey my sincere thanks to my Doctoral Studies Committee, *Dr Aveek Sarkar, Dr Manash Samal* and *Dr Bhuwan Joshi* for checking my progress time to time. Their valuable comments and remarks have always helped me to improve my scientific temperament. I express my gratitude to Director sir *Dr Anil Bhardwaj* for providing the necessary facilities to carry out the research work. I am also thankful to *Prof. Abhijit Chakraborty*, Astronomy and Astrophysics Division chairman at PRL, for his support towards the requirements of my research work. I am also indebted to all the faculty and staff members of our division for providing a pleasant research environment throughout all these years. I would like to extend my sincere thanks to the PRL Dean, Academic Committee Chairman and Registrar for their support during my research work at PRL. I am also thankful to the Dean and Head of Physics Department at Indian Institute of Technology, Gandhinagar (IIT-Gn), for their extended co-operation.

I would like to thank all the Mt. Abu observatory technical staff, canteen staff & the night assistants and TOTs with special mention to *Jain Sir, Mitesh, Vikram,* and *Dinesh* for their great help during observation times, especially covid time.

I would like to take this opportunity to thank all my collaborators for having time-to-time discussions to improve the research outcomes. Firstly and especially, I want to thank *Dr Main Pal*, who was a post-doctoral fellow at the time of my joining the group. He introduced the field of AGNs to me when I was completely naive and answered my stupidest questions.

He guided me throughout the duration of my first-ever research publication. I express my deepest thank to *Dr Arghajit Jana*, with whom I have collaborated on several projects. His dedication to work is the inspiration not only to me but for many. We had many scientific and non-scientific discussions.

Many people joined and left the group, and I am extremely fortunate to share the office space with them. I want to thank *Dr Gaurava Jaiswal*, the senior-most person of my group. Although, I have spend very little time with him but I have learnt some important things from him about research. I acknowledge my former officemate *Dr Prahlad Rameya Epili* for helping me with the software installation and working with ubuntu system. I admire his helpful and humble nature. I express my deepest and warmest love to my office colleagues and friends, *Shivangi di* and *Birendra*. I never felt bored in the office in the presence of them. *Shivangi di* was the one who made me comfortable, like an elder sister, to pour my heart out whenever I was worried about my academics. *Birendra*, my dearest junior, became a friend in no time after joining the group. He has been a soulful person and having deep discussions on life with him was very much enjoyable. I am thankful to him for always being there and maintaining the joyful atmosphere of the office with his sense of humour. I also want to acknowledge newly joined colleagues, *Dr Prantik* and *Narendra*, which provided a new atmosphere to the office, full of scientific discussions. I really admire the theoretical knowledge of *Prantik* on different subjects.

Life in PRL has been so lively with friends during five years of my stay in the hostel. Endless talks on life philosophies, society, stupid stories after office hour etc. made each day fulfilling. I will always cherish the times we have spent at PRL hostel. The chats we had on weekends or during night walks and other times count substantially in my life. *Sushant* is the person who has been the best of friends here, the most irritating person (in a good sense), with whom I could share my sadness, happiness and who has great tolerance for my anger. With *Abhay*, I can not remember how many stupid fights I have had, but I am grateful to have a trustworthy friend like him in my life. *Alka* provided me a comfortable space with whom I had many women-to-women discussions. *Ankit's* joyful nature always added charm to the my friend circle. I have learnt many nuances of life from these people. I want to draw a special mention to *Vipin* and *Rekha*, who gave home like atmosphere whenever I visited their place. I can not thank enough to *Shanwalee* for the "sister-care" she showed when I was suffering from dengue. She is the kind of person one can count upon. Here, I can not forget to thank my other good friends, *Anshika, Partha, Hirdesh, Abhijit, Biswajit, Aravind, Rituparna, Hrushi,* *Satyajit, Himanshu, Shivani*, and *Madhusudan* for being nice to me always. It is not possible to name everyone here, so I want to thank collectively all my batchmates. I also thank all the seniors & juniors in Astronomy division with special mention to *Sandeep, Archita, Naval, Akanksha, Namita, Arup, Vineet* and *Sanjay*.

I know no words can do justice for the contribution of my family in my life. Nothing would have been possible without their constant support, love and care. Still, I want to express my soulful thanks to my family for providing me good education, which is the most essential gift any human being can get.

This thesis, in a way, is the contribution of all the people I have ever met throughout my life, especially my teachers, who shaped me into the person I am today, which led to the completion of this highest rewarding degree.

- Neeraj Kumari

Abstract

Active Galactic Nuclei (AGNs) are the most luminous (luminosity $\sim 10^{42} - 10^{48}$ erg/s) persistent astronomical objects in the Universe, emitting in almost entire wavelength range of the electromagnetic spectrum, starting from radio to Gamma rays. This enormous radiation is attributed as due to the accretion of the surrounding material onto a supermassive black hole (SMBH) located at the centre of a galaxy. Usually, the AGNs are X-ray loud and emit profoundly in the $0.1 - 100$ keV energy band. The spectral energy distribution of type 1 AGNs (e.g. Seyfert galaxies) shows the presence of primary spectral components such as a big blue bump in the UV range, soft X-ray excess below ~ 2 keV, Fe emission lines in $6 - 7$ keV, reflection hump in $10 - 50$ keV range and a power-law continuum emission with high energy cut-off. These components are thought to be originating from distinct regions of the AGN and are expected to vary differently. One of the most important properties of these objects is that they are highly variable on different time scales. The observed X-rays show rapid variability on the time scale of as short as an hour which is comparable to the size of the immediate region around the black hole. This makes X-ray emission, along with emission in other wavelengths, an important proxy to probe the extreme environment of the black hole. Our understanding of the variability properties of these objects is still not complete. Therefore, the spectral and timing studies of the AGNs can provide a better understanding of the central engine and its surrounding medium. The present thesis work is dedicated to the substantial understanding of three Seyfert galaxies: Mrk 509, NGC 1566 and NGC 4051.

To fulfil the thesis objectives, the data from various space-based observatories, such as Swift, XMM-Newton and NuSTAR are utilized. To disentangle the origin of short-term variabilities in Seyfert 1 galaxy Mrk 509, long-term Swift data from 2006 to 2019 in multi-wavebands (X-ray, UV and optical) have been used. We analyzed a total of 275 pointed observations to study the variability properties of the source in the optical/UV to X-ray emission. The average spectrum over the entire duration of observations exhibits a strong soft X-ray excess above the power-law continuum. The soft X-ray excess is well described by two thermal components with temperatures of $kT_{BB1} \sim 120$ eV and $kT_{BB2} \sim 460$ eV. The warm thermal component is likely due to the presence of an optically thick and warm Comptonizing plasma in the inner accretion disc. We calculated the fractional variability amplitude in each band and found it to be decreasing with increasing wavelength i.e., from the soft X-ray ($0.3 - 2$ keV) to UV/optical emission. However, the hard X-ray (2–8 keV) emission shows very low variability. The strength of the correlation within the UV and the

optical bands is found to be stronger ($0.95 - 0.99$) than the correlation between the UV/optical and X-ray bands (0.40–0.53). These results clearly suggest that the emitting regions of the X-ray and UV/optical emission are likely distinct or partly interacting. After removing the slow variations in the light curves, we find that the lag spectrum (time lag vs wavelength) is well described by the 4/3 rule of the standard Shakura–Sunyaev accretion disc when we omit X-ray lags. Nearly zero time lag and marginal variability difference between UV bands suggest that the UV emitting region in the disc is not smooth but is instead a stratified region. All these results suggest that the real disc is complex and the UV emission is likely reprocessed in the accretion disc to give X-ray and optical emission.

Another detailed spectral and timing study has been performed for the 2018 outburst of the Changing-look AGN (CL-AGN) NGC 1566, where its intensity increased up to $\sim 25 - 30$ times its quiescent state intensity. This main outburst was accompanied by small recurrent outbursts. The CLAGNs are a newly emerging class of AGNs where an AGN switches its type over the years. The study was performed during pre-outburst, outburst and post-outburst epochs using semi-simultaneous observations with the XMM-Newton, NuSTAR and Swift Observatories. The broad-band 0.5–70 keV spectra were fitted with phenomenological models as well as physical models. A strong soft X-ray excess is detected in the spectra during the outburst, while it was weak before and after the outburst. The soft excess can produce most of the ionizing flux necessary to create broad optical lines. The broad lines appeared during the outburst, therefore, could be due to the strong soft excess, leading to the changing-look event. The soft excess emission is found to be complex and could originate in the warm Comptonizing region in the inner accretion disc. Using the obtained results, we find that the increase in the accretion rate, which could be due to the disc instability, is responsible for the sudden rise in luminosity and rule out the possibility of a tidal-disruption event (TDE). This is supported by the 'q'-shape of the hardness-intensity diagram that is generally found in outbursting black hole X-ray binaries. From our analysis, we find that NGC 1566 most likely harbours a low-spinning black hole with the spin parameter $a \sim 0.2$. We also propose a possible scenario where the central core of NGC 1566 could be a merging pair of supermassive black holes. This scenario could explain the recurrent outburst.

To investigate the cause of ubiquitous small X-ray flares in AGNs, a small flaring event of ~ 120 ks in narrow-line Seyfert 1 (NLS1) galaxy NGC 4051 has been studied in detail using simultaneous XMM-Newton and NuSTAR observations. The ~ 300 ks long NuSTAR observation and the overlapping XMM-Newton exposure were segregated into pre-flare, flare

and post-flare segments. We found that during the flare, the NuSTAR count rate peaked at 2.5 times the mean count rate before the flare. We explored the variation of X-ray emission in three phases using various phenomenological and physical models. The $0.3-50$ keV X-ray spectrum of the source is described by a composite model consisting of a primary continuum, reprocessed emission, warm absorber and ultra-fast outflows. From the spectral analysis, we find that the reflection fraction drops significantly during the flare, accompanied by the increase in the coronal height to $\sim$ 12.2 R_g from $\sim$ 9.6 R_g (during the pre-flare phase) above the disc. The spectrum became softer during the flare showing the "softer when brighter" nature of the source. After the alleviation of the flare, the coronal height drops to $\sim$ 7.4 R_g, and the corona heats up to the temperature of $\sim$ 228 keV. This indicates that there could be inflation of the corona during the flare. We did not find any significant change in the inner accretion disc or the seed photon temperature during the observation. These results suggest that the flaring event occurred due to the change in the coronal properties rather than any notable change in the accretion disc.

List of Publications

I. In Refereed Journals included in the Thesis

1. Complex optical/UV and X-ray variability in Seyfert 1 galaxy Mrk 509: **Neeraj Kumari**, Main Pal, S. Naik , A., Jana, G. K. Jaisawal, P. Kushwaha, 2021, PASA, 38, e042

2. Broadband X-Ray Observations of the 2018 Outburst of the Changing-Look Active Galactic Nucleus NGC 1566 : A. Jana, **Neeraj Kumari**, P. Nandi, S. Naik, A. Chatterjee, G. K. Jaisawal, K. Hayasaki, C. Ricci, 2021, MNRAS, 507, 687-703

3. Investigation of a small flaring event in NLS1 galaxy NGC 4051: **Neeraj Kumari**, Arghajit Jana, Sachindra Naik, Prantik Nandi, 2022, MNRAS (***Under review***)

II. Additional Publications in Refereed Journals

1. Absorption variability of the highly obscured active galactic nucleus NGC 4507: A. Jana, C. Ricci, S. Naik, A. Tanimoto, **Neeraj Kumari**, H-K Chang, P. Nandi, A. Chatterjee, S. Safi-Harb, MNRAS, 512, 5942-5959

2. Evidence of heavy obscuration in the low-luminosity AGN NGC 4941: A. Jana, S. Naik, **Neeraj Kumari**, JOAA, 43, 4

3. AstroSat observation of X-ray dips and state transition in the black hole candidate MAXI J1803-298: A. Jana, S. Naik, G K Jaisawal, B. Chhotaray, **Neeraj Kumari**, S. Gupta, 2022, MNRAS, 511, 3922–3936

4. Blazar OJ 287 After First VHE Activity: Tracking the Re-emergence of the HBL like Component in 2020: P. Kushwaha, Main Pal, N. Kalita, **Neeraj Kumari**, S. Naik, A. C. Gupta, E. M. de Gouveia Dal Pino, M. Gu, 2021, ApJ, 921, 11

5. Spectro-timing analysis of a highly variable narrow-line Seyfert 1 galaxy NGC 4748 with AstroSat and XMM-Newton : Main Pal, **Neeraj Kumari**, P. Kushwaha, K. P. Singh, Alok C. Gupta, Sachindra Naik, G. C. Dewangan, P. Tripathi, Rathin Adhikari, O. Adegoke, H. Nandan, 2021, JApA, 42, 81

6. Short-timescale variability of the blazar Mrk 421 from AstroSat and simultaneous multi-wavelength observations: R. Chatterjee, S. Das, A. Khasnovis, R. Ghosh, **Neeraj Kumari**, S. Naik, V. M. Larionov, T. S. Grishina, E. N. Kopatskaya, E. G. Larionova, A. A. Nikiforova, D. A. Morozov, S. S. Savchenko, Yu. V. Troitskaya, I. S. Troitsky, A. A. Vasilyev, 2021, JApA, 42, 80

7. Imaging and photometric studies of NGC 1316 (Fornax A) using Astrosat/UVIT : N. D. Vagshette, S. Naik, **Neeraj Kumari**, M. K. Patil, 2021, JApA, 42, 34

8. NICER observations of the black hole candidate MAXI J0637-430 during the 2019-2020 outburst: A. Jana, G. K. Jaisawal, S. Naik, **Neeraj Kumari**, B. Chhotaray, D. Altamirano, R. A. Remillard, K. C. Gendreau, 2021, MNRAS, 504, 4793-4805

9. Accretion properties of MAXI J1813-095 during its failed outburst in 2018: A. Jana, G. K. Jaisawal, S. Naik, **Neeraj Kumari**, D. Chatterjee, K. Chatterjee, R. Bhowmick, S. K. Chakrabarti, H. Chang, D. Debnath, 2021, RAA, 21, 125

10. Probing the nuclear and circumnuclear properties of NGC 6300 using X-ray observations: A. Jana, A. Chatterjee, **Neeraj Kumari**, P. Nandi, S. Naik, D. Patra, 2020, MNRAS, 499, 5396-5409

11. Revisiting the spectral and timing properties of 4U 1909+07 with NuSTAR and Astrosat : G. K. Jaisawal, S. Naik, W. C. G. Ho, **Neeraj Kumari**, Prahlad Epili, G. Vasilopoulos, 2020, MNRAS, 498, 4830

12. Accretion Flow Evolution of a New Black Hole Candidate MAXI J1348-630 during the 2019 Outburst : A. Jana, D. Debnath, D. Chatterjee, K. Chatterjee, S. K. Chakrabarti, S. Naik, R. Bhowmick, **Neeraj Kumari**, 2020, ApJ, 897, 3

Contents

List of Figures

List of Tables

Physical Constants

Speed of light	$c = 2.997 \times 10^{10}$ cm s^{-1}
Planck constant	$h = 6.626 \times 10^{-27}$ erg s^{-1}
Gravitational constant	$G = 6.672 \times 10^{-8}$ cm^3 g^{-1} s^{-2}
Boltzmann's constant	$k_B = 1.380 \times 10^{-16}$ erg K^{-1}
Mass of electron	$m_e = 9.109 \times 10^{-28}$ g
Mass of proton	$m_p = 1.673 \times 10^{-24}$ g
Parsec	pc $= 3.086 \times 10^{18}$ cm
Solar Mass	$M_\odot = 1.989 \times 10^{33}$ g
Solar Luminosity	$L_\odot = 3.826 \times 10^{33}$ erg s^{-1}
Solar Radius	$R_\odot = 6.959 \times 10^{10}$ cm

List of Abbreviations

AGN	Active Galactic Nucleus
BLR	Broad Line Region
EUV	Extreme Ultra Violet
NUV	Near UltraViolet
FWHM	Full Width at Half Maximum
LOS	Line Of Sight
NED	NASA/IPAC Extragalactic Database
NLR	Narrow Line Region
QSO	Quasi-Stellar Object or quasar
SED	Spectral Energy Distribution
WA	Warm Absorber
XMM-Newton	X-ray Multi-Mirror Mission - Newton
NLS1	Narrow Line Seyfert 1
SMBH	SuperMassive Black Hole
CL-AGNs	Changing-Look Active Galactic Nuclei
CS-AGNs	Changing-State Active Galactic Nuclei
CO-AGNs	Changing-Obscuration Active Galactic Nuclei

Chapter 1

Introduction: Active Galactic Nuclei (AGNs)

The emission from normal galaxies in optical and infrared light is dominated primarily by stars, gas and dust. However, there are galaxies which emit sufficiently in multi-wavelength bands. This emission comes from a very small central region of an *active galaxy* which is called *Active Galactic Nucleus (AGN)*. Huge amount of emission from an AGN is associated with the material accreting onto the super massive black hole ($M_{BH} = 10^6 - 10^9\ M_\odot$; Kormendy & Richstone (1995)). A black hole is defined as the place in space-time where gravity is so high that even light can not escape from it.

This chapter is dedicated to the brief introduction of AGNs, their classification, X-ray properties and physical processes going on near extreme gravity.

1.1 Historical background

In 1750, Thomas Wright postulated that the clusters of "nebula" were galaxies too far from us. In the eighteenth century, Immanuel Kant, who was interested in astronomy, also postulated that "nebulae" are different "worlds" similar to our own Milky Way. He coined the term "island Universe", though there was no observational evidence to support this model. Only after the great work by Edwin Hubble in the 20th century, who calculated the distances of these "nebulae" and found that the distances of these objects were much greater than the size of our own Galaxy. In this way, the extragalactic objects were identified and galaxies were redefined as "islands" in the "sea" called the Universe.

In 1908, astronomers discovered an unusual optical spectra of a nearby galaxy (later called NGC 1068 galaxy) at Lick observatory, showing multiple strong emission lines over the continuum flux (Fath, 1909). After that, these emission spectra were recorded in many other galaxies (e.g. NGC 1068, NGC 1275, NGC 4151). However, a systematic study of these findings was only performed by Carl Seyfert in 1943, which led to the beginning of a new class of galaxies (Seyfert, 1943). He noted that these galaxies have very high surface brightness, and this emission comes from a very compact region (within 100 pc of the galactic centre) at the centre that outshines the entire galaxy. It was pointed out that the emission lines in their spectra are of very high excitation and extremely broad (e.g. $\Delta v \sim 10000$ km/s). The high excitation energy of some emission lines shows that the responsible atom must have been excited by very highly energetic photons. Seyfert, 1943 work was so important that one of the classes of these objects is named after him: *the Seyfert galaxies*. With time, many more Seyfert galaxies were discovered, and their properties were better constrained. In 1959, Lodewijk Woljer claimed that the extent of the bright core could not be greater than 100 pc otherwise, they could be spatially resolved.

With the advent of radio astronomy around the 1950s, a milestone was achieved with the discovery of quasars (3C and 3CR radio catalogues; Edge et al. 1959) that opened the doors of a new extremely energetic Universe. These discoveries drew the attention of astronomers and astrophysicists, and the physics of AGNs became the area of extensive research since then. In 1963, Thomas Matthews and Allan Sabdage showed that the quasar 3C48 is a point-like source of magnitude 16, consisting of a blue continuum and strong emission lines (Greenstein, 1963). In the same year, with the calculation of the high cosmological redshift of the 3C273, the idea of accretion of matter onto the black hole was kept forward to support the enormous amount of emission from the small spatial region (Shields, 1999). Later, this idea was encouraged by the discovery of black hole X-ray binary sources in our Galaxy. Recently reported images of the supermassive black holes (SMBH) at the centres of the Milky Way and M87 galaxies by EHT collaboration (Event Horizon Telescope Collaboration et al., 2019, 2022) confirm the idea of SMBH at the centre of each galaxy. Still, there are several important questions which remain unanswered on the formation and fuelling of the super massive black hole at the centre, the geometry of the central region, the emission mechanisms in different wavebands, the launching and collimation of jets, and other aspects. The AGNs are so complex that they will remain a topic of intense research in astronomy and astrophysics for the foreseeable future.

1.2 AGN taxonomy & Unified model

The classification of AGNs is complex and somewhat confusing. Different classes of AGNs correspond to different observational appearances irrespective of the intrinsic physical nature of the source. We discuss later in the context of the Unified model how the appearance of AGNs depends on the orientation with respect to our line of sight. Here, we state some simple taxonomy of the AGNs:

Seyfert galaxies- This is the category which was first identified as AGNs. They come with moderate bolometric luminosity ($L_{bol} = 10^{41-45}$ erg s^{-1}). They are generally radio-quiet and have high surface brightness at the core. From the optical images, their host galaxies are identified as spirals with massive galactic bulges whose spectra show strong high-ionization emission lines. The Seyfert galaxies are divided into two categories such as Seyfert 1 and Seyfert 2.

Type 1 Seyferts show two sets of emission lines in their spectra, i.e. (i) highly ionized broad permitted lines with widths up to thousands of km/s and (ii) narrow permitted lines with width of several hundred km/s. The broad emission lines originate from the regions closer to the supermassive black hole (within 0.1-1 parsec) called broad-line regions (BLRs). The BLRs are thought to be dense ($n_e \geq 10^9$ cm^{-3}; Ilić et al. 2010) and highly ionized on the basis of broad lines. The location of the BLRs can be estimated from the observed time delay due to the additional path travel by photons from the continuum source to the line emitting gas before reaching the observer. The narrow lines originate from comparatively low density ($n_e \sim 10^{3-6}$ cm^{-3}; Peterson 2006) and low ionization regions called the narrow-line regions (NLRs). There is another subclass of Seyferts called narrow-line Seyfert 1 (NLS1) galaxies which also show broad lines, but they are relatively narrower than that of the typical Seyfert 1s.

Type 2 Seyfert galaxies are bright in the infrared band apart from the characteristic bright core. Their spectra show narrow forbidden lines. They have [OIII] λ5007 to Hβ λ4860 ratio of < 3 (Shuder & Osterbrock, 1981). It is thought that the difference between the type 1 and 2 arises from the orientation of these galaxies with respect to our line of sight. This point will be discussed in detail later. There are intermediate classes of Seyfert galaxies (e.g. 1.2, 1.5, 1.8), first introduced by Donald Osterbrock in 1981 (Osterbrock, 1981), where the strength of the broad line component is less compared to the narrow line component.

Quasi-Stellar Objects (QSOs) or Quasars- The QSOs are the most luminous of the

AGN family ($L_{bol} = 10^{44-47}$ erg s^{-1}), usually found at higher redshift ($z > 0.1$). Their core luminosity is so high that they outshine their host galaxies and appear as point-like sources in optical images. Radio-loud quasars, which constitute 10% (Peterson, 1997) of the total population of quasars, emit significantly in the radio band, and emission in radio band is associated with the relativistic jets. There is a type 2 category of quasars, where the direct view of the accretion disc and the broad-line region is obscured by dust and gas, as in the case of the Seyfert 2 galaxies. Therefore, they are considered the luminous counterparts of the Seyfert 2 galaxies.

Radio Galaxies - These are bright in radio emission, which is known to be coming from the extended jets due to the synchrotron process (Krolik, 1999). Their host galaxies are known to be elliptical and are detected at large distances. They show lobes or plumes extending up to the megaparsec scale. They can be classified as broad-line radio galaxies (BLRGs) and narrow-line radio galaxies (NLRGs), depending on their optical/UV spectra. In 1974, Fanaroff and Riley divided radio galaxies into two categories (FRI and FRII) on the basis of the morphology of their large-scale radio structure (Fanaroff & Riley, 1974). The FRIs typically have bright jets at the centre, and the FRIIs have bright hot spots at the end of the lobes.

Flat Spectrum Radio Quasars (FSRQs) and BL Lacs- One subclass of AGNs, known as Optically Violently Variable (OVVs), is characterized by rapid variability by a significant fraction on a short time scale in radio to optical energy bands. The FSRQs are nearly isomorphic to the old OVV class. Apart from the highest variability, these sources show relatively high polarization in the optical emission. The BL Lacs (named after their prototypical source BL Lacertae) show highly variable emission but without showing strong emission or absorption lines in their spectra. Due to the lack of strong lines, sometimes it becomes difficult to estimate their redshift. Sometimes, the redshift is calculated from the absorption lines which are assumed to have originated from their host galaxy. The FSRQs and BL Lacs are collectively known as blazars. All the known blazars are strong emitters of radio and X-ray radiation though copious γ-rays are also usually detected. Blazars are dominated by power-law continua in the IR through UV bands. Only some of the FSRQs have a detectable thermal component in their spectra.

LINER- In 1980s, Timothy Heckman identified a subclass of AGNs called Low-Ionization Nuclear Emission Line Region (LINER). This class is identified with weakly-ionized or neutral emission lines.

1.2.1 Unified model

The Unified scheme is generally referred to two categories: IR-optical-UV-X-ray unification and radio unification. The first category can explain the differences between the type-I (or type 1) and type-II (or type 2) AGNs. According to this Unified model, all radio-quiet AGNs are intrinsically the same, and the differences in their observational characteristics come from different inclination angles of obscuring torus (see section 1.3.3) with respect to our line-of-sight. The second category takes into account the torus with relativistic jets. The radio unification is used to explain certain observed features of the compact and extended radio-loud AGNs (Urry, 2003; Tadhunter, 2008). Here, the discussion is restricted to category 1 only.

It is now largely accepted that type-I and II house the same engine at the core. In 1985, Antonucci and Miller (Antonucci & Miller, 1985) analyzed the optical spectra of Seyfert 2 galaxy NGC 1068 in polarized light. The scattered spectra showed broad emission lines very similar to those observed ubiquitously in Seyfert 1 spectra. This implies that the type-I and type-II Seyfert galaxies are intrinsically the same. Due to the hidden view of the BLRs, some of the features of Seyfert 1 are absent in Seyfert 2 galaxies and vice versa, while the NLRs are visible for both. According to this model, every AGN has a supermassive black hole ($M_{BH} > 10^6$ $M_\odot$) at the centre, which is accreting matter from the surrounding medium. This accreting material forms a disc around the supermassive black hole where the gravitational energy is converted into heat energy and radiation (Shakura & Sunyaev, 1973a). The disc emission is in the form of a multicolour blackbody which usually peaks in the UV band for AGNs. The photons from the inner part of the disc interact with the relativistic hot electron plasma called "corona" or "Compton cloud" and give rise to the X-ray emission (see Section 1.5.1). In the immediate circumnuclear environment, there are clouds of hot gas in Keplerian motion (BLR regions) and that produce broad emission lines in type-I AGNs. In radio-loud AGNs, the relativistic jets are present, which are highly collimated and perpendicular to the accretion disc plane. Beyond the BLRs, the central region is enshrouded by an optically thick putative torus which is made of gas and dust. In radio-quiet AGNs like Seyferts, it is the orientation of this torus which decides whether a galaxy is observed as a Seyfert 1 or a Seyfert 2 (see Figure 1.1). Therefore, an observer looking at the edge-on of the torus is obscured from the direct view of the BLR emission and only NLRs are visible to the observing eye. On the other hand, if our line of sight is face-on (i.e. near the axis of the torus), we can directly peek into the innermost region of the AGN. Therefore, the Unified

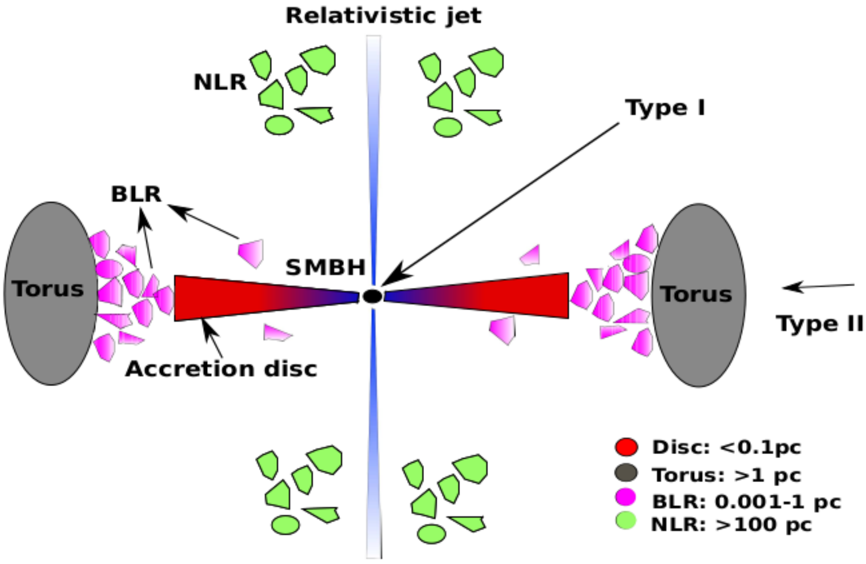

Figure 1.1: The Unified model showing different components of an AGN with their typical distances from the centre. It consists of a SMBH, an accretion disc, obscuring torus, the BLRs and NLRs. Image adapted from Antonucci, 1993.

model can explain the differences between type-I and type-II with a minimum number of assumptions. Although this model explains the basic phenomenology of complex AGNs, it ceases to successfully explain an increasing set of observations which are in disagreement with the unified model (Bianchi et al., 2012).

1.3 Structure of an AGN

1.3.1 The central engine

As mentioned in Section 1.1, the enormous amount of energy produced in the AGNs must be related to the supermassive black hole at the centre. The extremely strong gravity of the supermassive black hole at the centre is responsible for the very high luminosity of the AGNs. The most efficient "usual" method for energy production is nuclear fusion, as in the case of the stars, where hydrogen is burnt into iron. The binding energy per nucleon of iron is 8 MeV, or we can say 0.008 $m_p c^2$ per nucleon energy is released in the fusion. In this way, the efficiency of this process is only $\sim 0.8\%$. Thus, a physical mechanism such as accretion of matter onto the massive black holes at the centre of the host galaxies can provide highly efficient ($\sim 6 - 29\%$) conversion of gravitational potential energy to radiation (Kembhavi & Narlikar, 1999). Here, the process of accretion is described in detail:

Accretion - The idea of accretion of matter onto the stars was first proposed by Bondi, 1952 which involved the spherical accretion and gas dynamics in the gravitational field. In this case, the steady-state accretion rate ($\dot{m}$) onto a star is determined by the conditions of the surrounding medium in the interstellar medium at large distances and flow conditions, whether it is subsonic or supersonic. However, for this kind of accretion, $\dot{m}$ is too small to show any observational signature. For a massive black hole such as the one at the galactic centre, the net angular momentum of the gas shed by nearby stars should be substantial enough to lead to the formation of a disc around the black hole. The disc could be thick or thin depending on whether its height (H) is comparable to its radius (R). Here, further discussion will be restricted to the thin disc ($H << R$).

The accreted gas approaching the black hole loses its gravitational energy and converts a part of it into kinetic energy and the rest into radiation and heat energy. This accreting gas surrounding the black hole forms a geometrically thin, optically thick disc (Shakura & Sunyaev, 1973a) in which the gas loses its angular momentum. The gas in the disc is heated by internal friction. This friction also reduces the rotational velocity, whereby the gas slowly moves inwards. The total energy released through the process of accretion is given by:

$$L_{acc} = \eta \dot{m} c^2$$

where, η is the efficiency of converting mass into radiation, and c is the speed of light. The efficiency depends on the compactness of the accreting object as $\eta = GM/Rc^2 = R_s/2R$, where R_s is the Schwarzchild radius for a non-rotating black hole. For a non-spinning black hole, the radius of the Innermost Stable Circular Orbit (ISCO) is defined as $R_{ISCO} = 6GM/c^2 = 3R_s$, whereas for a maximally rotating black hole, $R_{ISCO}\sim$ 1.235 R$_s$. The luminosity (L_{acc}) depends on the mass accretion rate, which further depends on the mass of the central black hole. There is an upper limit on the luminosity called *Eddington luminosity* which is reached when the radiation force becomes equal to the gravitational pull of the black hole. For a spherical geometry of accretion and gas of fully ionized hydrogen, the *Eddington luminosity* is defined as

$$L_{acc} \leq L_{Edd} = \frac{4\pi G c m_p}{\sigma_T} M_\bullet = 1.3 \times 10^{38} (M_\bullet/M_\odot)\ erg\ s^{-1}$$

where G, m_p, σ_T, $M_\odot$ and $M_\bullet$ are the gravitational constant, the mass of the proton, Thomson cross-section, mass of the Sun, and mass of the central black hole, respectively. In reality, the geometry is not spherically symmetric. Many a time, the luminosity exceeds the Eddington limit, which is called *super-Eddington emission* and some of the accreted gas is expelled due to the high radiation pressure. In practice, the Eddington ratio ($\lambda_{Edd} = L_{acc}/L_{Edd}$) is often used to estimate the mass accretion rate in AGNs.

Temperature profile of an accretion disc- Formation of the accretion disc takes place when the angular momentum of the gas is lost locally though the total angular momentum is conserved. For the conservation of angular momentum, the angular momentum lost due to the in-falling of matter has to be recovered through the angular momentum gained by the matter in the outer part of the disc. In 1973, Nikolai Shakura and Rashid Sunyaev gave an approximate solution to the problem of "angular momentum transport" for an optically thick and geometrically thin accretion disc (Shakura & Sunyaev, 1973a). In their "α-disc model", the flow of accreted matter is assumed to be in the steady-state and in Keplerian motion locally. The turbulence in the gas is responsible for the generation of viscosity. For subsonic turbulence, the viscosity (called α-viscosity) can be approximated as:

$$\nu = \alpha c_s h$$

where, c_s and h are the sound speed in the matter and half-thickness of the disc, respectively. Here, α is a free parameter that depends on the rate of accretion. In this model, the rate is assumed to be constant. The equation of the temperature profile of the disc can be solved by using the equation of hydrostatic equilibrium, mass and angular momentum conservation for a thin disc. Here, we describe an approximate solution of the temperature equation through fundamental physics.

Suppose a particle of mass m at a distance of $R+\Delta R$ around a compact object (black hole in the case of AGNs) of mass M reaches the distance R due to the influence of the gravitational force of the compact object. Then, half of the gravitational energy of the particle is dissipated in the form of heat due to the gravitational potential of the black hole. Assuming the disc as optically thick, geometrically thin and locally emitting as a blackbody, the luminosity of the disc can be expressed as;

$$\Delta L = \frac{GM\dot{m}}{2R^2}\Delta R$$

where $\dot{m}$ is the mass accretion rate. The disc ring between R and ΔR emits a luminosity,

$$\Delta L = 2 \times 2\pi R^2 \sigma_{SB} T^4 \Delta R$$

where T is the temperature of the disc at a radius R and σ_{SB} is the Stephan-Boltzmann

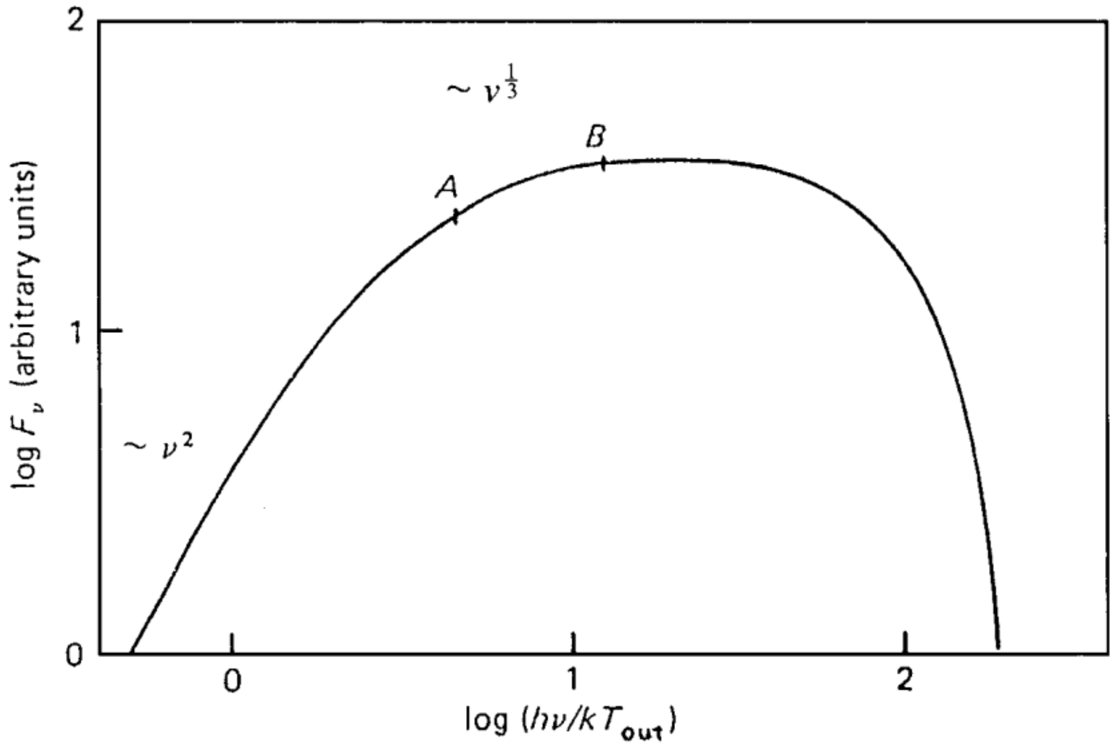

Figure 1.2: Accretion disc temperature profile for geometrically thin and optically thick disc. Credit: (Kembhavi & Narlikar, 1999)

constant. A factor of two has been incorporated to take into account the two faces of the disc. By equating and re-arranging these two equations, we get

$$T(R) = \Big(\frac{GM\dot{m}}{8\pi R^3 \sigma_{SB}}\Big)^{1/4}$$

A more accurate expression can be derived by considering the dissipation of energy through viscous torque. The expression for the resulting effective surface temperature becomes,

$$T(R) = \Big(\frac{3GM\dot{m}}{8\pi R^3 \sigma_{SB}}\Big)^{1/4}$$

for $R >> R_s$.

The above equation can be simplified again and scaled as,

$$T(R) \approx 6.3 \times 10^5 \Big(\frac{\dot{m}}{\dot{m}_{Edd}}\Big)^{1/4} \Big(\frac{M}{10^8 M_\odot}\Big)^{-1/4} \Big(\frac{R}{R_S}\Big)^{-3/4} \mathrm{K}$$

With this temperature profile, the thermal emission from an accretion disc becomes a multi-colour blackbody spectrum peaking in the UV band for an AGN (see Figure 1.2).

1.3.2 Narrow-Line and Broad Line Regions (NLRs & BLRs)

The type-I and type-II classes of AGNs are distinguished on the basis of the width of the emission lines in their optical spectra. These emission lines are the basic signatures of AGNs and have been extensively studied for more than 60 years. The representative lines in the AGN spectra are hydrogen Balmer lines like Hα λ6563, Hβ λ4861, Hγ λ4340, Lyman Hα λ1216 and heavy element ions Mg II λ2798, [C III] λ1909, and C IV λ1549. The observed width, variability and other properties of these lines show that they emanate from different regions of the AGN, designated as broad-line regions (BLRs) and narrow-line regions (NLRs).

The BLRs are present in all types of AGNs. These BLR clouds are located very close to the accretion disc, outspread within about 100 light days ($<$ 0.1 pc) from the centre in Seyfert 1 galaxies, and its outer edge is likely to be merged with the dusty torus (Suganuma et al., 2006). There is no well-established mechanism which can determine the effective radius of the region, although there are studies giving power-law relation between the BLR radius and the optical luminosity. The emitting medium is primarily in Keplerian motion with additional velocity components (Done & Krolik, 1996). The density of the BLR is $\sim 10^9$cm^{-3} and typical gas velocity calculated from the broadening of emission lines is up to 10^4 km s^{-1}. From the ionization state of the atoms corresponding to the observed emission lines, a typical temperature of the BLR can be calculated and comes out to be $\sim$ 20000 K. Studies of the BLR play an important role in understanding the accretion and emission mechanisms in the AGNs and in determining the mass (reverberation mapping method) of the corresponding supermassive black holes (Peterson et al., 2004; Bentz et al., 2007).

The NLRs are known to be located at larger distances as there is no evidence of variation echoing the continuum variation. The extent of this region is around 300 pc which can be resolved in optical bands through ground-based observations. The density of the NLR is 10^{3-6} cm^{-3} which is estimated through the forbidden lines in the spectra. The gas velocity or the line width is less than 2000 km s^{-1} which is considerably narrower than that of the BLRs but significantly broader than that found in the spectra of normal galaxies. The strongest line from this region is forbidden [O III] λ5007. The characteristic temperature of the gas, obtained from the allowed and forbidden line ratio, is T$\sim$16000 K which is lower than that of the BLRs. The morphology of the NLR is cone-shaped, which suggests that the ionization of the NLR is not isotropic, instead depending on the direction.

1.3.3 Dusty/molecular torus

The putative torus is an important component of the AGN structure (Krolik & Begelman, 1988). The unified model for the observational features of type-I and type-II AGNs is based on this toroidal structure. The direct observational evidence for the existence of torus are only available for a few nearby AGNs, e.g. NGC 1068 (Raban et al., 2009), Circinus (Tristram et al., 2014). The torus surrounding the central black hole and the accretion disc, at a distance of roughly 1 pc, consists of molecular gas and dust (temperature $\sim 10^3$ K). The simplest geometrical structure of the torus is considered as continuous matter distribution in toroidal form, although recent observational studies differ from this simple geometry and predict clumpy structure in the form of moving clouds. The obscuring material absorbs intrinsic emission coming from the centre and gets ionized at the inner radius of the torus. It re-radiates in the infra-red (IR) band, thus providing information about the dusty material. There are multiple hypotheses for the formation of the dusty structure (Nenkova et al., 2008a; Wada, 2012; Guainazzi et al., 2016).

1.3.4 Corona or Compton cloud

It is necessary to understand the way an accretion disc gets illuminated by the continuum X-ray emitter above the black hole, i.e. corona, to have a better understanding of the inner disc region. The formation and energetics of the corona are not completely understood. However, it is thought to be a result of acceleration and confinement of energetic particles by the magnetic field encapsulated to the accretion disc (Haardt & Maraschi, 1991). The geometry of this Comptonizing corona generating power-law continuum in X-ray is very complex. It could be a point-like, compact medium hovering above the black hole axis or extended over the inner part of the disc or of a patchy structure (Reynolds & Nowak, 2003).

In the disc-corona or two-phase model (Haardt & Maraschi, 1991), the X-rays are produced in a hot, optically thin corona (phase 1) embedding cold and optically thick inner accretion disc (phase 2) via inverse-Compton scattering. The seed (or soft thermal) photons are provided by the cold accretion disc for the cooling of hot plasma in the corona. Simultaneously, a fraction of the hard X-ray photons works as a source of heating the underlying cold disc, which reprocesses them into soft photons. In this way, these hot and cold phases are coupled with each other. The possible configuration for this kind of disc-corona system could be the two homogeneous isothermal layers in plane-parallel geometry where the hot layer is above the

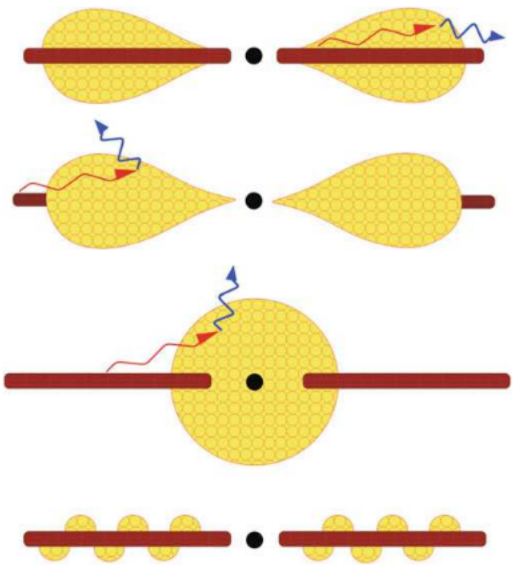

Figure 1.3: Different corona geometries are shown around the black hole (black) and above the accretion disc (brown). Slab or sandwiched geometry at the top panel, two middle panels referred as "sphere+disc" geometries and a patchy corona at the bottom panel are shown. Credit: Reynolds & Nowak, 2003.

cold disc. There could be other types of geometry where instead of a single smooth corona, there are several smaller regions above the disc. In this case, the patchy corona contains many blobs and a fraction of available energy is released in the corona. The patchy corona can be formed due to the magnetic loops in which energy is stored and lost through reconnection (Haardt et al., 1994). This model can explain the variability of emission that arises due to the change in the accretion rate or due to the variation in corona blobs. Different kinds of geometries have been shown in Figure 1.3.

Another widely accepted coronal geometry is the lamp-post model (Matt et al., 1991; Miniutti & Fabian, 2004). In this model, a point-like source is located at the rotation axis of the black hole above a certain height from the accretion disc and illuminates the disc. This model can successfully explain the absence of correlation between the iron line and the X-ray continuum emission. The effect of light bending due to the strong gravitational field of the BH and resulting variation of the reflection component as well as broadening of the iron line can be explained by this model readily. In this scenario, the AGN requires a compact corona which shows a reflection dominated spectrum (Fabian et al., 2012).

Compactness of the corona

It has been observed that the X-ray emission from the AGNs originated from the compact and hot medium. The rapid variability observed in the X-ray emission from many AGNs indicated that the corona is compact. The variability studies of the lensed quasars also support this conclusion and estimate the size of the corona to be approximately $6R_g$ (Zimmer et al., 2011), where $R_g(= GM/c^2)$ is called the gravitational radius. Other evidence of physically compact corona are provided through the emissivity profile of the iron line (Wilkins & Fabian, 2011) and variable obscuration of the corona by the clouds (Risaliti et al., 2011). Highly luminous and physically compact sources can also be compact radiatively, in the sense that the interactions between photons and particles involving energy exchange between them are very common in the medium. This property of the source is defined as the "compactness" (l) and can be described as the ratio between the luminosity and the size of the source (Ghisellini, 2013),

$$l = \frac{L}{R}\frac{\sigma_T}{m_e c^3}$$

where, L is the luminosity, R is the radius of the spherical source, σ_T is the Thomson cross-section and m_e is the mass of the electron.

In terms of Eddington luminosity L_E,

$$l = \pi\frac{m_p}{m_e}\frac{L}{L_E}\frac{R_g}{R}$$

From this equation, it can be calculated that the sources with luminosity greater than 1 percent of the Eddington luminosity with size less than $20R_g$ are compact with $l > 10$.

If the photons are energetic enough, they can lead to electron-positron pair production. The pair density in the source is directly proportional to the luminosity and temperature, and inversely proportional to the size of the source. The pair production becomes a run-away process, i.e. out-pacing annihilation, limiting a further rise in the temperature. The physical properties of the thermal plasma can be understood by looking at $\theta - l$ plane ($\theta = kT_e/m_ec^2$) (see Figure 1.4). The dominant process in the plasma would be the one for which the cooling time scale is shorter. In the coronal plasma, the dominant processes are inverse Compton scattering, Bremsstrahlung and pair production. Considering the spherical source size of radius R, optical depth τ and luminosity L, the Compton cooling time can be expressed as (Fabian et al., 2015)

$$t_C = \frac{3\pi R}{2cl(1+\tau)}$$

In terms of light crossing time $t_{cross} = R/c$,

$$t_C = \frac{3\pi}{2l(1+\tau)} t_{cross}$$

For $l > 2$, we have $t_C < t_{cross}$. This signifies that when l is greater than 1, the electron loses its energy sufficiently while crossing the size of the emitting region.

Bremsstrahlung cooling time for an electron is,

$$t_B = \frac{\theta^{1/2} R}{\tau \alpha_f c}$$

where, α_f is the fine structure constant. The upper limit of the compactness parameter can be obtained when,

$$l \approx 3\alpha_f \theta^{-1/2}$$

This means at higher compactness, the Comptonization process dominates. Two particle collisions are the basic heating and thermalization process. The electron-electron coupling occurs when,

$$l < 80\ \theta^{-3/2}$$

The electron-proton coupling dominates over the electron-electron coupling when (Fabian, 1994),

$$l < 0.04\ \theta^{-3/2}$$

As mentioned above, at a certain regime, the pair production becomes a pair runaway process and identified as pair runaway lines. The position of these lines depends on the shape of the source. Stern et al. (1995) calculated this line for a slab corona. Svensson (1984) computed pair balance line for an isolated cloud when,

$$l \sim 10\ \theta^{5/2}\ e^{1/\theta}$$

1.4 X-ray emission mechanism in AGNs

The electromagnetic radiation from an AGN is known to be a mixture of thermal (blackbody) and non-thermal radiation originating from different regions of the system. Here, we discuss

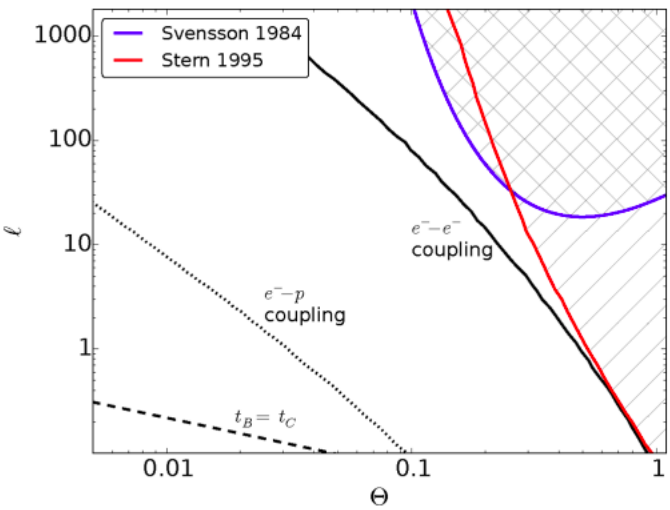

Figure 1.4: $\theta - l$ plane as described in the Section 1.3.4, Image credit:Ghisellini et al., 1993.

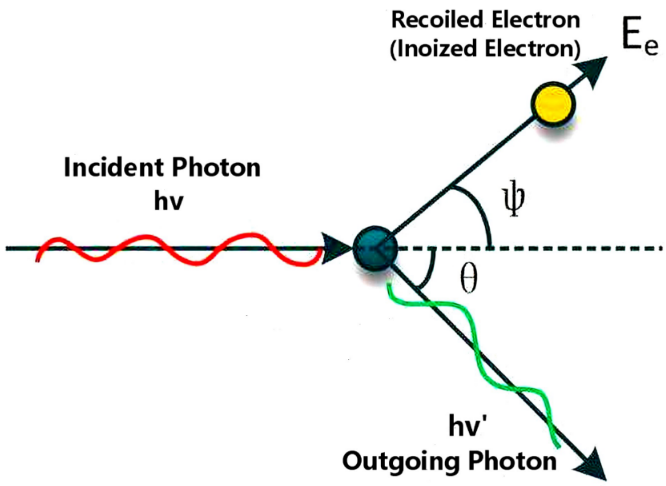

Figure 1.5: Illustration of scattering of a photon by an electron. Image credit: Qiao et al., 2021.

the three emission mechanisms briefly. A detailed discussion can be found in Rybicki & Lightman (1979), which we follow in the rest of this subsection.

1.4.1 Compton scattering

The scattering between a charged particle like an electron and a photon can happen in one of three ways depending on the energy of the photon and the rest mass energy of the charged particle. When the energy of the incoming photon is low compared to the charged particle ($h\nu << m_e c^2$), Thomson scattering occurs. This scattering is also called “coherent” or “elastic” scattering. Compton scattering is a phenomenon when the photon energy is comparable to or greater than the electron energy. In astrophysical sources, the inverse Compton scattering or Comptonization plays an important role than the Compton scattering process. In the process of Comptonization, a photon undergoes multiple scattering with a thermal distribu-

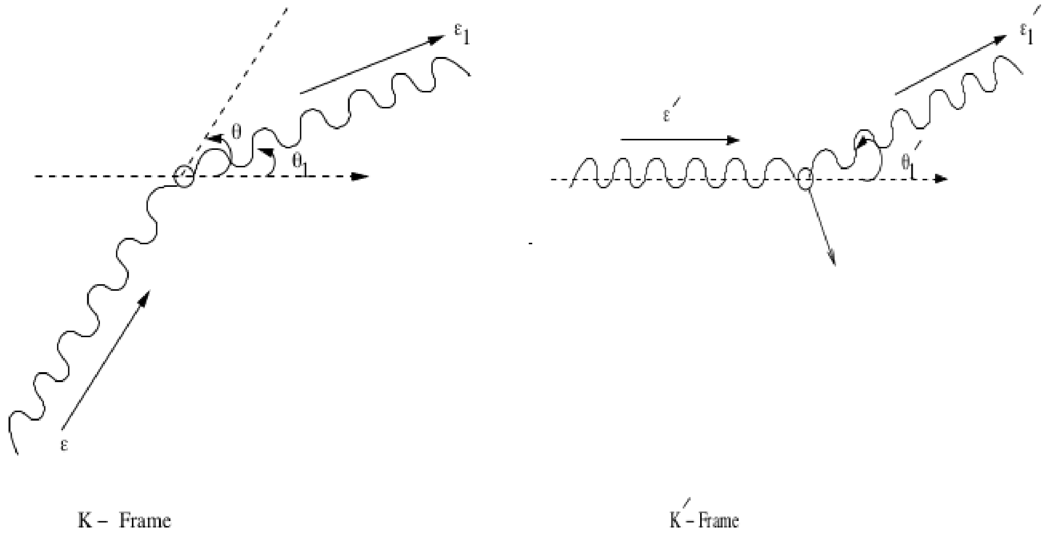

Figure 1.6: Illustration of scattering directions in the laboratory and rest frames of the electron. Image is taken from the lecture notes available at https://www.iucaa.in/ dipankar/ph217/.

tion of electrons. In this process, the photon gains energy from the energetic electrons.

The energy of the scattered photons can be estimated by applying the energy and momentum conservation laws in the rest frame of the electron. Considering the initial and final four-momentum of the photon as $\vec{P}_{\gamma i} = (\epsilon/c)(1, \vec{n}_i)$ and $\vec{P}_{\gamma f} = (\epsilon'/c)(1, \vec{n}_f)$, where $\vec{n}_i$ and $\vec{n}_f$ are the initial and final directions of the photon (Fig 1.5), and the initial and final momenta of the electron as $\vec{P}_{ei} = (m_e, 0)$ and $\vec{P}_{ef} = (E/c, \vec{p})$, the energy of the scattered photon can be expressed as,

$$\epsilon' = \frac{\epsilon}{1 + \frac{\epsilon}{m_e c^2}(1 - cos\theta)}$$

In terms of wavelength, it becomes

$$\lambda' - \lambda = \lambda_c(1 - cos\theta)$$

where $\lambda_c = h/m_e c = 0.02426$ Åis the Compton wavelength of the electron.

When the plasma is embedded in a radiation field of temperature T_{rad}, the scattering of photons and electrons continuously transfers energy between them. During scattering, the high energy photons with energy $m_e v^2 << \hbar\omega << m_e c^2$ transfer energy to low energy electrons, while the low energy photons gain energy from the high energy electrons with $\hbar\omega << m_e v^2$. In thermal equilibrium, there is no net energy transfer between the photons and electrons. If the temperature of the electron $T_e >> T_{rad}$, the electron are cooled by transferring energy to the photons and the process is called inverse Compton scattering. In astrophysical sources, this mechanism can substantially boost the energy of the optical/UV photons to X-ray range through multiple Compton scattering. Due to multiple scattering, the spectrum of the photons gets distorted.

Let us consider K and K' be the laboratory and rest frames of the electron, respectively (see Figure 1.6). The energy of the scattered photon ϵ' in the K frame can be expressed as,

$$\epsilon'_1 = \frac{\epsilon'}{1 + \frac{\epsilon'}{m_e c^2}(1 - cos\theta'_1)}$$

In the laboratory frame, the energy of the scattered photon is given by the Doppler formula,

$$\epsilon_1 = \gamma\epsilon'_1(1 + \beta cos\theta'_1)$$

where, γ is the Lorentz factor and β is the relativistic velocity of the electron in the K frame. In the rest frame of the electron, for $\theta'_1 = \pi/2$

$$\epsilon_1 \approx \gamma\epsilon'_1$$

Assuming, in the K' frame, $\epsilon' << m_e c^2$, so that $\epsilon' \approx \epsilon'_1$. Thus, we have $\epsilon_1 \approx \gamma\epsilon'$. From Doppler shift formula,

$$\epsilon' = \gamma\epsilon(1 - \beta cos\theta)$$

Thus we have, $\epsilon_1 \approx \gamma^2\epsilon$ It is clear that for relativistic electrons, the low energy photons gain energy by a factor of γ^2.

The power emitted by the photons for a single scattering is given by

$$P_{Compt} = \frac{4}{3}\ c\ \sigma_T\ \gamma^2\beta^2 U_{rad}$$

where, σ_T, c and U_{rad} are the Thomson cross-section, speed of light and initial radiation energy density, respectively. The Compton power for $N(\gamma)d\gamma$ number of relativistic electrons per unit volume can be expressed as :

$$P_{tot} = \left(\frac{4k_B T}{m_e c^2}\right) c\sigma_T n_e U_{rad}$$

The energy transfer from the electrons to the photons acts as the source of cooling of the relativistic plasma. The time scale for Compton cooling of an electron is given by,

$$t_{cc} \approx \frac{\gamma m_e c^2}{P_{Compt}}$$

Thermal Comptonization is a process of multiple scattering of photons by a thermal distribution of electrons. In this context, an important parameter is defined as *Compton y-parameter* that gives a condition on how significantly a photon changes its energy while traversing the plasma medium. The mean free path of the photon due to Thomson scattering is $\lambda_\gamma = (n_e \sigma_T)^{-1}$ in the medium of size l. If the optical depth of the medium $\tau (= l/\lambda) >> 1$, the photon undergoes many collisions in the plasma. In this condition, if N is the number of collisions in size l, we have $N = \tau^2$ for $\tau >> 1$ and $N = \tau$ for $\tau < 1$. Therefore, the number of scattering is $max(\tau, \tau^2)N$. The fractional energy of the photon in one collision is given by $\frac{4k_BT}{m_ec^2}$. Hence, for significant change of energy,

$$1 \approxeq N \frac{4k_BT}{m_ec^2} max(\tau, \tau^2)$$

Here, the Compton y-parameter is defined as $y = \frac{4k_BT}{m_ec^2} max(\tau, \tau^2)$ and for significant scattering, $y \approxeq 1$. The change in the energy of a photon after N scattering is given by

$$\frac{\epsilon'}{\epsilon} = \Big(1 + \frac{4k_BT}{m_ec^2}\Big)^N \approxeq exp\Big(\frac{4k_BT}{m_ec^2} N\Big) = exp(y)$$

If the initial mean frequency of the photons is ν with $h\nu << k_BT$, the photons gain energy from the electrons till their energy rises to $4k_BT$. In Figure 1.7, the spectrum of the photons is shown for two different ranges of optical depth.

1.4.2 Bremsstrahlung

"Bremsstrahlung" is a German word that stands for 'braking radiation'. When high energy electrons are bombarded at a target with a high atomic number (Z), some of the electrons get deflected towards the electric field of the protons in the nucleus. Due to the deflection, the electrons emit X-ray photons by losing their kinetic energy. Bremsstrahlung can have energy in the range from 0 to the maximum energy of the electron, depending on how much an electron gets affected due to the electric field, thus producing a continuous spectrum. The intensity of the emitted radiation is directly proportional to the square of the atomic

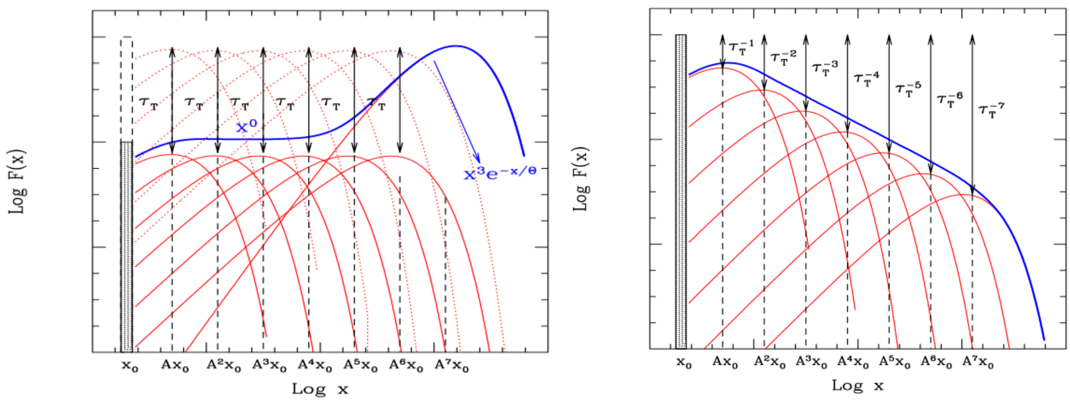

Figure 1.7: The resultant spectrum of the photons undergoing multiple Compton scattering for $\tau > 1$ and $y >> 1$ is shown in the left panel. In this case, almost all the photons are scattered and the number of photons escaping the medium at each scattering is the same. In the flat part of the spectrum, the photon frequency is of the order of k_BT and the photons and electrons are in equilibrium. The small fraction of escaping photons do not change their frequency and, therefore, give the Wien hump. The right panel shows the photon spectrum for multiple Compton scattering for $\tau < 1$. A fraction of the photons of the previous scattering undergo another scattering and increase the frequency by a factor of $(4k_BT/m_ec^2)$ until it reaches k_BT. After that, there is no change in the frequency. Credit: (Ghisellini, 2013).

number (Z), a number of bombarding particles and inversely proportional to the mass of the bombarding particles. Therefore, the light mass particles such as electrons are efficient emitters of Bremsstrahlung radiation.

The total power radiated in the case of an electron with charge e and moving with velocity v close to an ion of charge Ze with an impact factor b is given by

$$P = \frac{4}{3}\frac{Z^2e^6}{c^3m_e^2b^3v}$$

The total emissivity from a cloud of ions and electrons where electrons have the same fixed velocity can be expressed as

$$J(v,\nu) = \frac{32\pi Z^2e^6}{3c^3m_e^2}\frac{n_en_z}{v}ln\left[\frac{b_{max}}{b_{min}}\right]$$

The value of b_{max} is of the order of b/w, where w is called the characteristic frequency.

1.4.3 Synchrotron emission

When a relativistic electron gets accelerated in a magnetic field, the radiation emitted by the electron is called Synchrotron radiation. The photons emitted from the jet of AGNs are the result of Synchrotron emission. The Lorentz force experienced by a particle of rest mass m, charge e and velocity v in a magnetic field B which is given by,

$$\frac{d}{dt}(\gamma m\vec{v}) = \frac{e}{c}(\vec{v} \times \vec{B})$$

where $\gamma = (1 - v^2/c^2)^{-1/2} = (1 - \beta^2)^{-1/2}$, is the Lorentz factor. Due to this force, the particle moves in a helical path with its axis parallel to $\vec{B}$. The gyration frequency of the particle is $\nu_g = \frac{eB}{2\pi\gamma mc}$. The total power emitted by a charged particle is given by

$$P = \frac{2}{3}\Big(\frac{e^2}{mc^2}\Big)^2 c\beta^2\gamma^2 B^2 (\sin\alpha)^2$$

Here, α is the angle between the velocity and magnetic field and is known as the pitch angle. This power is emitted in a narrow cone shape with an opening angle $\sim 1/\gamma$. Since $P \propto m^{-2}$, the heavier particles are less effective than the lighter ones, e.g. the electrons. A radiating electron loses its energy and cools down. In a constant magnetic field, the time taken by the electron to lose half of its energy is,

$$t_{1/2} = 8.5 \times 10^9 \Big(\frac{B}{1\mu G}\Big)^{-2}\Big(\frac{E}{1\ GeV}\Big)^{-1} yr$$

Synchrotron emission from electrons ensemble - The emitted power i.e. energy emitted per unit frequency interval is given by (for a critical frequency ν_c),

$$p(E,\nu) = \frac{\sqrt{3}e^3 B\sin\alpha}{mc^2} F(\nu/\nu_c)$$

with $F(x) = x\int_x^\infty K_{5/3}(\zeta)d(\zeta)$, where $K_{5/3}(\zeta)$ is the modified Bessel function of order 5/3. If we consider an ensemble of electrons in the energy range (E_1, E_2) with number density $n(E)$, the power emitted by the electrons as a function of frequency is given by,

$$P(\nu) = \int_{E_1}^{E_2} p(E,\nu)n(E)d(E)$$

For power-law distribution of the electrons with number density $n(E) = CE^{-p}$ (C and p are constants),

$$p(\nu) \propto \int_{E_1}^{E_2} E^{-p} F(\nu/\nu_c)d(E)$$

Changing the variable $x = \nu/nu_c$,

$$p(\nu) \propto \nu^{-(p-1)/2} \int_{x_1}^{x_2} F(x) x^{(p-3)/2} d(x)$$

Here, $x1 = \nu/nu_1$ and $x2 = \nu/nu_2$ correspond to the energy limits E_1 and E_2, respectively. For, extreme limits i.e., $x1 = 0$ and $x2 = \infty$, above expression reduces,

$$P(\nu) \propto \nu^{-\alpha}$$

with spectral index $\alpha = (p-1)/2$

For extended radio sources, $\alpha \sim 0.5 - 1$ and $p = 2 - 3$. Practically, it is not possible for electron energies to extend over an interval $(0, \infty)$. Therefore, the energy spectrum must depart from the power law at the endpoints. But the power law approximation is valid when ν is far from ν_1 and ν_2 such that $\nu/\nu_1 >> 1$ and $\nu/\nu_2 << 2$.

1.5 Complex X-ray spectra of AGNs

The 0.1-100 keV X-ray spectrum of a radio-quiet AGN contains multiple spectral features, which provide important information on the physical processes going on in the extremely strong gravitational field of the supermassive black hole. The X-ray spectrum is dominated by the primary continuum, called the power-law continuum with high energy cut-off, which can be expressed in the mathematical form as :

$$N(E) = N_0 \times E^{-\Gamma} exp(-E/E_c)$$

where, Γ is known as photon-index (ranges from 1.3 to 2.6; Brandt et al. (1997)) which is related to the spectral-index as $\alpha = 1 - \Gamma$ and N_0 represents the number of photons at 1 keV. E_c is termed as a high energy cut-off that provides information on the "coronal temperature". In addition to the power-law continuum, the X-ray spectrum of a radio-quiet AGN shows a hump like structure above 10 keV called as "Compton hump", iron K_α emission line at around 6.4 keV, soft excess below 2 keV. Apart from these features, many AGNs show signatures of warm absorbers (WAs) and outflows in their spectra. All these features in the X-ray spectrum are shown in a schematic diagram (see Figure 1.8) and are discussed below in detail.

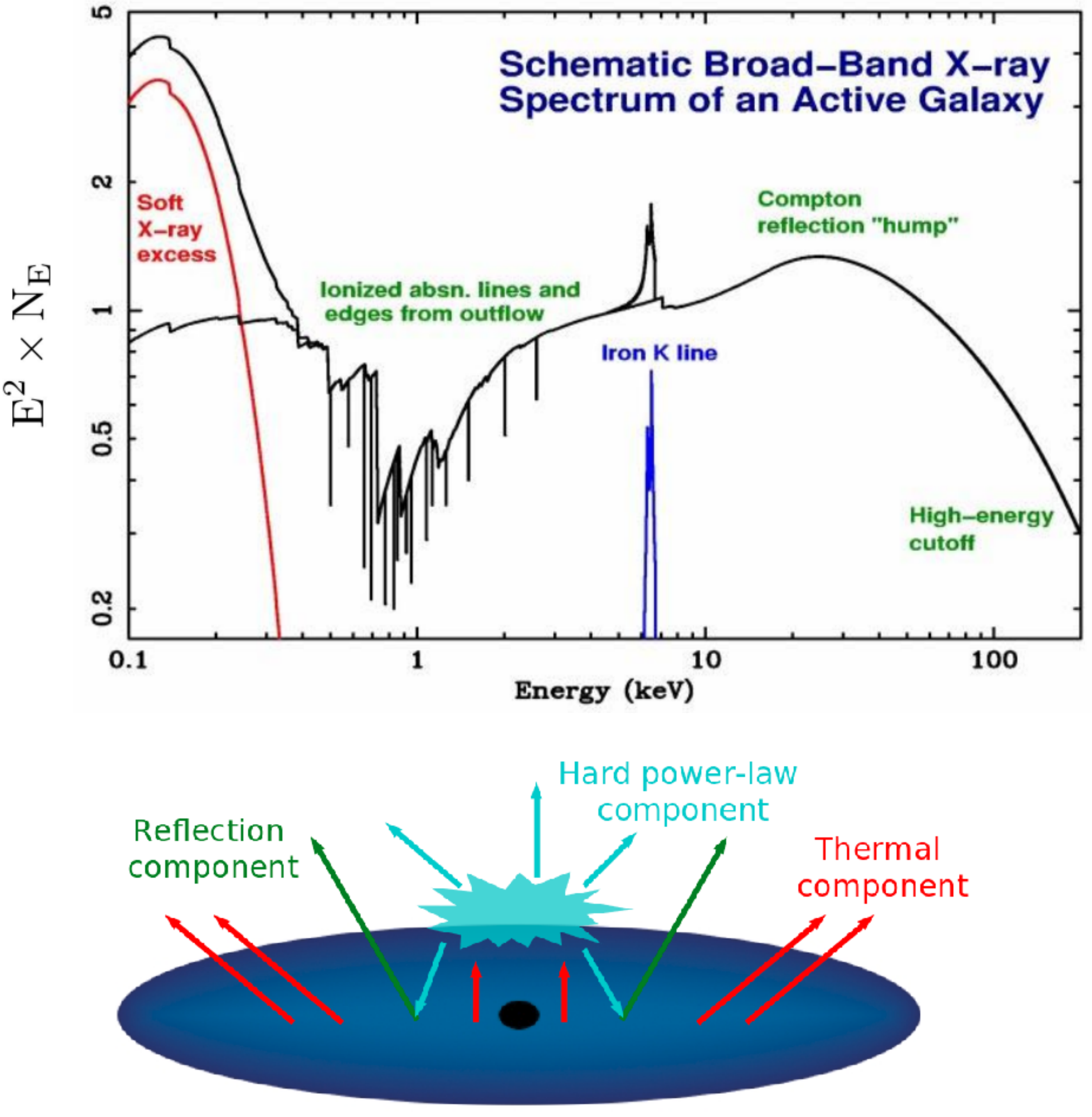

Figure 1.8: Different components in a typical X-ray spectrum of an AGN are shown. Credit: (Fabian & Miniutti, 2005) (top). A cartoon diagram consisting of black hole (in black), corona (in sky blue) and accretion disc (in blue) is shown at the bottom for the clarity of the emission regions.

1.5.1 Power-law continuum

The most accepted physical mechanism for producing the primary continuum in AGNs is the inverse Comptonization process. In this process, the soft photons (with temperature $\sim$ 50 eV) from the innermost part of the accretion disc get scattered from the relativistic electron plasma (temperature of $\sim$ 100 keV, optically thin and geometrically thick medium) and emitted as high energy photons due to multiple scattering (Haardt & Maraschi, 1991). The strength of interaction between the photon and electrons is given by a dimensionless Comptonization y-parameter (Rybicki & Lightman, 1979),

$$y = \frac{4kT}{m_e c^2} max(\tau, \tau^2)$$

where, k is the Boltzmann constant, T is the electron plasma temperature and τ is the optical depth ($\tau = n_e \sigma_T L$, where n_e is the electron density, σ_T is Thomson cross-section and L is the electron cloud size). For a slab geometry, the relation between the photon-index and the y-parameter is described by Sunyaev & Titarchuk (1980) as,

$$\Gamma = \frac{-1}{2} + \Big(\frac{9}{4} + \frac{4}{y}\Big)^{1/2}$$

The energy of a photon (E_f) after N scattering in the plasma is given by,

$$E_f = E_i \; exp\Big(\frac{4kT}{m_e c^2} N\Big)$$

Investigation of this X-ray continuum can provide information on the electron plasma (corona), such as size, geometry and temperature.

1.5.2 Compton hump and Fe-Kα emission line

The X-ray photons from the corona are emitted isotropically. A fraction of these photons are incident upon the accretion disc and interact with the material in various ways depending on their energy. The ratio between the reflected flux and the direct flux emitted at infinity is called the reflection fraction R. R is also considered as the solid angle subtended by the reflector (Magdziarz & Zdziarski, 1995). The reflection fraction, also termed as the reflection efficiency, is higher for Compton thick reflector and drops for the Compton thin reflector (Ghisellini et al., 1994). The hard X-ray photons are Compton scattered by the electrons to lower energies in the accretion disc as they have excess energy than the characteristic

Compton temperature of the scattering material. The photons with energy less than the Compton temperature gain energy resulting in the characteristic feature called "Compton hump" in the high energy X-ray. This reflection or Compton hump is an excess of photons in the 20-30 keV range above the power-law continuum. The soft photons interact with the material in the disc through photoelectric effect (Magdziarz & Zdziarski, 1995). The incoming photons are absorbed by the ion/atom and re-emitted through two processes. One is the Auger effect, where the absorbed photon imparts its energy to an inner shell electron to be ejected and that vacancy is filled by an electron in the outer shell by emitting a photon. This photon is again absorbed by another electron in the atom, ejecting an "Auger electron". In the alternative process, a photon is emitted as a result of an outer electron filling the inner shell vacancy giving fluorescent line emission. These lines are emitted when the absorbed photon has sufficient energy, at least equal to the energy separation between the levels of the atom. Absorption of soft photons with energy less than 10 keV can produce many fluorescent lines of heavy elements. Matt et al. (1997) found that the strongest emission line in X-ray from the accretion disc is the iron kα line because of the highest abundance among all elements and highest fluorescent yield. At 6.4 keV, doublet should occur from the neutral iron but current X-ray spectrometers are not able to resolve these lines. The Kα line arises when the X-ray photon of energy 7.1 keV gets absorbed and removes one K-shell electron and allows an electron from the L-shell to transit to the K-shell by emitting a photon of 6.4 keV. The reflected spectrum from the disc depends upon the spectrum of incident emission as well as the disc temperature, abundance and ionization of the atoms/ions present in the disc. The atomic abundances determine the intensities of the fluorescent lines and the ionization states regulate the energies as well as the intensities of the lines. The matter in the disc can also be ionized from the illumination of the primary X-ray photons coming from the corona. The amount of the ionization is evaluated by the ionization parameter ($\xi = L_{ion}/nr^2$, where L_{ion} is the ionizing luminosity, n is the number density and r is the radius). As the ionization increases, the photo-absorption cross-section decreases at lower energies.

1.5.3 Black hole spin

We digress here to explain one of the important properties of an isolated uncharged black hole i.e., spin. An uncharged black hole is characterized by two quantities such as its mass (M) and angular momentum (J). The spin of the black hole is expressed as the ratio between the angular momentum and the mass i.e., angular momentum parameter or spin parameter

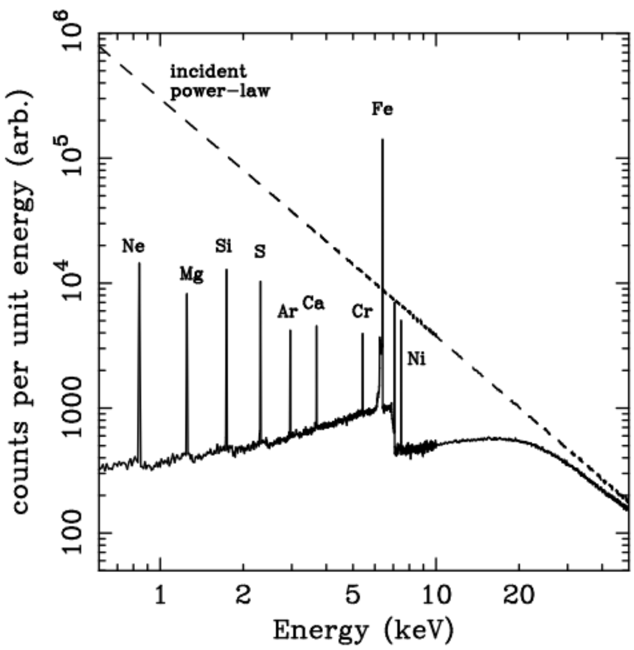

Figure 1.9: The incident power-law and reflected spectrum are shown for an accretion disc of constant density. Credit: Reynolds 1996, PhD Thesis.

$a^* = J/M$. For maximally spinning (Kerr) black hole, the spin parameter $a^* = 0.998$ while for non-spinning (Schwarzschild) black hole, $a^* = 0$. The black holes have enormous gravity which can distort and twist the space-time around it. This results in the bending of the light travelling from the vicinity of the black hole which can be studied in X-ray to get the information about the spin. Figure 1.10 shows the concept of the effect of the different types of black hole spin on the X-ray spectrum. This is the consequence of Einstein's general theory of relativity. In the retrograde rotation, the accretion disc moves in the opposite direction to the spin of the black hole while in the prograde motion, the disc rotates in the same direction as the black hole. The profile of the emission lines in the X-ray spectrum originating from the accretion disc is used to determine the spin parameter. The emission line profile is fitted using a relativistic emission line model which includes the black hole spin as a variable parameter. The spin of the black hole is related to the inner most stable orbit (ISCO) which is the inner most possible extent of the accretion disc. By varying the spin parameter, the ISCO is varied and thus gravitational redshift. Each annulus of the accretion disc is considered independent. On varying the spin parameter, one can determine the effect of black hole spin on the contribution from the inner annuli on the emission line. However, the emission line profile for the outer disc will not get affected by the spin of the black hole. Emission from the regions down to 1.235 R_g implies the maximally rotating black hole.

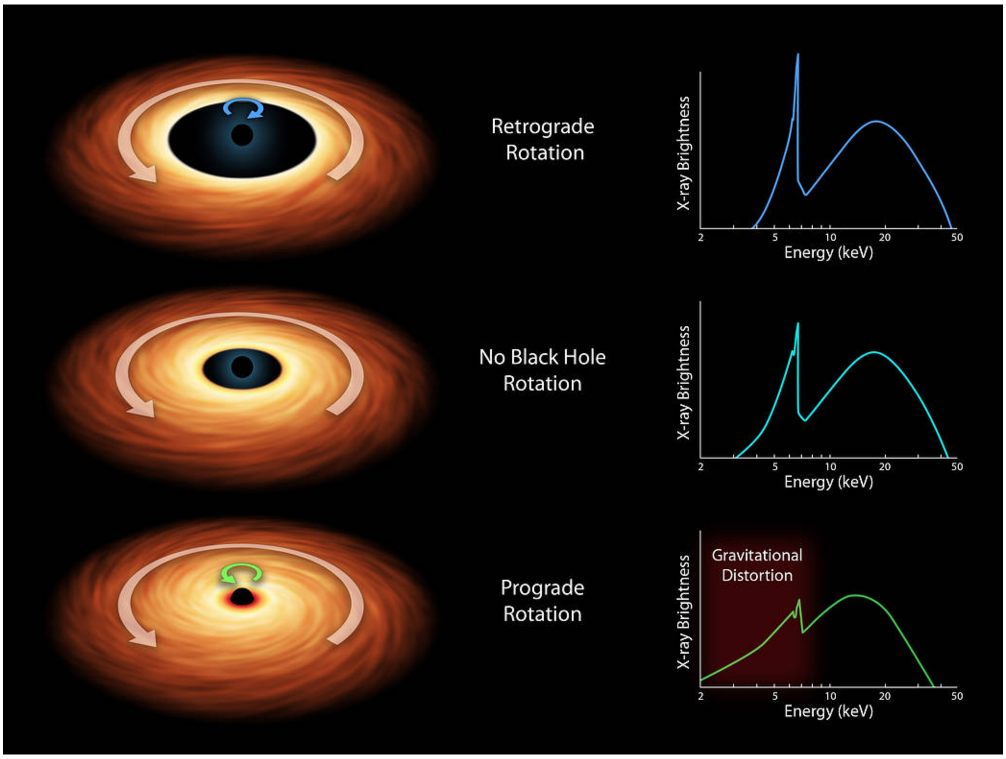

Figure 1.10: Cartoon picture showing the concept of the effect of black hole spin on X-ray spectra.

1.5.4 Soft excess

When 2-10 keV power-law is extrapolated down to the soft X-rays, many AGNs show excess over the power-law continuum in the low energy ranges. This excess in the low energy range of the X-ray spectrum is called soft excess. This feature was first observed in Mrk 841 (Arnaud et al., 1985) & Mrk 509 (Singh et al., 1985). Since then, it has been a common feature in the AGNs. However, the precise origin of this component is still not very clear (Bianchi et al., 2009a). In 1997, Piro et al. studied this component in 17 AGNs using ROSAT and Ginga data and found that no single model fitted the observed soft excess well, and the phenomena can vary for different sources. Phenomenologically, the soft excess can be fitted with a black-body component. However, the temperature obtained from the blackbody is too high to have originated from the thermal disc found in the case of AGNs (Gierliński & Done, 2004). Also, this temperature has a very narrow window irrespective of mass and mass accretion rate of the central black hole and requires fine tuning. This indicates that the origin of the soft excess is not certainly thermal. In a number of Seyfert galaxies, it has been shown that the soft X-ray excess can be explained through blurred reflection (Fabian et al., 2002; Walton et al., 2013). In this mechanism, the emission and absorption lines in the soft X-rays originating from the nearby regions of the SMBH get broadened due the gravitational and relativistic effects. The

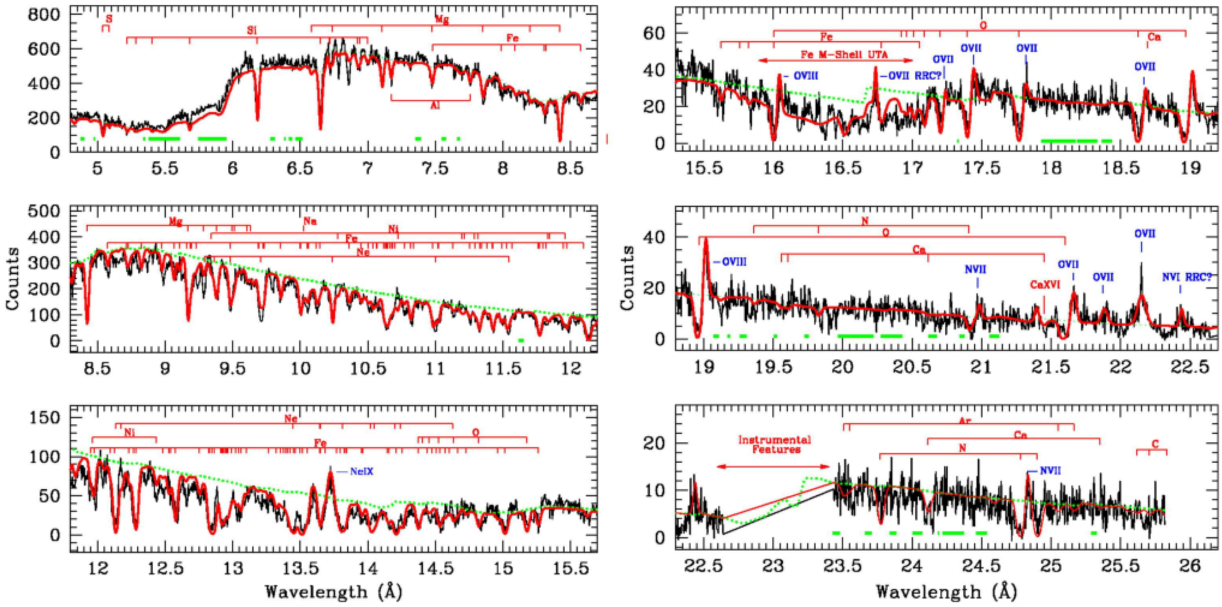

Figure 1.11: Absorption spectra of NGC 3783 in the rest frame of the absorbing gas. Absorption lines, emission lines and continuum (for the comparison) are plotted with red, blue and green colors, respectively. Credit: Krongold et al., 2003.

smoothened lines appear like a hump structure. The ionized disc reflection models explain not only the soft excess but also the finite width of the iron line. This component was also explained by the smeared absorption due to the ionized absorber in the line-of-sight. However, the latter is ruled out due to the requirement of high velocity of the absorber (Schurch et al., 2009). The most favourable origin for the soft excess is the Comptonized disc emission that requires an electron temperature of 0.1-0.2 keV and a large optical depth of ∼10-20 (Done & Krolik, 1996). Nandi et al. 2021 discussed a possibility for the origin of soft excess in a "bare" type AGN Ark 120, where the soft excess could be due to the less number of scatterings in the Compton cloud.

1.5.5 Absorption features

The AGN spectra are also affected by the absorption attributed to the complex structures around the central black hole. In the X-ray and UV spectra of the AGNs, the blue-shifted absorption lines have been found, which reveal the presence of the outflows of ionized gas. In type 1 sources, it is the intrinsic ionized absorption due to the warm absorbers and ultra-fast outflows. While in type 2 sources, the obscuring material is relatively cold and made up of dust and gas, which significantly attenuate the nuclear emission from the optical to soft X-rays.

In many radio-quiet AGNs, the signatures of absorption from the layer of photo-ionized gas, known as warm absorbers (WAs), have been found. Energetic X-ray photons can excite or ionize the atoms of the abundant elements from C to Ni and Fe. An example of absorption can be seen in the X-ray spectrum of the Seyfert 1 galaxy NGC 3783 in Figure 1.11 (Krongold et al., 2003). A region between $\sim 1-100$ pc, consistent with the location of BLR or NLR with ionization parameter of ($\log\xi$) $\sim 0-2$ erg s^{-1} cm and a column density of $N_H \sim 10^{21-23}$cm^{-2} is expected to show absorption in the X-ray spectrum at around $0.7-0.8$ keV. These absorbers with outflow velocity $\sim 100-1000$ km/s are known as warm absorbers. The origin of this gas has been associated with the optical-UV BLR or NLR or probably with the winds generated by the evaporation from the inner edge of the torus due to ionizing nuclear emission from the centre (Blustin et al., 2005; Krolik & Kriss, 2001). Krolik & Kriss (2001) argued for the two-phase model of the absorber. In this model, the cold and dense clouds having a small fraction of available volume associated with the optical-UV BLR or NLR are confined by a hot cloud medium provided by what is known as WA. However, later, this model was shown to be insufficient to explain the dynamic effect and unable to explain the formation of broad-line clouds.

Apart from the WAs, the blue-shifted Fe K absorption lines have been detected in the XMM-Newton spectra of a number of radio-quiet AGNs (Braito et al., 2007; Turner et al., 2008; Cappi et al., 2009). These absorption features are usually identified as Fe XXV and/or Fe XXVI K-shell resonant absorption from a high column density ($N_H \sim 10^{22-24}$cm^{-2}) and highly ionized ($\log\xi \sim 2-6$ erg s^{-1} cm) gas. The outflow velocity of these gases sometimes becomes mildly relativistic ($\sim 0.2-0.4$c), which is much greater than the typical X-ray warm absorber (McKernan et al., 2007). Variability due to these outflows has been reported to be at a time scale as short as 1 day. These are located very close to the SMBH with a distance of $\sim 0.01-0.1$ pc. The origin of these ultra-fast outflows (UFOs) has been associated with the accretion disc winds/ejecta (McKernan et al., 2007). These outflows carry a significant amount of mass and energy which can play a paramount role in the evolution of the host galaxy, such as quenching of star formation or enriching the interstellar medium.

Another type of absorption is photoelectric absorption by cold and neutral material along the line-of-sight, such as obscuring torus in the type 2 AGNs. From modelling, it is possible to estimate the column density of the obscuring material. If $N_H > 10^{24}$ cm^{-2}, the AGN is called Compton thick AGN, otherwise it is a Compton thin AGN. In the case of Compton thick AGNs, the X-ray photons with energy below $\sim$10 keV are completely absorbed, whereas the photons with energy beyond $\sim$10 keV are easily transmitted.

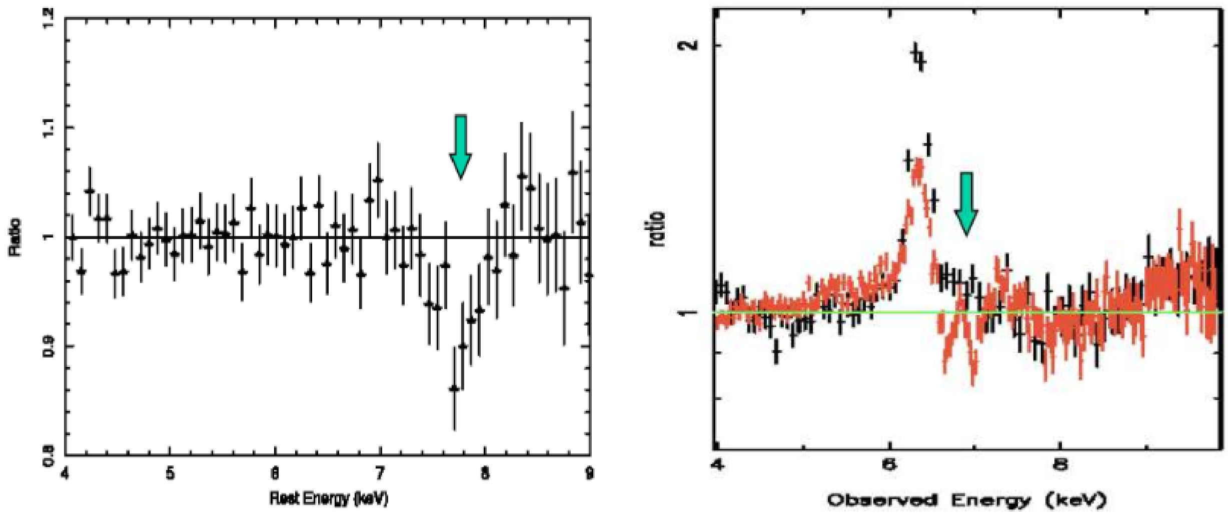

Figure 1.12: Examples of the blue-shifted Fe K absorption lines at energies > 7 keV for MGC-5-23-16 (left panel; Braito et al., 2007) and NGC 3516 (right panel; Turner et al., 2008) are shown. These spectra were collected with the XMM-Newton/pn instrument.

1.6 AGN variability

The X-ray and UV/optical flux from an individual AGN can be affected in many ways. The most obvious way is by altering the accretion rate onto the black hole. An increase in the mass accretion rate increases the accretion disc temperature causing an increase in the disc flux in all wavelengths. The increase in disc flux due to an increase in the temperature shifts the emission peak to higher frequencies. The increased disc flux also increases the number of seed photons incident in the corona producing X-ray power-law continuum emission. This enhancement in the power-law continuum emission cools the corona resulting in a steeper (softer) power-law. The X-ray and UV/optical flux can also be changed due to the change in the size of the corona. Increasing the size of the corona causes an increase in the X-ray flux and hardens the X-ray spectrum due to the increase in the number of inverse Compton scatterings that occur in a larger corona.

The flux at different wavelengths from an AGN is expected to correlate if the cause of emission at these wavelengths is linked in any way. Investigation of the presence of lags and correlations between the light curves at different wavelength bands, therefore, can be used to determine which, if any, of the possible causal links are in effect. The origin of variability in the UV/optical and X-ray bands is still a matter of debate. These variabilities are interpreted as due to i) the reprocessing of X-ray emission in the accretion disc (Krolik et al., 1991; Collier et al., 1998; Breedt et al., 2010), and ii) the intrinsic variations in the thermal disc emission (Arévalo et al., 2008). It is also possible that both of these processes can occur simultaneously in an AGN. Thus, multi-wavelength studies of the AGNs provide an opportunity to determine the dominant process.

1.6.1 X-ray reprocessing from the accretion disc

X-ray emission from the hot corona when incident on the accretion disc, heats it. The additional energy deposited in the accretion disc increases the resultant temperature and the flux for every disc element (i.e. disc annuli). This resultant temperature can be expressed as (Cackett et al., 2007) :

$$T(r) = \left[\frac{3GM\dot{M}}{8\pi\sigma r^3} \left(1 - \frac{r_{in}}{r}\right)^{(1/2)} + \frac{(1-A)L_x}{4\pi\sigma r_x^2} \cos(\theta x) \right]^{(1/4)}$$

where M, $\dot{M}$, r_{in}, A, L_x, r_x, and θx are mass of the central black hole, mass accretion rate, inner most stable radius (ISCO), albedo for X-ray heating, X-ray luminosity of the source, the distance of the disc element (i.e. annulus ring) from the X-ray source and angle between the normal to the annulus ring of the disc and the line connecting to the annulus ring and the X-ray source, respectively.

The reprocessed UV/optical emission from the accretion disc gets delayed on the light crossing time scale relative to the X-ray emission coming directly from the corona. For AGNs with black hole mass in the range of $10^6 - 10^8 M_\odot$, the lag time-scales are expected to be in the range of minutes to a few days (Breedt et al., 2010). The X-ray to UV/optical lag time-scales are expected to increase with the increasing wavelength (Cackett et al., 2007) as the longer wavelength emission originates at larger radii in the disc. Due to the continuous nature of the temperature profile of the accretion disc and the blackbody spectrum, the reprocessing of X-rays produces a transfer function consisting of contributions from X-ray emission reprocessed throughout the disc. The inclination also affects the shape of the transfer function as an edge-on disc results in larger lags but can result in a narrower peak than a face-on disc. If all of the UV/optical variabilities are due to reprocessing, then the conservation of energy would require that the absolute luminosity variation in the optical/UV bands should be smaller than the luminosity variation seen in the driving X-ray band.

1.6.2 Comptonization of the seed photons

The seed photons from the inner accretion disc enter the corona and gain energy as a result of inverse Compton scattering from the energetic electrons. The X-ray photons from the corona, therefore, are expected to be delayed relative to the soft photons from the accretion disc. The cause of this delay is the additional travel time via the corona as well as the time required for multiple scatterings to take place in the corona. Only emission from the central region of the disc near the corona is expected to contribute significantly to the X-ray flux. Hence, the lag expected in this case is even shorter than those from the reprocessing. However, unlike in the case of reprocessing, the longer wavelength emission is expected to lead.

1.6.3 Propagating fluctuations in the accretion disc

In the scenario where the UV/optical variations originate in the accretion disc, it is expected that these inward propagating accretion rate fluctuations result in variations in the X-ray emission. In this scenario, the X-ray variations lag behind the optical/UV variations. Eventually, the accretion rate fluctuations reach the central regions of the disc and produce seed photons which get Compton up-scattered in the corona. The lag time-scale is dictated by the viscous propagation time-scale, which is always much longer than the light-travel time, typically months to years for standard accretion disc around the black holes with mass in the range of $10^6 - 10^8 M_\odot$ (Lyubarskii, 1997; Czerny, 2006). The viscous time-scale is given by,

$$t_{visc} = \frac{1}{\alpha}\left(\frac{r}{h}\right)^2 t_{dyn}$$

where, α is the viscosity parameter from Shakura & Sunyaev (1973a), h is the height and r is the radius of interest within the disc and t_{dyn} is the dynamical time-scale. In this case, the X-ray emission is expected to lag behind the UV/optical emission by thousands of days. Like reprocessing, the effects are likely to be blurred by the continuous nature of the disc spectrum, and the time-scales are generally expected to be comparable to the monitoring programs, making them very difficult to observe.

1.7 Changing-look AGNs (CLAGNs)

One of the most interesting aspects of the strong variability has given birth to a new subset of AGNs, known as changing-look AGNs (CLAGNs). In X-ray wavelength, the CLAGNs are observed to show strong variability in the line-of-sight column density, i.e. sources are found to switch between Compton-thin and Compton-thick states. These are categorized as X-ray changing-look AGNs or changing-obscuration AGNs (CO-AGN) (Risaliti et al., 2010; Marinucci et al., 2016; Ricci et al., 2016). Another category of CLAGNs is the optical changing-look or changing-state AGNs (CS-AGNs), in which the optical/UV emission lines generated in the BLR appear or disappear within a few years, i.e. switching between type 1 (or type 1.2 or 1.5) and type 2 (or type 1.8 or 1.9). (Lawrence, 2018). There are about 20-30 CLAGNs discovered till now. However, the physical mechanism responsible for the CL events is still poorly understood. In fact, the CL event in AGNs throws challenges to the widely accepted unified model of AGNs over the past 30 years. The optical CLAGNs can not be explained through the changing obscuration proposition as the torus is not large enough to affect the BLR clouds, except for a narrow range of inclination angle. Secondly, these objects do not carry any signatures of X-ray obscuration along with changing their states (Denney et al., 2014). It has been proclaimed that the appearance or disappearance of the broad-line occurs due to the change in the accretion rate or instabilities in the accretion disc (Elitzur et al., 2014). In some of the AGNs, the luminosity increase could be due to the tidal disruption event (Merloni et al., 2015).

1.8 Motivation and thesis organization

The study of the AGNs, particularly the Seyfert galaxies, offers an opportunity to study the characteristics of the central engine through different spectral components such as big blue bump, power-law continuum, soft X-ray excess, warm absorbers, Fe-Kα line and the Compton reflection hump. Extensive work has been carried out on modelling the AGN spectra using a number of models. These spectral components arise from spatially distinct regions; for example, the broad iron lines primarily originate from the innermost region of the accretion disc and the power-law continuum arises from the compact and hot corona. Thus, the variability properties of different spectral components are expected to be different. Therefore, the study of variability in different spectral components and the relationship between them can shed light on the dynamics of the central engine. Such a study can constrain models in explaining the origin of several spectral components. Variability properties seen in X-ray emission and its relationship with the optical/UV emission from the accretion disc are being studied considerably with the advent of high-cadence providing observatories like Swift. In the literature, it has been seen that often geometry of the accretion disc deviates from the standard Shakura-Sunyaev disc. Thus, the aforementioned kind of studies can potentially constrain the dominant physical processes and the geometry of the disc. Similarly, the detailed spectral and timing studies of X-ray flares of very short duration (within hours or a day) can help to probe the dynamics of the hot corona. Other than this, the changing of the AGN type is a recently emerging interesting phenomenon that has challenged our understanding of the classification of AGNs. Therefore, our main scientific objectives to study these complex objects are:

- Characterizing the broadband X-ray spectrum of AGNs.
- Variability studies in multi-wavelength range and understanding the correlation between them.
- Searching for the origin of changing-look event in AGNs.
- Investigating the dynamic nature of the corona to explain the observed spectral variability.

After providing the above brief introduction of an AGN, its structure and emission processes in X-rays, we now describe the organization of the remainder of the thesis as follows. In Chapter 2, a brief description of the instruments onboard several X-ray observatories, from which the data has been used in this thesis, is presented along with the procedures followed for data reduction. We discuss the UV/optical and X-ray variability in Seyfert 1 galaxy Mrk 509 in Chapter 3, while in Chapter 4, we describe the detailed broadband X-ray analysis of the 2018 outburst in the changing-look AGN NGC 1566. We have discussed the investigation of a small flaring event in NLS1 galaxy NGC 4051 in Chapter 5. Finally, we summarize our results and future prospects in Chapter 6.

Chapter 2

X-ray Instruments & Data Reduction: Analysis and Techniques

In this thesis, we have utilized X-ray data from different instruments onboard three space based observatories: Neil Gehrels *Swift* observatory, *XMM-Newton* and Nuclear Spectroscopic Telescope Array (*NuSTAR*). This chapter is dedicated to a brief description on the instruments of each observatory mentioned above. Section 2.4 succinctly describes the data reduction procedure from the instruments we used in our work. We also touch upon the basic X-ray analysis techniques and basic models that are used in X-ray data fitting in Section 2.5.

2.1 *Swift* observatory

Swift observatory (Gehrels et al., 2004), previously known as *Swift* Gamma-Ray Burst Explorer, is a multi-wavelength space observatory which was primarily designed for studying gamma-ray bursts (GRBs). It was launched on November 20, 2004 by the Delta 7320 launch vehicle of NASA. This satellite is orbiting in a low earth orbit (LEO) at an altitude of about 600 km and an inclination of 20.6°. It has got its name "Swift" due to its unique rapid slew capability for transient objects in the sky. It is one of its kind that covers the wide wavelength range from optical/UV, X-ray to gamma-ray. Although the primary science goal of this observatory was to detect and study the GRBs, the multi-wavelength capability from the optical to hard X-ray bands makes it significantly useful for the study of other sources such as X-ray binaries and AGNs. Later on, this observatory was renamed as Neil Gehrels *Swif*t Observatory in 2018. This satellite is equipped with three science instruments: (i) the Burst Alert Telescope (BAT), sensitive in the hard X-ray band of 15–150 keV range,

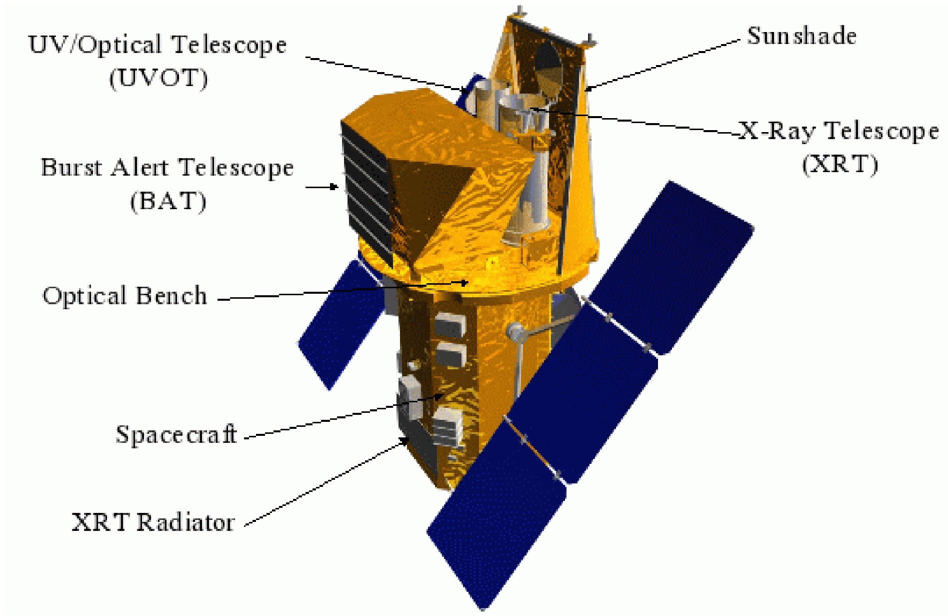

Figure 2.1: Schematic diagram of the *Swift* observatory with all the instruments. The image is taken from the webpage of NASA - `http://www.swift.ac.uk/about/instruments.php`**.**

(ii) the X-Ray Telescope (XRT), sensitive in the soft X-ray band of 0.2–10 keV, and (iii) the Ultraviolet/Optical Telescope (UVOT), sensitive in 170–600 nm wavelength range. The BAT is used to detect the possible GRBs while XRT and UVOT detect the after glows in X-ray and UV/Visible light, respectively. The *Swift*/BAT has the largest field of view among all while the XRT and the UVOT are high precision focusing instruments. Apart from the GRB events, Swift has been used extensively for other astronomical sources like AGNs, X-ray pulsars, black hole X-ray binaries (BHXBs) etc. Along with its unprecedented wavelength coverage, it provides high cadence data for the time scale of months to years. The data from Swift observatory are publicly available on HEASARC, maintained by NASA. The schematic view of the *Swift* observatory is provided in Figure 2.1.

2.1.1 X-Ray Telescope (XRT)

The *Swift*/XRT (Burrows et al., 2005) is an X-ray imaging telescope designed to extract light curves and spectra of objects over a wide dynamic range of more than seven orders of magnitude in flux. It provides accurate source positions, high time resolution light curves and moderate resolution spectroscopy in 0.2–10 keV range.

It is built with 12 nested mirrors in the Wolter type-I configuration that focuses the grazing incident X-ray photons on a CCD detector at the focal plane. A composite telescope tube holds the focal plane camera, containing a single CCD-22 detector. The CCD-22 detector, designed for the EPIC-MOS instruments on the XMM-Newton mission, is a three-phase frame-transfer device, using high resistivity silicon and an open-electrode structure to achieve a useful bandpass of 0.2-10 keV. The field of view of XRT is $23.6' \times 23.6'$ and it has a PSF of $18''$ at 1.5 keV.

The XRT is configured to operate in four different modes depending upon the brightness of the source being observed and the requirement of the science case. The modes of operation are : (i) Imaging (IM), (ii) Photo-Diode (PD), (iii) Photon Counting (PC) and (iv) Window Timing (WT) modes (Hill et al. 2004). The IM mode generates an integrated image measuring the total energy deposited per pixel. It does not permit spectroscopy but the accurate position of the source is possible to determine in imaging mode. The PD mode was made unavailable after May 2005. The PC mode is a traditional frame transfer operation of a CCD camera. The entire chip readout in this mode results in a complete 2D image of the source, thereby limiting the time resolution to the readout time of 2.5 s. While in the WT mode, high timing resolution of $\sim$1.8 ms could be achieved at the expense of losing the information about the source position. In this mode, the readout is restricted to a narrow part of the CCD. The central 200 columns ($\sim 8'$) are read out all at once in a single row, resulting in a collapsed 1D source image. Due to high timing resolution of this mode, photon pile-up could be avoided for moderately bright sources ($<$ 100 counts/s; Romano et al. 2006). The primary characteristic properties of this telescope are listed in Table 2.1.

2.1.2 Ultra-Violet Optical Telescope (UVOT)

The UVOT (Roming et al., 2005) has a modified Ritchey-Chrétien optical configuration with a 30 cm primary mirror working in the wavelength range of 170–600 nm. To collect the data, two micro-channel plate intensified CCDs are used that record the arrival time of photons and provide sub-arcsecond positioning of the source. Each of the detectors lies behind the 11-position filter wheel. The UVOT is mounted to the optical bench co-aligned with the BAT and XRT for broad spectral coverage and better position localization. The specification of the UVOT is given in Table 2.1.

2.1.3 Burst Alert Telescope (BAT)

The BAT (Barthelmy et al., 2005) is a gamma-ray telescope with a large field of view which uses coded masked aperture techniques to image the objects in the 15-150 keV range. The coded aperture casts shadow of sources at the detector plane, which is then used to reconstruct

Table 2.1: Specifications of the XRT and UVOT onboard Swift observatory.

Parameters	Instrument Specifications	
	XRT	UVOT
Telescope	Wolter I (3.5 m focal length)	Modified Ritchey-Chretien (30 cm diameter)
Field of view	$23.6' \times 23.6'$	$17' \times 17'$
Telescope PSF	$18''$ Half Power Diameter @ 1.5 keV, $22''$ Half Power Diameter @ 8.1 keV	$0.9''$ FWHM @ 350 nm
f-Number	–	12.7
Detector operation	photon counting	
Detector	EPIC MOS CCDs	MCP Intensified CCD
Detector element	600×600 pixels	2048×2048 after centroid
Spectral range	0.2-10 keV	170-650 nm
Filters	–	11
Pixel scale	–	$0.5'$/pixel
Position accuracy	$3'' - 5''$	–
Detector operation	Autonomous	Photon counting
Sensitivity	2×10^{-14} erg cm^{-2} s^{-1} in 10^4s	24.0 magnitude in white light in 1000s
Brightness limit	–	7.4 magnitude
Best Temporal resolution	0.14 ms, 1.8ms, 2.5s	11 ms
Energy/Spectral resolution (Grisms)	140 eV @5.9 keV	$\lambda/\delta\lambda \sim 200$ @ 400 nm

the source locations with arc-minute accuracy. The detector of the BAT is made up of CdZnTe (CZT) with a detector area of 5240 cm^2. The CZT detector consists of 32500 detector elements that can pin-point the location of sources within 1.4 arcminutes. The BAT has two operation modes : (i) the burst mode, which produces burst position and (ii) the hard X-ray survey mode.

2.2 The *XMM-Newton* observatory

The X-ray Multi-Mirror Mission (*XMM-Newton*; Jansen et al. (2001)) is an X-ray space observatory which was launched by European Space Agency (ESA) on December 10, 1999 and named after physicist and astronomer Sir Issac Newton. It has a highly elliptical orbit with perigee of 7000 km and apogee of 114000 km, and orbital period ∼48 hours. The spacecraft has been configured with three co-aligned X-ray telescopes and an optical/ultraviolet telescope with a length of 30 cm. This is the first spacecraft that was positioned to perform broad-range X-ray spectroscopy, and the first simultaneous imaging of objects in X-ray, optical and ultraviolet wavelengths. It provides pointing accuracy of 0.25 to 1$''$. A schematic diagram of the *XMM-Newton* telescopes is given in Figure 2.2. The instruments on-board this observatory includes three European Photon Imaging Cameras (EPIC) and two Reflection Grating Spectrometers (RGS) at the back-end of X-ray telescopes, and an Optical Monitor (OM). Each of the three telescopes consist of 58 nested cylindrical Wolter type-I mirrors providing a total effective area of 4425 cm^2 at 1.5 keV and 1740 cm^2 at 8 keV. There are two types of primary instruments EPIC: PN and MOS. In addition, there are two high resolution spectrometers known as Reflection Grating Spectrometers (RGS). The main characteristics of EPIC instruments is given in Table 2.2

2.2.1 European Photon Imaging Camera (EPIC)-PN/MOS

The three EPIC, two MOS-CCD (Turner et al., 2001) and one pn-CCD (Strüder et al., 2001) cameras are the primary instruments onboard *XMM-Newton* observatory. The two front illuminated Metal Oxide Semiconductor (MOS) CCD arrays MOS1 and MOS2 and a back-illuminated pn-CCD array together are called the EPIC. These instruments are sensitive in the energy range of 0.15-15 keV with a total field of view 30 arcminutes. These cameras operate in the following science modes depending on the source flux, image sensitivity and speed needed.

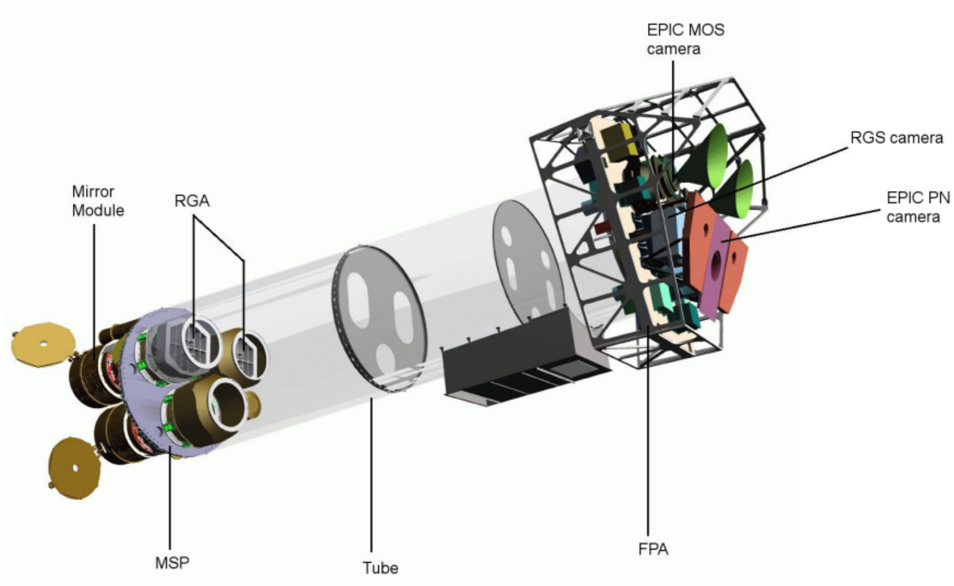

Figure 2.2: Schematic diagram of the *XMM-Newton* observatory with all the instruments. Image credit: Jansen et al. (2001)

Table 2.2: Specifications for the PN and MOS detectors onboard *XMM-Newton* observatory.

Parameters	Instrument Specifications	
	MOS	PN
Telescope	Wolter Type I	
Effective area	4650 cm^2 at 1 keV	
Energy range	0.2-10 keV	
Orbital target	5-135 ks	
Sensitivity	$\sim 10^{-14}$ erg s^{-1} cm^{-2}	
Field of View	$30'$	
PSF (FWHM/HEW)	$5''/14''$	$6''/15''$
Pixel size	40 μm	150 μm
Time resolution	1.75 ms	0.03 ms
Spectral resolution	$\sim$70 eV	$\sim$80 eV
Science modes	Full frame, Small window, Large window, Timing mode, Burst mode	

1. In the “Full Frame or Extended Full Frame”, the entire field of view (FOV) is covered due to the readout of all pixels of the pn-CCDs.

2. In the “Partial Window” mode of the MOS-cameras, the central CCDs of both the cameras can be operated in different modes and only a part of the CCD is readout.

3. In the “Large Window” and “Small Window” modes of pn camera, only half of the area of all 12 CCDs and only a part of CCD number 4 are used for data acquisition, respectively.

4. In the “Timing” mode, information is stored in one dimension. For the pn camera, the data is stored using the full width of CCD4, whereas for MOS, the data acquisition is reduced to $\sim$ 100 columns around boresight. “Burst” mode of the pn camera provides very high time resolution.

The EPIC focal plane imaging spectrometers use CCDs to record the events of the sources focused on the X-ray mirror telescope. Each MOS-CCD camera is composed of seven silicon chips with each chip containing 600×600 pixels. The pn-CCD is composed of a single chip with 12 individual CCDs containing 64×189 pixels on each CCD. Radiators are used to cool the CCDs down to the operating temperature of 150–170 K. About 50% astronomical light is diverted towards the RGS, away from the optical path of the EPIC-MOS.

2.3 Nuclear Spectroscopic Telescope Array (*NuSTAR*)

NuSTAR is the first hard X-ray focusing telescope that works in the energy range of 3-79 keV (Harrison et al., 2013). It was launched on June 13, 2012 as a Small Explorer satellite mission (SMEX) led by the California Institute of Technology (Caltech) and managed by Jet Propulsion Laboratory (JPL). It was set up into a low equatorial earth orbit (with an inclination $\sim 6°$) at an altitude of 600-610 km and an orbital period of 97.126 minutes. This telescope is designed with a Wolter type-I optics with 10.15 m focal length and is separated from the detectors with the help of a long deployable mast. To get the exact relative positions of the optics and the focal plane, a laser metrology system is used. A schematic view of the satellite (before and after deployment) is shown in Figure 2.3. In *NuSTAR*, the optics to focus hard X-ray photons uses 133 concentric shells where each shell is coated with depth-graded Pt/SiC and W/Si multilayers enabling reflectivity of X-rays up to 79 keV. Above this energy,

Table 2.3: Specifications of *NuSTAR* satellite.

Parameters	Instrument Specifications
Focal length	10.14 m
Field of View	12.2×12.2 arcmin
Angular resolution	$58''$ HPD $18''$ FWHM
Energy range	3 to 78.4 keV
Spectral resolution	400/900 eV at 10/68 keV
Temporal resolution	2×10^{-3}s
Sensitivity (in 10^6s)	2×10^{-15} erg s^{-1} cm^{-2} in 6-10 keV, 1×10^{-14} erg s^{-1} cm^{-2} in 10-30 keV

the mirror coating starts absorbing instead of reflecting hard X-ray photons. At the focal plane of the telescope, there are two solid state photon counting detector modules: FPMA & FPMB. Each module consists of a 2×2 array of CdZnTe (CZT) crystal detectors with 32×32 pixels, resulting in a field of view of about $\sim$12 arcminutes. The detectors are surrounded by CsI anti-coincidence shielding. The operating temperature of these detectors are kept at 15° C. Due to the triggered readout mode available with the FPMs, the *NuSTAR* data do not get affected due to pile-up effect. The key parameters of the *NuSTAR* spacecraft are tabulated in Table 2.3.

2.4 X-ray Data Reduction

X-ray detectors store three main information of each falling photon (referred as an event) such as arrival time, pulse height amplitude and arrival position on the detector. These three attributes are used to generate science products i.e., light curves (Count/flux vs. time plot), spectra and images. The raw event data files of each X-ray observation are stored in a Flexible Image Transport System (FITS) format and are processed for deriving the science products. The High Energy Astrophysics Software (HEASoft)[1] package is utilized for the data reduction and analysis of data obtained from the observatories. The HEASoft package is publicly available on NASA's High Energy Astrophysics Science Archive Research Centre (HEASARC)[2]. It is a multi-mission platform as the data from various observatories (known as supported missions) are publicly available in this platform. A Calibration Data Base (CALDB)[3] is maintained in HEASARC for each individual mission, which regularly gets

[1] https://heasarc.gsfc.nasa.gov/lheasoft
[2] https://heasarc.gsfc.nasa.gov/
[3] https://heasarc.gsfc.nasa.gov/docs/heasarc/caldb/caldb_supported_missions.html

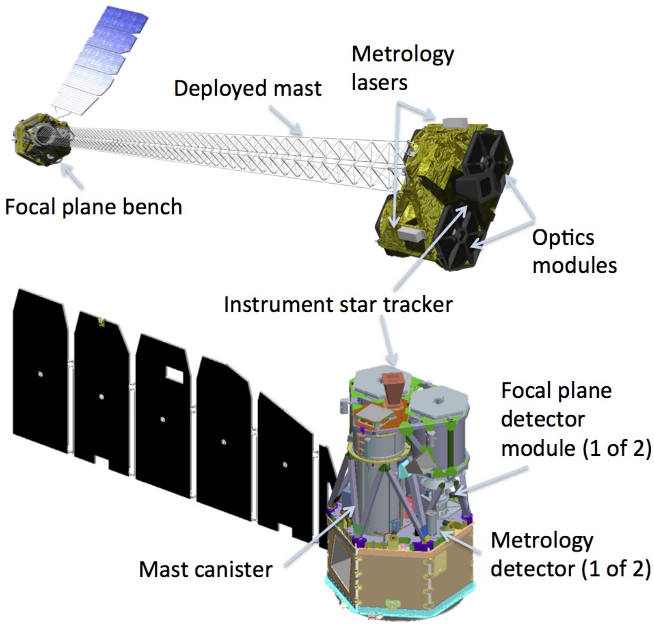

Figure 2.3: Schematic view of the *NuSTAR* observatory in the stowed (bottom) and deployed (top) configurations. The figure is taken from (Harrison et al., 2013).

updated as per the performance and condition of the instruments in space. To extract these scientific products, a standard procedure is followed for each instrument which is described below.

2.4.1 *Swift*-XRT data

The *Swift*/XRT (Burrows et al., 2005) data used in present work are analyzed using the standard procedures prescribed by the instrument team using the latest calibration files from the Swift CALDB. The data are reprocessed using the `xrtpipeline` task to generate the science products. There is default grade pattern (WT: 0-2, PC:0-12) of events that is used for data extraction. Then, the source photons for spectra and light curves are extracted using a circular region with an appropriate radius (in pixels) centered on the source. Background region is selected from the nearby uncontaminated region with a little larger radius than the source region. There are other effects that need to be corrected like CCD defects, exposures and PSF corrections using the auxiliary response file (ARF) generated using the `xrtmkarf` task. The XRT data can also be analyzed using the publicly available "Swift-XRT product generator tool" at the University of Leicester website[4]. This online tool has the capability to generate spectra, light curves and images from a particular observation or a sample of observations. For our study, as we used a large number of data sets, this tool has been proved very useful for data extraction. The detailed adopted methodology in the online tool is described in (Evans et al., 2007, 2009).

2.4.2 *Swift*-UVOT data

We followed standard procedure suggested by instruments team to reduce the UVOT data. The UVOT data are in event mode or imaging mode. We used aspect corrected (corrected for any shift or rotation from the source position) sky image files of available filters in each observation ID for a selected source region to get the average count rate. To avoid the UV or optical contamination from the host galaxy instrument team has suggested to take the circular region of 5 arcsec radius, centred at the source RA and DEC. We used a circular region of 20 arcsec away from the target source and any other contaminating object in the field to get the background products. The exposures of the UVOT filters are generally in the range of 10 s to 2 ks. To get the deepest image, the `UVOTISUM` [5] task was used to co-add multiple exposures, if available, in a particular observation ID. To get the background-corrected source count rate, the `UVOTSOURCE` [6] task was used. There are regions on UVOT detectors, called small-scale sensitivity (SSS) regions, where the throughput of the detector is comparatively low. We checked for the filters with such regions and removed that particular data point. Sometimes, few data points show an unusual drop in the count rate/flux fall and hence, resulting in large variability compared to the local mean. McHardy et al. (2014) reasoned this arises from the bad tracking of the telescope. We discarded those data points in our analysis. We also corrected the count rates to account for the loss of sensitivity of UV detectors with time by using filter correction files.

2.4.3 *XMM-Newton* EPIC-pn and MOS data

All *XMM-Newton* data are processed using standard System Analysis Software (SAS; Gabriel et al., 2004) and updated calibration files available at the time of processing. To check the presence of any flaring particle background, we created the source light curve above 10 keV.

[4]`http://www.swift.ac.uk/user-objects/`
[5]https://www.swift.ac.uk/analysis/uvot/image.php
[6]https://www.swift.ac.uk/analysis/uvot/mag.php

This is a necessary step in the data extraction process of EPIC since the data suffers from background flaring event due to the high apogee altitude of the satellite orbit. We created good time interval (GTI) files by excluding the time intervals containing particle background which were capped by count rate. We considered the event only with `PATTERN`$\leq$4 for EPIC-pn and excluded events in the bad pixels and at the edges of the CCD (FLAG=0). We also checked for the pile-up[7] effect using `epatplot` task. After examining the result of `epatplot`, one can decide whether the data set is significantly affected by pile-up by checking the ratio between the observed single or double events to the model predicted events. This ratio must be very close to 1 for non piled-up data. We extracted the source and background spectra from the circular regions of a particular radius depending on the individual object. We generated the light curves in different energy bands using ftool `xselect`. The redistribution matrix and ancillary response files were generated using `arfgen` and `rmfgen` tasks, respectively. Similar steps are followed for MOS detector.

2.4.4 *NuSTAR* data

To reduce the *NuSTAR* data, we used standard *NuSTAR* data analysis software (`NuSTARDAS`) available in the HEASoft package. The `nupipeline` task was run to extract the calibrated and cleaned event files from the raw data files. These events are further reprocessed to generate the science quality products i.e., light curves, energy spectrum, effective area files and response matrices for each detector (FPMA and FPMB) by using `nuproducts` task. The source light curves and spectra are accumulated by selecting a circular region centered around the source coordinates in the image obtained from the cleaned event file. The background products are extracted in the similar manner by selecting another circular area away from the source region. A detailed description of individual task could be found in the *NuSTAR* data analysis software guide[8].

2.5 X-ray Data Fitting Procedure

One of the main focuses of this work is the spectroscopic studies of Seyfert galaxies by using X-ray data from different space-based observatories. Various physical as well as phenomeno-

[7]The pile-up of source photons occurs when two or more soft X-ray photons are registered as a single high energy photon. However, it is possible to estimate the extent of pile-up effected area in the source image on the detector plane. For any scientific analysis, this pile-up effected area has to be estimated and removed from the event file

[8]`https://heasarc.gsfc.nasa.gov/docs/nustar/analysis/nustar_swguide.pdf`

logical models are used in our spectral fitting. In this thesis work, we used the X-ray spectral fitting package `XSPEC` (Arnaud, 1996) to fit the data. `XSPEC` is a command-driven X-ray spectral-fitting program which is available as an integrated part of `HEASoft`. It is independent of detectors from which the data have been collected. The `XSPEC` package comes with in-built models ranging from simple mathematical functions (e.g. constants, power laws, Gaussians, etc.) to highly complex physically-motivated models. `XSPEC` also gives the liberty to load external models in it and make use of fitting process.

The observed spectrum $D(I)$ of an X-ray source is a distribution of photon counts over the instrument channels (I). However, it is not the actual description of the source properties as the spectrum measured with the X-ray detectors are contaminated with the background contribution $B(I)$. Therefore, the observed spectrum of the source $D(I)$ is related to the actual spectrum $f(E)$ by:

$$D(I) = \int_{0}^{\infty} R(I,E) f(E) dE + B(I), \tag{2.1}$$

where $R(I,E)$ is the instrument response which is the probability that an incoming photon of energy E would be detected in channel I. The net source counts per channel (after background subtraction) could be thus derived by the quantity $D(I) - B(I)$. Since there are N number of discrete channels, the integral part of Equation 2.1 can be written as summation, i.e.,

$$D(I) - B(I) = C(I) = \sum_{i=1}^{N} f_i(E) R_i(I,E) \tag{2.2}$$

In principle, the response matrix function is a non-invertible matrix. Hence Equation 2.2 could not be solved directly to infer the actual source spectrum $f(E)$. Rather, an alternative approach is to choose a model spectrum $M(I)$, that can be described in terms of a few parameters. Then the model predicted counts are compared with the observed counts by using a fit statistics and used to evaluate whether the model spectrum “fits” the data obtained from the detector. The model parameters are varied to find the best fitted parameters according to fit statistics. The most commonly used fit statistic is chi-square statistics which is defined as:

$$\chi^2 = \sum_{i=1}^{N} \frac{(C_i(I) - M_i(I))^2}{\sigma_i(I)^2}, \tag{2.3}$$

where σi(I)=$\sqrt{C_i(I)}$ is the error associated with the observed counts $C(I)$ in a particular

Table 2.4: Table for $\delta\chi^2$ values for a number of parameters and corresponding confidence level.

Confidence	Parameters (n)		
	1	2	3
0.68	1.00	2.30	3.50
0.90	2.71	4.61	6.25
0.99	6.63	9.21	11.30

channel i assuming a Gaussian distribution (Wheaton et al., 1995). In general, for best-fit, the expected value of "Reduced-$\chi^2 = \chi^2/(\text{dof})$" is approximately equal to one for any acceptable model. Here, the number of degrees of freedom (dof) is calculated as the number of channels/bins minus the number of model parameters of the best-fitted model. For the case of low count statistics (or low source counts), it is more appropriate to use C-statistic (CSTAT) for the spectral fitting. In our analysis, we ensured that each channel consists of at least 20 counts to use χ^2 statistics. There may be cases when a number of models could be acceptable to fit the data with comparable goodness-of-fit. In such cases, the choice of best-fit model is driven by the scientific judgement and feasibility of the derived parameters. After having obtained the best-fit parameter values for the given model of choice, one needs to determine the range of values within which true value of parameter lies, called confidence interval. To calculate the confidence interval for a given parameter, the value is varied until the χ^2 increases by a particular amount (referred as the critical $\delta\chi^2$) above the best-fit value. $\delta\chi^2$ value depends on the confidence level required and on the number of parameters. The improvement in the fit with $\delta\chi^2$ values by adding n free parameters and their corresponding confidence level (Avni, 1976) are listed in Table 2.4. These values are taken from the `XSPEC` manual. In the present work, we have estimated the best-fit parameter values for 90% confidence level unless stated otherwise.

We used the various models available for X-ray continuum (ZCUTOFFPL, ZPOWERLW), absorption (PHABS, TBABS, ZXIPCF), reflection (PEXRAV, XILLVER, RELXILL), Comptonization (NTHCOMP, OPTXAGNF) and others for our work. Some of them are table models which are used as the local model such as RELXILL, XILLVER. These models are described in detail in the following chapters wherever they are used. Here, we provide a brief description of these models.

1. **X-ray continuum**- As described in Chapter-1, X-ray continuum is a result of Comptonization of thermal seed photons coming from the disk in the hot electron plasma. The spectrum of this continuum can be well described by simple power-law. The math-

ematical form ZPOWERLW is written as:

$$A(E) = N[E(1+z)]^{-\Gamma}, \tag{2.4}$$

where N is the normalization of the power law, representing the photon flux in Photons keV^{-1} cm^{-2} s^{-1} units, Γ is the photon index of the power law, varying in the range of $\sim$ 1.5-2.5 for AGNs and z is the redshift of the galaxy. Actually, power-law has an exponential cutoff at energies, generally, above 100 keV which can be constraint with high energy telescopes, e.g. *NuSTAR* . The mathematical form of ZCUTOFFPL is:

$$F(E) = N[E(1+z)]^{-\Gamma} e^{-E(1+z)/E_{cut}}, \tag{2.5}$$

where E_{cut} is the cutoff energy.

NTHCOMP (Zdziarski et al., 1996; Życki et al., 1999) is a physical model which is commonly used for thermal Comptonization. In this model, the high energy cutoff is parameterized by the electron temperature ($\mathrm{kT_e}$). It is sharper than an exponential cutoff of ZCUTOFFPL. At low energy end of the spectrum, a rollover is formed which is driven by the seed photon energy. Between these two rollovers, the shape of the spectrum is governed by the electron temperature and the electron scattering optical depth.

COMPPS (Poutanen & Svensson, 1996) is a model in which Comptonization is computed for different geometries (slab, cylinder, sphere, hemisphere) of the source using exact numerical solution of radiative transfer equation. The Comptonization spectra depend on the geometry of the source, optical depth of the source medium, electron distribution parameters (e.g. electron temperature), spectral distribution of the seed photons (blackbody or multicolor disc), the way seed photons are injected to the electron cloud and the inclination angle. Instead of directly fitting the parameter for optical depth, the Compton parameter $y = 4 * tau * theta$ (where theta = electron temperature in keV/511) is used as the y-parameter is directly related to the spectral index and is stable in the fitting process. The electron distribution can be chosen as a power-law, Maxwellian, cutoff Maxwellian or hybrid. There are two ways to inject seed photons into the electron cloud, either isotropically and homogeneously throughout the cloud or from the bottom of the slab/cylinder/hemisphere or centre of the sphere. Besides the

X-ray continuum, this model also includes the reflected spectrum from the cold medium and the general relativistic effects of the rotating disc on it. The parameter space region for which numerical methods in this model gives reasonable outcome is: electron temperature should be greater than 10 keV and optical depth is less than 1.5 for slab geometry and 3 for other geometries.

OPTXAGNF is another Comptonization model for AGNs which is for colour temperature corrected disc and is energetically coupled model. This model includes a standard disc, optically thick and low temperature Comptonization region to produce soft X-ray excess and optically thin and high temperature thermal Comptonization region to produce power law emission. These three regions are powered by the gravitational energy released due to the mass accretion. When energy released is not fully thermalized, it is possible that a fraction of that energy is dissipated in the inner part of the accretion disc and elevates its temperature such that it acts as an optically thick Comptonizing medium. The disc emission is released up to a radius R_{corona}. Below this radius, the energy is distributed between powering the power-law and soft excess emission. The colour temperature corrected disc partly contributes to the soft excess. Remaining contribution comes from the Compton upscattering of inner disc photons in the cold Comptonization ($\mathrm{kT_e} \sim 0.2$keV) medium. A fraction of the total gravitational energy is also consumed in the hot corona ($\mathrm{kT_e} \sim 100$keV) which gives rise to the X-ray continuum emission.

2. **Absorption**- The intrinsic continuum emission from the source gets absorbed by the our local galactic medium before reaching the X-ray detectors. This absorption mostly affect the soft X-rays below 10 keV. The spectral model PHABS (i.e., photoelectric absorption model) describe the continuum absorption, is expressed as:

$$F(E) = exp[-N_H \sigma(E[1+z])], \tag{2.6}$$

where N_H is the density of the absorbing material measured in atoms cm^{-2} and is normalized to the total hydrogen number density, known as equivalent hydrogen column density, σ(E) represents the cross-section (excluding Thomson scattering) for the absorption of X-ray photon with energy E . It is mainly derived by considering the individual contribution of three different cross sections of gas, grain and molecules present in the interstellar medium (ISM) (see Wilms et al. (2000) for a detailed discussion). In TBABS model, updated photoionization and gas phase cross sections have been used as a result of updates to the ISM abundances.

ZXIPCF (Reeves et al., 2008) is another model which is an XSTAR-based absorption model, simulated for X-ray continuum with slope of 2.2 and turbulent velocity 0f 200 km/s. XSTAR is a computer program for probing the emission spectra and physical conditions of photoionized gas. This is used for ionized and partially covering absorbers along the line of sight to the nuclear source.

3. **Blackbody emission**- As mentioned previously, AGNs have also been observed to show an excess at soft X-ray ranges, in addition to the continuum emission (below $\sim$2 keV). This is known as 'soft X-ray excess'. Although there are physical model to fit this feature, but in phenomenological model it is modeled with a thermal blackbody spectrum of the form:

$$F(E) = N \times 8.0525 \frac{E(1+z)^2}{((1+z)kT)^4(exp(E(1+z)/kT)-1)} dE, \tag{2.7}$$

where N is blackbody normalization in the units of 10^{39} erg s^{-1} (10 kpc)$^{-2}$ and kT is the blackbody temperature.

4. **Reflection**- There are many different models used to fit the reflection component of an AGN spectrum. One of the model, PEXRAV (Magdziarz & Zdziarski, 1995), consists of the cutoff power law continuum model and the component reflected from the accretion disc. It considers Compton reflection of X-rays and γ-rays by cold electrons. In the Compton reflection, the photons emitted by a source (e.g. corona) fall onto a slab (e.g. an accretion disc) and re-emitted with different energy altered by Compton scattering and bound-free absorption. In this model, the angular dependence of the reflection spectrum has been taken into account. In the hard X-ray or γ-ray regime, the reflected spectrum hardens with increasing viewing angle. Some of the parameters characterizing PEXRAV model are photon index, cutoff energy, inclination angle and reflection scaling factor. The reflection scaling factor is the relative reflection. Only the reflection component can also be derived by setting this factor negative.

The other physical reflection model is RELXILL (García et al., 2014; Dauser et al., 2014) which is a combination of the advanced code XILLVER (García & Kallman, 2010; García et al., 2013) and the relativistic line-emission kernel RELLINE (Dauser et al., 2010). This model takes into account the angular dependence of reflection with accretion disc radius and includes recent photoionization data. RELXILL provides two types of coronal geometry for the calculation of emissivity- (1) the extended corona (RELXILL) and (2) the lamppost corona (RELXILLLP). In the extended corona geometry, the emissivity profile of the accretion follows a broken power law, while the lamppost corona is assumed to be a point-like structure above the disc at a certain height along the rotation axis. This model includes both the reflected spectrum as well as illuminating continuum. There are two options for the illuminating continuum- (1) a power law with exponential cutoff and (2) an NTHCOMP type thermal Comptonization. The model parameters include the reflection fraction which is a ratio between the flux reflected from the disk and the flux that directly reaches the observer. The observed reflected emission not only depends on the emissivity profile but also on the ionization state, disk density, iron abundance of the accretion disk and the disc inclination angle. This model also estimates the spin of the black hole by fitting a relativistically smeared fluorescent iron line. Another variant of this model is called RELXILLLPION, which approximates the variation in the ionization parameter of the disc as a power law. These models are in developing stage and several assumptions have been made in the RELXILL family models. For example, the disc density is assumed to be height independent, the irradiation angle is kept constant at 45° and the element abundances are fixed to solar values except for iron. Apart from these, other important effects which have not been taken into account, found to affect the spectroscopy (Niedźwiecki et al., 2016). In the lamppost model, for a small height of the continuum source and steep emissivity profiles, the gravitational redshift is neglected. This affects the shape of the reflected spectrum and the cutoff energy of the Comptonization spectrum. Also, the reflected photons due to the light-bending effect can irradiate the disc which can change the refection spectrum. This kind of second order effect is significant for smaller height. These limitations are corrected in the latest reflection model REFLKERR (Niedźwiecki et al., 2019), where the continuum spectrum is calculated using the COMPPS model and agrees well with the simulations.

Chapter 3

Complex optical/UV and X-ray variability in Seyfert 1 galaxy Mrk 509

Active galactic nuclei (AGNs) emit radiation in multi-wavelength ranges, originating from different regions. Simultaneous observation in multi-bands provides an opportunity to establish connections between various bands from radio to γ-ray. Although simultaneous broadband coverage of AGNs using ground and space-based observatories is quite difficult to schedule due to many different factors, the space-based observatories such as *XMM-Newton*, Swift and AstroSat have capabilities to provide simultaneous coverage from X-rays to UV/optical bands. Due to its high cadence capability, Swift has been used in monitoring programs of many AGNs that provided an insight into the UV/optical and X-rays variabilities on short as well as long term time scales. These campaigns have shown a remarkably strong correlation between emission in different bands. The X-ray reprocessing is interpreted as the most likely origin of the variabilities in UV/optical emission. In this chapter, a detailed spectral and timing analysis of a Seyfert 1 galaxy Mrk 509 is presented. In this work, data from the *Neil Gehrels Swift* observatory that spanned over $\sim$13 years between 2006 and 2019 are used. This chapter is structured as follows: Section 3.1 presents the basic introduction and previous studies of this source. In Section 3.2, the observation details and data reduction processes have been discussed. Spectral fitting, correlation analysis between original light curves, filtering of the light curves for long term variations and corresponding results are described in Section 3.3. Finally, the discussion and summary of our findings are presented in Section 3.4 and 3.5. This work is published as Kumari et al. (2021) in the *Publication of the Astronomical Society of Australia (PASA).*

3.1 Introduction

As discussed in Chapter 1, AGNs are strongly believed to be fuelled through the accretion of matter from the surrounding medium around the SMBH at the center. This has been recently confirmed through the observations of a nearby radio-galaxy M87 with the Event Horizon Telescope (EHT; Akiyama et al. 2019). Imaging the central black hole and the accretion disk at the center of other galaxies that are farther away is impossible even with the EHT. There are, however, other indirect methods that are used to derive the physical structure and size of these objects. Continuum reverberation mapping (RM; Blandford & McKee 1982; Peterson 2014) technique is one such method in which the estimated time lag between the continuum emission in shorter and longer wavelength ranges has been used to derive the size of the BLR and hence the black hole virial mass in several AGNs (Peterson et al., 2004; Bentz et al., 2009). Understanding of the emission mechanism in AGNs has been a topic of intense research for several decades. However, the origin of emission in different wavelength ranges of the electromagnetic spectrum and correlation between them remain ambiguous to date. The general picture is that the low energy photons (seed photons) in ultraviolet (UV) and optical bands are believed to be originated from the accretion disk and the BLR. These photons get inverse Compton scattered in the hot electron plasma (corona), causing X-ray emission from the AGNs (Haardt & Maraschi, 1991).

The origin of the UV/optical and X-ray variabilities and correlation between them have been one of the most intriguing questions in the studies of the physical size and structure of AGNs. In Seyfert galaxies, the energy spectrum is dominated by UV radiation which is believed to be originated from a multi-colour blackbody disk (Koratkar & Blaes, 1999). The X-ray/UV/optical emission from the accretion disk shows variabilities over timescales ranging from a few hours to years in the AGNs with black hole mass in $10^6 - 10^9$ $M_\odot$ range. Although the cause of the observed variabilities is not very well understood, several possible explanations are presented to interpret the results. The first and the obvious one is the fluctuations in the mass accretion rate (Arévalo et al., 2008). However, fluctuation in the mass accretion rate is insufficient to explain the variabilities on short time scales (i.e., hours to days) as these fluctuations drift on a viscous time scale, which is in years for AGNs. In many Seyfert galaxies, variations in X-rays have been found to lead UV/optical variations on short-time scales (McHardy et al., 2014), which can not be explained by density fluctuations. Fluctuations in X-ray leading over the UV/optical band is explained by the so-called "reprocessing model". In this model, X-ray radiation from the central corona directly illuminates the accretion disk, thereby increasing its temperature. Heating of the accretion disk due to radiation from the corona makes the disk a source of enhanced radiation in UV/optical bands. In this process, the time delay between the driving radiation and reprocessed radiation is given by $\tau \propto \lambda^{\beta}$, where $\beta = 4/3$ for the standard Shakura-Sunyaev accretion disk (Cackett et al., 2007; McHardy et al., 2014; Edelson et al., 2015; Fausnaugh et al., 2016; Troyer et al., 2016; Edelson et al., 2017). Earlier studies were mainly performed with radiation in UV and optical bands and were found to be consistent with the 4/3 dependence.

The often seen strong temporal correlation between the X-ray and UV/optical emission indicates a connection between the two. Thus, simultaneous multi-wavelength observations are necessary to probe the physical processes taking place near the central engine. Before the advent of simultaneous multi-frequency observatories, e.g. *XMM-Newton*, *Swift* and *AstroSat*, many coordinated monitoring programs have been carried out using the space-based and ground-based observatories (Maoz et al. 2002; Arévalo et al. 2008; Evans et al. 2009; Breedt et al. 2010). Coordinated observations with the *Rossi X-ray Timing Explorer (RXTE)* and many ground-based telescopes divulged the lag of optical emission with respect to the X-rays and showed a pretty good correlation between them (Shemmer et al., 2003; Uttley et al., 2003; Arévalo et al., 2008; Marshall et al., 2008; Arévalo et al., 2009). In some other cases, however, the radiation in longer wavelengths was found to be leading the shorter wavelength emission (Papadakis et al., 2001; McHardy et al., 2004).

Simultaneous multi-wavelength and high cadence capabilities of the *Swift* observatory has given a thrust to the field of variability studies of AGNs. Originally designed for and focused on mainly gamma-ray bursts (GRBs), *Swift* has been utilized for the RM studies of many Seyfert 1 galaxies (Ebrero et al., 2011; McHardy et al., 2014; Edelson et al., 2015; Buisson et al., 2016; Noda et al., 2016; Troyer et al., 2016; Pal et al., 2016; Connolly et al., 2016; McHardy et al., 2016; Fausnaugh et al., 2016; Edelson et al., 2017; Starkey et al., 2017) and revealed the correlation between the radiation in UV/optical and X-ray bands, corroborating the reprocessing scenario. However, the observed correlation between X-ray and UV/optical emission in most cases has been found to be weak compared to that between the UV and optical emission (Edelson et al., 2019). In several AGNs, the time lag has been found to be $\sim 2-3$ times larger than the lag expected from the standard accretion disk model (McHardy et al., 2014). This indicates that there are other reprocessing regions apart from the accretion disk. Excess lag in the U-band of *Swift* containing the Balmer jump compared to either X-ray or extreme UV band hints towards the contribution of BLR (Korista & Goad, 2001; Korista & Goad, 2019). Earlier results from the *Swift* observations revealed that the extrapolation of the measured lag-spectrum, following the $\tau \propto \lambda^{4/3}$ relation down to X-rays, showed large deviation (Dai et al., 2009; Morgan et al., 2010; Edelson et al., 2015; Fausnaugh et al., 2016; McHardy et al., 2018). Possible explanations for this excess lag could be (i) the size of the accretion disk is larger than that predicted by standard disk (Pal et al., 2016), (ii) reprocessing of FUV photons in the inner "puffed-up" Comptonized disk region (Gardner & Done, 2017), (iii) reprocessing of X-rays from scattering atmosphere (Narayan, 1996). On filtering out the longer timescale variabilities from the light curves, the excess lags are found to decrease significantly, making the X-ray and UV/optical correlation stronger. This behaviour has been found in NGC 5548 (Edelson et al., 2015), NGC 4593 (McHardy et al., 2018), NGC 7469 (Pahari et al., 2020).

In this work, we analyzed the *Swift* multi-band observations of Mrk 509, spanning over 2006 to 2019, to investigate the cause of variations on different time scales and the effect of filtering the long term variations on the time-delay between X-ray and UV/optical bands. Mrk 509 is a bright ($L_{Bol} = 1.07 \times 10^{45}$ erg s^{-1}; Woo & Urry, 2002) Seyfert 1 galaxy, located at a distance of 145 Mpc (z=0.0344; Huchra et al., 1993) with a central black hole of mass $1.43 \times 10^{8} M_{\odot}$ (Peterson et al., 2004). This is the first AGN in which soft X-ray excess emission was discovered using HEAO-1 X-ray satellite (Singh et al., 1985). It has been the target of interest for multi-wavelength campaigns due to its variability properties, brightness, nature of soft X-ray excess, warm absorbers and outflow characteristics (Ebrero et al., 2011; Kaastra et al., 2012).

.

3.2 Observations and Data Reduction

In this work, we used archival data of Mrk 509 from *Swift* observatory that spanned 2006 July 18 to 2019 May 8. The observations were carried out simultaneously in UV/optical and X-ray bands with the UltraViolet-Optical Telescope (UVOT; Roming et al. 2005) and X-ray Telescope (XRT; Burrows et al. 2005), respectively. The UV/optical observations were carried out using six filters viz. UVW2 (192.8 ± 65.7 nm), UVM2 (224.6 ± 49.8 nm), UVW1 (260 ± 69.3 nm), U (346.5 ± 78.5 nm), B (439.2 ± 97.5 nm), and V (546.8 ± 76.9 nm) (Poole et al., 2007), whereas the X-ray observations were obtained in 0.3-10 keV range. The details

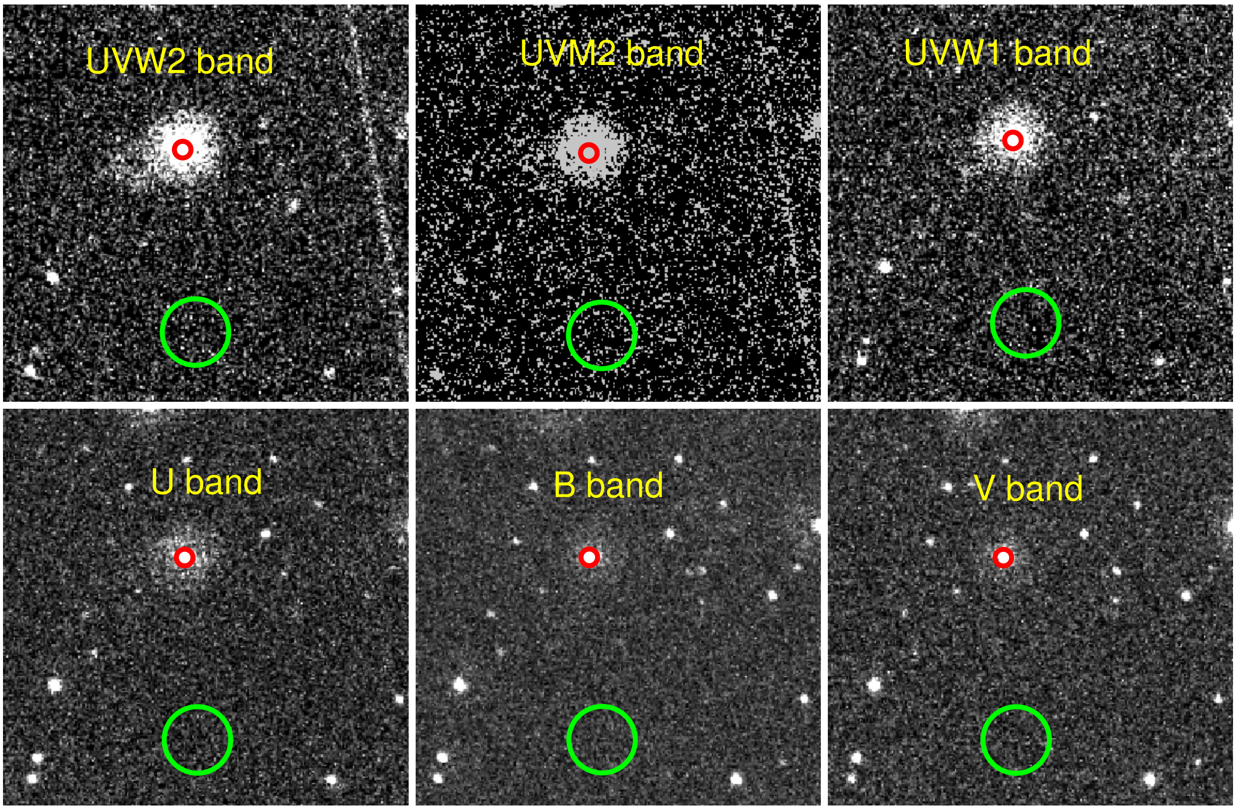

Figure 3.1: Images of Mrk 509 in six filters of UVOT (marked in each panel) are shown for observation ID : 00035469003 (20 April, 2006). Circular regions of 5 arcsec (red, centered at source position) and 20 arcsec (green, away from the source) radii were selected for the source and background regions, respectively.

of the observations used in the present work are listed in Table 3.1.

We extracted light curves in different energy ranges and spectra using the online XRT product generator tool[1]. The method used in the online tool is described in Evans et al. (2007, 2009). As already described in Section 2.4.1, each event file was divided into individual snapshots for generating light curves and spectra, and further in time intervals for pile-up correction. The source extraction radius is chosen depending on the mean-count rate. The pile-up correction was performed on the time intervals in photon counting (PC) mode where mean count rate is greater than 0.6 counts s^{-1}, by fitting the wings of the source PSF with the King function. For each interval, a source event list and an Ancillary Response File (ARF) were generated and then combined. While combining, each ARF was weighted according to the total counts in the source spectrum extracted from that particular time interval. The background spectrum was extracted by selecting an annular region with inner and outer radii of 142 arcsec and 260 arcsec, respectively, within the detector window. Any other source in the background region was excluded from the extraction region. The average count rate was calculated for each observation ID in PC mode of XRT for further timing and spectral analysis of the source.

Standard procedure was followed to reduce the UVOT data. We used aspect corrected sky image files of each observation ID in every filter to get the average count rate for the selected source region. A circular region of 5 arcsec radius, centered at the source, was selected as the source region to minimize contamination from the host galaxy. For background products, a circular region of 20 arcsec was selected away from the source to avoid contamination from the host galaxy as well as from any other source in the field. The regions selected for the source and background are shown in red and green circles in Figure 3.1, respectively. The exposures of the UVOT filters are generally in the range of 10 s to 2 ks. To get the deepest image, `UVOTISUM`[2] task was used to co-add multiple exposures, if available, in each observation ID. The `UVOTSOURCE`[3] task was used to get the background-corrected source count rate/flux densities in different filters. We also checked for small scale sensitivity (SSS) regions where throughput of the detector is comparatively low by running `UVOTSOURCE` task with additional command `lssfile=sssfile5.fits.` Apart from this, there are a number of data points where the count rate/flux fall rapidly and show large variability compared to the local mean. This may be due to the bad tracking of the telescope, as described in McHardy et al. (2014).

[1] http://www.swift.ac.uk/user_objects/
[2] https://www.swift.ac.uk/analysis/uvot/image.php
[3] https://www.swift.ac.uk/analysis/uvot/mag.php

Table 3.1: Log of observations of Mrk 509 with the *Swift* observatory

Observation ID	00035469001–00095002006
Duration of observation	2006 July 18 - 2019 May 8
MJD	53812.05 - 58611.70
No. of IDs for XRT used	275
No. of IDs for UVOT used	271

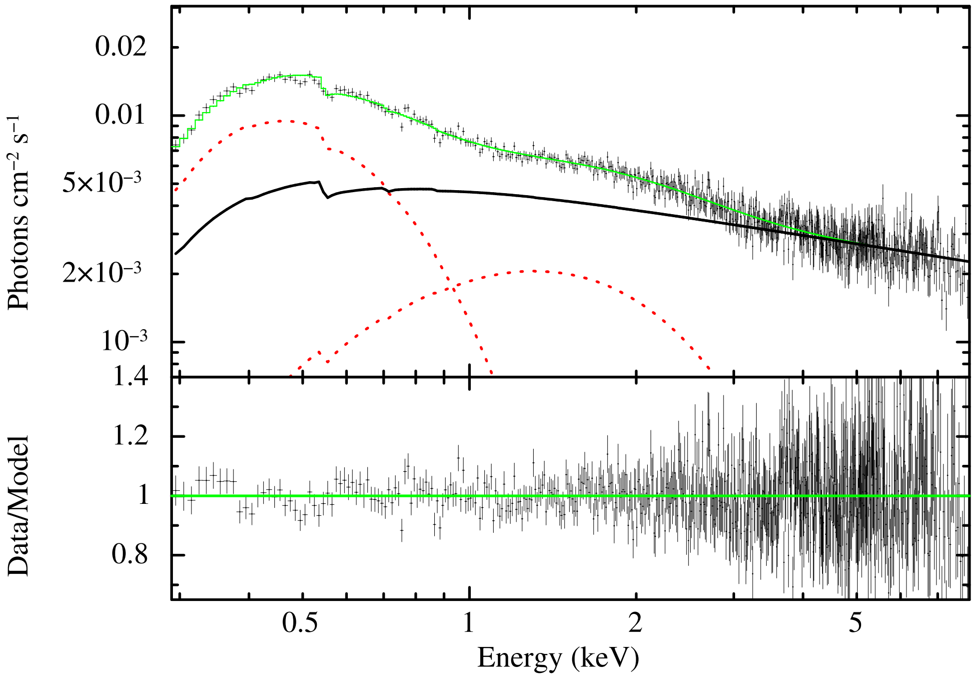

Figure 3.2: Time-averaged *Swift*/XRT spectrum of Mrk 509 and best-fit model (green line) are shown along with individual spectral components (red dotted lines for two blackbody components and solid black line for the power-law continuum model) in the top panel. Corresponding residuals are shown in the bottom panel.

We discarded those data points from further analysis. We also corrected the count rates to account for the loss of sensitivity of UV detectors with time by using filter correction files[4].

3.3 Data Analysis & Results

3.3.1 Spectral analysis

The AGNs spectra, especially of Seyferts, in 0.3-10 keV range (the range of operation of *Swift*/XRT) generally consist of soft X-ray excess and a power-law continuum along with the iron emission lines in $\sim$ $6-7$ keV range. In order to investigate the origin of the soft X-ray excess and power-law continuum, we carried out spectral analysis using data from all the *Swift*/XRT observations of Mrk 509. We extracted the time-averaged spectrum of all the

[4]https://www.swift.ac.uk/analysis/uvot/index.php

Table 3.2: Best-fit parameters obtained from spectral fitting of *Swift*/XRT data.

Spectral parameter	Value
Absorption column density N_H [10^{20} cm^{-2}]	3.95 (f)
Blackbody Temperature kT_{BB1} [keV]	0.121±0.002
Blackbody Normalization kT_{norm1} [10^{-5}]	17.4±0.8
Blackbody Temperature kT_{BB2} [keV]	0.46±0.01
Blackbody Normalization kT_{norm2} [10^{-5}]	9.0±1.0
Power-law Photon Index Γ	1.39±0.04
Power-law Normalization Γ_{norm} [10^{-3}]	5.3±0.4
C/dof	730.1/764

Best fit model : TBABS × [(ZBBODY+ZBBODY+ZPOWERLW)].

observation IDs using the online XRT product generator tool[1] (Evans et al., 2009). We fitted the spectrum in `XSPEC` and used C-statistics for minimization to obtain the best-fit parameters. The errors on each parameter are quoted at 90% confidence level. Using the source and background spectra and appropriate response matrices, we attempted to fit the data in 2-8 keV range with a redshifted `power-law` model along with the multiplicative component `tbabs` to incorporate the modification due to the Galactic absorption. In our fitting, the Galactic column density was fixed at 3.95×10^{20} cm^{-2} (HI4PI Collaboration et al., 2016). The fit statistic was found to be $C/dof = 580.8/597$ for a best-fit power-law photon index of 1.68 ± 0.02. We extrapolated the fitted model down to 0.3 keV. This showed strong positive residuals in the soft X-ray range (below 1 keV). This confirms the presence of soft X-ray excess in the spectrum. The soft X-ray excess above the power-law continuum was fitted with a simple redshifted blackbody (`zbbody`) model. The positive residuals were still present up to ∼3 keV. We added another redshifted blackbody component to the above model to describe these residuals. The fit-statistic improved by $\Delta C = -91$ with two additional parameters. The best-fit model `tbabs`×`(zbbody+zbbody+zpowerlaw)` resulted in $C/dof = 730.1/764$. The best-fit value of the power-law photon index was found to be $\Gamma = 1.39 \pm 0.04$, which is consistent with that reported by Mehdipour et al. (2011). The best-fit model, data and residuals are shown in Figure 3.2. The best-fitted parameters are given in Table 3.2.

Following the time-averaged spectroscopy, we attempted to fit the spectra from individual observation IDs with exposures of ∼1 ks. Each spectrum was grouped at a minimum of 1 count per bin to use C-statistics in `XSPEC` spectral fitting. We fitted each spectrum with a simple phenomenological model `tbabs`×`(zbbody+zpowerlw)` as the second thermal component was

[1]http://www.swift.ac.uk/user_objects/

not required in fitting. While fitting the spectrum of individual IDs with the above model, we estimated source flux in 0.3-8 keV, 0.3-2 keV, and 2-8 keV ranges for further analysis. The total flux in 0.3-8 keV range, best-fit spectral parameters and the reduced C for all observation IDs are shown in Figure 3.3. The variation/non-variation of flux and spectral parameters over the duration of the observations can be clearly seen in the figure. We attempted to search for the presence of any correlation between different parameters obtained from spectral fitting. The correlations between the power-law flux (in 2-8 keV range), blackbody flux (BB flux in 0.3-2 keV range), power-law photon index and blackbody temperature are shown in Figure 3.4. From this analysis, we found a moderate correlation between the blackbody flux and power-law flux with Pearson's coefficient $\rho \sim 0.56$, between the blackbody temperature and blackbody flux with $\rho \sim 0.31$, and between the blackbody temperature and photon index with $\rho \sim -0.38$.

Considering the narrow energy range of XRT and short exposure of observations, there is a possibility of presence of degeneracy between parameters. Therefore, we investigated marginal posterior distributions of all the fitted parameters to determine the degree to which the parameters are correlated due to the degeneracies within the spectral fitting. In order to search through the parameter space, the data from the observation with maximum exposure, i.e. ~7 ks (Obs. ID 00035469003 : 20 April 2006) were used for fitting by applying the Markov Chain Monte-Carlo (MCMC) sampling procedure. We used the affine-invariant sampler developed by Goodman & Weare, 2010 and implemented in `XSPEC` as `CHAIN` task. For `tbabs`×`(zbbody+zpowerlw)` model, we considered 20 walkers with a total chain length of 100000 and burning initial steps of 20000. In Figure 3.6, we showed one and two-dimensional (1D and 2D) marginal posterior distributions for the spectral parameters. The median values of the parameters with 90% credible interval are shown above each 1D histogram. The Pearson's correlation coefficients for these distributions are -0.26 for kT_{BB} & kT_{norm}, -0.49 for Γ & kT_{BB}, -0.47 for Γ & kT_{norm}, -0.59 for Γ_{norm} & kT_{BB}, -0.44 for Γ_{norm} & kT_{norm}, and 0.85 for Γ_{norm} & Γ with p-value $< 10^{-5}$. It is evident from the figure that the correlation between the blackbody temperature and the photon index is not physical, instead spurious. On a careful investigation of correlation between spectral parameters from spectral fitting of all the observations and the MCMC sampling procedure, it is confirmed that there exists a certain degree of degeneracy between power-law photon index and blackbody temperature. However, the narrow energy range of *Swift*/XRT and short exposure time (~1 ks) of individual observations make it extremely difficult to remove this degeneracy through spectral fitting. Considering this, we proceeded with time-series analysis using data from all the *Swift*/XRT

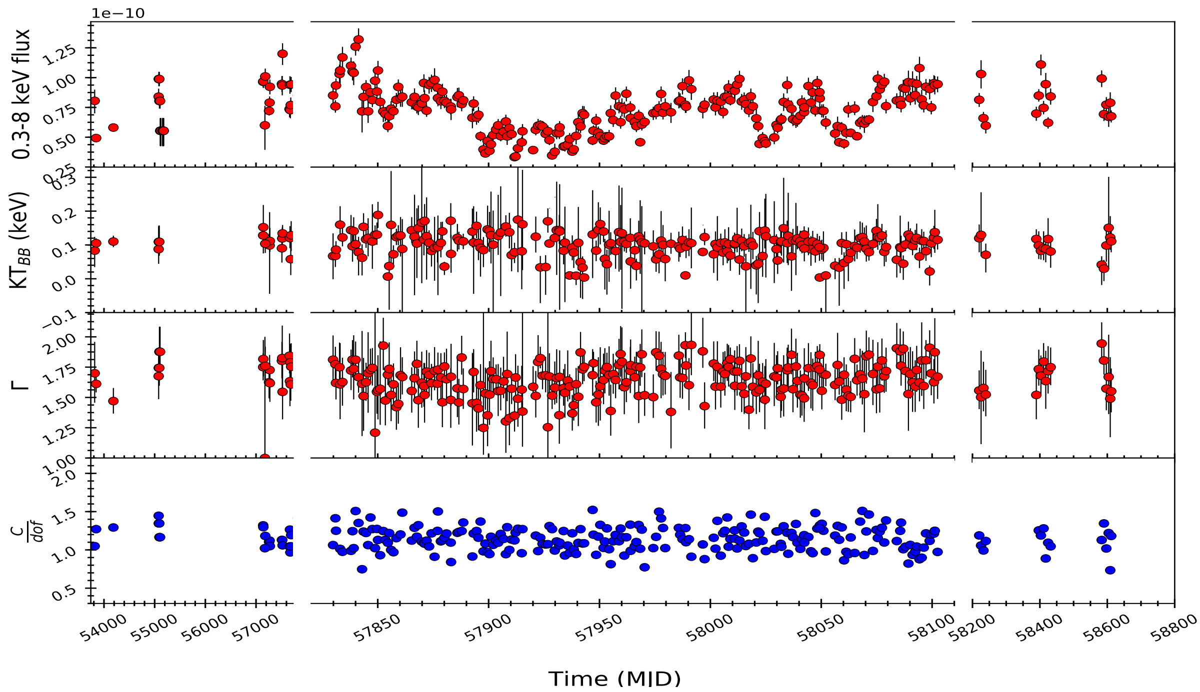

Figure 3.3: Variation of the source flux in 0.3-8 keV range, blackbody temperature (kT) and power-law photon index (Γ) with time (MJD) are shown in top three panels. The reduced *C*-stat obtained from the spectral fitting of each observation ID is plotted in the bottom panel.

observations.

3.3.2 Timing analysis

Variability amplitudes & nature of variability

As described in Section 3.2, the source flux densities for all six UVOT filters were estimated from all observation IDs. Soft X-ray (0.3-2 keV range) and hard X-ray (2-8 keV) fluxes were estimated from the spectral analysis of *Swift*/XRT data of each observation ID (see Section 3.3.1). Using these estimated flux densities, simultaneous X-ray and UVOT light curves of Mrk 509, for the duration of the *Swift* monitoring campaign, i.e. from 2006 June 18 to 2019 May 8, are generated and shown in Figure 3.5. It can be clearly seen that the light curves in different bands show variabilities in short-term as well as long-term time scales. To quantify the observed variabilities in X-ray and UV/optical light curves, we calculated fractional variability F_{var} and its uncertainty using the relations,

$$F_{var} = \sqrt{\frac{S^2 - \overline{\sigma_{err}^2}}{\bar{x}^2}}$$

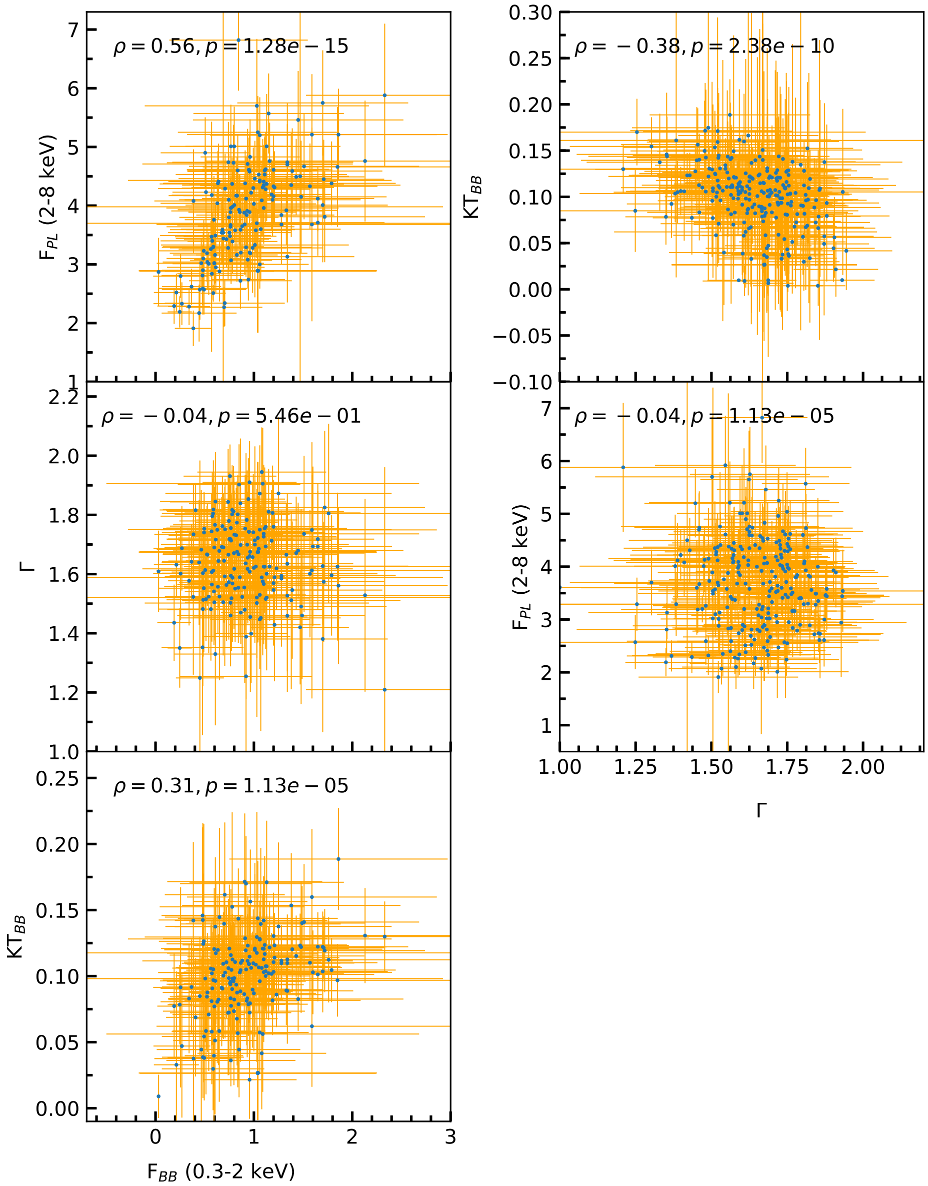

Figure 3.4: Pearson's correlation coefficients (ρ, p-value) between different spectral parameters extracted from fitting of individual observations using phenomenological model tbabs×[bbody+zpowerlw]. The 0.3-2 keV blackbody flux (F$_{BB}$; in units of 10^{-11} erg s^{-1} cm^{-2}) has been plotted against 2-8 keV power-law flux (F$_{PL}$; in units of 10^{-11} erg s^{-1} cm^{-2}), photon-index (Γ) and blackbody temperature KT$_{BB}$ (in keV) from top to bottom, respectively, in the left panels of the figure. In the right panels, the plots for Γ vs KT$_{BB}$ and Γ vs F$_{PL}$ have been shown.

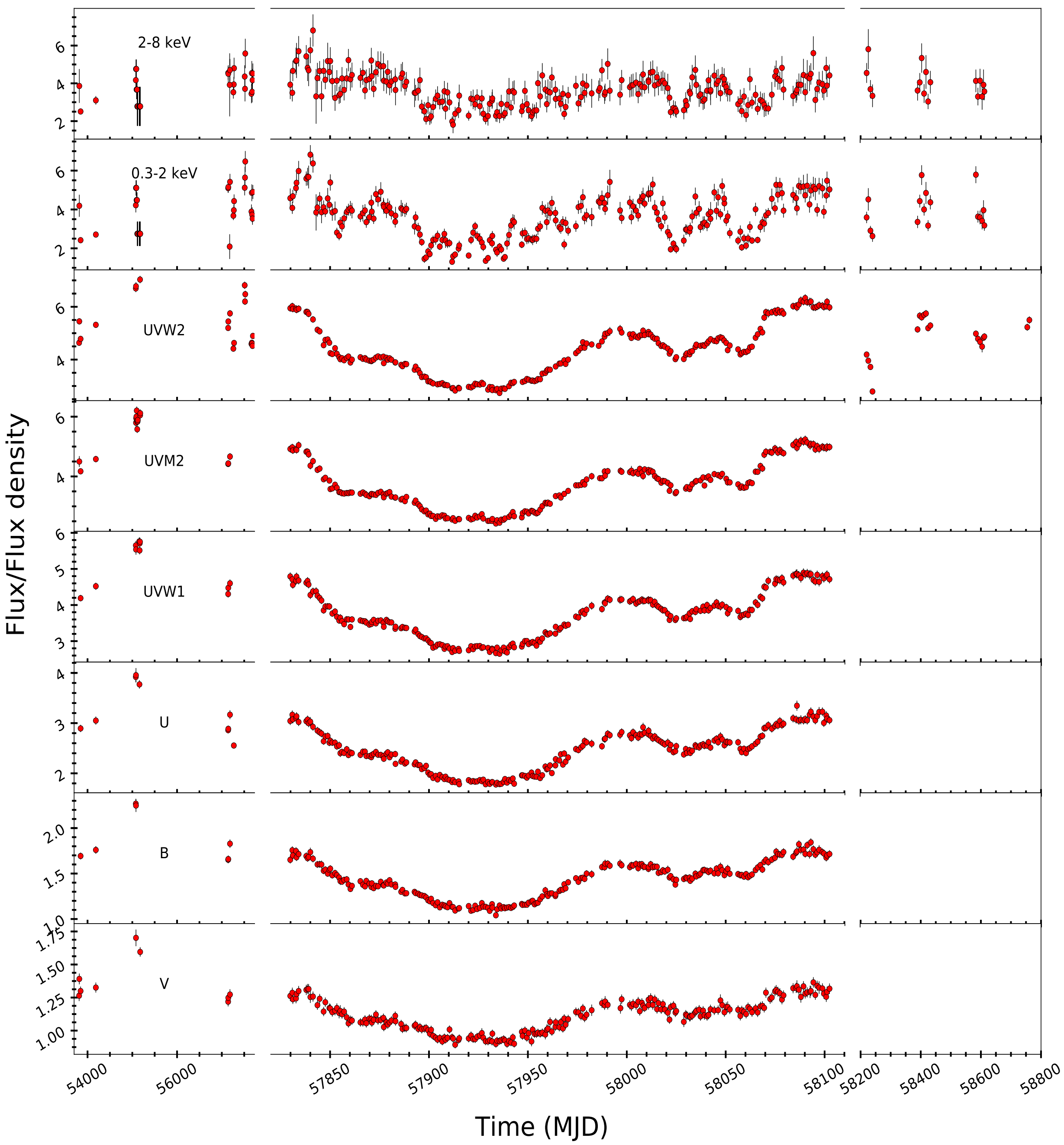

Figure 3.5: Simultaneous UV/optical and X-ray light curves of Mrk 509 from *Swift* observations during 2006 June 18 to 2019 May 8. The UV/optical (UVW2, UVM2, UVW1, U, B, V) flux densities (in 10^{-14} erg s^{-1} cm^{-2} Å^{-1}) of the source are plotted with the hard X-ray (2-8 keV) and soft X-ray (0.3-2 keV) flux densities (in 10^{-11} erg s^{-1} cm^{-2}). The X-ray flux densities are estimated from spectral fitting of data from the individual observation IDs. Two breaks in the light curves are due to the large observation gaps.

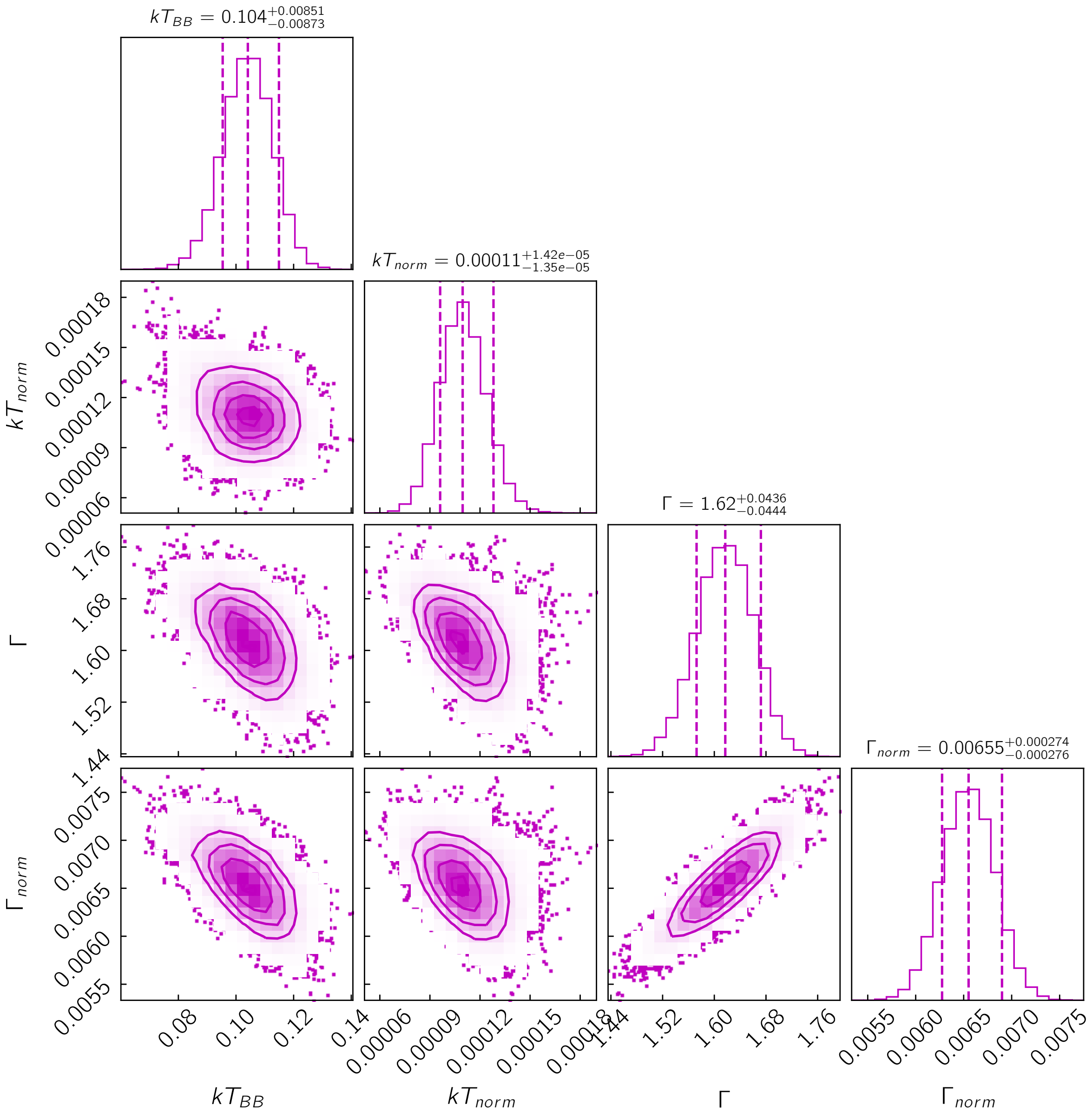

Figure 3.6: 1D and 2D marginal posterior distributions for power-law photon index (Γ) and its normalization (Γ_{norm}), blackbody temperature (kT_{BB}, in keV) and its normalization (kT_{norm}) for Obs. ID 00035469003 (20 April 2006) fitted with tbabs$\times$[zbbody+zpowerlw] model. Vertical lines in 1D distributions show 16%, 50% and 90% quantiles. CORNER.PY (Foreman-Mackey, 2016) was used to plot these distributions.

and uncertainty in F_{var} as

$$\sqrt{\left(\sqrt{\frac{1}{2N}}\frac{\overline{\sigma_{err}^2}}{\bar{x}^2 F_{var}}\right)^2 + \left(\sqrt{\frac{\overline{\sigma_{err}^2}}{N}}\frac{1}{\bar{x}}\right)^2}$$

where $\bar{x}$, S, $\overline{\sigma}_{err}$ and N are the mean, total variance, mean error and number of data points, respectively (Vaughan et al., 2003), for X-ray and UV/optical bands. Using above expressions, the fractional variabilities in hard X-ray (2-8 keV), soft X-ray (0.3-2 keV), UVW2, UVM2, UVW1, U, B, and V bands are derived to be 0.152±0.010, 0.281±0.006, 0.223±0.001, 0.234±0.002, 0.184±0.002, 0.174±0.002, 0.147±0.002 and 0.114±0.002, respectively. Within the UV/optical bands, the variability amplitudes are found to decrease with the increase in wavelength. This trend has been reported in many previous studies (Fausnaugh et al., 2016; Edelson et al., 2019) as emission at longer wavelengths is expected to originate from regions in accretion disk at larger radii and thus, prone to get diluted with other effects like emission from the BLR and NLR or the host galaxy. From the spectral analysis, we found a complex soft X-ray excess which can be described by two thermal components. Thus, high variability in the soft X-ray band could be due to a mixture of different spectral components i.e., thermal plasma in the inner disk or/and X-ray reprocessing close to the inner edge of the disk. Since the signatures of warm absorbers have already been reported in earlier studies (Ebrero et al., 2011; Steenbrugge et al., 2011), and we see residuals below 1 keV (Figure 3.2), variability due to the warm absorbers can not be ruled out.

Based on the probability spectral density (PSD) studies, the nature of variability in AGNs is considered to be red-noise variability (Papadakis & Lawrence, 1993). This is very similar to the one that is observed in Galactic black holes, where the PSD is described by a broken power-law at a specific frequency depending on the spectral state. Switching between different states indicates that the variability process is non-stationary. Statistically, in non-stationary process, the moments of the probability distribution function (i.e. mean and variance) vary with time. In the left panel of Figure 3.7, we plotted the change of mean $< x >$, excess variance σ_{xs}^2 and fractional rms amplitude F_{var} (computed by taking 10 data points) in 0.3-10 keV range light curve with time. All these quantities are found to change with time. In the bottom panel, the averaged rms has been shown (binned over 5 data points of individual rms), which also changes with time, indicating the non-stationarity of the variability process. We divided the entire light curve into two segments covering the time from 57829 to 57967 MJD and 57968 to 58102 MJD, respectively (marked with a dotted line in the top left panel of

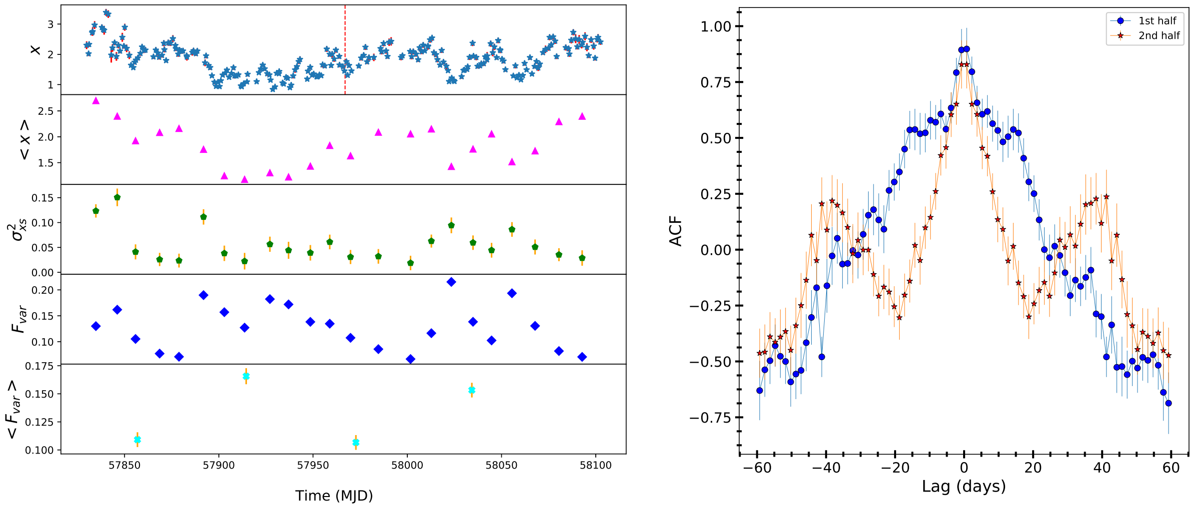

Figure 3.7: Left panel: Light curve of Mrk 509 in 0.3-10 keV range is shown in the top panel. The mean count rate, excess variance and fractional rms amplitude measured from the segment of 10 points are shown in the 2nd, 3rd and 4th panel from top. In the bottom panel, averaged fractional rms amplitude is shown by binning 5 amplitudes. Right panel : Auto-correlations calculated for two segments (from 57829 to 57967 MJD and 57968 to 58102 MJD, as marked with a dotted line in the top left panel) of 0.3-10 keV light curves are shown.

Figure 3.7) and calculated the auto-correlation function (ACF) of each segment (Gliozzi et al., 2004). The rate at which the ACF decays for each segment is different. This suggests that there is an intrinsic difference in the temporal properties in both segments. This indicates non-stationary variability, though we can not claim it firmly due to the quality of the data used. We also did not find any signature of apparent state change over the duration of the observations (see Figure 3.3).

Table 3.3: Variability in X-ray and UV/optical bands are shown. N = number of data points or length of the light curve, F_{max} & F_{min} = maximum & minimum flux in the light curve in units of erg s^{-1} cm^{-2} $Å^{-1}$, R = peak-to-peak ratio (F_{max}/F_{min})

Energy band	N	$F_{\rm max}$ (10^{-11})	$F_{\rm min}$ (10^{-11})	R	Mean (10^{-11})	$\sigma^2_{\rm NXS}$ (10^{-3})	$F_{\rm var}$ (%)
0.3-2 keV	289	6.82	1.31	5.21	3.63	7.90	28.11 ± 0.11
2-8 keV	289	6.8	1.81	3.76	3.66	2.31	15.20 ± 0.96
		(10^{-14})	(10^{-14})		(10^{-14})	(10^{-3})	(%)
UVW2	258	7.03	2.74	2.57	4.47	4.99	22.35 ± 0.15
UVM2	233	6.20	2.43	2.55	3.80	5.49	23.43 ± 0.17
UVW1	234	5.76	2.65	2.17	3.76	3.42	18.48 ± 0.16
U	239	3.95	1.77	2.22	2.48	3.03	17.41 ± 0.18
B	237	2.27	1.04	2.17	1.44	2.17	14.72 ± 0.16
V	235	1.7	0.89	1.90	1.12	1.29	11.38 ± 0.15

Count–Count Correlation with Positive Offset (C3PO)

We defined $0.3 - 2$ keV and $2 - 8$ keV energy ranges as soft and hard X-ray bands. The soft X-ray band has several complex features such as soft X-ray excess, emission lines, blurred reflection and absorption features, while the hard band is mainly dominated by primary continuum resulted from multiple inverse Compton scattering of seed photons with electron plasma in the corona. We plotted light curves in soft X-ray band, hard X-ray band and all the filters of optical and UV bands in Figure 3.5. From visual inspection, all the light curves seem to be correlated. The variations in UV/optical bands are smoother than the X-rays.

We attempted to quantify the correlations and variabilities seen in UV/optical and X-ray light curves using C3PO method. The C3PO method was first used by Churazov et al. (2001) in the black hole binary system Cygnus X-1 to find the varying and stable components in high/soft state. After that, this technique has been used in many AGNs (Taylor et al., 2003; Noda et al., 2011, 2013, 2016; Pal & Naik, 2017). We fitted a linear function $y = mx + c$ between the reference band as abscissa and secondary bands as ordinate, where m and c are the slope and offset, respectively. In the left and right panels of Figure 3.8, the hard X-ray (2-8 keV) and UVW2 bands are taken as reference bands, respectively, and all other bands are considered as secondary. For uniformity, the plots have been shown for flux densities though there was no difference in the fitted values when plotted in count rates. We also used Pearson's correlation coefficient 'ρ' to quantify the strength of inter-band correlation and determined the significance of the strength of the correlation. All the values of slopes, offset, Pearson's coefficient are given in Tables 3.4 and 3.5. From the linear fitting, we found a reasonable correlation between hard X-rays and all UV/optical bands ($\rho \sim 0.40 - 0.53$). However, the correlation between the UVW2 and other UV-optical bands is found to be stronger ($\rho \sim 0.95 - 0.99$). When fitted relative to UVW2 band, a positive offset (except for soft X-rays) has been found for all other UV/optical bands, including the hard X-ray band. This indicates that the less variable component is possibly coming from the BLR and the host galaxy. Similar results have been drawn from the flux-flux analysis for other systems, e.g. Fairall 9 (Hernández Santisteban et al., 2020).

Filtering of slow and linear variations

To understand the short term variabilities in different bands due to reprocessing, i.e. X-ray reprocessing or Comptonizaton, we focused on the fast variations in the light curves.

Table 3.4: Slope, offset and Pearson's coefficient for hard X-ray vs soft bands (soft X-ray & UV/optical bands).

Band	slope(m) & offset(c)	χ^2_ν, dof	Pearson's coefficientρ, p
Soft X-ray	$m = 1.50 \pm 0.05$ $c = (-1.79 \pm 0.17) \times 10^{-11}$	0.61, 289	0.82, 1.80×10^{-71}
UVW2	$m = 2.17 \pm 0.21$ $c = (-2.97 \pm 0.70) \times 10^{-11}$	2.03, 251	0.52, 1.15×10^{-18}
UVM2	$m = 1.97 \pm 0.21$ $c = (-2.90 \pm 0.70) \times 10^{-11}$	2.14, 246	0.40, 4.95×10^{-11}
UVW1	$m = 1.51 \pm 0.16$ $c = (-1.37 \pm 0.53) \times 10^{-11}$	2.13, 240	0.44, 6.98×10^{-13}
U	$m = 0.92 \pm 0.09$ $c = (-0.62 \pm 0.30) \times 10^{-11}$	2.13, 239	0.52, 4.64×10^{-18}
B	$m = 0.47 \pm 0.05$ $c = (-0.14 \pm 0.16) \times 10^{-11}$	2.18, 237	0.53, 8.64×10^{-19}
V	$m = 0.25 \pm 0.023$ $c = (0.27 \pm 0.08) \times 10^{-14}$	2.16, 234	0.48, 3.67×10^{-15}

Table 3.5: Slope, offset and Pearson's coefficient for UVW2 vs other UV/optical bands.

Band	slope(m) & offset(c)	χ^2_ν, dof	Pearson's coefficient ρ, p
Hard X-ray	$m = 0.46 \pm 0.04$ $c = (1.34 \pm 0.19) \times 10^{-11}$	2.07, 238	0.51, 2.41×10^{-17}
Soft X-ray	$m = 0.96 \pm 0.05$ $c = (-0.85 \pm 0.20) \times 10^{-14}$	6.04, 238	0.75, 5.76×10^{-44}
UVM2	$m = 0.79 \pm 0.004$ $c = (0.25 \pm 0.02) \times 10^{-14})$	0.26, 224	0.99, 6.37×10^{-241}
UVW1	$m = 0.66 \pm 0.005$ $c = (0.85 \pm 0.02) \times 10^{-14}$	0.38, 224	0.99, 4.82×10^{-212}
U	$m = 0.43 \pm 0.006$ $c = (0.59 \pm .02) \times 10^{-14}$	1.10, 225	0.98, 2.74×10^{-150}
B	$m = 0.21 \pm 0.003$ $c = (0.50 \pm 0.01) \times 10^{-14}$	1.35, 225	0.97, 8.27×10^{-133}
V	$m = 0.12 \pm 0.002$ $c = (0.60 \pm 0.01) \times 10^{-14}$	0.97, 225	0.95, 1.01×10^{-113}

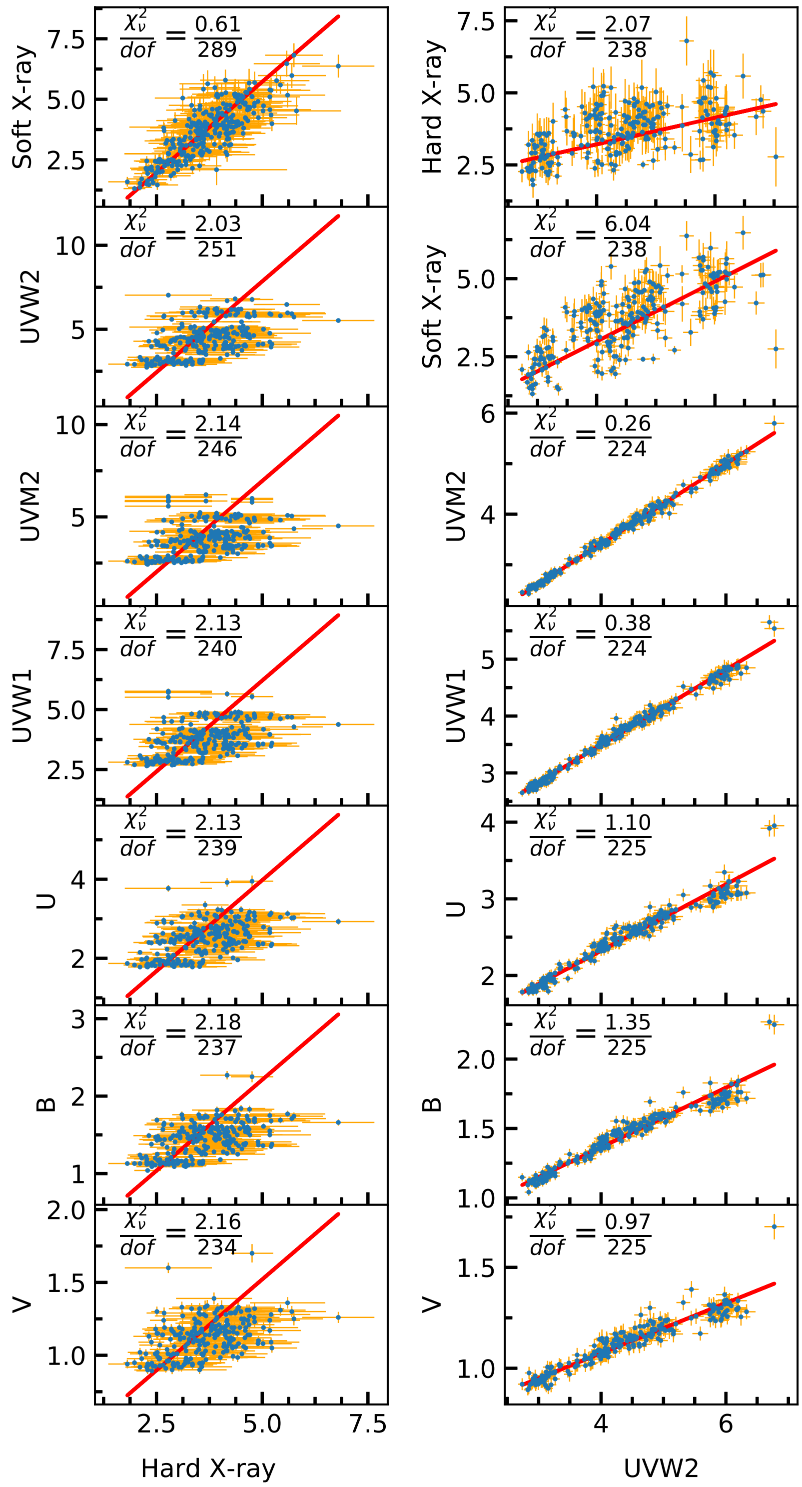

Figure 3.8: The C3PO plots are shown with hard X-ray band (left panels) and UVW2 band (right panels) as reference bands. The best-fitted linear equations are presented as red solid lines in each panel. The units of the fluxes are 10^{-11} erg s^{-1} cm^{-2} for X-ray bands and 10^{-14} erg s^{-1} cm^{-2} Å^{-1} for UV/optical bands.

It is well known that the long term variations can distort the short term time lags while estimating CCFs (Welsh, 1999). So we attempted to remove the slow variations, i.e long term variations due to the changes in the accretion rate, from the light curves. As mentioned above, Figure 3.5 shows short term variations as well as long term variations in the curves in all bands. Therefore, the long term variations should be filtered out from the light curves to determine short time information. Such filtering has been carried out in recent studies in a few AGNs, e.g. NGC 5548 (McHardy et al., 2014), NGC 4593 (McHardy et al., 2018), NGC 7469 (Pahari et al., 2020), to eliminate the effect of long term variations. We used the locally weighted scatter smoothing (LOWESS) method for the filtering process, which is based on non-parametric and non-linear least square regression method (Cleveland & Devlin, 1988). In this method, a regression surface is estimated by fitting a low-degree polynomial locally to a subset of the data. The polynomial is fitted with weighted least-squares, giving more weight to the near data points and least weight to the farthest ones. The tricube function, $w(s) = (1-|s|^3)^3$ is used to calculate the weight, where s is the distance of a given data point from the neighbouring point scaled to lie in the range of 0 to 1. Here, $s(t) = (t - t_i/\Delta t)$ is the time difference between time t and t_i at the data point i in terms of filtering time Δt. For this work, we used different filtering time to calculate the time lags as well as to investigate the effect of filtering of the long term variations. Since the filtering process has a limitation that it can only be performed on densely populated sample, we, therefore, applied the LOWESS filtering to the data in the range of MJD 57829 to MJD 58102 and calculated the time lags.

We filtered out the slow variations of the order of more than 10, 15, 18, 20 and 25 days from all light curves shown in Figure 3.5. The light curves obtained after filtering of variations of 18 days are shown in Figure 3.10. Although, the average cadence of the observations was about 1 day, filtering for less than 10 days was not feasible due to the gap of 6 days between two observations. Filtered light curves for the UVW2 and UVW1 bands, after removing slow variations of the order of 20 days, are shown in Figure 3.9 (top panel).

For determining the short time delay between two filtered light curves, we applied ICCF method (described in detail in Section 3.3.2). The estimated time delays between UVW2 and other bands after filtering have been listed in Table 3.6. The CCF lag-distribution for 20 days filtering and without filtering have been plotted in the bottom panel of Figure 3.9 to compare the effect of filtering on CCF distribution. It can be seen from the figure that after filtering, the distribution is significantly narrower than the unfiltered one. This indicates that the slower variations were causing the wider CCF which became narrower after filtering the

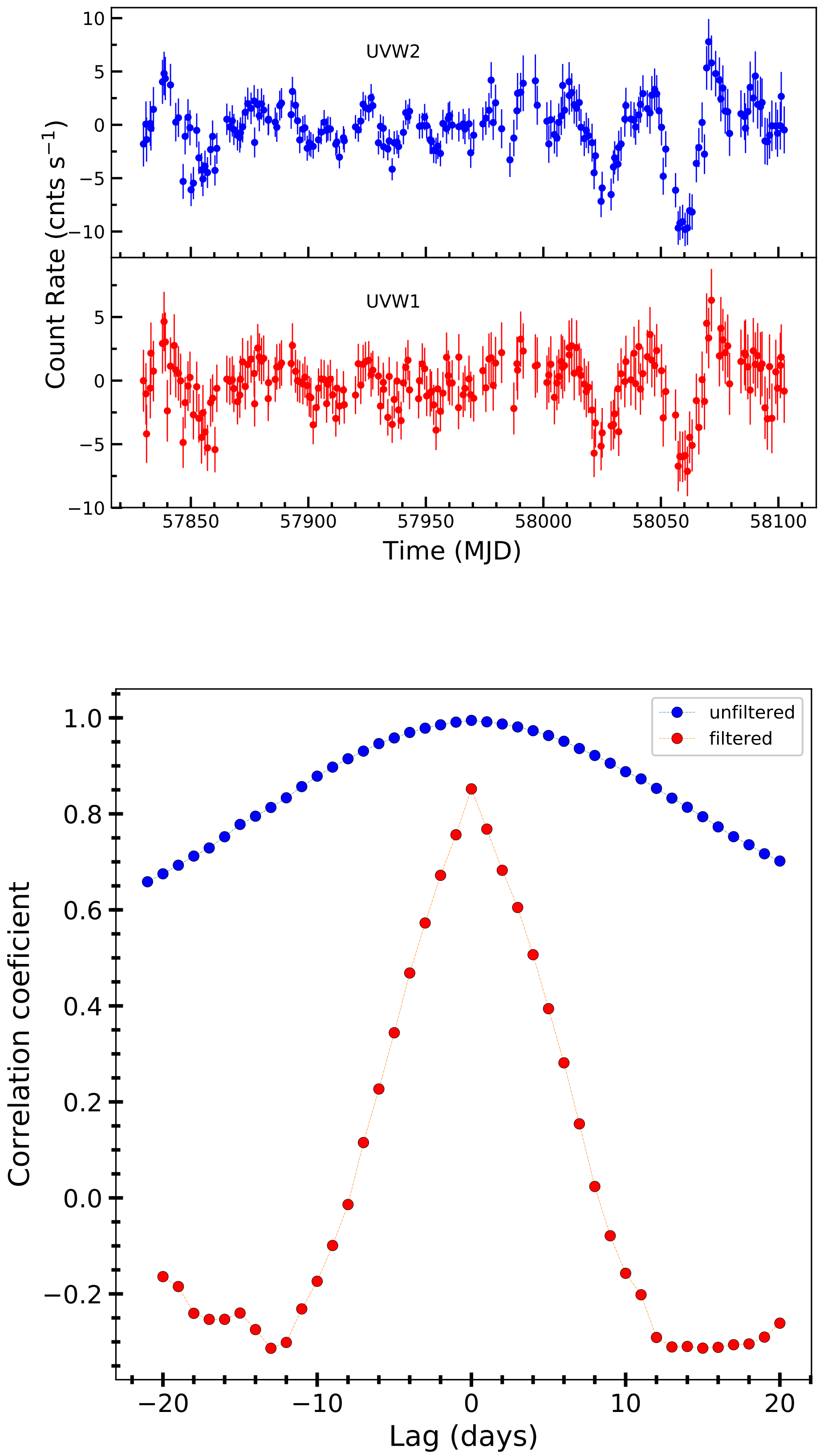

Figure 3.9: The light curves, filtered for the variations longer than 20 days, in UVW2 and UVW1 bands are shown in the top panel. These filtered light curves are cross-correlated using ICCF method and resulting CCF distribution is shown in the bottom panel (in red circle) along with unfiltered CCF distribution (in blue circle).

long term variations from the light curves. The derived lags of X-ray emission with respect to the UVW2 emission from the unfiltered and filtered light curves clearly show the effect of the removal of slow variations (See Table 3.6). Further, to check the effect of different filtering among UV and optical bands, we filtered slow variations for different days from all the light curves and estimated time lags with respect to the UVW2 band.

Time lag estimation

After removing the slow variations from the observed light curves, we measured the lags in different bands with respect to the UVW2 band. For the estimation of time lags, we used two methods that are interpolation cross-correlation function (ICCF; Gaskell & Peterson 1987, Peterson et al. 1998) and JAVELIN (Zu et al., 2011). The lags estimated using these two methods were similar except that the errors calculated from JAVELIN were smaller, as previously noted by Fausnaugh et al., 2016. In the ICCF method, we assume that two light curves, say $a(t)$ and $b(t)$ are displaced by a time lag of τ. First, each observed data point of the curve $b(t)$ is correlated with a linearly interpolated value of $a(t)$ at a time difference of τ. Similarly, each observed data point in curve $a(t)$ is correlated with an interpolated value in $b(t)$. In this way, two correlation coefficients are calculated for each value of time lag τ and then averaged out to get the final value of the correlation coefficient. Uncertainties on the lag measurements are estimated using flux randomisation (FR) and random subset selection (RSS) methods. In the RSS method, the N selections are drawn randomly from the light curve of N data points for each Monte Carlo realisation, similar to the bootstraping method. The data point which is selected M times, the uncertainty is decreased by $M^{1/2}$. To assess the flux uncertainty, the random Gaussian deviates are added to the data points (FR). After multiple Monte Carlo realisations, a cross-correlation function is obtained having correlation coefficient at the peak and centroid lags (usually measured above the 80% of peak value). The peak and centroid lag values differ for asymmetric ICCF distribution. We performed 2000 Monte Carlo simulations for each pair of light curves of UVW2 and other bands and rejected those cross-correlation coefficients that were below 0.2. Time lags calculated with and without filtering have been tabulated in Table 3.6. Edelson et al. (2019) calculated time lags using average count rates in the light curves for this source without removing any slow variations which are found to be consistent with the values reported in the present work (within error). However, there is a difference in the centroid value of lags in UVM2 and UVW1.

We also applied JAVELIN method to calculate the inter-band lags. Instead of linearly

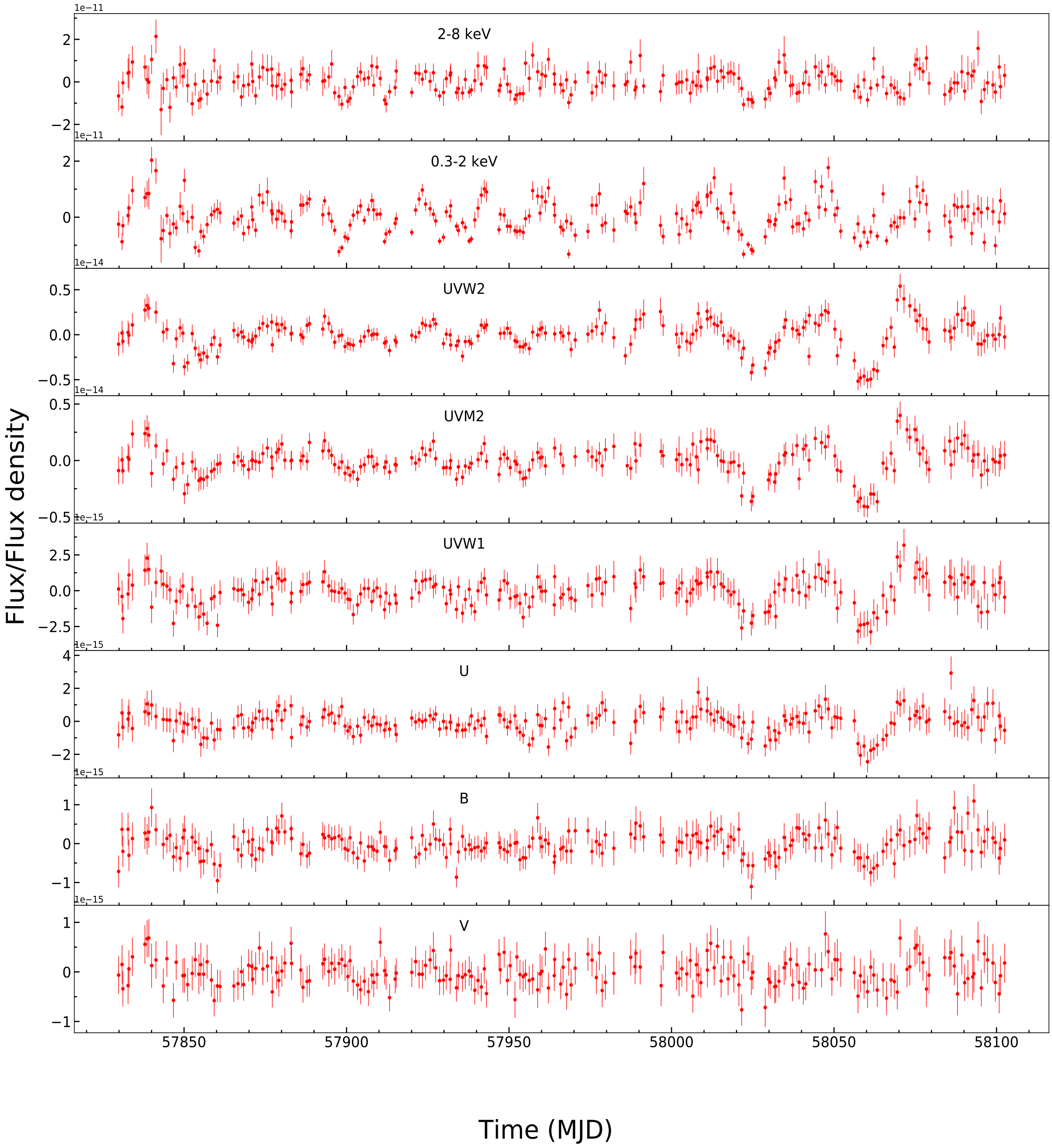

Figure 3.10: Simultaneous UV/optical and X-ray light curves of Mrk 509 after filtering for variations greater than 18 days. The filtered UV/optical (UVW2, UVM2, UVW1, U, B, V) flux densities (in 10^{-14} erg s^{-1} cm^{-2} Å^{-1}) of Mrk 509 are plotted with filtered the hard X-ray (2-8 keV range) and soft X-ray (0.3-2 keV range) flux densities (10^{-11} erg s^{-1} cm^{-2}).

interpolating between the gaps, JAVELIN models the light curves by making an assumption that the driving light curve is modeled by a damped random walk (DRW) that has been generally applied in quasars (Zu et al., 2013) and the derived light curves are related to the driving light curve via a top-hat transfer function. This method was first applied by Kelly et al. (2009). The time lags for X-rays, UVM2, UVW1, U, B, V bands relative to UVW2 band, without filtering are -2.086 ± 3.041, -0.311 ± 0.218, 0.132 ± 0.196, 1.656 ± 0.337, 1.298 ± 0.404 and 2.458 ± 0.607, respectively. After 20 days filtering, these lags were found to be -1.232 ± 0.509, -0.123 ± 0.239, -0.023 ± 0.266, 0.729 ± 0.488, 1.086 ± 0.639, and 2.474 ± 1.246, respectively. These lags are consistent with that found with the ICCF method.

Table 3.6: Time lags (in days) in different energy band relative to the UVW2 band estimated from the ICCF correlation method.

Band	Wavelength	Time lag τ (in days)					
	(Å)	without filtering	10 days	15 days	18 days	20 days	25 days
0.3-8 keV	20.7	$3.384^{+0.976}_{-0.959}$	$0.000^{+1.463}_{-1.000}$	$-0.476^{+0.971}_{-0.959}$	$-0.476^{+0.541}_{-0.903}$	$-0.459^{+0.538}_{-0.914}$	$-0.068^{+0.874}_{-0.539}$
0.3-2 keV	23.8	$2.859^{+0.944}_{-0.921}$	$-0.013^{+1.484}_{-1.013}$	$-0.502^{+0.974}_{-0.949}$	$-0.502^{+0.557}_{-0.545}$	$-0.488^{+0.526}_{-0.541}$	$-0.459^{+0.519}_{-0.514}$
2-8 keV	3.72	$5.021^{+1.557}_{-2.224}$	$0.048^{+1.549}_{-2.409}$	$0.022^{+1.138}_{-1.436}$	$0.013^{+1.045}_{-1.447}$	$0.062^{+1.065}_{-1.415}$	$0.460^{+1.387}_{-1.025}$
UVW2	1928	-	–	–	–	–	–
UVM2	2246	$-0.488^{+0.505}_{-0.884}$	$0.000^{+0.516}_{-0.483}$	$-0.041^{+0.890}_{-0.511}$	$-0.066^{+0.879}_{-0.522}$	$-0.447^{+0.506}_{-0.893}$	$-0.466^{+0.497}_{-0.891}$
UVW1	2600	$0.481^{+0.515}_{-0.506}$	$0.000^{+0.547}_{-0.963}$	$0.015^{+0.526}_{-0.940}$	$0.017^{+0.527}_{-0.929}$	$0.015^{+0.522}_{-0.907}$	$0.015^{+0.522}_{-0.907}$
U	3467	$2.017^{+0.521}_{-0.901}$	$0.000^{+0.954}_{-2.537}$	$0.514^{+0.970}_{-1.424}$	$0.957^{+0.964}_{-0.979}$	$0.982^{+0.952}_{-0.962}$	$1.039^{+0.554}_{-0.917}$
B	4392	$1.452^{+0.910}_{-0.718}$	$1.469^{+1.522}_{-5.134}$	$1.504^{+1.493}_{-2.036}$	$1.449^{+1.446}_{-1.501}$	$1.495^{+1.090}_{-1.032}$	$1.485^{+0.991}_{-0.997}$
V	5468	$1.622^{+0.980}_{-0.922}$	$1.456^{+2.456}_{-3.562}$	$2.474^{+2.474}_{-2.507}$	$2.473^{+2.472}_{-2.062}$	$2.523^{+2.520}_{-2.411}$	$2.485^{+1.971}_{-1.960}$
Soft X-ray (0.3-2 keV) lag wrt Hard X-rays (2-8 keV)							
		$-0.487^{+0.503}_{-0.492}$	$0.000^{+0.000}_{-0.000}$	$0.000^{+0.462}_{-0.452}$	$0.000^{+0.466}_{-0.453}$	$0.000^{+0.469}_{-0.454}$	$-0.003^{+0.468}_{-0.455}$

We derived the lag spectrum, i.e. lag as a function of wavelength for unfiltered and filtered (for 18 days filtering) light curves and showed it in the left and right panels of Figure 3.11, respectively. We then used a phenomenological power law model to model the lag spectrum. An expression of such power law model in terms of lags, i.e. the time-delay between a reference wavelength (λ_0) and other wavelength (λ) can be given as

$$\tau = \alpha \left[\left(\frac{\lambda}{\lambda_0} \right)^{\beta} - 1 \right]$$

where τ, α and β are time delay between reprocessing and reprocessed emission, power-law normalization and power-law index, respectively. In the standard accretion disk theory, the value of power-law index β is considered to be 4/3 (Collier et al., 1999; Cackett et al., 2007). We modelled the lag spectrum with the power law model in the following ways: (a) varying normalization α and power-law index β with and without hard and soft X-ray lags, and (b) by fixing the value of β as 4/3 and varying normalization only. Since there was an excess lag in U band for unfiltered case, it was removed from the lag spectrum. Here, the UVW2 band is considered as the reference waveband. The parameters obtained from fitting the lag spectrum for unfiltered light curves are (a) α = 0.14$\pm$0.75, β = 2.71$\pm$5.08 (including all the wavebands), and α = 1.49$\pm$5.71 β = 0.78$\pm$2.11 (excluding X-ray and U bands), and (b) α = 0.51$\pm$0.44. After 18 days filtering of light curves, the parameters are (a) α = 0.26$\pm$0.15, β = 2.28$\pm$0.59 (including all wavebands), α = 0.20$\pm$0.19, β = 2.52$\pm$0.98 (excluding X-ray bands), and (b) α = 0.61$\pm$0.12. The lag spectrum along with fitted power law models (as described above) without filtering and 18 days filtering of light curves are shown in the left and right panels of Figure 3.11, respectively. From the figure, it is clear that there is a large discrepancy between the model and observed lag even after filtering the light curves for long term variations.

3.4 Discussion

3.4.1 Correlations observed in the X-ray and UV/optical emission

From the analysis, we found that the average spectrum over a duration of thirteen years shows the presence of a complicated soft X-ray excess over the power-law continuum. The soft X-ray excess is described well with a combination of two thermal components with temperatures of $kT_{bb1} \sim$ 120 eV and $kT_{bb2} \sim$ 460 eV. The low temperature thermal component is normally required in Seyfert 1 AGNs (Leighly, 1999). However, the warm thermal component may be an analogy to the warm Comptonization, as described by Done et al. (2012), to explain the soft X-ray excess. According to this model, the warm Comptonizing plasma ($\sim 0.2 - 0.5$ keV) is embedded inside the optically thin and hot Comptonizing plasma (~ 100 keV). The soft X-ray excess due to warm Comptonization was also reported in this AGN by Mehdipour et al. (2011). Such a geometry of disk/X-ray plasma may be supported due to the observed correlation between the soft X-ray and hard X-ray emission ($\rho \sim 0.82$, log$p \sim -71$). In that case, the variability amplitude observed in the UV and soft X-ray bands should be, at least, equal to that of the highly variable power-law continuum flux. From the estimation of fractional variability, we found a low variability amplitude of the power-law continuum flux ($\sim 15\%$). This suggests that the hot X-ray plasma may not be lying over the warm Comptonizing plasma, but situated at a different location closer to the SMBH. Further, the correlation between the derived spectral components such as power-law flux and BB flux and BB temperature and BB flux are weak or moderate while other combinations do not show any correlation (see Figure 3.4). The observed weak anti-correlation between the power-law photon index and blackbody temperature, though both the components overlap only in a narrow energy range (below 2 keV), is apparently due to the degeneracy between both the parameters. Therefore, the emitting regions are likely to be partly interacting or distinct. At the same time, the variability observed in the UV emission, which is supposed to be radiated from regions close to the SMBH as compared to the optical emission, is also higher than that observed in the hard X-ray emission. However, the hard X-ray emission variability is higher relative to the changes found in the V-band. This also suggests that the UV and hard X-ray emission may be associated with disjoint regions or partly interacting regions. Similarly, the C3PO analysis gives a negative offset for the soft X-ray and UV/optical bands (except the V band) while taking the hard X-ray band as the abscissa. This indicates that these bands are more variable than the hard X-ray.

Weak/moderate correlations between the X-rays and the UV/optical emission may be interpreted as due to the presence of fluctuations of different time scales. These fluctuations may be associated with the changes in the accretion rates according to the fluctuation propagation model proposed by Lyubarskii (1997). Typical time scale of variations expected for the UV/optical bands due to changes in the accretion rates are of the order of thousands or more years for AGNs like Mrk 509. These time scales are estimated for 1H 0419-577 by Pal et al. (2018), which has a similar supermassive black hole mass ($\sim 10^8$ $M_\odot$).

The soft excess in AGNs is often explained by the relativistic blurred disk reflection model (Fabian et al., 2000, 2009). According to this model, the accretion disk is illuminated by the X-ray power-law continuum emission from the corona, producing a reflected spectrum. Reflection of continuum photons from the relativistically rotating inner disk gives rise to several smeared emission lines which look like a hump (an excess over the continuum emission) below ~ 2 keV. In the case of Mrk 509, however, the soft X-ray leads the hard X-ray (power-law) emission as shown in Table 3.6, which is not compatible with the reflection model. Secondly, the low variability in hard X-ray and weak/moderate correlation between hard X-ray and UV/optical bands make it unlikely that the UV/optical emissions are driven by reflection.

3.4.2 Possibility of the X-ray reprocessing

X-ray reprocessing phenomenon is a process in which X-ray emission from the optically thin and hot plasma is reprocessed in the distant accretion disk to re-emit in the longer wavelengths (Krolik et al., 1991; Collier et al., 1999). Confirmation of the X-ray reprocessing was first observed from UV/optical to infrared bands in a Seyfert 1 AGN NGC 2617 by Shappee et al., 2014 and the lags at the longer wavelengths were found to be consistent with the predictions of the X-ray reprocessing in the standard accretion disk. In recent times, NGC 5548 has been the most studied AGN for the reverberation mapping of the accretion disk (Edelson et al., 2015; Fausnaugh et al., 2016), and most of the studies hint towards a larger size of the accretion disk. Theoretically, in a geometrically thin and optically thick accretion disk, which is heated internally by viscous dissipation and externally by irradiation of the central UV/X-ray source, the temperature at a radius R from the center is given by

$$T(R) = \left(\frac{3GM\dot{M}}{8\pi\sigma R^3} + \frac{(1-A)L_x H}{4\pi\sigma R^3} \right)^{1/4} \tag{3.1}$$

where G, M, $\dot{M}$, L_x, A, H and σ are the gravitational constant, mass of the central SMBH, mass accretion rate, luminosity of the heating radiation, albedo of the accretion disk, height of the central heating source and Stefan-Boltzmann constant, respectively (Cackett et al., 2007). In this equation, the effects of inclination angle, relativistic effects in the inner part of the disk and the inner edge of the disk have been neglected. Following the steps given in Fausnaugh et al. (2016), the time delay τ relative to the reference time-delay τ_0 corresponding to reference wavelength λ_0 is given by

$$\tau - \tau_0 = \frac{1}{c}\left(X\frac{k\lambda_0}{hc}\right)^{4/3}\left(\frac{3GM\dot{M}}{8\pi\sigma} + \frac{(1-A)L_xH}{4\pi\sigma}\right)^{1/3} \times \left[\left(\frac{\lambda}{\lambda_0}\right)^{4/3} - 1\right] \tag{3.2}$$

where, X is the multiplicative factor that takes into account systematic issues in the conversion of temperature T to wavelength λ for a given R. The value of this factor is 4.87 when the temperature corresponding to the observed emission wavelength is given by Wein's law and 2.49 when flux-weighted radius is used. In the flux-weighted case, the temperature profile of the accretion disk is described by the Shakura & Sunyaeav disk ($T \propto R^{-3/4}$). In both the cases, the disk is assumed to have a fixed aspect ratio all over. Eqn. 3.2 can be simplified by taking $(1-A)L_xHR = \kappa GM\dot{M}/2R$, where κ is the local ratio of external to internal heating and independent of radius. Using luminosity of Mrk 509 L_x as 10^{44} erg s^{-1} (Vasudevan & Fabian, 2009), coronal height H as 1.53 $r_g(= GM/c^2)$ (García et al., 2019) and assuming albedo A equal to 0.2 (as used in several AGNs e.g. McHardy et al. (2014), Pal & Naik (2017)), the value of κ comes out as $\sim$0.016. The smaller value of κ indicates that the contribution towards time delay due to external heating is insignificant (0.5%, estimated from Eqn. 3.2) compared to viscous heating. Therefore, using Eqn. 3 from Edelson et al. (2017), the time delays with respect to UVW2 ($\tau_0 = 0$) band can be expressed as

$$\tau = 0.09\left(X\frac{\lambda}{1928\text{Å}}\right)^{4/3} M_8^{2/3}\left(\frac{\dot{m}_{edd}}{0.10}\right)^{1/3} \times \left[\left(\frac{\lambda}{\lambda_0}\right)^{4/3} - 1\right] days \tag{3.3}$$

where, M_8 and $\dot{m}_{edd}$ are mass of the black hole in units of 10^8 $M_\odot$ and the Eddington ratio ($\dot{M}/\dot{M}_{edd}$). This equation assumes negligible external heating by the UV/X-ray source compared to the internal viscous heating and radiation efficiency to be 0.1. We use the mass of the central SMBH of Mrk 509 to be 1.43×10^8 $M_\odot$ (Peterson et al., 2004), $\dot{m}_{edd}$ equal to 0.0951 (Vasudevan & Fabian, 2009) and X=2.49 for flux-weighted radius. Using above values, the time-delays with respect to the UVW2 band are estimated to be $-0.367, -0.366, 0.083, 0.180, 0.367, 0.733$ and 1.106 days for hard X-rays, soft X-rays, UVM2, UVW1, U, B and V bands, respectively. In our analysis of unfiltered light curves of Mrk 509, we found delayed emission in hard X-ray, soft X-ray, UVW1, U, B and V bands with respect to the emission in UVW2 band (Figure 3.11 & Table 3.6) while the delayed emission in the X-ray reprocessing is expected to be in the longer wavelength bands compared to the X-ray emission. Therefore, the observed positive lags in the X-ray bands are unexpected while

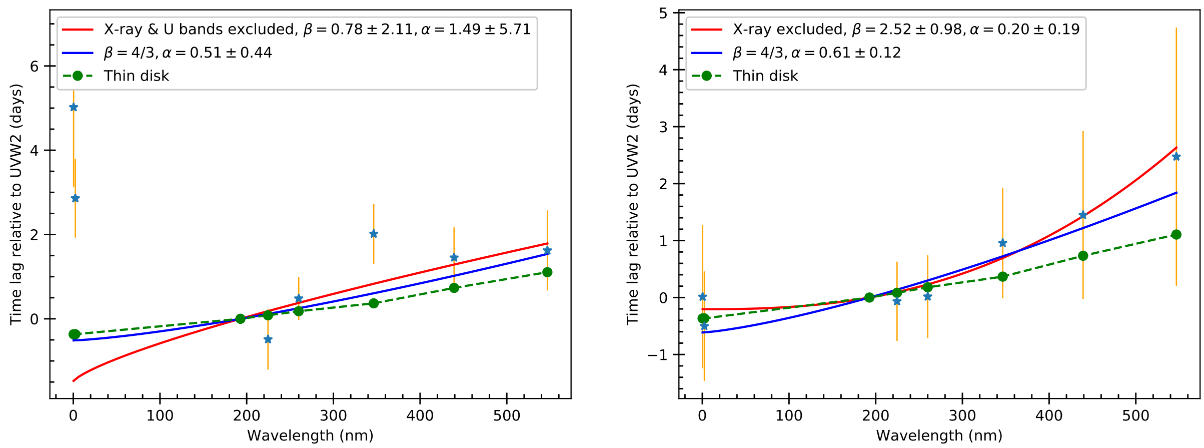

Figure 3.11: Wavelength dependent lag spectrum modeling is shown for without filtering (left panel) and 18 days filtering (right panel) of light curves (i) with power law model $\tau \propto \lambda^{\beta}$ excluding X-ray data points (and U in the case of without filtering) and extrapolated down to X-ray (red solid line) (ii) with simple 4/3 power law (blue solid line) (iii) Theoretically estimated time-delay with respect to UVW2 band (green dashed line). Blue stars are the time lag values calculated from ICCF method.

considering the reprocessing scenario.

The estimated lags from the observed light curves may be affected due to the slow variations, for example, due to the fluctuations in the accretion flow. The reprocessed variable component in longer wavelength is diluted with the intrinsic emission due to the viscous heating in the accretion disk. Therefore, a possible origin of the variability in longer wavelengths could be a combination of two effects: reprocessing and propagating fluctuations. In the propagating fluctuation scenario, one expects the longer wavelength emission leading to the shorter wavelength emission. As the fluctuations propagate inwards through the accretion flow, it modulates the UV/optical and X-ray emission. Since the X-ray emitting region is very close to the central engine, it shows rapid fluctuations. These X-rays are again reprocessed to give longer wavelength emission. Therefore, there is always a tussle between the reprocessing and propagating fluctuations and the resultant time lag depends on the dominant process. Therefore, the geometry of the corona and the accretion disk are complex and both are not so simple as assumed in the lamp-post model. After removing the slow variations of about 18 days, the trend in the estimated lags appear to be the same as the delayed hard X-ray emission as well as the optical emission (right panel of Figure 3.11).

3.4.3 Excess lags in U and X-ray band with respect to UVW2 band

The lags derived without removing the slow variations are shown in the left panel of Figure 3.11. This shows clear "excess" lags in U as well as in X-ray bands with respect to the UVW2 band when fitted with the power law model $\tau \propto \lambda^{4/3}$. Excess lag in U band was first reported by Korista & Goad (2001) in NGC 5548 and then in later studies (Edelson et al., 2015; Fausnaugh et al., 2016; Pal & Naik, 2017; Naik et al., 2019) in different AGNs. Cackett et al. (2018) also found a strong excess in the Balmer jump region in NGC 4593. Korista & Goad, 2001 predicted that there is a significant contribution of diffused emission from the BLR in UV bands. The wavelength-dependent lag across UV-optical energy range can imitate the lag spectrum originated as a result of X-ray reprocessing from the accretion disk. Similar results were found by Lawther et al. (2018) and they emphasized on the importance of diffuse continuum contribution while inferring the disk sizes on the basis of inter-band continuum delays. This feature has been observed in many Seyfert 1 galaxies, as shown by Edelson et al. (2019) in four AGNs, including Mrk 509. Hernández Santisteban et al. (2020) modelled the lag spectrum of Fairall 9 by taking into account the contribution from the BLR (Figure 6 of their paper). Their modelling was based on the previous work on NGC 5548 by Korista & Goad (2019). On the basis of these results, it can be safely inferred that the BLR contribution in the inter-band lag spectra is unavoidable. As a result, the variability within the UV/optical can be inferred as the mixing of two effects: emission from standard Shakura-Sunyaev disk and diffused continuum emission from the BLR as discussed above.

In the simple picture of reprocessing model, X-ray emitting central corona illuminates and heats the accretion disk. The reprocessing model predicts that when $\tau \propto \lambda^{4/3}$ relation in UV/optical is extrapolated down to X-rays, it should fit the data well. But Figure 3.11, generated from unfiltered light curves for long term variations, shows a huge discrepancy. Even after filtering, although excess lag was decreased significantly, the lags in hard X-rays still appear to be higher, which can not be explained by a simple reprocessing model.

3.4.4 Complex nature of the accretion disk

As the X-ray reprocessing phenomenon is unable to explain the observed lag spectrum successfully, this compels us to look for alternative models in explaining the observed correlated variability in the X-ray/UV/optical wave-bands. One such model is given by Gardner & Done (2017) in which the excess lag of X-ray relative to UV band in NGC 5548 is explained.

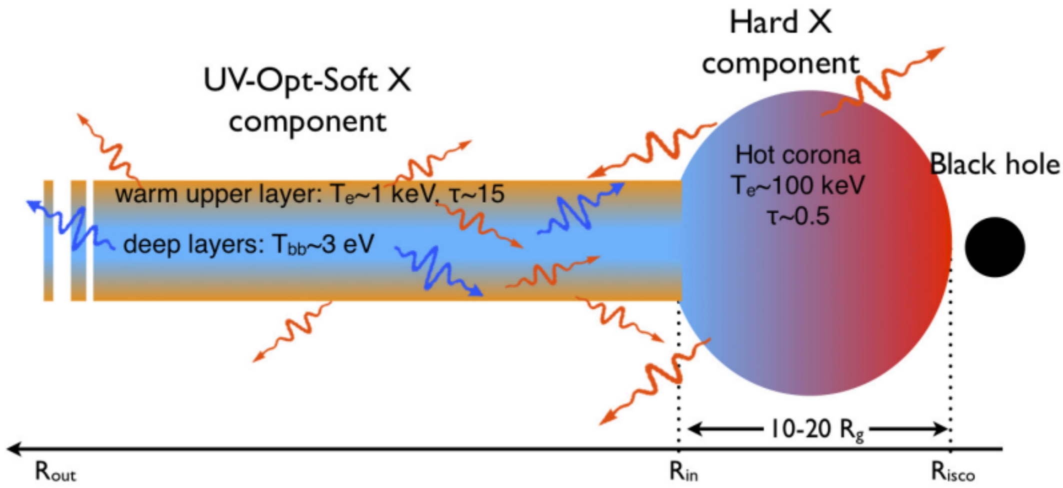

Figure 3.12: A cartoon diagram depicting the inner accretion flow of Mrk 509. The hot corona (temperature $T \sim 100$ keV and optical depth $\tau \sim 0.5$) is producing hard X-rays and forming warm Comptonizing disc layer (temperature $T \sim 1$ keV and optical depth $\tau \sim 15$). The warm Comptonizing region produces soft X-ray emission. Image courtesy: Petrucci et al. (2013)

According to this model, the inner part of the accretion disk is called the Comptonization region, which is "puffed up" and emits in EUV energy band. This region is heated by the hard X-rays coming from the central corona, producing heating waves which dissipate outwards. In response to these heating waves, the outer region of the disk expands and contracts and produces continuum lags. The model suggests the shorter wavelength lead the longer wavelength variations, which is not the case with Mrk 509 even after filtering. So this model does not explain the short term variability seen in Mrk 509 for this particular duration of observations. Using *XMM-Newton* and *Swift* observations of Mrk 509 for a few days, Mehdipour et al. (2011) inferred that the soft X-ray excess below 2 keV is produced by the Comptonization of the seed photons from the UV-optical disk into a warm and optically thick corona. A similar geometry was suggested by Petrucci et al. (2013) and is shown in Figure 3.12. This result seems to be consistent with the positive lag between UVW2 and X-rays found in our analysis.

The best-fitted value of power-law normalization α gives the size of the emitting region of reference wavelength, i.e. 1928Å (the central wavelength of the UVW2 band) if we assume the face-on standard disk. The size of the emitting region for the UVW2 emission can be estimated to be $0.61 \times 24 \times 60 \times 60 \times 3 \times 10^{10} = 1.58 \times 10^{15}$cm which is equivalent to $\sim 80 R_g$. Therefore, the size for the UVM2 and UVW1 emission would be similar as these bands show the time delays consistent with zero for the UVM2 and UVW1 bands with respect to the UVW2. In the case of variability, the fractional variability found in the UVW2 band is marginally higher than that seen in the UVM2 and UVW1 bands. The lags consistent with zero and similar amplitude of the variability in the UV bands suggest that the disk does not appear to have a smooth surface. Although, the β =4/3 wavelength rule does not fit the lag spectrum well when the X-ray and U band lags are included; the spectrum is well described by this rule when those excess lags are excluded. This implies that the reprocessed optical emission is likely caused by the UV emission with some delay. Excluding the X-ray lags, the fits corresponding to $\beta = 2.52 \pm 0.98$ and the $\beta = 4/3$ values describe the lag spectrum well (right panel of Figure 3.11). These fits suggest that the UV emission is probably reprocessed in optical as well as in X-ray bands.

The fitted β values (0.78 ± 2.11 without X-ray and U; 2.52 ± 0.98 after filtering) imply a complex structure of the accretion disk and even rules out a shell-like geometry ($\tau \propto \lambda^2$) of emitting/reprocessing regions around the SMBH. Therefore, the actual disk is likely to be partly puffy, warped and inhomogeneous in nature and thus, the standard accretion theory seems not viable in the case of Mrk 509. The reason for getting lower lags after the process of filtering slow variations can not be explained simply. In this process of removing slow components, it is not clear about the increased lags of V band, i.e. $\sim$ 1 day for 10 days filtering and $\sim$ 3 days for 20 days filtering. To answer the above questions and exploring such a complex nature of the accretion disk of Mrk 509 require a longer monitoring program with a good cadence of observations compared to the available one.

3.5 Summary

Using multi-wavelength observations of Seyfert 1 galaxy Mrk 509 from *Swift* observatory, we investigated the short-term variabilities in X-ray and UV/optical emission. We quantified the variabilities in each band by calculating fractional variability. We employed different techniques to investigate the correlation between X-ray and UV/optical bands. Flux-flux correlation was used to find the presence of slowly varying component compared to UVW2 and hard X-ray band. We filtered the light curves to remove the slow variations. To estimate the time lags between UVW2 and other UV/optical/Xray energy bands, we applied ICCF and JAVELIN methods. After filtering light curves for variations greater than 10, 15, 18, 20 and 25 days, we generated the lag spectrum and compared it with the predicted lag spectrum for standard accretion disk. The highlighted results from this work are summarized below.

1. Average spectrum over the entire duration shows that the soft X-ray excess is well described by two blackbody components with temperatures $kT_{bb1} \sim 120$ eV and $kT_{bb2} \sim 460$ eV.

2. We found a moderate/weak correlation between (i) the power-law flux and BB flux, and (ii) the blackbody temperature and BB flux.

3. Mrk 509 shows strong variability on short as well as long term time scale (see variability amplitudes in Section 3.3.2) in all bands. Interestingly, the X-ray power-law continuum shows smaller variability amplitude ($\sim$15%) compared to the soft X-ray and UV bands ($\sim$18-28%). The peak-to-peak ratio (R) and fractional variability amplitude $F_{\rm var}$ show that the variability decreases with the increase in wavelength. This is because emission at longer wavelengths is expected to originate from the regions in the accretion disk at larger radii and get diluted with the emission from BLR and narrow-line region (NLR). Interestingly, hard X-ray emission shows less variability than other bands.

4. The variability process in this AGN seems to be non-stationary (Figure 3.7). However, no spectral transition is observed over the years, as can be seen in Figure 3.3 where the power-law photon index and blackbody temperature do not show any significant change.

5. The value of Pearson's correlation coefficients for the UV/optical bands ($\rho = 0.95 - 0.99$ with respect to the UVW2 bands and $\rho = 0.40 - 0.53$ with respect to the hard X-ray) and corresponding p values show that UV and optical bands are significantly correlated as compared to that of the X-ray emission and UV/optical bands. The hard X-ray emission is found to be well correlated with the soft X-ray emission (ρ=0.82) while the hard X-ray and soft X-ray emission are correlated to the UVW2 emission with ρ values of 0.51 and 0.75, respectively.

6. The flux-flux plot between UVW2 and other bands (X-ray and UV/optical bands) shows that the UVW2 emission is strongly correlated with other UV and optical emission whereas it is moderately correlated with the X-ray emission. The presence of positive offset for other UV/optical bands suggests the weakly variable disk component while positive offset for hard X-ray hints that the X-ray and UV/optical emission regions are partially interacting.

7. Light curves were filtered for long term variations greater than 10, 15, 18, 20 and 25 days and time lags were estimated for each filtering. Time lags were calculated between UVW2 band and other bands using ICCF and JAVELIN methods and found to be

consistent (within errors). Without filtering the light curves, an excess is found in X-ray and U band. The excess in U band could be due to diffusion emission due to the BLR. After filtering, excess in X-ray and U band was reduced significantly. However, the lag in soft (considering error) and hard X-ray does not fit into the lags predicted from standard accretion disk model.

8. The observed lags were found to increase with wavelength and were fitted with power law model by (i) keeping power-law parameters (i.e., α & β) free with and without excluding hard and soft X-ray (ii) fixing β at 4/3 according to Shakura-Sunyaev accretion disk geometry.

9. Our results favour the warm Comptonization region, located above the inner part of the accretion disk as the origin of the observed soft X-ray emission from Mrk 509. However, zero time lag and marginal variability difference between UV bands suggest that the UV emitting region in the disk is not smooth, but instead is stratified.

Chapter 4

Broadband X-Ray Observations of the 2018 Outburst of the Changing-Look Active Galactic Nucleus NGC 1566

As described in Chapter 1, the AGNs are classified as type 1 or type 2, depending on the presence or absence of broad optical emission lines. The existence of different classes of AGNs can be explained by the Unified model (Antonucci, 1993), which is based on the orientation of the optically thick torus with respect to our line-of-sight. Recently, a new sub-class of AGNs, known as changing look AGNs (CLAGNs), has been identified through optical observations. These objects display the appearance or disappearance of the broad optical emission lines, transitioning from type-1 (or type 1.2/1.5) to type-2 (or type 1.8/1.9) and vice versa. Several nearby galaxies, such as Mrk 590 (Denney et al., 2014), NGC 2617 (Shappee et al., 2014), Mrk 1018 (Cohen et al., 1986), NGC 7582 (Aretxaga et al., 1999), NGC 3065 (Eracleous & Halpern, 2001), have been found to show such a peculiar behaviour. In the X-rays, a different type of changing-look events has been observed, with the AGN switching between Compton-thin and Compton-thick states (Risaliti et al., 2002; Matt et al., 2003). These X-ray changing-look events have been observed in many AGNs, namely, NGC 1365 (Risaliti et al., 2007), NGC 4388 (Elvis et al., 2004), NGC 7582 (Piconcelli et al., 2007; Bianchi et al., 2009b), NGC 4395 (Nardini & Risaliti, 2011), IC 751 (Ricci et al., 2016), NGC 4507 (Braito et al., 2013), NGC 6300 (Guainazzi, 2002; Jana et al., 2020). In this chapter, we discuss the nature of the changing-look Active Galactic Nucleus NGC 1566 during its June 2018 outburst. During the outburst, the X-ray intensity of the AGN increased up to $\sim 25-30$ times compared to its quiescent state intensity. We performed timing and spectral analysis of the source during pre-outburst, outburst and post-outburst epochs using semi-simultaneous observations with the *XMM-Newton*, *NuSTAR* and *Swift* Observatories covering a broad energy range (0.5−70 keV). In Section 4.1, the observations and data reduction process are described. In Section 4.3 & 4.3.1, we present results obtained from our timing and spectral analysis, respectively. In Section 4.4, we discuss our findings. Our conclusions are given in Section 4.5. This work has been published as Jana et al., 2021 in MNRAS.

4.1 Introduction

The origin of the changing look (CL) events is still unclear. The X-ray changing-look events could be explained through the variability of the line-of-sight column density ($N_{\rm H}$) associated with the clumpiness of the BLR or of the circumnuclear molecular torus (Nenkova et al., 2008a,b; Elitzur, 2012; Yaqoob et al., 2015; Guainazzi et al., 2016; Jana et al., 2020). On the other hand, the optical CL events could be related to changes in the accretion rate (Elitzur et al., 2014; MacLeod et al., 2016; Sheng et al., 2017), which could be linked with the appearance and disappearance of the broad line regions (BLRs) (Nicastro, 2000; Korista & Goad, 2004; Runnoe et al., 2016). Some of these optical CL events could also be associated with the tidal disruption of a star by the supermassive black hole (SMBH) at the centre of the galaxy (Eracleous et al., 1995; Merloni et al., 2015; Ricci et al., 2020, 2021).

NGC 1566 is a nearby (z=0.005), face-on spiral galaxy, classified as a type SAB(s)bc (de Vaucouleurs, 1973; Shobbrook, 1966). The AGN has been intensively studied over the last 70 years and is one of the first galaxies where variability was detected (Quintana et al., 1975; Alloin et al., 1985, 1986; Winkler, 1992). In 1960s, NGC 1566 was classified as a Seyfert 1, with broad Hα and Hβ lines (de Vaucouleurs & de Vaucouleurs, 1961). Later, the Hβ line was found to be weak, leading to the source being classified as a Seyfert 2 (Pastoriza & Gerola, 1970). In the 1970s and 1980s, NGC 1566 was observed to be in the low state with weak Hβ emission (Alloin et al., 1986). Over the years, it was observed to change its type again from Seyfert 1.9-1.8 to Seyfert 1.5-1.2 (da Silva et al., 2017), with two optical outbursts in 1962 and 1992 (Shobbrook, 1966; Pastoriza & Gerola, 1970; da Silva et al., 2017; Oknyansky et al., 2019).

INTEGRAL caught NGC 1566 during an outburst in the hard X-ray band in June 2018 (Ducci et al., 2018). Follow-up observations were carried out in the X-ray, optical, ultraviolet (UV), and infrared (IR) bands (Grupe et al., 2018a; Ferrigno et al., 2018; Kuin et al., 2018;

Dai et al., 2018; Cutri et al., 2018). The flux of the AGN was found to increase in all wavebands and reached its peak in July 2018 (Oknyansky et al., 2019, 2020; Parker et al., 2019). Long-term ASAS-SN and NEOWISE light curves showed that the optical and IR flux started to increase from September 2017 (Dai et al., 2018; Cutri et al., 2018). The *Swift*/XRT flux increased by about $\sim 25 - 30$ times (Oknyansky et al., 2019) as the source changed to Seyfert 1.2 from Seyfert 1.8-1.9 type (Oknyansky et al., 2019, 2020). The source became type-1 with the appearance of strong, broad emission lines (Oknyansky et al., 2019; Ochmann et al., 2020). After reaching the peak, the fluxes declined in all wavebands. After the main outburst, several small flares were observed (Grupe et al., 2018b, 2019).

Table 4.1: Log of observations of NGC 1566

ID	UT Date	*NuSTAR*	Exp (ks)	Count s^{-1}	*XMM-Newton*	Exp (ks)	Count s^{-1}	*Swift*/XRT	Exp (ks)	Count s^{-1}
X1	2015-11-05	–	–	–	0763500201	91.0	1.21 ± 0.01	–	–	–
O1	2018-06-26	80301601002	56.8	1.99 ± 0.01	0800840201	94.2	26.40 ± 0.02	–	–	–
O2	2018-10-04	80401601002	75.4	0.55 ± 0.01	0820530401	108.0	4.92 ± 0.01	–	–	–
O3	2019-06-05	80502606002	57.2	0.19 ± 0.01	0840800401	94.0	3.78 ± 0.01	–	–	–
O4	2019-08-08	60501031002	58.9	0.60 ± 0.01	–	–	–	00088910001	1.9	0.55 ± 0.02
O5	2019-08-11	–	–	–	0851980101	18.0	4.83 ± 0.02	–	–	–
O6	2019-08-18	60501031004	77.2	0.33 ± 0.01	–	–	–	00088910002	1.7	0.27 ± 0.01
O7	2019-08-21	60501031006	86.0	0.36 ± 0.01	–	–	–	00088910003	2.0	0.21 ± 0.01

4.2 Observation and Data Reduction

In the present work, we used data from *NuSTAR*, *XMM-Newton* and *Swift* observations of NGC 1566, carried out at different epochs, as reported in Table 4.1. Out of the eight available epochs, X1 and O1 were studied by Parker et al. (2019). We also included those observations for a complete study of the source at different phases (pre-outbursts, outburst and post-outburst periods).

4.2.1 *NuSTAR*

NuSTAR is a hard X-ray focusing telescope, consisting of two identical modules: FPMA and FPMB (Harrison et al., 2013). NGC 1566 was observed with *NuSTAR* six times between 26 June 2018 and 21 August 2019, simultaneously with either *XMM-Newton* or *Swift* (see Table 4.1). Reprocessing of the raw data was performed with the *NuSTAR* Data Analysis Software (`NuSTARDAS`, version 1.4.1). Cleaned event files were generated and calibrated by using standard filtering criteria in `nupipeline` task and the latest calibration data files available in the NuSTAR calibration database (CALDB) [1]. The source and background products were extracted by considering circular regions with radii 60 arcsec and 90 arcsec, respectively. While the source region was centred at the coordinates of the optical counterparts, the background spectrum was extracted from a region devoid of other sources. The spectra and light curves were extracted using the `nuproduct` task. The light curves were binned at 500 s. We re-binned the spectra with 20 counts per bin by using the `grppha` task. No background flare was detected during the *NuSTAR* observations.

4.2.2 *XMM-Newton*

NGC 1566 was observed by *XMM-Newton* (Jansen et al., 2001) at five epochs between November 2015 and August 2019. Out of these five observations, the source was observed simultaneously with *NuSTAR* in three epochs (see Table 4.3). We used the Science Analysis System (`SAS v16.1.0`[2]) to reprocess the raw EPIC-pn data (Strüder et al., 2001). We considered only unflagged events with `PATTERN` ≤ 4. Particle background flares were observed above 10 keV in the observations X1 and O5. The Good Time Interval (GTI) file was generated considering only intervals with < 0.65 counts^{-1}, using the SAS task `tabgtigen`. No flare

[1] `http://heasarc.gsfc.nasa.gov/FTP/caldb/data/nustar/fpm/`
[2] `https://www.cosmos.esa.int/web/xmm-newton/sas-threads`

was observed in the observations O1, O2 and O3. The source and background spectra were initially extracted from a circular region of 30″ centered at the position of the optical counterpart, and from a circular region of 60″ radius away from the source, respectively. Then we extracted the spectrum using the SAS task '`especget`'. The observed and expected pattern distributions were generated by applying `epaplot` task on the filtered events. We found that the source spectrum would be affected by photon pile-up and as a result, the expected distributions were significantly discrepant from the observed ones. We, therefore, considered an annular region of 30″ outer radius and different values of inner radii for the source and checked for the presence of pile-up. We found that, with an inner radius of 10″, the source would be pile-up free[3]. We, therefore, used this inner radius for the spectral extraction. The response files (*arf* and *rmf* files) were generated by using `SAS` tasks `ARFGEN` and `RMFGEN`, respectively. Background-subtracted light curves were produced using the `FTOOLS` task `LCMATH`. It is also to be noted that we ran SAS task '`correctforpileup`' when we generated the pile-up corrected rmf file by using '`rmfgen`'.

4.2.3 *Swift*

Swift monitored NGC 1566 over a decade in both window-timing (WT) and photon counting (PC) modes. The source was observed simultaneously with *Swift*/XRT and *NuSTAR* three times (see Table 4.1 for details). The $0.3-10$ keV spectra were generated using the standard online tools provided by the UK *Swift* Science Data Centre (Evans et al., 2009) [4]. For the present study, we used both WT and PC mode spectra in the $0.3-10$ keV range. We also generated long-term light curves in the $0.3-10$ keV band using the online-tools[5].

4.3 Results

4.3.1 Timing Analysis

We studied the long term *Swift*/XRT light curves of NGC 1566 in the $0.3-10$ keV energy range for the timing analysis. Along with the *Swift*/XRT light curves, the $0.5-10$ keV and $3-70$ keV light curves (500 s time-bin) from *XMM-Newton* and *NuSTAR* observations were also analysed.

[3] `https://www.cosmos.esa.int/web/xmm-newton/sas-thread-epatplot`
[4] `http://www.swift.ac.uk/user_objects/`
[5] `http://www.swift.ac.uk/user_objects/`

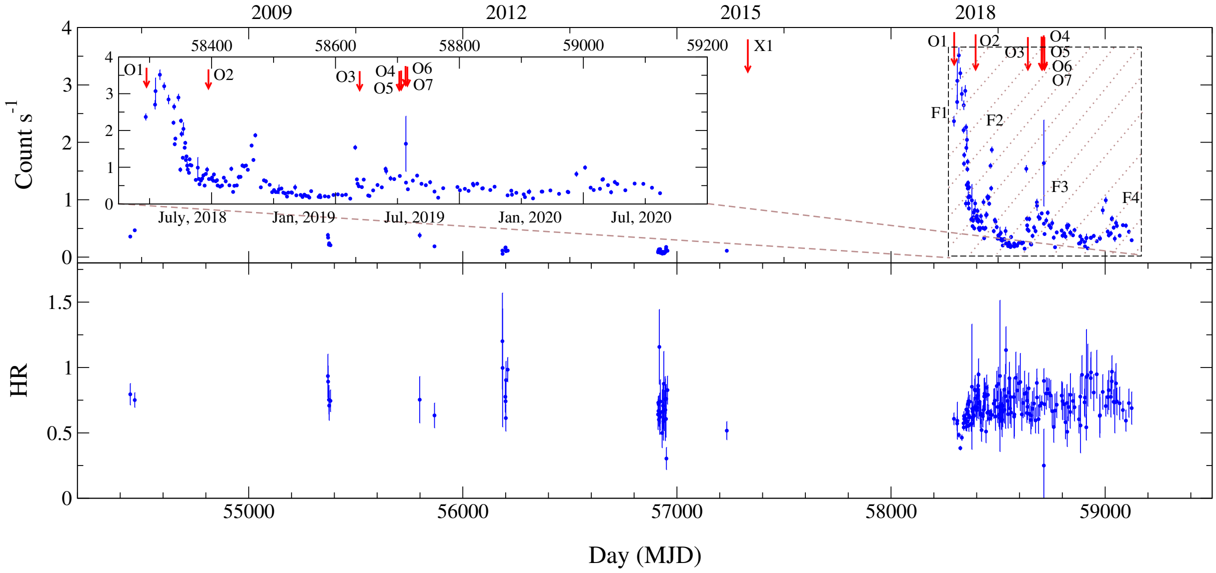

Figure 4.1: The long-term, $0.3-10$ keV *Swift*/XRT light curve of NGC 1566 is shown in the top panel. The shaded region shows the light curve between 2018 and 2020. The inset figure in the top panel shows the expanded light curve of the shaded region from 2018 to 2020 for clarity. The red arrows represent the *NuSTAR*, *XMM-Newton* and *Swift*/XRT observations of the source (see Table 4.1 for details). In the bottom panel, we illustrate the variation of the hardness ratio (HR). The HR is defined as the ratio between count rates in the $1.5-10$ keV and the $0.3-1.5$ keV bands.

Table 4.2: Variability in different energy bands are shown here. In some cases, the average error of observational data exceeds the 1σ limit, resulting negative excess variance. In such cases, we obtained imaginary F_{var}, which are not included in this table.

ID (1)	Energy (keV) (2)	N (3)	F_{max} (Count s^{-1}) (4)	F_{min} (Count s^{-1}) (5)	R (6)	Mean (7)	σ (10^{-3}) (8)	σ^2_{XS} (10^{-3}) (9)	σ^2_{NXS} (10^{-3}) (10)	F_{var} (%) (11)
X1	0.5-3	178	1.04	0.63	1.66	0.82	71 ± 2	2.74	3.3 ± 0.7	5.8 ± 0.6
X1	3-10	178	0.19	0.07	2.63	0.12	19 ± 1	–	–	–
O1	0.5-3	185	27.84	16.69	1.67	21.89	2573 ± 78	6.55	13.7 ± 0.2	11.7 ± 0.6
O1*	3-10	145	2.35	1.31	1.80	1.81	210 ± 11	2.2	9.7 ± 1.0	9.8 ± 0.8
O1	10-70	145	1.21	0.54	2.23	0.80	98 ± 5	4.94	7.8 ± 1.5	8.8 ± 1.0
O2	0.5-3	213	5.69	2.98	1.91	4.05	628 ± 15	380.2	93.9 ± 0.6	30.6 ± 0.8
O2*	3-10	197	0.86	0.29	2.99	0.52	98 ± 3	6.50	24.4 ± 2.6	15.6 ± 1.2
O2	10-70	197	0.47	0.12	3.78	0.25	51 ± 2	1.11	17.2 ± 0.4	13.1 ± 1.6
O3	0.5-3	185	3.74	2.52	1.48	3.13	289 ± 11	72.2	23.1 ± 0.5	15.2 ± 0.4
O3*	3-10	161	0.48	0.08	6.46	0.22	48 ± 2	0.16	3.2 ± 5.4	5.7 ± 4.8
O3	10-70	161	0.47	0.04	12.5	0.16	45 ± 2	0.28	11.2 ± 0.9	10.6 ± 4.3
O4	3-10	145	0.99	0.36	2.78	0.55	86 ± 3	4.76	15.4 ± 2.2	12.4 ± 1.1
O4	10-70	145	0.37	0.15	2.42	0.26	40 ± 1	0.39	5.9 ± 2.8	7.7 ± 1.8
O5	0.5-3	27	3.71	3.33	1.12	3.52	109 ± 12	0.46	0.1 ± 0.3	0.6 ± 2.2
O5	3-10	27	0.55	0.15	3.68	0.39	116 ± 3	10.78	71.5 ± 14.7	26.7 ± 4.6
O6	3-10	191	0.45	0.16	2.77	0.31	52 ± 2	1.27	13.1 ± 2.6	11.4 ± 1.3
O6	10-70	191	0.23	0.08	2.83	0.16	30 ± 1	0.12	4.9 ± 3.8	7.0 ± 02.7
O7	3-10	208	1.46	0.21	6.85	0.35	98 ± 7	2.50	20.3 ± 7.4	14.3 ± 2.7
O7	10-70	208	0.73	0.09	8.22	0.17	53 ± 4	–	–	–

Columns in the table represent – (1) ID of observation, (2) energy range, (3) number of data points or length of the light curve, (4) maximum count of the light curve, (5) minimum count of the light curve, (6) ratio of maximum count to minimum count, $R = F_{\mathrm{max}}/F_{\mathrm{min}}$, (7) mean count of the light curve, (8) standard deviation of the light curve, (9) excess variance, (10) normalized excess variance, (11) fractional rms amplitude of the light curve.

*During O1, O2 and O3, we reported only *NuSTAR* observation in $3-10$ keV energy range, although both *XMM-Newton* and *NuSTAR* data were available in $3-10$ keV energy band.

Outburst Profile

NGC 1566 was observed intensively with many observatories for about 70 years, starting from 1950s. In this time period, NGC 1566 showed two major outbursts in optical wavebands, in 1962 and 1992, along with several flaring episodes (Alloin et al., 1986; da Silva et al., 2017). Before the major X-ray outburst in 2018, a flaring event was observed in 2010 with the *Swift*/BAT survey[6] (Oknyansky et al., 2018, 2019). Since then, NGC 1566 remained in the low state with a luminosity of $L \sim 10^{41}$ erg s^{-1} in 2–10 keV energy band.

NGC 1566 was monitored by *Swift*/XRT over a decade and it was caught in an outburst in June 2018, when the X-ray intensity increased by $\sim 25 - 30$ times compared to the quiescent state (Oknyansky et al., 2019). During the 2018 X-ray outburst, the source also brightened in the optical, ultraviolet (UV) and infrared (IR) wavebands (Dai et al., 2018; Cutri et al., 2018). The optical and near-infrared (NIR) observations showed that the AGN started to brighten since September 2017 (Dai et al., 2018). In the upper panel of Figure 4.1, we show the long term $0.3 - 10$ keV *Swift*/XRT light curve. From this figure, it can be seen that the source experienced a major outburst in June 2018 (F1), which was followed by three smaller flaring events in December 2018 (F2; Grupe et al., 2018b), May 2019 (F3; Grupe et al., 2019), and May 2020 (F4). The smaller outbursts (F2, F3 and F4) were not as bright as the main outburst (F1). In the bottom panel of Figure 4.1, we show the evolution of the hardness ratio (HR; i.e. the ratio between the $1.5 - 10$ keV and $0.3 - 1.5$ keV count rates) with time. Unlike the *Swift*/XRT light curve (top panel), the HR plot did not show any significant long-term variability. In Figure 4.2, we show hardness-intensity diagram (Homan et al., 2001; Remillard & McClintock, 2006) for the main outburst (F1), where the *Swift*/XRT count rate is plotted as a function of HR. The HID or 'q'-diagram appeared to show a 'q'-like shape, which is ubiquitous for outbursting Galactic black hole X-ray binaries. Interestingly, we did not observe any clear sign of 'q'-shape HID for the next three recurrent outbursts.

Variability

We studied the source variability in different energy bands. As the soft excess in AGNs is generally observed below 3 keV, whereas the primary emission is observed beyond 3 keV, we analyzed the *XMM-Newton* light curves in $0.5 - 3$ keV and $3 - 10$ keV energy ranges. We also studied the *NuSTAR* light curves in two separate bands ($3 - 10$ keV and $10 - 70$ keV ranges).

[6] `https://swift.gsfc.nasa.gov/results/bs105mon/216`

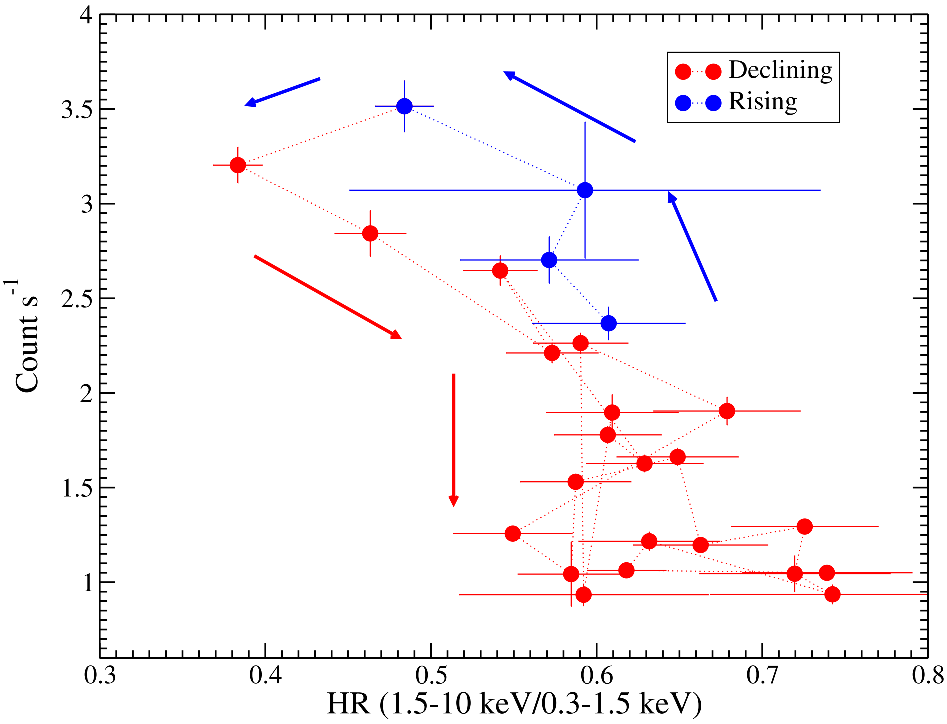

Figure 4.2: Hardness-intensity diagram (HID) for the first outburst F1 (from MJD 58308 to MJD 58380). The $0.3-10$ keV *Swift*/XRT count rate is plotted as a function of hardness ratio (HR). The arrow marks in the figure represent the evolution of the outburst.

We calculated the peak-to-peak ratio of the light curves, which is defined as $R = F_{\rm max}/F_{\rm min}$, where $F_{\rm max}$ and $F_{\rm min}$ are the maximum and minimum count rates, respectively. The light curves in different energy bands ($0.5-3$ keV, $3-10$ keV, and $10-70$ keV) showed different magnitude of variability. In all observations, R was higher in the $3-10$ keV energy band than in the $0.5-3$ keV range. In the $10-70$ keV energy band, R was higher than in the lower energy band, except for O4. The mean value of R in $0.5-3$ keV, $3-10$ keV, and $10-70$ keV energy bands are $<R>= 1.34, 3.43$, and 5.33, respectively. Thus, it is clear that the light curves showed higher variability in the higher energy bands in terms of R. However, this is too simplistic as very high or low count could be generated due to systematic/instrumental error. Hence, we calculated the normalized variance ($\sigma^2_{\rm NXS}$) and fractional variability ($F_{\rm var}$ to study the variability.

We calculated the fractional variability ($F_{\rm var}$) (Edelson et al., 1996, 2001; Edelson & Malkan, 2012; Nandra et al., 1997; Vaughan et al., 2003) in the 0.5–3, 3–10 and 10–70 keV bands for a light curve of x_i counts s^{-1} with uncertainties σ_i of length N, with a mean μ and standard deviation σ is given by,

$$F_{\rm var} = \sqrt{\frac{\sigma^2_{\rm XS}}{\mu^2}}, \tag{4.1}$$

where, $\sigma^2_{\rm XS}$ is the excess variance (Nandra et al., 1997; Edelson et al., 2002) which is given by,

$$\sigma^2_{\rm XS} = \sigma^2 - \sigma^2_{\rm err}, \tag{4.2}$$

where, $\sigma^2_{\rm err}$ is the mean squared error. The $\sigma^2_{\rm err}$ is given by,

$$\sigma^2_{\rm err} = \frac{1}{N}\sum_{i=1}^{N}\sigma^2_{\rm i}. \tag{4.3}$$

The normalized excess variance is given by,

$$\sigma^2_{\rm NXS} = \frac{\sigma^2_{\rm XS}}{\mu^2}. \tag{4.4}$$

The uncertainties in $F_{\rm var}$ and $\sigma_{\rm NXS}$ (Vaughan et al., 2003) are given by,

$$\mathrm{err}(F_{\rm var}) = \sqrt{\left(\sqrt{\frac{1}{2N}}\frac{\sigma^2_{\rm err}}{\mu^2 F_{\rm var}}\right)^2 + \left(\frac{1}{\mu}\sqrt{\frac{\sigma^2_{\rm err}}{N}}\right)^2}, \tag{4.5}$$

and

$$\mathrm{err}(\sigma^2_{\rm NXS}) = \sqrt{\left(\sqrt{\frac{2}{N}}\frac{\sigma^2_{\rm err}}{\mu^2}\right)^2 + \left(\sqrt{\frac{\sigma^2_{\rm err}}{N}}\frac{2F_{\rm var}}{\mu}\right)^2}. \tag{4.6}$$

For a few observations, we could not estimate excess variance due to large errors in the data. Thus, from the normalized variance ($\sigma^2_{\rm NXS}$), the trend of variability was not clear. We calculated the fractional rms variability amplitude ($F_{\rm var}$) to study the variability. We obtained the highest fractional variability ($F_{\rm var}$) in the $0.5-3$ keV energy range for four observations (X1, O1, O2 & O3), while the highest variability is observed in $3-10$ keV range for O5. The mean value of the fractional variability in $0.5-3$ keV, $3-10$ keV, and $10-70$ keV energy ranges were $< F_{\rm var} >= 12.8 \pm 0.5\%, 12.0 \pm 2.8\%$, and $7.9 \pm 2.4\%$, respectively. This indicates that the strongest variability is observed in the $0.5-3$ keV energy range. The variability parameters discussed here are reported in Table 4.2.

Correlation

To investigate the origin of the soft excess, we calculated the time delay between the soft X-ray photons ($0.5-3$ keV range) and the continuum photons ($3-10$ keV range) using cross-correlation method from the *XMM-Newton* observations. We used the ξ-transformed

Table 4.3: ZDCF results.

ID	soft excess $\Delta t^{\dagger}$ (min)	$\sigma^{\dagger}$ (min)	amp†
X1	-10.5 ± 13.0	145.2 ± 8.3	0.24 ± 0.07
O1	13.8 ± 3.1	103.3 ± 8.3	0.84 ± 0.08
O2	11.7 ± 5.9	222.9 ± 8.3	0.90 ± 0.07
O3	13.9 ± 7.8	263.4 ± 8.3	0.69 ± 0.07
O5	–	–	–

† ZDCF correlation between primary X-ray continuum ($3-10$ energy band) and soft excess ($0.5-3$ keV energy band). σ's and amp's are FWHM and amplitude of the ZDCF function. Note that the maximum amplitude can be 1.

discrete correlation function (ZDCF) method (Alexander, 1997)[7] to investigate the time-delay between the soft-excess and the X-ray continuum. The ZDCF co-efficient was calculated for two cases: omitting the zero lag points and including the zero lag points. In both cases, similar results were obtained. A strong correlation between the $0.5-3$ keV and $3-10$ keV energy bands was observed (amplitude > 0.7) during observations O1, O2 and O3. However, no significant delay was observed during those observations. The values of ZDCF coefficient with time delay are presented in Table 4.3.

4.3.2 Spectral Analysis

We carry out the X-ray spectral analysis using data obtained from the *Swift*/XRT, *XMM-Newton* and *NuSTAR* observations of NGC 1566 using `XSPEC` v12.10 package (Arnaud, 1996)[8]. The spectral analysis was performed using simultaneous *XMM-Newton* and *NuSTAR* observations in the $0.5-70$ keV energy band for three epochs, simultaneous *Swift*/XRT and *NuSTAR* observations ($0.5-70$ keV) for three epochs, and *XMM-Newton* observations for two epochs ($0.5-10$ keV), between 5 November 2015 and 21 August 2019 (see Table 4.1).

For the spectral analysis, we used various phenomenological and physical models, namely, `powerlaw` (PL)[9], `NTHCOMP`[10] (Zdziarski et al., 1996; Życki et al., 1999), `OPTXAGNF`[11] (Done et al., 2012), and `RELXILL`[12] (García et al., 2014; Dauser et al., 2014) to understand the X-ray properties of NGC 1566. In general, an X-ray spectrum of an AGN consists of a power-law continuum, a reflection hump at around $15-40$ keV, a Fe Kα fluorescent line, and a soft X-ray

[7] `http://www.weizmann.ac.il/particle/tal/research-activities/software`
[8] `https://heasarc.gsfc.nasa.gov/xanadu/xspec/`
[9] `https://heasarc.gsfc.nasa.gov/xanadu/xspec/manual/node213.html`
[10] `https://heasarc.gsfc.nasa.gov/xanadu/xspec/manual/node205.html`
[11] `https://heasarc.gsfc.nasa.gov/xanadu/xspec/manual/node206.html`
[12] `www.sternwarte.uni-erlangen.de/~dauser/research/relxill/`

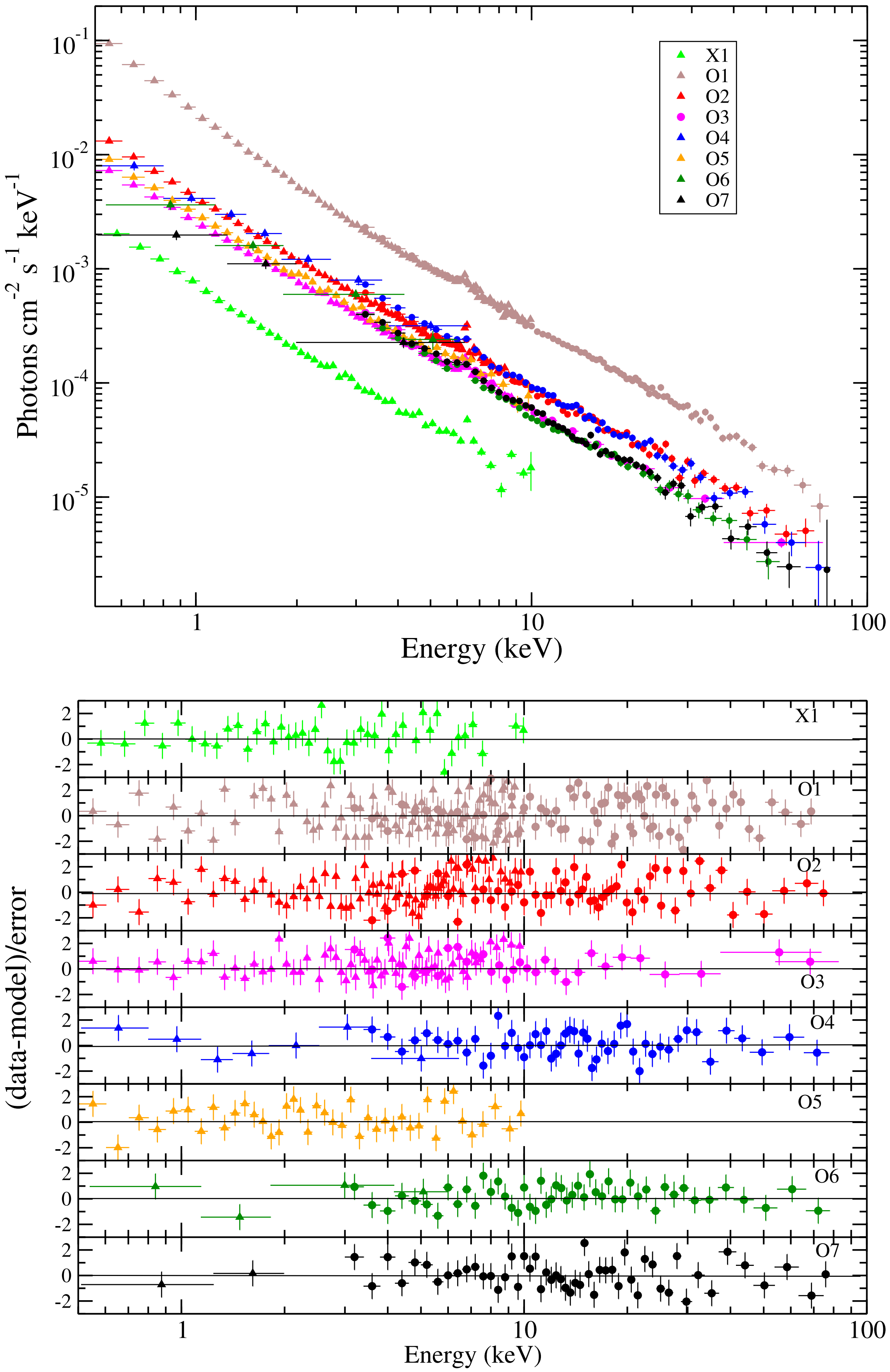

Figure 4.3: The top panel shows the unfolded spectra obtained from each observations. Triangles represent the *XMM-Newton* or *Swift*/XRT data, while circles represent the *NuSTAR* data. The light-green, brown, red, magenta, blue, orange, dark green and black points represent the observation X1, O1, O2, O3, O4, O5, O6 and O7, respectively. The residuals obtained after fitting the source spectra with Model–1 and Model–3 are shown in the bottom panels. The spectra are re-binned to improve clarity.

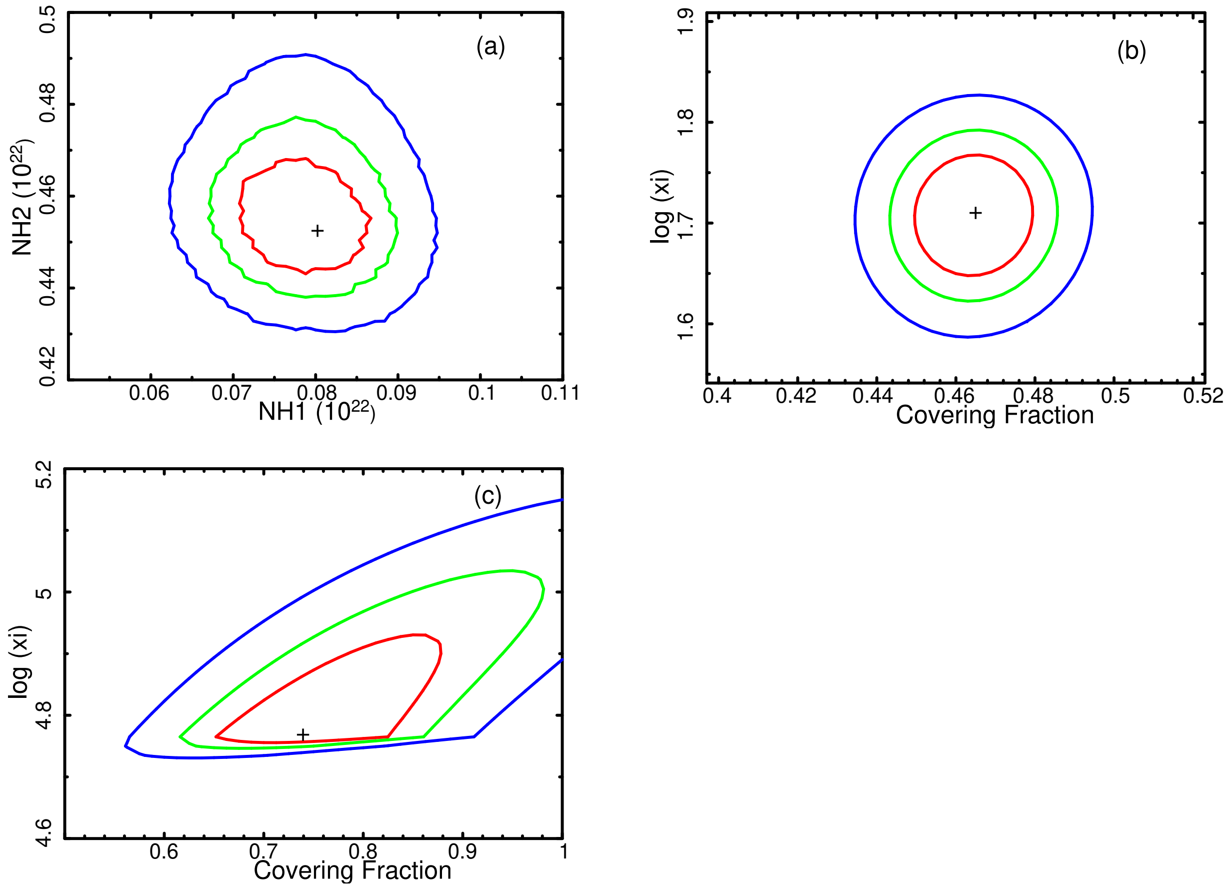

Figure 4.4: Top left panel shows the 2D contours between the column density of the low-ionizing absorber ($N_{\mathrm{H},1}$) and high-ionizing absorber ($N_{\mathrm{H},2}$) for O1. The top right and bottom panels show 2D contours between log ξ and covering fraction for low and high-ionizing absorbers, respectively.

component below 2 keV (Netzer, 2015; Padovani et al., 2017; Ricci et al., 2017). The observed X-ray emission also suffers from absorption caused by the interstellar medium and the torus. In our analysis, we used two absorption components. For the Galactic interstellar absorption, we used `TBabs`[13](Wilms et al., 2000) with fixed hydrogen column density of $N_{\mathrm{H}} = 7.15 \times 10^{19}$ cm^{-2}(HI4PI Collaboration et al., 2016). In addition, we also used a ionized absorption model `zxipcf`. For both the absorption components, we used the *wilms* abundances (Wilms et al., 2000) and the Verner cross-section (Verner et al., 1996). In this work, we used the following cosmological parameters : $H_0 = 71$ km s^{-1} Mpc $^{-1}$, $\Omega_\Lambda = 0.73$, and $\Omega_M = 0.27$ (Bennett et al., 2003). The uncertainties in each spectral parameters are calculated using the '`error`' command in `XSPEC`, and reported at the 90% confidence (1.6 σ).

[13]`https://heasarc.gsfc.nasa.gov/xanadu/xspec/manual/node265.html`

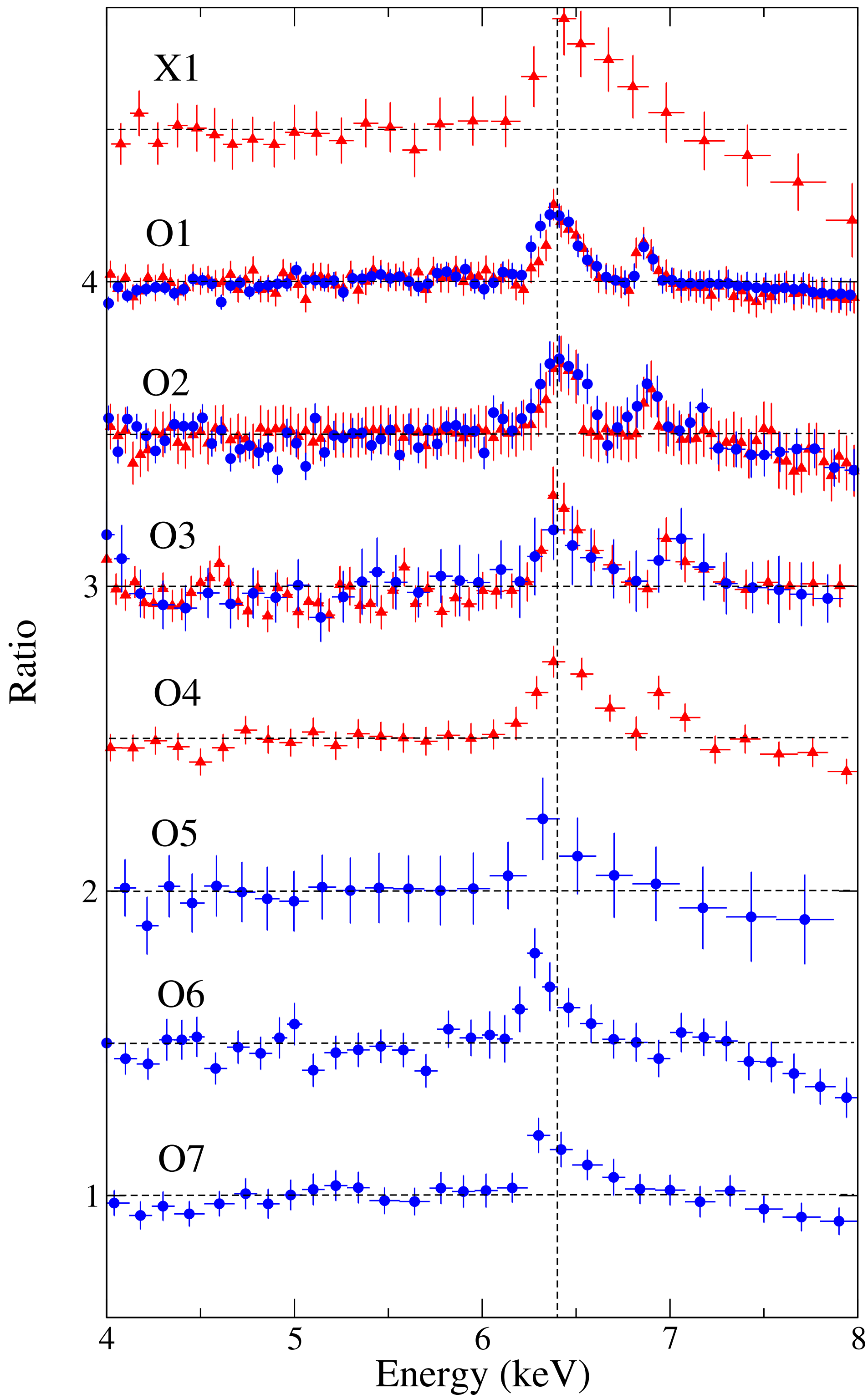

Figure 4.5: Evolution of Fe complex. The ratio of *XMM-Newton* and *NuSTAR* data to the power-law continuum model for every observations are shown. The red triangles and blue circles represent the ratio obtained from *XMM-Newton* and *NuSTAR* data, respectively. The vertical dashed line represents E=6.4 keV. The horizontal dashed lines represent the data/model=1 for each observation. The ratios are re-scaled by adding 0.5 in the Y-axis separating the observations.

Model 1: POWERLAW

We built our baseline spectral model with `power-law` continuum, along with the soft-excess, and Fe K-line emission. We used a blackbody component (`bbody` in `XSPEC`) for the soft-excess and one or more Gaussian functions to incorporate the Fe K complex. Out of the eight epochs, two Gaussian lines were required for six observations. Two ionized absorbers were also needed while fitting the data from three observations. The final model (hereafter Model–1) reads in `XSPEC` as,

`TB` $\times$ `zxipcf1` $\times$ `zxipcf2` $\times$ `( zPL1+ zGa + zGa + bbody).`

We started our analysis with the pre-outburst *XMM-Newton* observation X1 (in the $0.5-10$ keV energy range), $\sim$2.5 years prior to the 2018 outburst. Model–1 provided a good fit to the *XMM-Newton* data, with $N_{\rm H} = (3.53 \pm 0.06) \times 10^{21}$ cm^{-2} and power-law photon index of $\Gamma = 1.72 \pm 0.05$, with $\chi^2 = 1073$ for 998 degrees of freedom (dof). Along with this, an iron Kα emission line at $\sim$6.4 keV with an equivalent width (EW) of $\sim 206^{+4}_{-18}$ eV was detected.

Next, we analyzed simultaneous observations of NGC 1566 with *XMM-Newton* and *NuSTAR* in the rising phase of the 2018 outburst (O1). First, we included one `zxipcf` component in our spectral model. The fit returned with $\chi^2 = 2850$ for 2562 degrees of freedom (dof). However, negative residuals were clearly observed in soft X-rays (<1 keV). Thus, we included another `zxipcf` component, and our fit improved significantly with $\Delta\chi^2 = 106$ for 3 dof. The spectral fitting in $0.5 - 70$ keV range returned $\Gamma = 1.85 \pm 0.04$, and $\chi^2 = 2744$ for 2559 dof. The Fe Kα line was detected at 6.38 keV with EW of 114 ± 15 eV, as well as another emission feature at 6.87 keV, with EW < 37 eV. This line could be associated with Fe XXVI line. We required two ionized absorber to fit the spectra, one low-ionization absorber ($\xi \sim 10^{1.7\pm0.1}$) with $N_{\rm H,1} = (8.1 \pm 2.2) \times 10^{20}$ cm^{-2}, and one high-ionization absorber ($\xi \sim 10^{4.7\pm0.4}$) with $N_{\rm H,2} = (4.3 \pm 0.4) \times 10^{21}$ cm^{-2}. The high-ionizing absorber required a high covering fraction ($CF > 0.73$), while the low-ionizing absorber a moderate covering fraction with $CF \sim 0.46 \pm 0.04$.

The next observation (O2) was carried out on 10 October 2018, simultaneously with *XMM-Newton* and *NuSTAR*, covering the $0.5 - 70$ keV energy range. The source was in the decay phase of the outburst at the time of the observation. We started our fitting with one `zxipcf` component. Although, the model provided a good fit to the data with $\chi^2 = 2298$ for 2130 dof, an absorption feature was seen in the residuals. Thus, we added a second `zxipcf` component, and our fit returned with $\chi^2 = 2224$ for 2127 dof. The photon index decreased marginally compared to O1 ($\Gamma = 1.78 \pm 0.02$), while the column density increased slightly for both low and high-ionizing absorbers. The Fe Kα and Fe XXVI lines were detected at 6.41 keV and 6.89 keV, with EWs of 126^{+3}_{-21} eV and < 49 eV, respectively. The next simultaneous observations of NGC 1566 with *XMM-Newton* and *NuSTAR* (O3) were carried out $\sim$8 months after the end of the outburst. The source was in a low state during the observation. Similar to O1 and O2, adding second absorption component improved the fit $\Delta\chi^2 = 67$ for 3 dof. The column density increased to $N_{\rm H,1} = (1.24 \pm 0.14) \times 10^{21}$ cm^{-2} for the low-ionization absorber, while the column density decreased to $N_{\rm H,2} = (8.9 \pm 0.2) \times 10^{20}$ cm^{-2} for the high-ionization absorber. The photon index was found to be $\Gamma = 1.68 \pm 0.02$ in this observation. We detected both Fe Kα and Fe kβ lines at 6.39 keV and 7.04 keV, with EWs of 117 ± 14 eV and < 92 eV, respectively.

The last four observations (O4, O5, O6 & O7) were carried out in the span of 13 days. Observation O4 was made during the second small flare (F2), after the 2018 main outburst. During these four observations, the photon index was nearly constant ($\Gamma \sim 1.67 \pm 0.07 - 1.69 \pm 0.06$), while the column density of the low-ionizing absorber was found to vary in the range of $N_{\rm H,1} \sim 1.2 - 1.3 \times 10^{21}$ cm^{-2}. A high-ionization absorber was not required to fit the spectra of these four observations. We also observed a low covering fraction in these four observations (see Table 4.4). The Fe Kα line was detected in all four observations, with EW > 100 eV (except O5). During our observations, the blackbody temperature ($T_{\rm bb}$) was observed to be remarkably constant with $T_{\rm bb} \sim 110$ eV. The parameters obtained by our spectral fitting results are listed in Table 4.4. Model–1 fitted spectra of NGC 1566 are shown in the top panel of Fig. 4.3, whereas the corresponding residuals are shown in the bottom panels. To test for the presence of degeneracies between the column densities of two ionizing absorbers, we plotted the 2D contour in Figure 4.4a for the observation O1. In Figure 4.4b and Figure 4.4c, we show 2D contours between $\log(\xi)$ and covering fraction for the low and high-ionizing absorbers, respectively, for observation O1. In Figure 4.5, we show the residuals above the continuum in $4 - 8$ keV energy range for Fe line emission. In Figure 4.6a, we also show the unfolded spectrum fitted with Model–1 for observation O2.

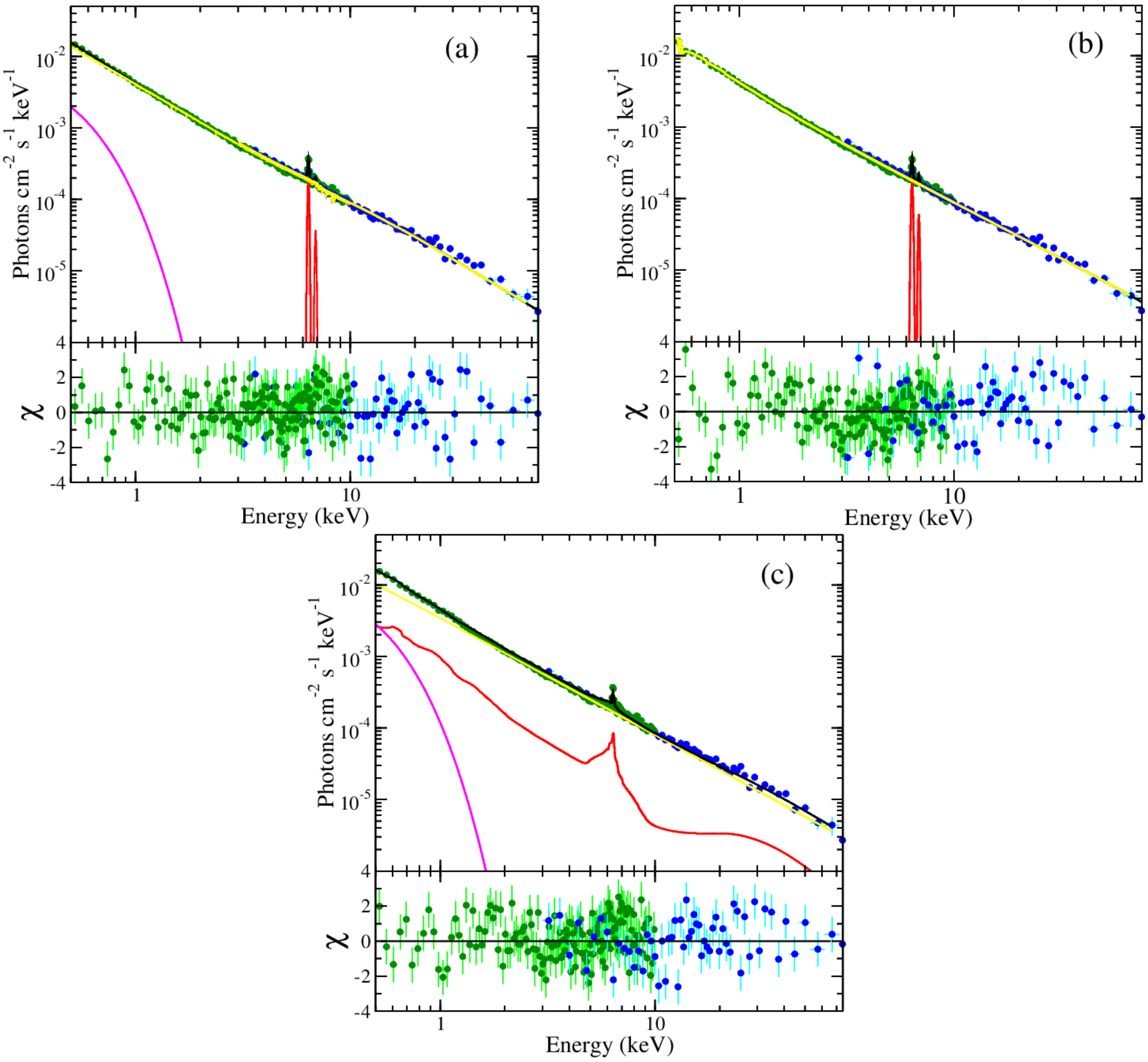

Figure 4.6: Best-fit unfolded spectra using Model–1, Model–3 and Model–4 are shown in the top left, top right, and bottom panels, respectively, for O2. The corresponding residuals are shown in the bottom of each panel. Top left panel: the black, yellow, magenta and red lines represent the total, primary emission, soft excess and Fe line emission, respectively. Top right panel: the black, yellow, and red lines represent the total emission, the AGN emission and Fe line emission, respectively. Bottom panel: the black, yellow, magenta and red lines represent the total emission, primary emission, soft excess and reflection component, respectively.

Table 4.4: Best-fit parameters obtained from the spectral fitting of the source spectra with Model–1 (`POWER-LAW`) & Model–2 (`NTHCOMP`).

Parameters		X1	O1	O2	O3	O4	O5	O6	O7
$N_{\mathrm{H,1}}$ (10^{21} cm^{-2})		$3.53^{+0.05}_{-0.06}$	$0.81^{+0.13}_{-0.22}$	$0.96^{+0.15}_{-0.18}$	$1.24^{+0.14}_{-0.11}$	$1.33^{+0.14}_{-0.10}$	$1.18^{+0.08}_{-0.09}$	$1.25^{+0.12}_{-0.16}$	$1.30^{+0.17}_{-0.22}$
logξ_1		$-3^{\dagger}$	$1.71^{+0.12}_{-0.11}$	$1.81^{+0.10}_{-0.08}$	$1.37^{+0.08}_{-0.09}$	$1.10^{+0.04}_{-0.08}$	$0.26^{+0.09}_{-0.05}$	$0.17^{+0.14}_{-0.05}$	$0.21^{+0.03}_{-0.08}$
Cov Frac1		$0.20^{+0.13}_{-0.05}$	$0.46^{+0.04}_{-0.03}$	$0.31^{+0.09}_{-0.04}$	$0.33^{+0.07}_{-0.12}$	< 0.12	$0.24^{+0.12}_{-0.15}$	$0.17^{+0.04}_{-0.08}$	< 0.1
$N_{\mathrm{H,2}}$ (10^{21} cm^{-2})		–	$4.31^{+0.41}_{-0.26}$	$4.56^{+0.58}_{-0.47}$	$0.89^{+0.22}_{-0.17}$	–	–	–	–
logξ_2		–	$4.73^{+0.40}_{-0.02}$	$3.56^{+0.26}_{-0.08}$	$3.07^{+0.19}_{-0.07}$	–	–	–	–
Cov Frac2		–	> 0.73	$0.61^{+0.26}_{-0.21}$	$0.54^{+0.23}_{-0.39}$	–	–	–	–
Γ		$1.72^{+0.05}_{-0.05}$	$1.85^{+0.04}_{-0.04}$	$1.78^{+0.02}_{-0.02}$	$1.68^{+0.02}_{-0.02}$	$1.67^{+0.05}_{-0.07}$	$1.68^{+0.03}_{-0.04}$	$1.69^{+0.04}_{-0.06}$	$1.67^{+0.05}_{-0.07}$
PL Norm (10^{-3})		$1.59^{+0.16}_{-0.18}$	$14.6^{+1.43}_{-2.05}$	$5.97^{+0.06}_{-0.10}$	$2.45^{+0.05}_{-0.10}$	$4.71^{+0.07}_{-0.08}$	$2.84^{+0.13}_{-0.09}$	$2.78^{+0.11}_{-0.15}$	$2.58^{+0.10}_{-0.17}$
Fe Kα	LE (keV)	$6.44^{+0.03}_{-0.04}$	$6.38^{+0.04}_{-0.04}$	$6.41^{+0.03}_{-0.06}$	$6.39^{+0.07}_{-0.10}$	$6.29^{+0.08}_{-0.14}$	$6.28^{+0.07}_{-0.11}$	$6.29^{+0.05}_{-0.09}$	$6.19^{+0.05}_{-0.10}$
	EW (eV)	206^{+4}_{-18}	114^{+11}_{-15}	126^{+3}_{-21}	117^{+14}_{-10}	106^{+1}_{-6}	< 95	155^{+12}_{-16}	108^{+15}_{-22}
	FWHM (km s^{-1})	2329^{*}	8695^{+924}_{-1243}	2108^{*}	4796^{+863}_{-982}	2337^{*}	4461^{+1045}_{-845}	6025^{+946}_{-1194}	6613^{+1275}_{-1223}
	Norm (10^{-5})	$6.83^{+0.15}_{-0.22}$	$11.74^{+1.10}_{-1.22}$	$3.47^{+0.14}_{-0.10}$	$2.56^{+0.18}_{-0.13}$	$1.91^{+0.07}_{-0.09}$	$0.93^{+0.04}_{-0.10}$	$2.14^{+0.10}_{-0.13}$	$2.43^{+0.10}_{-0.08}$
Fe XXVI	LE (keV)	–	$6.87^{+0.04}_{-0.04}$	$6.89^{+0.04}_{-0.03}$	$7.04^{+0.05}_{-0.04}$	$6.93^{+0.04}_{-0.03}$	–	–	–
	EW (eV)	–	< 37	< 49	< 92	< 42	–	–	–
	FWHM (km s^{-1})	–	< 4452	< 4049	< 4943	< 3913	–	–	–
	Norm (10^{-6})	–	$21.09^{+1.02}_{-0.94}$	$7.88^{+0.13}_{-0.22}$	$8.95^{+1.06}_{-0.94}$	$7.30^{+0.31}_{-0.73}$	–	–	–
kT_{bb1} (eV)		116^{+7}_{-8}	112^{+6}_{-8}	117^{+11}_{-7}	115^{+5}_{-9}	108^{+8}_{-12}	114^{+9}_{-6}	117^{+12}_{-14}	122^{+17}_{-10}
N_{bb1} (10^{-5})		$0.49^{+0.03}_{-0.06}$	$28.6^{+2.29}_{-3.42}$	$8.30^{+1.09}_{-0.65}$	$4.35^{+0.76}_{-0.96}$	$5.33^{+0.51}_{-1.04}$	$0.98^{+0.24}_{-0.19}$	$4.71^{+0.72}_{-1.13}$	$2.65^{+0.80}_{-0.56}$
χ^2/dof		1073/998	2744/2559	2224/2127	1608/1646	693/654	835/834	535/542	576/567

$N_{\rm H,1}$ (10^{21} cm^{-2})	$3.46^{+0.06}_{-0.05}$	$0.78^{+0.10}_{-0.21}$	$0.96^{+0.17}_{-0.16}$	$1.22^{+0.13}_{-0.15}$	$1.32^{+0.12}_{-0.16}$	$1.19^{+0.10}_{-0.09}$	$1.26^{+0.12}_{-0.18}$	$1.27^{+0.15}_{-0.19}$
$\log\xi_1$	$-3^{\dagger}$	$1.66^{+0.10}_{-0.08}$	$1.85^{+0.06}_{-0.11}$	$1.32^{+0.07}_{-0.10}$	$1.05^{+0.04}_{-0.06}$	$0.26^{+0.05}_{-0.07}$	$0.15^{+0.12}_{-0.07}$	$0.21^{+0.04}_{-0.05}$
Cov Frac1	$0.20^{+0.07}_{-0.05}$	$0.46^{+0.03}_{-0.03}$	$0.32^{+0.07}_{-0.04}$	$0.34^{+0.05}_{-0.14}$	< 0.12	$0.22^{+0.11}_{-0.16}$	< 0.15	< 0.1
$N_{\rm H,2}$ (10^{21} cm^{-2})	–	$4.25^{+0.32}_{-0.23}$	$4.50^{+0.64}_{-0.43}$	$0.82^{+0.27}_{-0.19}$	–	–	–	–
$\log\xi_2$	–	$4.63^{+0.45}_{-0.09}$	$3.32^{+0.33}_{-0.10}$	$3.11^{+0.23}_{-0.16}$	–	–	–	–
Cov Frac2	–	> 0.75	$0.59^{+0.22}_{-0.25}$	$0.56^{+0.23}_{-0.45}$	–	–	–	–
Γ	$1.74^{+0.05}_{-0.07}$	$1.88^{+0.04}_{-0.06}$	$1.75^{+0.03}_{-0.03}$	$1.72^{+0.02}_{-0.03}$	$1.71^{+0.03}_{-0.05}$	$1.69^{+0.04}_{-0.04}$	$1.68^{+0.05}_{-0.05}$	$1.69^{+0.04}_{-0.05}$
$kT_{\rm e}$ (keV)	$101.8^{+4.9}_{-4.3}$	$60.8^{+5.5}_{-6.7}$	$85.7^{+7.4}_{-5.9}$	$92.2^{+8.4}_{-9.4}$	$75.2^{+8.3}_{-7.6}$	$104.2^{+5.6}_{-6.9}$	$105.8^{+6.9}_{-5.5}$	$96.7^{+7.5}_{-8.2}$
τ	$1.27^{+0.17}_{-0.11}$	$1.60^{+0.33}_{-0.18}$	$1.43^{+0.16}_{-0.15}$	$1.41^{+0.17}_{-0.12}$	$1.66^{+0.24}_{-0.17}$	$1.30^{+0.14}_{-0.12}$	$1.34^{+0.15}_{-0.13}$	$1.41^{+0.19}_{-0.13}$

ξ's are in the unit ergs cm s^{-1}. PL norm is in unit of ph cm^{-2} s^{-1}. Fe line norm are in the unit of ph cm^{-2} s^{-1}.

τ's are calculated using Eqn. 1.

† pegged at the lowest value.

* Gaussian fitted with fixed line width, $\sigma = 0.05$ keV.

Model 2: NTHCOMP

While fitting the source spectra with Model–1 provided us with information on the spectral shape and hydrogen column density, it provided limited information on the physical properties of the Comptonizing plasma. The Comptonizing plasma can be characterized by the electron temperature ($kT_{\rm e}$) and optical depth (τ). In order to understand the properties of the Compton cloud, we replaced the `powerlaw` continuum model with `NTHCOMP` (Zdziarski et al., 1996; Życki et al., 1999) in Model–1. The `NTHCOMP` model provided us the photon index (Γ) and the hot electron temperature of the Compton cloud ($kT_{\rm e}$). The optical depth can be easily calculated from the information on Γ and $kT_{\rm e}$ using the following equation (Sunyaev & Titarchuk, 1980; Zdziarski et al., 1996),

$$\tau \sim \sqrt{\frac{9}{4} + \frac{m_e c^2}{kT_{\rm e}} \frac{3}{(\Gamma - 1)(\Gamma + 2)}} - \frac{3}{2}. \tag{4.7}$$

This model (hereafter Model–2) reads in `XSPEC` as,

`TB` $\times$ `zxipcf1` $\times$ `zxipcf2` $\times$ `(NTHCOMP + zGa + zGa + bbody)`.

We fixed the seed photon temperature at $kT_{\rm s} = 30$ eV, which is reasonable for a BH of mass $\sim 8.3 \times 10^6\ M_\odot$(Shakura & Sunyaev, 1973b; Makishima et al., 2000). We required two absorption component during O1, O2 and O3. Inclusion of second absorption improved the fit significantly with $\Delta\chi^2 = 108$, 84, 78 for 3 dof, during O1, O2 and O3, respectively. The photon indices and column densities obtained are similar to those obtained using Model–1. We found that $kT_{\rm e} = 102 \pm 5$ keV for observation X1. During the rising phase of the outburst (observation O1), the Compton cloud was found to be relatively cooler, with $kT_{\rm e} = 61 \pm 7$ keV. The Compton cloud was hot during the later observations, with the electron temperature increasing up to 106 ± 7 keV within the eight observations analyzed here. A nearly constant photon index and a variable temperature would imply a variation in the density of the Comptonizing cloud. This would suggest that the optical depth was varying during the observations in the range of $\sim 1.27 - 1.66$. The results obtained from our spectral fitting with this model are listed in Table 4.4.

Model 3: OPTXAGNF

The X-ray spectra of AGN typically show a soft excess below 2 keV (Arnaud et al., 1985; Singh et al., 1985). Although the soft excess in AGNs was first detected in the 1980s, its origin is still very debated. In Models 1 & 2, we fitted the soft excess component with a

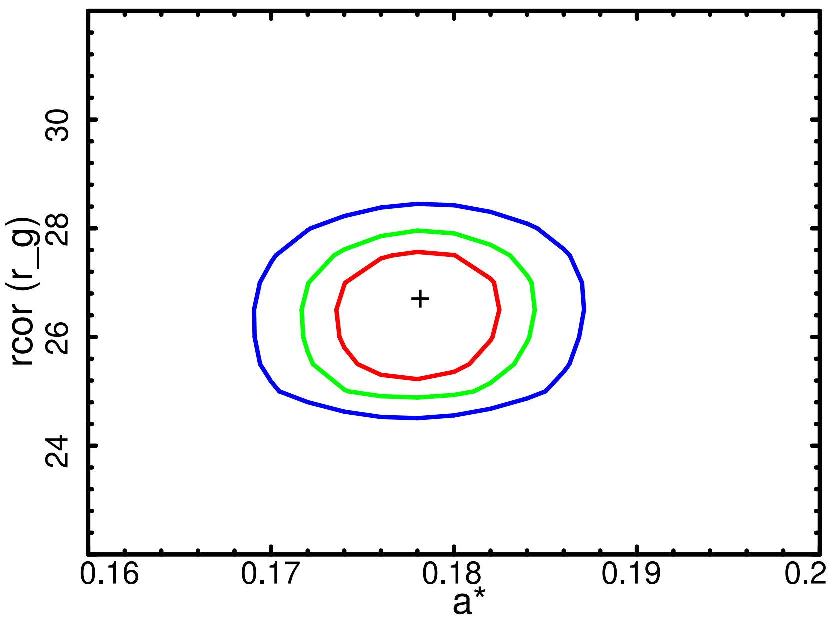

Figure 4.7: 2D contour plot between $R_{\rm cor}$ and a^{*} for Model–3 during the observation O2.

phenomenological `blackbody` model. To shed light on the origin of the soft excess in this source, we used a more physical model, `OPTXAGNF` (Done et al., 2012).

The `OPTXAGNF` model (hereafter Model–3) computes the soft excess and the primary emission self-consistently. In this model, total emission is determined by the mass accretion rate and by the BH mass. The disc emission emerges as a colour temperature corrected blackbody emission at radii $R_{\rm out} > r > R_{\rm cor}$, where $R_{\rm out}$ and $R_{\rm cor}$ are the outer edge of the disc and the corona, respectively. At $r < R_{\rm cor}$, the disc emission emerges as the Comptonized emission from a warm and optically-thick medium, rather than thermal emission. The hot and optically-thin corona is located around the disc and produces the high energy power-law continuum. The total Comptonized emission is divided between the cold and hot corona, and the fraction of the hot-Comptonized emission ($f_{\rm PL}$) can be found from the model fitting. The temperature of the cold corona ($kT_{\rm S}$), temperature of the seed photon, and the optical depth of the cold corona (τ) at $r = R_{\rm cor}$ determine the energy of the up-scattered soft excess emission. The power-law continuum is approximated as the `NTHCOMP` model, with the seed photon temperature fixed at the disc temperature at $r = R_{\rm cor}$, and the electron temperature fixed at 100 keV.

When using the `OPTXAGNF` model, we included two Gaussian components to incorporate the Fe emission lines. The model reads in `XSPEC` as,

`TB` $\times$ `zxipcf1` $\times$ `zxipcf2` $\times$ `( OPTXAGNF + zGa + zGa).`

While fitting the data with this model, we kept the BH mass frozen at $M_{\rm BH} = 8.3 \times 10^6$ $M_\odot$ (Woo & Urry, 2002). As recommended, we fixed normalization to unity during our analysis. Initially, we started our analysis with one absorption component. However, an absorption feature was seen during O1, O2 and O3. Thus, we added second absorption component in the spectra of O1, O2 and O3. Adding second `zxipcf` component significantly improved the fit with $\Delta\chi^2 = 88$, 76, 65 for 3 dof, during the observation O1, O2 and O3, respectively. Overall, this model provided a good fit for all the observations. A clear variation in the Eddington ratio and size of the corona were observed in the different observations. In the rising phase of the 2018 outburst (observation O1), a high Eddington ratio ($L/L_{\rm Edd} \sim 0.23$) and a large corona ($R_{\rm cor} = 43 \pm 3\ R_{\rm g}$) were observed. These values were found to be higher than the pre-outburst observation (X1; $L/L_{\rm Edd} \sim 0.04$; $R_{\rm cor} = 12^{+2}_{-1}\ R_{\rm g}$). In later observations, both Eddington ratio and size of the X-ray corona decreased to $L/L_{\rm Edd} \sim 0.06 - 0.07$ and $R_{\rm cor} \sim 15 \pm 2 - 26 \pm 2\ R_g$, respectively. In the observation O1, the electron temperature of the optically thick Comptonizing region was observed to be $kT_{\rm S} \sim 1.4 \pm 0.1$ keV, along with optical depth $\tau \sim 4.6 \pm 1$. The temperature of the optically-thick medium decreased to $kT_{\rm S} \sim 0.5 - 0.6$ keV in the later observations (O3 – O7). However, the optical depth did not change much and varied in the range of $\tau \sim 4 - 5$. A significant fraction of the Comptonized emission was emitted from the optically thin corona with $f_{\rm PL} > 0.79$ during all the observations. We allowed the spin of the BH to vary. The best-fitted spin parameter fluctuated in the range of $a^* \sim 0.18^{+0.01}_{-0.02} - 0.21^{+0.03}_{-0.02}$, suggesting that the SMBH is spinning slowly. The variation of the column density ($N_{\rm H}$) and of the photon indices (Γ) was similar to that observed using Model–1. All the parameters obtained from our spectral analysis using Model–3 are presented in Table 4.5. In Figure 4.6b, we show the unfolded spectrum fitted with Model–3 for observation O2. In Figure 4.7, we display the contour plot of $R_{\rm cor}$ and a^*, which shows that there is no strong degeneracy between those two parameters.

Model–4 : RELXILL

Reprocessed X-ray radiation is a feature often observed in AGN spectra. This reflection component typically consists of a reflection hump at $\sim 15 - 40$ keV and fluorescent iron lines. In Model 1 – 3 we did not include a reprocessed X-ray radiation, hence, we add a relativistic reflection component `RELXILL` (García et al., 2014; Dauser et al., 2014, 2016) to our baseline model.

In this model, the strength of reflection is measured from the relative reflection fraction

($R_{\rm refl}$), which is defined as the ratio between the observed Comptonized emission and the radiation reprocessed by the disc. `RELXILL` assumes a broken power-law emission profile ($E(r) \approx r^{-q}$), where r is the distance from the SMBH, $E(r)$ is the emissivity, and q is the emissivity index. At a larger disc radii, in a non-relativistic domain, the emissivity profile has a form of $E(r) \sim r^{-3}$. However, in the relativistic domain, the emissivity profile is steeper. The break radius ($R_{\rm br}$) separates the relativistic and non-relativistic domains. In our analysis, we fixed $q_2 = 3$ for emission at $r > R_{\rm br}$.

In our spectral analysis, we used `RELXILL` along with the absorbed `power-law` continuum. We only considered the reflection component from `RELXILL` model by setting $R_{\rm refl}$ to a negative value. The model (hereafter Model–4) read in `XSPEC` as,

`TB` $\times$ `zxipcf1` $\times$ `zxipcf2` $\times$ `(zPL1 + RELXILL + bbody)`.

Table 4.5: Best-fit parameters obtained from the spectral fitting of the source spectra with Model–3 (OPTXAGNF).

	X1	O1	O2	O3	O4	O5	O6	O7
$N_{\rm H,1}$ (10^{21} cm^{-2})	$3.49^{+0.05}_{-0.05}$	$0.80^{+0.08}_{-0.16}$	$0.94^{+0.15}_{-0.15}$	$1.20^{+0.15}_{-0.11}$	$1.34^{+0.10}_{-0.12}$	$1.17^{+0.08}_{-0.11}$	$1.25^{+0.08}_{-0.14}$	$1.29^{+0.15}_{-0.22}$
logξ_1	$-3^{\dagger}$	$1.67^{+0.07}_{-0.06}$	$1.82^{+0.03}_{-0.06}$	$1.30^{+0.07}_{-0.09}$	$1.08^{+0.07}_{-0.10}$	$0.23^{+0.07}_{-0.10}$	$0.18^{+0.06}_{-0.04}$	$0.20^{+0.03}_{-0.04}$
Cov Frac2	$0.18^{+0.08}_{-0.06}$	$0.45^{+0.03}_{-0.04}$	$0.34^{+0.09}_{-0.06}$	$0.35^{+0.05}_{-0.11}$	< 0.12	$0.21^{+0.12}_{-0.17}$	< 0.14	< 0.15
$N_{\rm H,2}$ (10^{21} cm^{-2})	–	$4.28^{+0.45}_{-0.38}$	$4.56^{+0.51}_{-0.46}$	$0.89^{+0.21}_{-0.16}$	–	–	–	–
logξ_2	–	$4.52^{+0.39}_{-0.22}$	$3.15^{+0.21}_{-0.18}$	$2.93^{+0.32}_{-0.19}$	–	–	–	–
Cov Frac2	–	> 0.79	$0.54^{+0.22}_{-0.17}$	$0.51^{+0.28}_{-0.21}$	–	–	–	–
$L/L_{\rm Edd}$	$-1.98^{+0.03}_{-0.04}$	$-0.64^{+0.02}_{-0.02}$	$-0.78^{+0.03}_{-0.03}$	$-1.16^{+0.03}_{-0.04}$	$-0.81^{+0.02}_{-0.03}$	$-0.97^{+0.04}_{-0.05}$	$-1.20^{+0.03}_{-0.03}$	$-1.17^{+0.02}_{-0.01}$
a^*	$0.19^{+0.01}_{-0.01}$	$0.18^{+0.01}_{-0.02}$	$0.18^{+0.01}_{-0.01}$	$0.21^{+0.01}_{-0.02}$	$0.20^{+0.02}_{-0.03}$	$0.19^{+0.03}_{-0.02}$	$0.21^{+0.03}_{-0.02}$	$0.19^{+0.01}_{-0.01}$
$R_{\rm cor}$ ($R_{\rm g}$)	12^{+2}_{-1}	43^{+3}_{-2}	26^{+2}_{-2}	15^{+1}_{-2}	22^{+2}_{-2}	20^{+2}_{-3}	17^{+2}_{-3}	18^{+1}_{-1}
$kT_{\rm S}$ (keV)	$0.32^{+0.04}_{-0.05}$	$1.39^{+0.10}_{-0.15}$	$0.90^{+0.07}_{-0.11}$	$0.65^{+0.05}_{-0.10}$	$0.61^{+0.08}_{-0.06}$	$0.56^{+0.07}_{-0.08}$	$0.59^{+0.07}_{-0.03}$	$0.54^{+0.04}_{-0.03}$
τ	$4.16^{+0.28}_{-0.21}$	$4.56^{+0.12}_{-0.14}$	$4.30^{+0.27}_{-0.20}$	$4.33^{+0.18}_{-0.21}$	$5.23^{+0.30}_{-0.19}$	$4.92^{+0.34}_{-0.39}$	$4.29^{+0.39}_{-0.45}$	$3.54^{+0.34}_{-0.46}$
Γ	$1.77^{+0.03}_{-0.03}$	$1.74^{+0.02}_{-0.02}$	$1.66^{+0.04}_{-0.05}$	$1.73^{+0.02}_{-0.04}$	$1.72^{+0.02}_{-0.04}$	$1.70^{+0.03}_{-0.02}$	$1.72^{+0.02}_{-0.02}$	$1.66^{+0.03}_{-0.03}$
$f_{\rm PL}$	$0.84^{+0.01}_{-0.02}$	$0.79^{+0.01}_{-0.02}$	$0.81^{+0.03}_{-0.02}$	$0.84^{+0.03}_{-0.03}$	$0.88^{+0.03}_{-0.03}$	$0.83^{+0.03}_{-0.04}$	$0.88^{+0.03}_{-0.04}$	$0.94^{+0.03}_{-0.03}$
χ^2/dof	1070/995	2784/2551	2311/2120	1677/1643	706/649	827/831	526/535	571/560

ξ's are in the unit ergs cm s^{-1}. † pegged at the lowest value.

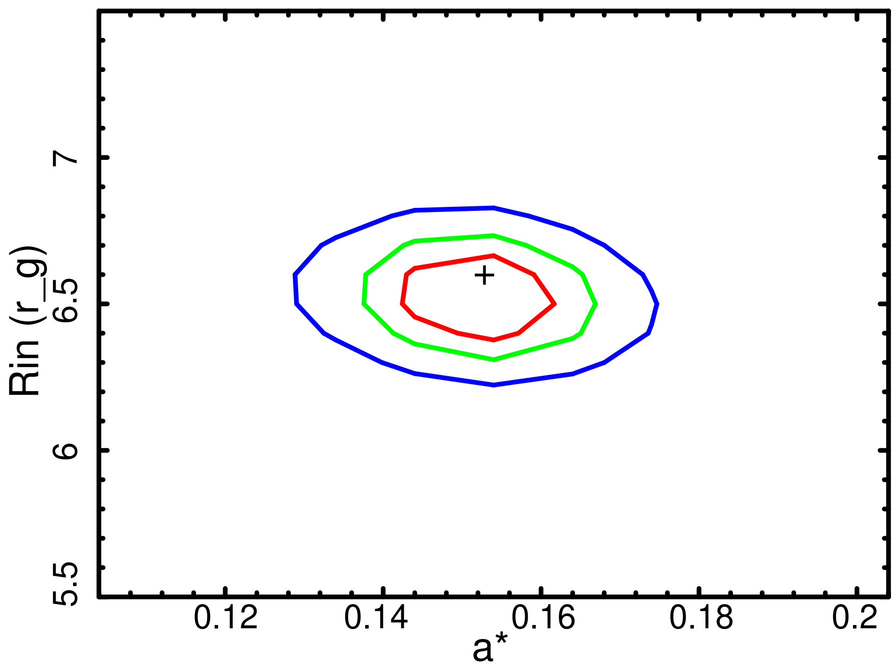

Figure 4.8: 2D contour plot between $R_{\rm in}$ and a^* for Model–4 during the observation O2.

While fitting the data with this model, we tied the photon indices of the `RELXILL` component to that of the `power-law` model. Although, we started our analysis with one absorption component, we required two absorption component during O1, O2 and O3. The second absorption component improved the fit with $\Delta\chi^2 = 82$, 68 and 59 for 3 dof, during O1, O2 and O3 respectively. Throughout the observations, we obtained a fairly unchanged value of the iron abundances with $A_{\rm Fe} \sim 3.7 - 4.2\ A_{\odot}$. Disc ionization was also constant during our observation period with $\xi \sim 10^{1.9-2.2}$ erg cm s^{-1}. The emissivity profile was quite stable with $q_2 \sim 4 - 5$, although $R_{\rm br}$ was found to change. This parameter reached its maximum during the observation O1 ($R_{\rm br} = 42^{+3}_{-2}\ R_g$). In the later observations, it decreased and varied in the range of $R_{\rm br} \sim 16 - 26\ R_g$. The inner edge of the disc varied in the range of $R_{\rm in} \sim 4 - 7\ R_g$. The best-fit inclination angle of the AGN was obtained in the range of $10.3^{+4.9\circ}_{-6.1}$– $17.7^{+2.9\circ}_{-5.2}$. The spin of the BH in NGC 1566 was observed to be low, with the best-fitted spin parameters found to be in the range of $0.15^{+0.03}_{-0.03} - 0.21^{+0.04}_{-0.02}$, which is consistent with what we found from the `OPTXAGNF` model. In all the observations, the reflection component was found to be relatively weak with reflection fraction varied in the range of, $R_{\rm refl} \sim 0.10 - 0.18$. The `RELXILL` model fitted spectral analysis results are given in Table 4.6. We show the unfolded spectrum fitted with Model–4 for observation O2 in Figure 4.6. In Figure 4.8, we show the contour plot of $R_{\rm in}$ and a^* for the observation O2.

4.4 Discussion

We studied NGC 1566 during and after the 2018 outburst event using data from *XMM-Newton*, *Swift* and *NuSTAR* observatories in the $0.5-70$ keV energy band. From a detailed spectral and timing analysis, we explored the nuclear properties of the AGN.

4.4.1 Black Hole Properties

NGC 1566 hosts a supermassive black hole of mass $M_{\rm BH} \approx 8.3 \times 10^6\ M_\odot$ (Woo & Urry, 2002). We kept the mass of the BH frozen during our spectral analysis with Model–3. Fitting the spectra with Model–3 and Model–4, we estimated the spin parameter (a^*) to be in the range $0.18^{+0.01}_{-0.02} - 0.21^{+0.03}_{-0.02}$ and $0.15^{+0.2}_{-0.3} - 0.21^{+0.04}_{-0.02}$, respectively. Both models favour a low spinning BH with the spin parameter $a^* \sim 0.2$, which is consistent with the findings of Parker et al., 2019.

The inclination angle was a free parameter in Model–4, and it was estimated to be in the range of $10.3^{+4.9}_{-6.1}{}^\circ$– $17.7^{+2.9}_{-5.2}{}^\circ$. Parker et al. (2019) also found a consistent inclination angle ($\theta_{\rm incl} < 11^\circ$).

Table 4.6: Best-fit parameters obtained from the spectral fitting of the source spectra with Model–4 (RELXILL).

	X1	O1	O2	O3	O4	O5	O6	O7
$N_{\mathrm{H},1}$ (10^{21} cm^{-2})	$3.51^{+0.03}_{-0.04}$	$0.77^{+0.06}_{-0.11}$	$0.95^{+0.11}_{-0.14}$	$1.18^{+0.12}_{-0.10}$	$1.28^{+0.08}_{-0.10}$	$1.16^{+0.07}_{-0.06}$	$1.28^{+0.10}_{-0.08}$	$1.31^{+0.12}_{-0.18}$
$\log\xi_1$	$-3^{\dagger}$	$1.63^{+0.05}_{-0.04}$	$1.85^{+0.05}_{-0.04}$	$1.31^{+0.07}_{-0.08}$	$1.05^{+0.05}_{-0.08}$	$0.21^{+0.05}_{-0.06}$	$0.19^{+0.06}_{-0.03}$	$0.24^{+0.04}_{-0.03}$
Cov Frac2	$0.17^{+0.05}_{-0.06}$	$0.44^{+0.04}_{-0.06}$	$0.36^{+0.05}_{-0.08}$	$0.33^{+0.06}_{-0.12}$	< 0.14	< 0.18	< 0.16	< 0.13
$N_{\mathrm{H},2}$ (10^{21} cm^{-2})	–	$4.36^{+0.34}_{-0.47}$	$4.58^{+0.37}_{-0.42}$	$0.95^{+0.19}_{-0.26}$	–	–	–	–
$\log\xi_2$	–	$4.58^{+0.41}_{-0.26}$	$3.10^{+0.19}_{-0.24}$	$2.96^{+0.26}_{-0.29}$	–	–	–	–
Cov Frac2	–	> 0.74	$0.52^{+0.18}_{-0.23}$	$0.53^{+0.31}_{-0.25}$	–	–	–	–
Γ	$1.77^{+0.03}_{-0.04}$	$1.76^{+0.05}_{-0.03}$	$1.68^{+0.04}_{-0.02}$	$1.73^{+0.03}_{-0.03}$	$1.65^{+0.04}_{-0.03}$	$1.67^{+0.05}_{-0.03}$	$1.71^{+0.02}_{-0.03}$	$1.68^{+0.03}_{-0.04}$
N_{PL} (10^{-3} ph cm^{-2} s^{-1})	$1.48^{+0.10}_{-0.14}$	$22.35^{+1.02}_{-0.93}$	$6.15^{+0.45}_{-0.68}$	$2.54^{+0.32}_{-0.47}$	$4.41^{+0.41}_{-0.57}$	$2.82^{+0.26}_{-0.32}$	$2.72^{+0.15}_{-0.22}$	$2.55^{+0.21}_{-0.28}$
A_{Fe} ($A_{\odot}$)	$3.68^{+0.22}_{-0.28}$	$3.89^{+0.26}_{-0.35}$	$4.06^{+0.32}_{-0.22}$	$4.15^{+0.34}_{-0.38}$	$3.77^{+0.27}_{-0.38}$	$4.12^{+0.27}_{-0.37}$	$3.95^{+0.38}_{-0.42}$	$4.18^{+0.27}_{-0.39}$
$\log(\xi)$	$1.96^{+0.03}_{-0.02}$	$2.09^{+0.05}_{-0.04}$	$2.18^{+0.03}_{-0.02}$	$2.11^{+0.02}_{-0.02}$	$2.07^{+0.02}_{-0.03}$	$2.18^{+0.04}_{-0.03}$	$2.13^{+0.02}_{-0.03}$	$1.98^{+0.02}_{-0.02}$

$\theta_{\rm incl}$ (degree)	$13.8^{+2.7}_{-4.1}$	$11.8^{+4.1}_{-5.5}$	$16.2^{+2.8}_{-4.7}$	$14.3^{+4.4}_{-3.9}$	$10.3^{+4.9}_{-6.1}$	$13.2^{+2.5}_{4.7}$	$17.7^{+2.9}_{-5.2}$	$12.1^{+4.5}_{-5.8}$
$R_{\rm refl}$	$0.11^{+0.02}_{-0.02}$	$0.16^{+0.03}_{-0.04}$	$0.15^{+0.03}_{-0.02}$	$0.13^{+0.02}_{-0.02}$	$0.18^{+0.02}_{-0.03}$	$0.16^{+0.03}_{-0.02}$	$0.10^{+0.03}_{-0.02}$	$0.12^{+0.03}_{-0.02}$
q_2	$3.66^{+0.17}_{-0.41}$	$4.69^{+0.68}_{-0.35}$	$4.41^{+0.25}_{-0.37}$	$5.35^{+0.45}_{-0.29}$	$5.31^{+0.29}_{-0.41}$	$4.81^{+0.42}_{-0.63}$	$4.56^{+0.72}_{-0.89}$	$4.94^{+0.60}_{-0.76}$
$R_{\rm br}$ (R_g)	12^{+3}_{-2}	42^{+3}_{-2}	26^{+2}_{-3}	17^{+3}_{-1}	18^{+2}_{-3}	21^{+2}_{-3}	21^{+2}_{-1}	16^{+2}_{-3}
a^*	$0.15^{+0.02}_{-0.03}$	$0.16^{+0.03}_{-0.03}$	$0.15^{+0.03}_{-0.03}$	$0.17^{+0.02}_{-0.03}$	$0.21^{+0.04}_{-0.02}$	$0.15^{+0.03}_{-0.03}$	$0.16^{+0.02}_{-0.03}$	$0.20^{+0.02}_{-0.04}$
$R_{\rm in}$ (R_g)	$4.71^{+0.65}_{-0.88}$	$5.78^{+0.43}_{-0.77}$	$6.61^{+0.33}_{-0.37}$	$4.76^{+0.28}_{-0.48}$	$6.73^{+0.59}_{-0.73}$	$4.06^{+0.32}_{-0.62}$	$4.88^{+0.74}_{-0.91}$	$6.92^{+0.65}_{-0.85}$
$N_{\rm rel}$ (10^{-5} ph cm^{-2} s^{-1})	$0.62^{+0.08}_{-0.10}$	$7.11^{+0.42}_{-0.62}$	$0.49^{+0.06}_{-0.07}$	$1.18^{+0.03}_{-0.04}$	$1.87^{+0.14}_{-0.23}$	$0.67^{+0.07}_{-0.10}$	$1.10^{+0.12}_{-0.06}$	$0.56^{+0.04}_{-0.07}$
χ^2/dof	983/992	2845/2550	2275/2119	1648/1640	685/646	829/828	541/532	533/557

ξ's are in the unit ergs cm s^{-1}. † pegged at the lowest value.

Table 4.7: Luminosities of NGC 1566 in the observations analyzed here.

ID	Day	$L_{\rm nuc}$ (10^{42} erg s^{-1})	$L_{\rm soft}$ (10^{41} erg s^{-1})	$L_{0.1-100}$ (10^{42} erg s^{-1})	$L_{\rm bol}$ (10^{43} erg s^{-1})	$\lambda_{\rm Edd}$
X1	57331	0.34 ± 0.01	0.89 ± 0.06	0.43 ± 0.01	0.09 ± 0.01	0.003 ± 0.001
O1	58295	13.42 ± 0.08	4.89 ± 0.33	13.91 ± 0.08	7.11 ± 0.04	0.066 ± 0.001
O2	58395	4.02 ± 0.05	2.45 ± 0.14	4.26 ± 0.05	1.84 ± 0.03	0.017 ± 0.001
O3	58639	2.36 ± 0.01	1.16 ± 0.25	2.48 ± 0.03	1.19 ± 0.02	0.011 ± 0.001
O4	58703	4.01 ± 0.05	1.56 ± 0.22	4.17 ± 0.05	2.04 ± 0.03	0.019 ± 0.001
O5	58706	2.16 ± 0.06	1.64 ± 0.21	2.32 ± 0.06	1.33 ± 0.05	0.012 ± 0.001
O6	58713	1.96 ± 0.12	1.54 ± 0.29	2.11 ± 0.12	1.29 ± 0.07	0.012 ± 0.001
O7	58716	2.40 ± 0.03	1.59 ± 0.31	2.58 ± 0.04	1.31 ± 0.03	0.012 ± 0.001

$L_{\rm nuc}$ and $L_{\rm soft}$ are calculated for the primary power-law and soft excess components, respectively. Eddington ratio, $\lambda_{\rm Edd}$ is calculated using $L_{\rm bol}/L_{\rm Edd}$ for a BH of mass 8.3×10^6 $M_\odot$.

4.4.2 Corona Properties

The X-ray emitting corona is generally located very close to the central BH (Fabian et al., 2015). This corona is characterized by the photon index (Γ), temperature ($kT_{\rm e}$) and optical depth (τ) of the Comptonizing plasma. While using a simple power-law model gives us information only about the photon index, the `NTHCOMP` model can provide us with information on the electron temperature of the Compton cloud ($kT_{\rm e}$), while the optical depth (τ) is calculated from Equation 4.7. We found that the photon index varied within a narrow range of $\Gamma \sim 1.7-1.8$, and can be considered as constant within the uncertainties. To constrain the photon index with more accuracy, we fitted the source spectra from *NuSTAR* observations in $3-70$ keV and $10-70$ keV energy ranges to approximate only the power-law part. We found similar results as from the simultaneous fitting of the *XMM-Newton* and *NuSTAR* data in $0.5-70$ keV range. From the spectral analysis with Model–3, we estimated the Compton cloud radius to be $12-43$ $R_{\rm g}$.

We calculated the intrinsic luminosity ($L_{0.1-100}$) of the AGN from Model–1. The intrinsic luminosity was observed to be low during the pre-outburst observation, X1, with $L_{0.1-100} \sim (4.3\pm0.1)\times10^{41}$ erg s^{-1}. During O1, the source was observed to be maximum with $L_{0.1-100} \sim (1.39\pm0.01)\times10^{44}$ erg s^{-1}. Later, the intrinsic luminosity decreased and varied in the range of $2.1-4.3\times10^{43}$ erg s^{-1}. We also computed the luminosity for the primary emission ($L_{\rm nuc}$) and soft excess ($L_{\rm soft}$) from the individual components while analyzing the spectra with Model–1. We calculated the bolometric luminosity ($L_{\rm bol}$) using the 2–10 keV bolometric correction, $\kappa_{\rm bol,2-10\ keV} = 20$ (Vasudevan & Fabian, 2009). The Eddington ratio ($\lambda_{\rm Edd} = L_{\rm bol}/L_{\rm Edd}$), assuming a BH of mass of 8.3×10^6 $M_\odot$(Woo & Urry, 2002), was estimated to be $\lambda_{\rm Edd} \sim 0.003-0.066$ in different epoch which is consistent with other nearby Seyfert-1 galaxies (Wu

& Liu, 2004; Sikora et al., 2007; Koss et al., 2017).

In the pre-outburst observation in November 2015 (X1 : see Table 4.7), we obtained a bolometric luminosity of $L_{\rm bol} = (0.9 \pm 0.1) \times 10^{42}$ erg s^{-1}, with corona size $R_{\rm cor} = 12 \pm 3\ R_{\rm g}$ and hot electron plasma temperature $kT_{\rm e} = 102 \pm 5$ keV. In the observation during the outburst in June 2018 (O1), the luminosity of the AGN increased by a factor of about ∼25, compared to the November 2015 observation (X1). During this observation, the corona was large ($R_{\rm cor} = 43 \pm 3\ R_{\rm g}$) with hot electron plasma temperature $kT_{\rm e} = 61 \pm 7$ keV and the observed spectrum was harder. As the outburst progressed, the bolometric luminosity and the corona size decreased. As $R_{\rm cor}$ decreased, the electron plasma temperature increased. Overall, $kT_{\rm e}$ varied in a range of $\sim 61 - 106$ keV during the observations. In general, the plasma temperature is observed in a wide range, with a median at $kT_{\rm e} \sim 105 \pm 18$ keV (Ricci et al., 2018). Thus, the plasma temperature is consistent with other AGNs. During these observations, the optical depth of the Compton cloud varied within $\sim 1.2 - 1.7$. Interestingly, the photon index (Γ) was almost constant, although some of the properties of the corona evolved with time. This appears to imply that both the optical depth and the hot electron temperature changed in such a way that the spectral shape remained the same.

We found several correlations and anti-correlations between the spectral parameters and show them in Figure 4.9. We fitted the data points with linear regression method using $y = mx + c$. The fitted value of the slope (m) and intercept (c) are mentioned in each panel of Figure 4.9. We found that the nuclear luminosity ($L_{\rm nuc}$) and the soft excess luminosity ($L_{\rm soft}$) are strongly correlated with the Eddington ratio with the Pearson correlation indices of 0.84 and 0.85, respectively. We also found that the bolometric luminosity ($L_{\rm bol}$) and the Compton cloud temperature ($kT_{\rm e}$) are anti-correlated ($\rho_{\rm s} = -0.85$). The electron temperature is found to be anti-correlated with the Eddington ratio ($\rho_{\rm s} = -0.85$), while the size of the Compton corona and the luminosity are positively correlated ($\rho_{\rm s} = 0.93$). We also observed that the electron temperature is anti-correlated with the size of the Compton cloud ($\rho_{\rm s} = -0.84$). The above correlations can be explained thinking that, as the accretion rate increased, the energy radiation increased, thereby, increasing the luminosity. An increase in the mass accretion rate makes the cooling more efficient, leading to a decrease in the electron temperature of the Comptonizing region (Haardt & Maraschi, 1991; Done et al., 2007).

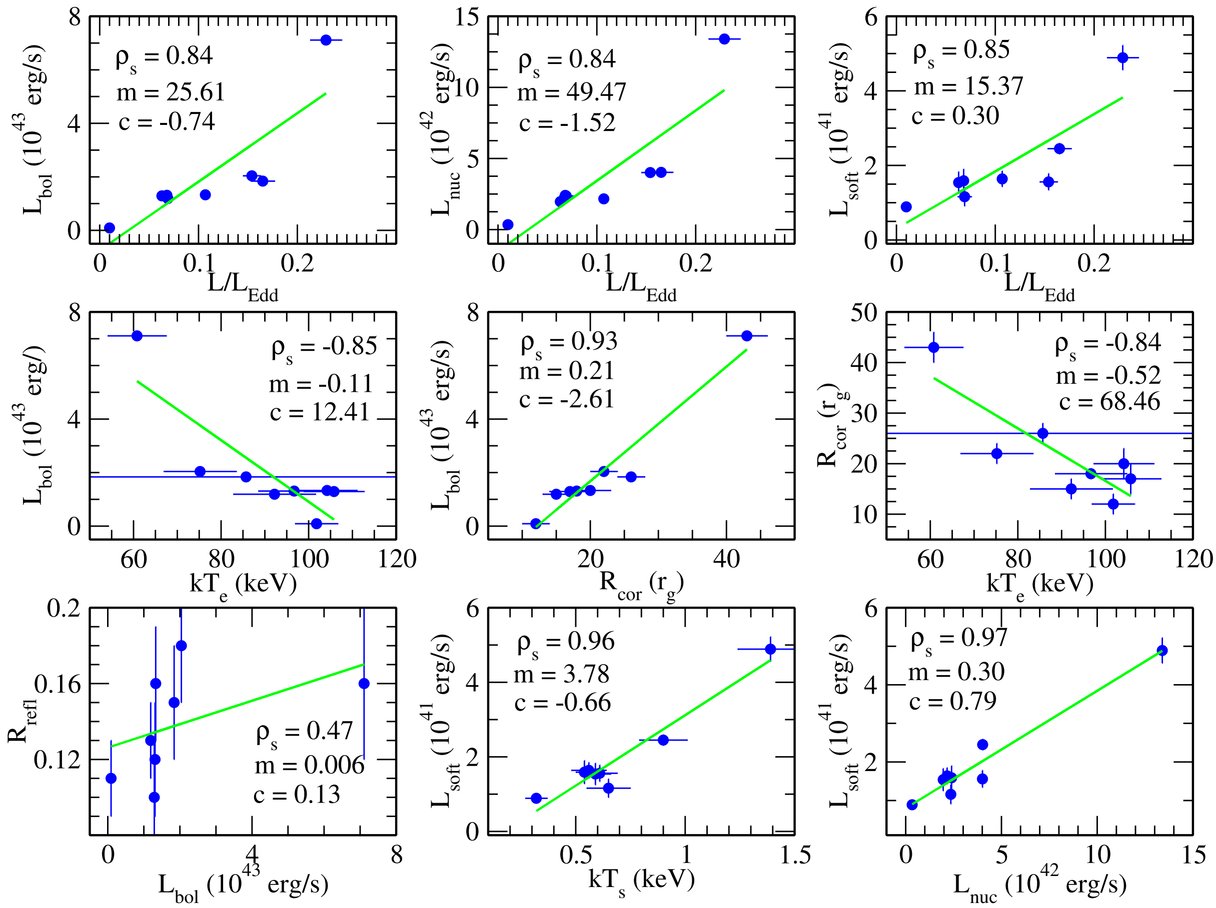

Figure 4.9: Correlation between different spectral parameters. In each panel, the corresponding Pearson correlation co-efficient (ρ_s) is quoted. The solid green line in each panel represent the linear fit, y=mx+c. Corresponding fitted values of the slope (m) and intercept (c) are also mentioned in each panels.

4.4.3 Reflection

The hard X-ray photons from the corona are reflected from cold material in the accretion disc, BLR and torus, producing a reflection hump and a Fe-K emission line (George & Fabian, 1991; Matt et al., 1991). When fitted with a simple power-law model, NGC 1566 showed the presence of Fe Kα emission line along with a weak reflection hump at $\sim 15-40$ keV energy range (see Figure 4.6). Thus, we fitted the spectra with the relativistic reflection model `RELXILL` to probe the reflection component.

Parker et al. (2019) analyzed O1 observation with `RELXILL` and `XILLVER` models in their spectral analysis. They found $\xi = 10^{2.4\pm0.1}$ erg cm^{-2} s^{-1}, $A_{\rm Fe} = 3 \pm 0.2 A_\odot$ and $R_{\rm refl} = 0.091 \pm 0.005$. In the present work, we obtained $\xi = 10^{2.09\pm0.05}$ erg cm^{-2} s^{-1}, $A_{\rm Fe} = 3.89 \pm 0.35$, and $R_{\rm refl} = 0.16 \pm 0.04$ for O1. The marginal difference between our results and those of Parker et al., 2019 could be ascribed to the different spectral models used. We observed fairly constant ionization ($\xi \sim 10^{1.9-2.2}$ erg cm s^{-1}) and iron abundances ($A_{\rm Fe} \sim 4-5\ A_\odot$) across the observations. This is expected within our short period of observation. In all the spectra, we found a very weak reflection with reflection fraction, $R_{\rm refl} < 0.2$. We found a weak correlation between the reflection fraction ($R_{\rm refl}$) and the luminosity with the Pearson correlation coefficient of 0.47. In general, reflection becomes strong with increase in the luminosity (Zdziarski et al., 1999). The low inclination angle of the source also results in a weak reflection (Ricci et al., 2011; Chatterjee et al., 2018). Therefore, the observed weak correlation between the reflection fraction and luminosity in NGC 1566 could be due to the low inclination angle of the source.

During the observations, a strong Fe Kα emission line with equivalent width $EW > 100$ eV was detected, despite a weak reflection component, except for O5. This could be explained by high iron abundances in the reflector. From the spectral analysis with model–4, we found the inner edge of the disc extends up to $\sim 5\ R_{\rm g}$. If iron originates from the inner disc, a broad iron line is expected. However, we did not observe a broad iron line. Either the broad line was absent or it was blurred beyond detection. However, during our observation, a narrow iron line was detected, which given its width, originates in the material further out than the accretion disc. Hence, from the full-width at half maximum (FWHM) of the line, we tried to constraint the Fe Kα line emitting region. During our observation period, the FWHM of Fe Kα line emission was found to be < 8700 km s^{-1}, which corresponds to the region $> 1200\ R_{\rm g}$ from the BH. This corresponds to the distance at which we expect to find the BLR (Kaspi et al., 2000). Thus, the BLR is the most probable Fe Kα line emitting region in NGC 1566.

4.4.4 Soft Excess

The origin of the soft excess in AGNs is still debated. Several models have been proposed to explain it. Relativistic blurred ionized reflection from the accretion disc has been put forward as a likely explanation for the soft excess in many sources (Fabian et al., 2002; Ross & Fabian, 2005; Walton et al., 2013; García et al., 2019; Ghosh & Laha, 2020). An alternative scenario considers Comptonization by a optically thick, cold corona (Done et al., 2012). In this model, the Comptonizing region is located above the inner accretion disc as a thin layer. Heating of circumnuclear region by bulk motion Comptonization in AGN with high Eddington ratio is also considered to be the reason for the soft excess (Kaufman et al., 2017). Recently, Nandi et al. (2021) argued from long-term observations and Monte-Carlo simulations (see Chatterjee et al. (2018) and references therein) that the thermal Comptonization of photons which have suffered fewer scatterings could explain the origin of soft excess in Ark 120.

In our analysis, we used a `bbody` component to take into account the soft excess. The blackbody temperature ($kT_{\rm bb}$) was roughly constant with $kT_{\rm bb} \sim 110$ eV during our observations. This is consistent with the observation of other nearby AGNs (Gierliński & Done, 2004; Winter et al., 2009; Ricci et al., 2017; García et al., 2019). A good-fit with the `OPTXAGNF` model favoured soft Comptonization by an optically thick corona as the origin of the soft excess. During observation O1, the temperature of the optically-thick corona was observed to be ~ 1.4 keV. Later, the optically thick corona cooled with decreasing luminosity.

We tried to estimate delay and correlation between the soft excess and X-ray continuum light curves (see Section 4.3.1). In the `OPTXAGNF` scenario, the total power depends on the mass accretion rate and is divided between the soft-Comptonization (soft-excess) and hard-Comptonization (nuclear or primary emission). We found a strong correlation between the soft excess luminosity ($L_{\rm soft}$) and nuclear luminosity ($L_{\rm nuc}$). The soft-excess luminosity and the Eddington ratio ($L/L_{\rm Edd}$) were found to be correlated ($\rho_{\rm s} = 0.78$). This indicated that the soft excess strongly depended on the accretion rate, supporting the soft-Comptonization as the origin of the soft excess. We also found a delay of ~ 10 minutes between the soft excess and primary emission, indicating the origin of the soft excess was beyond the corona, possibly the accretion disc. Higher variability was also observed in the soft excess (see Section 4.3.1) during observations X1, O1, and O3. This could indicate a higher stochasticity in the origin of the soft-excess. It should be noted that, theoretically, infinite scattering produces blackbody which has the lowest variability. As Nandi et al. (2021) suggested, fewer scattering which could generate higher variability than the large number of scatterings, possibly lead to the origin of soft-excess. Overall, the soft excess in NGC 1566 has a complex origin, including reflection from the accretion disc and soft-Comptonization.

4.4.5 Changing-Look Event and its Evolution

The physical drivers of CL events are still highly debated, and could change from source to source. Tidal disruption events (TDEs), changes in obscuration, and variations in the mass accretion rate could all be possible explanations for the CL events.

In the pre-outburst observation, X1, the absorber was not strongly ionized ($\xi_1 < 0.001$), and had a column density of $N_{\rm H,1} = (3.53 \pm 0.06) \times 10^{21}$ cm^{-2}. Two ionizing absorbers were detected during the observations O1, O2, and O3 which could be associated with an outflow. Parker et al., 2019 also observed two ionized absorbers during O1, and suggested that they could be associated with an outflow. The highest ionization (for both absorbers) was observed in O1, which corresponded to the epoch in which the observed luminosity was the highest. During the 2018 outburst, when the X-ray intensity increased, the emitted radiation may have caused the sublimation of the dust along the line of sight, thereby decreasing the hydrogen column density (Parker et al., 2019). As the X-ray intensity decreased after the main outburst, the dust could have condensed, leading to an increase in the column density. Eventually, during the August 2019 observations, the dust formation was stable as the hydrogen column density was approximately constant ($N_{\rm H} \sim 1.3 \times 10^{21}$ cm^{-2}). Generally, the dust clouds can recover in the timescale of several years (Kishimoto et al., 2013; Oknyansky et al., 2017). In this case, we observed that the dust clouds already recovered with an increase in $N_{\rm H}$ from $\sim 6 \times 10^{20}$ cm^{-2} to 1.3×10^{21} cm^{-2} in $\sim$14 months time. If this is correct, we would expect the $N_{\rm H}$ to reach at its pre-outburst value of $N_{\rm H} \sim 3.5 \times 10^{21}$ cm^{-2} in next few months.

The strong correlation between the accretion rate and the bolometric luminosity suggests that the accretion rate is responsible for the CL events in NGC 1566 during the 2018 outburst. Parker et al. (2019) also discussed several possibilities for the CL event in NGC 1566 and concluded that the disc-instability is the most likely reason for the outburst. The instability at the outer disc could propagate through the disc and cause the outburst. Noda & Done (2018) explained the flux drop and changing-look phenomena in Mrk 1018 with the disc-instability model where the time-scale for the changing-look event was $\sim$ 8 years. The time-scale for changing-look event for NGC 1566 was $\sim$ 10 months as the flux started to increase from September 2017 (Dai et al., 2018; Cutri et al., 2018). The time-scales are similar if we consider the mass of the BH. As the mass of Mrk 1018 is $M_{1018} \sim 10^{7.84}$ $M_\odot$ (Ezhikode et al., 2017), the expected time-scale for NGC 1566 is $\sim$ 8 years/10 $\sim$ 10 months. The observed 'q'-shape in the HID during the main outburst (F1), also suggests of disc instability as seen in the case of the outbursting black holes. The 'q'-shaped HID is very common for the outbursting black holes (Remillard & McClintock, 2006) where disc instability is believed to lead the outburst. Noda & Done, 2018 also suggested that the soft-excess would decrease much more compared to the hard X-ray with decreasing $L/L_{\rm Edd}$. NGC 1566 also showed the strongest soft-excess emission during the highest $L/L_{\rm Edd}$ (O1), while the soft-excess emission dropped as $L/L_{\rm Edd}$ decreased. In the pre-outburst quiescent state, no soft-excess was observed in NGC 1566. As the soft-excess can produce most of the ionizing photons necessary to create broad optical lines (Noda & Done, 2018), the broad line appeared during O1 (when the soft-excess was strong), leading to the changing-look event.

A TDE might be another possible explanation for the 2018 outburst of NGC 1566. A TDE could supply the accreting matter to the central SMBH, which would lead to an increase in luminosity. Several recurrent outbursts (F2, F3 & F4) and nearly periodic X-ray variations were observed after the main outburst (F1) as seen in the upper panel of Figure 4.1 and Figure4.10. In TDEs, some amount of matter could be left out and cause recurrent outbursts (Komossa, 2017). In the case of a classic TDE, after a star is tidally disrupted by the SMBH, a decay profile of the luminosity with $t^{-5/3}$ is expected (Rees, 1988; Komossa, 2015, 2017), which is not observed in this case. During all observations, the source showed a relatively hard spectrum with $\Gamma \sim 1.6 - 1.7$. This is in clear contrast with the classic TDEs which typically show much softer spectra ($\Gamma \geq 3$) (Komossa, 2017). During the June 2018 outburst (F1), the X-ray luminosity changed by $\sim$ 25 times compared to the low state which is low in comparison to other candidate TDEs. For example, 1ES 1927+654 and RX J1242-1119 showed a change in luminosity by over 4 orders of magnitude (Ricci et al., 2020) and 1500 times (Komossa et al., 2004), respectively. In general, no iron emission line was observed in the X-ray band during the TDE (Saxton et al., 2020), whereas in the case of NGC 1566, a strong Fe Kα line was observed. Considering all these, we deem unlikely that the June 2018 outburst of NGC 1566 was triggered by a TDE.

An alternative explanation could be that a star is tidally disrupted by a merging SMBH binary at the center of NGC 1566. According to Hayasaki & Loeb (2016), after the stellar tidal disruption, the debris chaotically move in the binary potential and are well-stretched. The debris orbital energy is then dissipated by the shock due to the self-crossing, leading to the formation of an accretion disc around each black hole after several mass exchanges

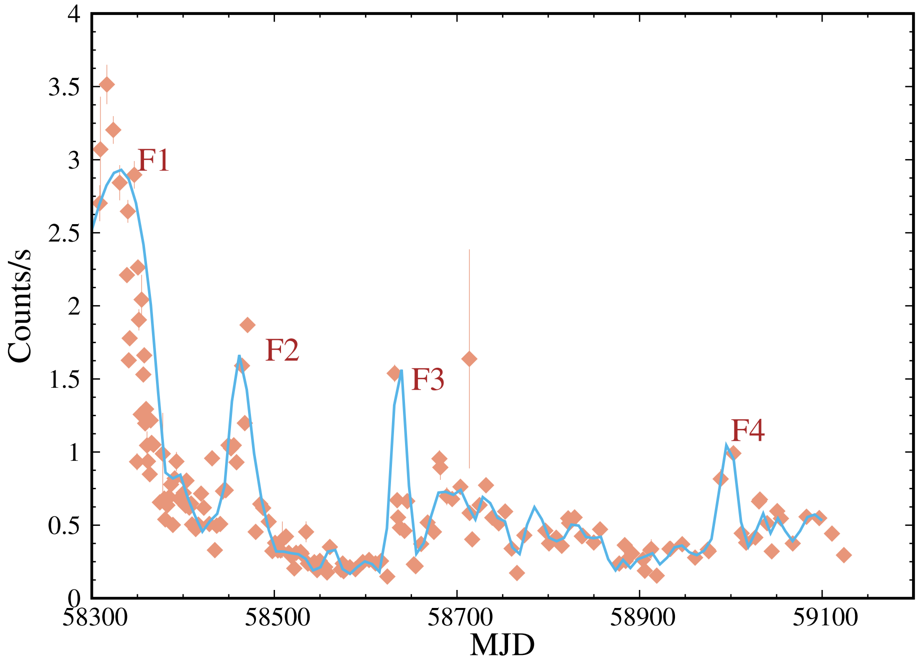

Figure 4.10: Light curve of NGC 1566 between June 2018 and August 2020 with smooth lines showing near-periodic variation of count rate.

through the Lagrange (L1) point of the binary system. If the orbital period of an unequal-mass binary is short enough ($<$ 1000 days) to lose the orbital energy through gravitational wave (GW) emission, the secondary, less massive SMBH orbits around the center of mass at highly relativistic speed, while the primary SMBH hardly moves. Therefore, the electromagnetic emission from the accretion disc around the secondary black hole would be enhanced periodically by relativistic Doppler boosting. This scenario could explain the recurrent outburst observed in case of NGC 1566 (see Figure 4.10). From this figure, the orbital period is estimated to be $P_{\rm orb} \sim 160$ days (between F1 & F2). Taking into account the SMBH mass ($M_{\rm BH} = 8.3 \times 10^6$ $M_\odot$), we obtain $a \sim 710$ $r_{\rm s} \approx 5.6 \times 10^{-4}$ pc as a binary semi-major axis, where $r_{\rm s} = 2GM_{\rm BH}/c^2$ is the Schwarzschild radius. The merging timescale of two SMBH with mass ratio q due to GW emission is given by (Peters, 1964),

$$t_{\rm gw} = \frac{5}{8}\frac{(1-q)^2}{q}\frac{r_s}{c}\left(\frac{a}{r_s}\right) \sim 5.0 \times 10^6 yr. \tag{4.8}$$

This suggests that more than 100 TDEs could occur before the SMBH merger, considering the TDE rate for a single SMBH (10^{-4} to 10^{-5} yr^{-1} per galaxy Stone et al., 2020). However, the event rate can be enhanced up to 0.1 yr^{-1} per galaxy due to chaotic orbital evolution and Kozai-Lidov effect in the case of SMBH binaries (Chen et al., 2009; Li et al., 2015). Moreover, if the stars are supplied by accretion from a circumbinary disc (eg, Hayasaki et al., 2007; Amaro-Seoane et al., 2013), then the TDE rate could be higher up to ~ 0.2 yr^{-1} if the mass supply rate is at the Eddington limit (Wolf et al., 2021). Therefore, the detection of similar, periodic burst events in the next few years to tens of years would support this interpretation.

4.5 Summary

We analyzed the X-ray emission of the changing-look AGN NGC 1566 between 2015 and 2019. Our key findings are the following.

1. NGC 1566 showed a giant outburst in June 2018 when the X-ray luminosity increased by $\sim 25 - 30$ times compared to that during the low state. After the main outburst, several recurrent outbursts were also observed.

2. NGC 1566 hosts a low-spinning BH with the spin parameter, $a^* \sim 0.2$.

3. The inclination angle is estimated to be in the range of $i \sim 10°$–$21°$.

4. The variation of the accretion rate is responsible for the evolution of the Compton corona and X-ray luminosity.

5. A rise in the accretion rate is responsible for the change of luminosity. The HID or 'q'-diagram links the CL event of NGC 1566 with the outbursting black holes.

6. A strong soft excess was observed when the luminosity of NGC 1566 was high. The origin of the soft excess is observed to be complex.

7. We rule out the possibility that the event was triggered by a classical TDE, where a star is tidally disrupted by the SMBH.

8. We propose a possible scenario where the central core is a merging binary SMBH. This scenario could explain the recurrent outburst.

Chapter 5

Investigation of a small flare in NLS1 galaxy NGC 4051

As mentioned earlier, Active Galactic Nuclei (AGNs) are the accreting supermassive black holes (SMBH) of mass $> 10^5$ $M_\odot$ located at the centre of almost every galaxy. These are considered to be the powerful sources (luminosity up to 10^{48} erg s^{-1}) in the Universe that emit in the entire range of the electromagnetic spectrum. The ultraviolet/optical photons originating from a thermal accretion disk are inverse Comptonized in the hot corona of relativistic electrons near the black hole and produce X-ray continuum emission (Haardt & Maraschi, 1993), that can be approximated by a power-law with an exponential cut-off. However, the origin of the compact corona and its nature, structure and location are still unknown. Recent studies put forward the hint of the connection between the corona and the jet (Zhu et al., 2020). It is hypothesized that in Seyfert galaxies (or radio-quiet AGNs), the corona may be powered by the magnetic flux tubes associated with the accretion disk near the black hole. These flux tubes get inflated due to the differential rotation of the black hole and the accretion disk, and strong confinement from the surrounding medium quenches the launching of jets. As a result, the plasma gets heated up and produces X-ray emission (Yuan et al., 2019). The X-ray emission shows high variability in the timing and spectral properties on short as well as long timescales. The rapid and small variability, where the count rate in different energy ranges changes by a factor of two or three, is frequently observed in the AGNs and primarily attributed to the change in the coronal topology. In this chapter, we have studied a small-scale X-ray flare through detailed timing and spectral studies. Section 5.1 presents the previous studies on NGC 4051, whereas Section 5.2 describes the observations of NGC 4051 with *XMM-Newton* and *NuSTAR* observatories and corresponding data reduction processes. The results from the time-resolved spectral analysis and timing analysis are discussed in Section 5.3. The implications of the results are discussed in Section 5.4. In the end, the conclusions are summarized in Section 5.5.

5.1 Introduction

Narrow-Line Seyfert galaxies (NLS1s) are the subcategory of AGNs and believed to be accreting mass at a higher rate or close to the Eddington limit (Komossa et al., 2006). In the X-ray band, the NLS1s show a steep X-ray spectral slope ($\Gamma \sim 1.6 - 2.5$; Vaughan et al. 1999). It is proposed that when the accretion rate is high, more soft photons are produced causing the corona to cool down rapidly, producing brighter and softer spectra (Shemmer et al., 2008). The NLS1s are known to show strong reprocessed emission, soft excess below 2 keV and signatures of ionized or neutral absorbers (Fabian et al., 2002; Wang et al., 1996) in their spectra. Moreover, strong outflows associated with high mass accretion rate, have been observed in these objects (Laha et al., 2021). The NLS1s are well known to show strong soft X-ray excess below 2 keV though the origin of this feature is still debatable. There are different models to explain the origin of this component, e.g., warm Comptonization in a relatively cool and optically thick plasma (Done et al., 2012; Kubota & Done, 2018) and relativistic blurred reflection from the inner disk (Fabian et al., 2004). It has also been suggested that fewer scatterings in the corona which can generate higher variability than a large number of scatterings, may possibly lead to the origin of soft-excess (Nandi et al., 2021).

NGC 4051, a nearby (z=0.00234) galaxy, is one of the brightest NLS1 galaxies with mass $\sim 1.7 \times 10^6$ $M_\odot$ (Denney et al., 2009). This is a low-luminosity ($\sim 10^{41}$ erg s^{-1}) NLS1 galaxy which shows rapid flux and spectral variability (Guainazzi et al., 1996) on different timescales and a number of emission/absorption features in the spectrum. The X-ray spectral and timing variabilities of this AGN have been studied copiously in the past. Using 1000 days of data from 1996 to 1999, Lamer et al. (2003) reported a very hard spectrum during its low state. There was an underlying reflection emission likely from the molecular torus in all the flux states. They found an anti-correlation between the X-ray flux and spectral hardness. Similar results have been reported by Pounds et al. (2004), where the reflection of hard X-rays from the cold matter was found along with a non-variable and narrow Iron Kα fluorescent line. The difference between the low and high flux spectral states was interpreted in terms of varying properties of the outflowing gas. Ponti et al. (2006) studied the time-resolved spectra using *XMM-Newton* observation and calculated the slope-flux correlation in the low and high flux states. Mizumoto & Ebisawa (2016) found the presence of different kinds of warm absorbers (WAs) in the X-ray spectrum and their variability. In 2018, Seifina et al. (2018) reported correlation between the X-ray spectral photon-index and the mass accretion rate using the *XMM-Newton*, *Suzaku* and *RXTE* observations. This provided an estimate of the lower limit of the black hole mass in NGC 4051 as 6×10^5 $M_\odot$. In the present work, we report the results from X-ray timing and spectral analysis of simultaneous *XMM-Newton* and *NuSTAR* observations of NGC 4051 in November 2018. We investigated the spectral variability at three time intervals of the observations to examine the changes in the X-ray emitting corona with flux variability.

5.2 Observations and Data reduction

NGC 4051 was observed with *NuSTAR* (Harrison et al., 2013) and *XMM-Newton* (Jansen et al., 2001) multiple times in the last two decades. Most recently, it was observed with *NuSTAR* in November 2018 simultaneously with *XMM-Newton*. The observation details are given in Table 5.1. Two observation IDs of *XMM-Newton* that are used in this work, were studied by Wu et al. (2020). They have studied the "softer when brighter" nature of this source by utilizing data in the energy range of 2-10 keV. They found that the "softer when brighter" empirical relation weakens with decreasing timescale and concluded that the power law shape of the spectrum is not dependent only on source brightness.

XMM-Newton

In this work, we used the European Photon Imaging Camera (EPIC)-pn (Strüder et al., 2001) small window mode data due to its higher sensitivity. We reprocessed the EPIC-pn data using standard System Analysis Software (SAS v.19.1.0; Gabriel et al., 2004) and updated calibration files. To check the presence of any flaring particle background, we generated a light curve above 10 keV. We created good time interval (GTI) files by excluding the time intervals containing particle background, which were capped by count rate. We used <0.15 and <0.2 count s^{-1} for 0830430801 and 0830430201 Obs. IDs, respectively. This resulted in corresponding net exposures of ~ 73.8 and ~ 68.8 ks. We considered events with `PATTERN`$\leq$4 for EPIC-pn. We also checked for the photon pile-up effect using the `epatplot` task. We extracted source and background spectra by selecting circular regions of 30 arcsec

Table 5.1: Log of November 2018 simultaneous observations of NGC 4051 with *NuSTAR* and *XMM-Newton*. The quoted count rate for *NuSTAR* observation is the average count rate over entire observation.

UT Date (start)	UT Date (end)	Observation ID.	Exposure (ks)	Counts s^{-1}
XMM-Newton Observation				
2018-11-07 09:59:39	2018-11-08 10:26:15	0830430201	83.2	13.84
2018-11-09 09:48:58	2018-11-10 09:02:59	0830430801	85.5	8.59
NuSTAR Observation				
2018-11-04 12:56:09	2018-11-11 14:46:09	60401009002	311.1	0.45

radii for both the observations. We generated light curves in different energy bands using the `xselect` task of `FTOOLS`. The redistribution matrix and ancillary response files were generated by `arfgen` and `rmfgen` tasks, respectively. We grouped the spectral data sets to a minimum of 30 counts per bin using the `grppha` task.

NuSTAR

NuSTAR consists of two hard X-ray focusing telescopes called Focal Plane Modules FPMA and FPMB. The level 1 data files from both the modules were reprocessed with the *NuSTAR* Data Analysis Software (NuSTARDAS v2.0.0) package incorporated in the latest `heasoft` package (v6.28). The level 2 cleaned and calibrated data products were produced using `nupipeline` task with the latest calibration files (CALDB)[1]. We considered circular regions of 80 arcsec radii to extract source and background spectra from the event files. The source region was centered at the coordinates of the optical counterpart and the background region was selected away from the source. The `nuproducts` task was used to generate the spectra and light curves. We generated time-resolved spectra (pre-flare, flare and post-flare) by using the `nuproduct` task. We also generated spectra for the rising and decay phases of the flare separately. The spectra are binned with 30 counts per bin. We used the spectral range up to 50 keV where the count rate was significantly higher than the background.

In Figure 5.1, the light curves of NGC 4051 from the *NuSTAR* and *XMM-Newton* observations are shown. The *NuSTAR* light curve showed the occurrence of a small flare at around 3×10^5 s from the beginning of the observation that lasted for ~ 120 ks (duration between two vertical lines in Figure 5.1). During this flare, the peak count rate was ∼2.5 times the average count rate observed before and after the flare. This flaring event was probably also

[1]`http://heasarc.gsfc.nasa.gov/FTP/caldb/data/nustar/fpm/`

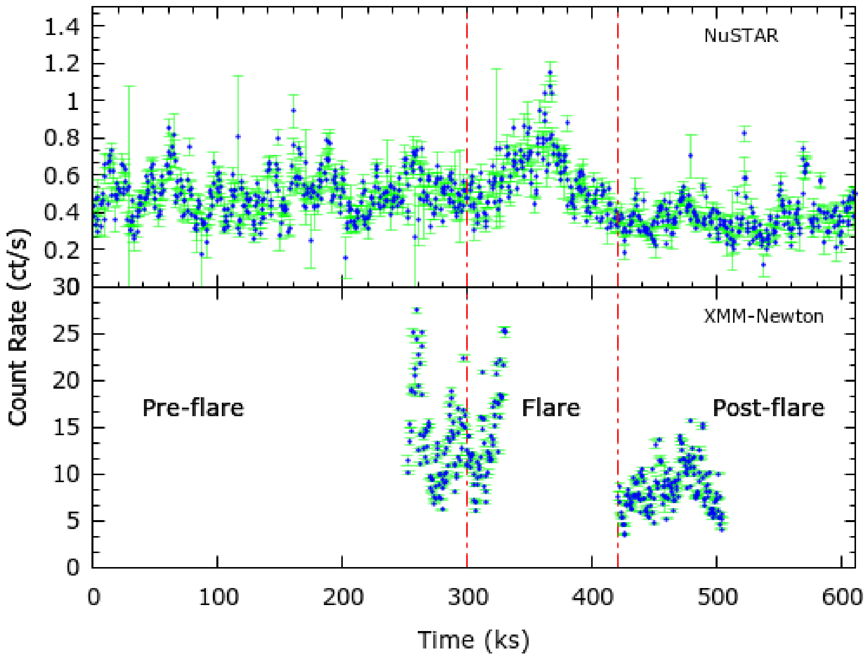

Figure 5.1: The X-ray light curves of NGC 4051 in $3-50$ keV and $0.3-10$ keV ranges, obtained from the November 2018 *NuSTAR* (upper panel) and *XMM-Newton* (bottom panel) observations, respectively, are shown for 500 s time bin. In the *NuSTAR* light curve, a flare of ∼120 ks duration with peak count rate reaching by a factor of ∼2.5 compared to the quiescent duration is detected. The red dotted lines divide the light curves (observations) into three time segments: pre-flare, flare and post-flare segments.

present in the *XMM-Newton* light curve, though the lack of observation coverage during the flare did not make it evident. However, to avoid the ambiguity, we tried to correlate 3-10 keV count rate for overlapping pre-flare phase from the *XMM-Newton* and *NuSTAR* observations (see Figure 5.2) and found Pearson's correlation coefficient to be ∼0.82 with p-value <0.01.

5.3 Data Analysis and Results

5.3.1 Timing analysis

Fractional variability

In the beginning, we attempted to investigate the timing variability of NGC 4051 using *XMM-Newton* and *NuSTAR* observations. To check the temporal variability, we calculated the fractional variability ($F_{\rm var}$; Nandra et al. (1997), Vaughan et al. (2003)) in different energy bands using the equation,

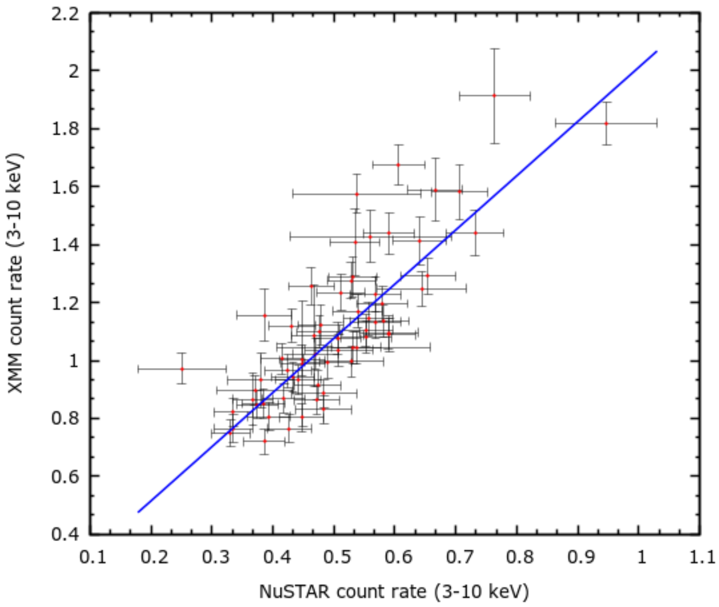

Figure 5.2: The count rates in 3-10 keV range are shown for the overlapping pre-flare phase of the *XMM-Newton* and *NuSTAR* observations.

$$F_{\rm var} = \sqrt{\frac{S^2 - \overline{\sigma_{\rm err}^2}}{\bar{x}^2}}$$

and uncertainty in $F_{\rm var}$ as,

$$\sqrt{\left(\sqrt{\frac{1}{2N}}\frac{\overline{\sigma_{\rm err}^2}}{\bar{x}^2 F_{\rm var}}\right)^2 + \left(\sqrt{\frac{\overline{\sigma_{\rm err}^2}}{N}}\frac{1}{\bar{x}}\right)^2}$$

where, $\bar{x}$, S, $\overline{\sigma}_{\rm err}$, and N are the mean, total variance, mean error and number of data points, respectively. We generated the variability spectrum, i.e. $F_{\rm var}$ as a function of energy (see Figure 5.3) using background subtracted EPIC-pn (obs. ID 0830430201) light curves in increasing energy binning. The Pearson's correlation coefficient was calculated to be -0.95 with the null hypothesis probability of $\sim 10^{-9}$. The spectrum shows that the low energy components, e.g., soft X-ray excess or/and ionized absorbers are more variable than the high energy ones.

To have an initial guess of the spectral variability during the observation, we plotted variation of the hardness ratio (HR), i.e. the ratio between the hard X-ray and soft X-ray light curves, with respect to time. For *NuSTAR* observation, we computed HR by taking the ratio between the light curves in the $10-50$ keV and $3-10$ keV energy ranges, whereas for *XMM-Newton* observation, we estimated HR by taking the ratio between the $2-10$ keV and $0.3-2$ keV light curves. From Figure 5.4, we observed a considerable spectral variability in

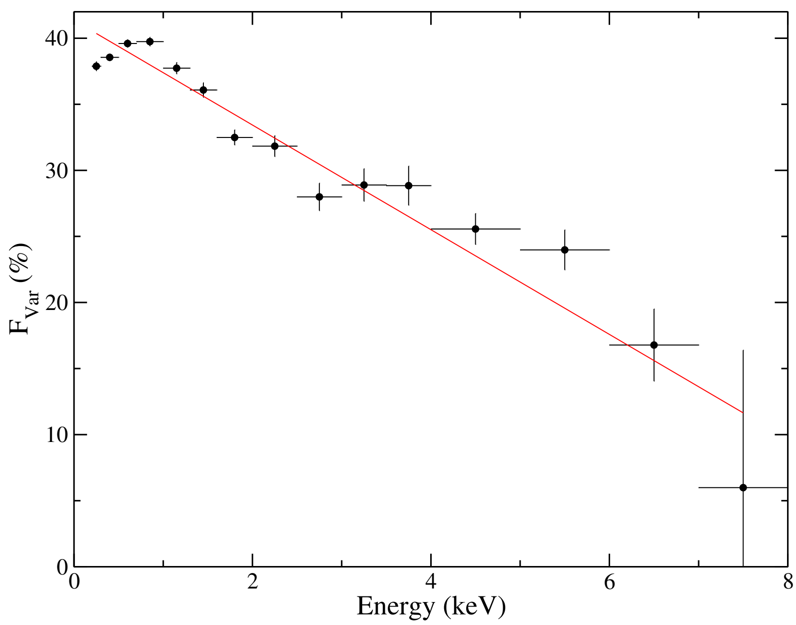

Figure 5.3: The fractional variability spectrum is shown for the EPIC-pn data from the *XMM-Newton* observation (Obs. ID 083043201) of NGC 4051. The red line represents the linear fit to the observed data points.

the soft X-rays. The spectrum became soft at the beginning of the flare. Careful examination reveals that there is 'softer when brighter' trend, which is corroborated by the hardness-intensity diagram (HR vs total count rate) in Figure 5.5. On the other hand, the variability seen in the *NuSTAR* spectrum is comparatively less. The *NuSTAR* HR is more or less constant except softening marginally during the flaring phase (upper panel of Figure 5.4 and left panel of Figure 5.5).

Correlation

For correlation analysis in the X-ray band ($3.0-50.0$ keV), we divided the entire *NuSTAR* observation of NGC 4051 into the pre-flare (MJD 18429.4 to MJD 18430.0), flare (MJD 18430 to MJD 18431.6) and post-flare (MJD 18431.6 to MJD 18432.4) segments that are marked with vertical lines in Figure 5.1. For each segment, we segregated the X-ray light curve into soft X-ray (3.0 to 10.0 keV) and hard X-ray (10.0 to 50.0 keV) bands. Corresponding light curves with time resolutions of 50 s are shown in the top panels of Figure 5.6. During the entire duration of the observation, the source count rate in the hard X-ray band was always less than that of the soft X-ray band. At the peak of the flaring event, the source count rate in both the bands increased by a factor of 2-3 compared to the average count rate during the pre- and post-flare segments. We performed cross-correlation analysis using `crosscor`[2] and

[2]`https://heasarc.gsfc.nasa.gov/xanadu/xronos/help/crosscor.html`

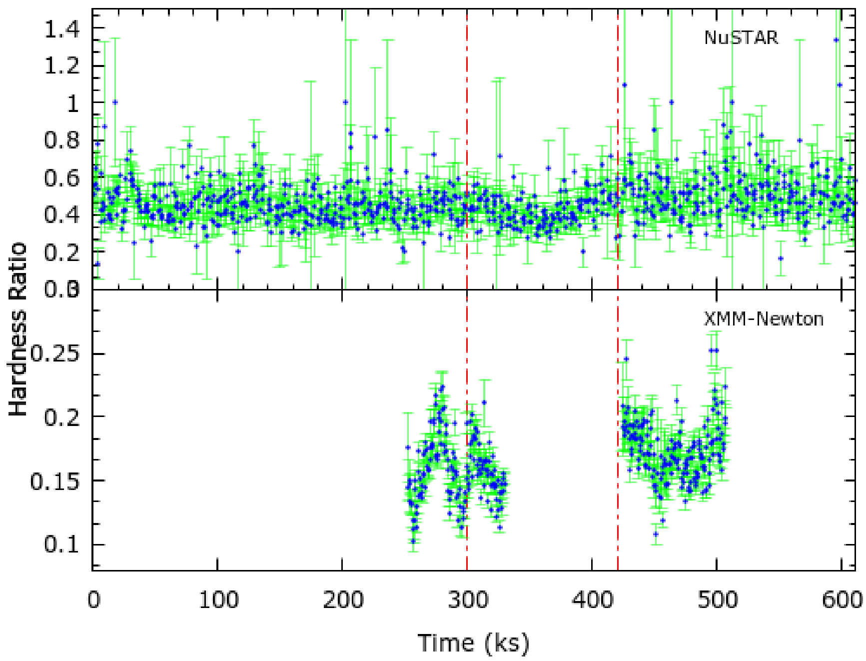

Figure 5.4: The hardness ratios are shown for *NuSTAR* (upper panel) and *XMM-Newton* (bottom panel) observations of NGC 4051. The hardness ratios are obtained by taking ratio between the light curves in 10-50 keV and 3-10 keV bands (for *NuSTAR*), and 2-10 keV and 0.3-2 keV bands (for *XMM-Newton*).

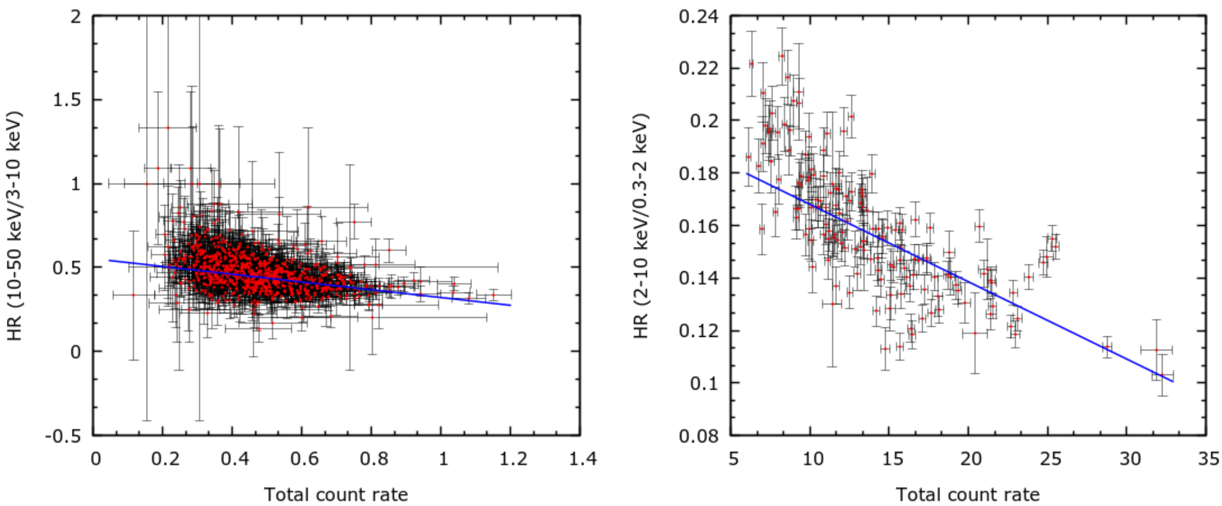

Figure 5.5: Hardness-Intensity diagrams of NGC 4051 are shown from the *NuSTAR* (left panel) and *XMM-Newton* (right panel) observations. Corresponding correlation coefficients are -0.42 and -0.73, respectively.

ζ-discrete cross-correlation function (`ZDCF`[3]; Alexander, 1997) for comparison of light curves in two different bands. For the error estimation, we considered 12000 simulation points in the `ZDCF` code for the light curves. The soft and hard band light curves during the pre- and post-flare segments yielded an acceptable $\chi^2_{\rm red} < 1.5$ when fitted with a straight line. However, the data during the flare yielded poor statistics with high residuals when fitted with a linear function. We carried out delay estimation through the discrete correlation function using *NuSTAR* data during three segments separately.

The discrete correlation function analysis, performed on the light curves from three different segments, generated three different patterns as shown in the bottom panels of Figure 5.6. In the pre-flare and post-flare phases, the soft and hard X-ray bands are found to be very poorly correlated. The values of correlation function for pre-flare and post-flare segments were found to be <0.1 (left bottom panel of Figure 5.6) and <0.2 (right bottom panel of Figure 5.6), respectively, for the time delay range of -10 to $+10$ kilo-second (ks). However, the flaring event data showed a moderately strong correlation between the soft and hard bands in both the algorithms. From the ZDCF, we found the peak of the correlation function at 0.0 ± 0.05 ks with correlation coefficient of 0.48 ± 0.02 ks and for the CCF, calculated through `crosscor`, the peak appears at 0.0 ± 0.05 ks with correlation coefficient of 0.4 (middle bottom panel of Figure 5.6). Although from the CCF analysis of post-flare segment data, a minor peak is observed near 0.0 ± 50 ks time delay, it is not prominent as the peak value is 0.13 (bottom right panel of Figure 5.6). Therefore, we are not considering this as a peak in the correlation function. We do not notice any significant peak in ζ-discrete cross-correlation function in this post-flaring segment. From the correlation analysis, we conclude that the soft and hard X-ray light curves are moderately correlated only during the flare segment.

5.3.2 Spectral analysis

We used `XSPEC` (v12.11.1) software package (Arnaud, 1996) to analyse the spectral data and χ^2 statistics to find the best-fitting models. Throughout the spectral analysis, the uncertainties in various parameters are calculated using `'error'` command in `XSPEC` at 90% confidence level unless or otherwise stated. As mentioned earlier, the data from the *NuSTAR* and *XMM-Newton* observations are divided into three segments such as pre-flare, flare and post-flare segments (see Figure 5.1). We carried out the spectral analysis in the $0.3 - 50$ keV energy range using simultaneous *XMM-Newton* and *NuSTAR* observations for all three segments.

[3]`https://www.weizmann.ac.il/particle/tal/research-activities/software`

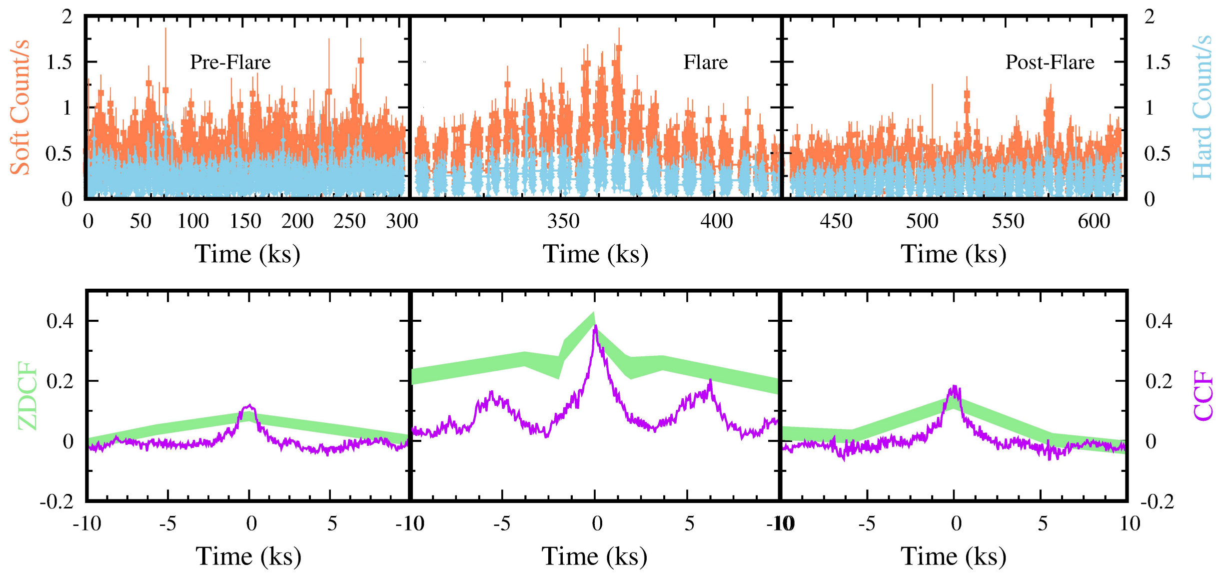

Figure 5.6: Top panel : The light curves of NGC 4051 in soft X-ray (3.0 – 10.0 keV range : salmon) and hard X-ray (10.0 – 50.0 keV range : light blue) bands obtained from the *NuSTAR* observation are shown for pre-flare, flare and post-flare segments. Bottom panel : The discrete cross-correlations between the soft X-ray and hard X-ray light curves are plotted. A moderately strong correlation between these bands can be seen during the duration of the flare, which is absent in the pre- and post-flare segments. The Cross-Correlation Functions (CCFs) are presented in a solid-magenta line, whereas the green bands represent the ζ-discrete cross-correlations.

The X-ray spectrum of an AGN is typically described by a power-law continuum, complex iron emission lines in $\sim 6-7$ keV range, reflection hump in $\sim 20-40$ keV range and soft X-ray excess below 2 keV. We used various phenomenological as well as physical models and included all the features in our analysis. We used `zpowlw`[4], `borus` (Baloković et al., 2018) , and `relxilllpion`, modified version of `relxill`[5] model (Dauser et al., 2016). For Galactic absorption and local ionized absorption, we used `phabs` or `tbabs`(Wilms et al., 2000) and `zxipcf`[6] models, respectively.

We started our spectral analysis with *NuSTAR* observation in the $3-50$ keV range to have an initial idea of spectral changes with the flux variability. As mentioned earlier, we dissected *NuSTAR* observation into three parts: pre-flare, flare and post-flare segments. To investigate the spectral changes during the flare, we further divided the flare duration into two sub-segments, such as rising phase and declining phase. Our basic model reads in `XSPEC` as:

[4] `https://heasarc.gsfc.nasa.gov/xanadu/xspec/manual/node212.html`
[5] `http://www.sternwarte.uni-erlangen.de/~dauser/research/relxill/`
[6] `https://heasarc.gsfc.nasa.gov/xanadu/xspec/models/zxipcf.html`

phabs × (atable{borus} + zphabs × cabs × zcutoffpl + constant × zcutoffpl)

In the above expression, we used the cutoff power-law model to fit the primary continuum. In this model, 'constant' stands for the relative normalization of leaked or scattered unabsorbed intrinsic continuum. The zphabs× cabs component represents the line-of-sight absorption, including the Compton scattering losses out of the line of sight. Here, the additive borus model is used for the reprocessed emission from the cold and neutral gas. This model calculates the fluorescent line emission and reprocessed continuum self-consistently. We simultaneously fitted all four time-resolved spectra with the above model. While fitting, the inclination angle, covering factor ($\mathrm{C_{F,Tor}}$) and average column density ($\mathrm{N_{H,Tor}}$) of the obscuring materials are tied across the four segments. These parameters are unlikely to change during such a short observation span. The foreground Galactic absorption column density is fixed at $N_{\mathrm{H,Gal}} = 1.2 \times 10^{20}\mathrm{cm^{-2}}$(HI4PI Collaboration et al., 2016) in the source direction and modelled with phabs. We obtained a good fit (χ^2/dof=1669/1603) with this model. All the fitted parameters are listed in Table 5.2. From this fitting, we found that the photon index (Γ) was relatively higher during the flare phase as compared to pre- and post-flare phases. We could not constrain the cutoff energy ($\mathrm{E_{cut}}$) in all four phases. The inclination angle obtained from this fitting was found to be around 30 degrees which is reasonable for type-1 Seyfert galaxies.

It is found that the photon index remained unchanged during the rising and declining phases of the flare. Therefore, we clubbed these two time intervals together for further spectral analysis. Next, we fitted simultaneous *XMM-Newton* (0.3−10 keV range) and *NuSTAR* (3−50 keV range) spectra in three segments (pre-flare, flare and post-flare) together using different models. All the fitted spectra are shown in Figure 5.8. The advantage of fitting spectra of three intervals simultaneously is that it produces the spectral variability in a more physical way.

Model-1: We built our baseline model with the power-law with a high energy cutoff as the source continuum. We used a redshifted black body component (zbbody) for the soft excess, a Gaussian line (zgaus) for the iron K-alpha emission line and the pexrav model for the reflection component above 10 keV (Magdziarz & Zdziarski, 1995). We set the reflection fraction (R_{refl}) as negative so that the pexrav component is considered as only the reflection spectrum. We fixed the inclination angle at 30 degrees as obtained from the previous model. The iron and heavy element abundances were tied for three intervals. The photon index

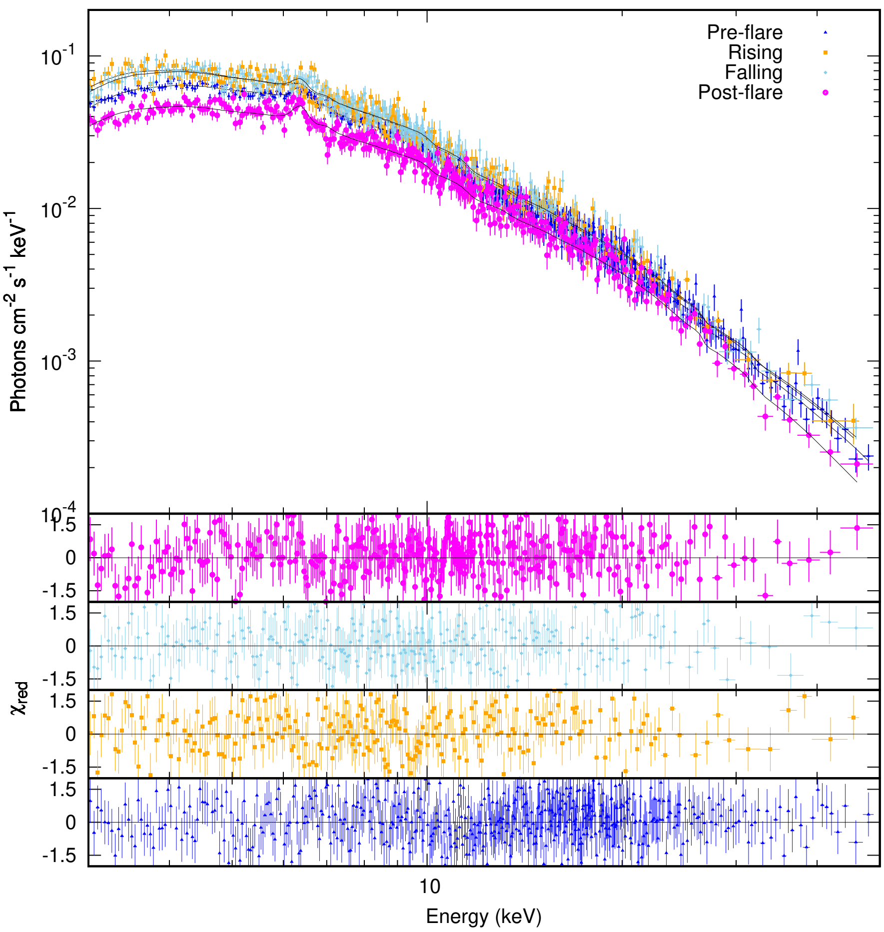

Figure 5.7: Top panel: The best fit model spectra (fitted simultaneously) for the pre-flare, rising and falling part of the flare, post-flare phases in the $3-50$ keV energy range from $NuSTAR$ observation. Bottom four panels show corresponding residuals. The magenta, cyan, orange and green points represent the data from the pre-flare, rising part, declining part of the flare and post-flare phases, respectively.

Table 5.2: The best-fitted parameters obtained by fitting the $3-50$ keV *NuSTAR* time-resolved spectra of NGC 4051 with the `borus` model.

Parameters	Pre-flare segment	Rising phase	Declining phase	Post-flare segment
Torus column density $N_{\rm H,Tor}$ (10^{22} cm^{-2})	$24.50^{+0.07}_{-0.06}$	f	f	f
Torus covering fraction $C_{\rm F,Tor}$	$0.87^{0.07}_{-0.03}$	f	f	f
Inclination (deg.)	30^{+5}_{-5}	f	f	f
Iron abundance $A_{\rm Fe}$	$1.10^{+0.33}_{-0.14}$	$0.97^{+0.27}_{-0.23}$	$1.01^{+0.35}_{-0.28}$	$0.82^{+0.22}_{-0.17}$
Norm (10^{-3})	$6.20^{+1.1}_{-1.1}$	$7.42^{+0.32}_{-0.92}$	$8.09^{+0.66}_{-1.00}$	$3.29^{+1.30}_{-0.73}$
Line-of-sight column density $N_{\rm H,ref}$ (10^{22} cm^{-2})	$1.22^{+0.50}_{-0.55}$	< 0.62	$0.83^{+0.59}_{-0.70}$	$1^{\dagger}$
Photon indexΓ	$1.89^{+0.06}_{-0.08}$	$1.97^{+0.05}_{-0.09}$	$1.97^{+0.03}_{-0.08}$	$1.64^{+0.09}_{-0.07}$

f represents the parameter fixed at corresponding value at the pre-flare phase.
† pegged at this value

of the `pexrav` model was linked with that of the cutoff power-law model. Since the cut-off energy could not be constrained, we fixed it at 370 keV for low Eddington Seyfert galaxies as suggested in the statistical study by Ricci et al. (2017). We needed two absorbers while fitting the spectra to get the best fit model. The final model in `XSPEC` reads as,

$$\texttt{constant} \times \texttt{tbabs} \times \texttt{zxipcf} \times \texttt{zxipcf} \times (\texttt{zbbody} + \texttt{pexrav} + \texttt{zcutoffpl})$$

We applied a constant factor in the composite model to take into account the calibration uncertainties between different instruments. This model provided a good fit to the *XMM-Newton* and *NuSTAR* data with $\chi^2 = 5385$ for 5104 degrees of freedom (dof). We required two ionized absorbers for the residuals below 2 keV. To take into account this absorption feature, we included two `zxipcf` models for partially covering and partially ionized absorbing material. The obtained redshift ($z =\sim 0.20$) of the first absorber was similar to the ultra-fast outflows (UFOs) (Tombesi et al., 2013) during three intervals. The second absorber showed the redshift comparable to the warm absorbers (WAs) (Ebrero et al., 2011). The value of the blackbody temperature was found to be ~ 100 eV which was non-variable during the observation period. The spectrum became softer during the flare with the best fitted photon-index $\Gamma = 2.10 \pm 0.005$. As we are considering only reflection component of the `pexrav` model and using a separate continuum model, we could not constrain the value of the reflection scaling factor and fixed it at -1. We calculated the soft excess and power-law flux (see Table 5.6) from corresponding model component. The soft excess flux was found to be decreasing with time while the power-law flux was highest during the flaring phase.

Model-2: Time-resolved spectral fitting of *NuSTAR* and *XMM-Newton* data with Model-1 provided information on the spectral changes, presence of warm absorber and UFO in the three time intervals. However, it did not provide any physical properties of the Comptonizing plasma, i.e., the corona. To get information on the change in coronal properties, we replaced `zcutoffpl` with the Comptonization model `compPS` (Poutanen & Svensson, 1996). This model produces X-ray continuum for different geometries using the exact numerical solution of the radiative transfer equation, which depends on the geometry, optical depth of the hot electron plasma, spectral distribution of the seed photons, inclination angle and the way seed soft photons are injected into the hot plasma. This model also takes into account the reflection spectra from the cold medium as well as blurred reflection smeared out by the rotation of the disk and relativistic effects. In the fitting process, we fixed certain parameters based on a prior guess of the system so that fitting could converge.

We considered a spherical geometry of the plasma in this model. The inclination was fixed at 30 degrees. The values of R_{in} and R_{out} were fixed at 6 and 2000 R_s, respectively. The parameters obtained from fitting the data from three segments are tabulated in Table 5.4. Instead of the optical depth, this model incorporates Compton y-parameter (τ_y) as one input which relates to the optical depth as $\tau = \tau_y/(4kT_e/m_ec^2)$, where kT_e is the hot electron temperature in keV. Iron and heavy element abundances were tied for the time intervals. The absolute value of Fe Kα line energy marginally varies in three phases while the equivalent width (EW) is lowest in the flare phase. Inner disk temperature is found to be invariable (within error) with an average temperature of $\sim$18 eV. From this model, interestingly we found that the coronal temperature increased to $\sim$228 keV post-flare while it was similar before and during the flare with a value around $\sim$182 keV. Moreover, the reflection fraction was found to be decreasing during the flare while it substantially increased after the flare.

.

Model-3: Reflection from the photoionized accretion disk is considered to be one of the explanations of the origin of the soft X-ray excess in the AGNs. Emissions from the compact, hot and relativistic plasma irradiate the accretion disk. The X-ray illumination is stronger

Table 5.3: The best fitted parameters obtained from fitting 0.3 − 50 keV time-resolved spectra simultaneously using *XMM-Newton* and *NuSTAR* observations with phenomenological model `zcutoffpl`. Column density ($N_{\rm H}$), ionization fraction ($\log \xi$), velocity (v), maximum (r_{max}) and minimum (r_{min}) locations of the two absorbers.

Parameters	Pre-flare segment	Flare segment	Post-flare segment
$N_{\rm H,1}$ (10^{22} cm^{-2})	$9.38^{+1.22}_{-1.61}$	$14.87^{+2.47}_{-2.86}$	$11.13^{+1.65}_{-1.69}$
$\log \xi_1$	$1.08^{+0.08}_{-0.95}$	$1.09^{+0.14}_{-0.56}$	$1.31^{+0.06}_{-0.09}$
Cov Frac1	$0.24^{+0.02}_{-0.01}$	$0.20^{+0.02}_{-0.007}$	$0.23^{+0.01}_{-0.03}$
z1	$-0.20^{+0.04}_{-0.06}$	$-0.21^{+0.04}_{-0.07}$	$-0.22^{+.02}_{-0.05}$
v/c	-0.20	-0.21	-0.22
r_{max} (pc)	0.1686	0.1095	0.0576
r_{min} (10^{-4}pc)	0.0409	0.0371	0.0338
r_{min} (R_s)	25	23	21
$N_{\rm H,2}$ (10^{22} cm^{-2})	$0.62^{+0.52}_{-0.51}$	$2.28^{+0.79}_{-0.89}$	$2.99^{+0.52}_{-0.55}$
$\log \xi_2$	$2.07^{+0.15}_{-0.45}$	$2.08^{+0.14}_{-0.14}$	$2.01^{+0.07}_{-0.03}$
Cov Frac1	$0.39^{+0.58}_{-0.09}$	$0.30^{+0.07}_{-0.05}$	$0.40^{+0.03}_{-0.02}$
z2	$0.04^{+0.02}_{-0.02}$	$0.02^{+0.02}_{-0.02}$	$0.03^{+0.01}_{-0.01}$
v/c	0.037	0.017	.027
r_{max} (pc)	0.260	0.073	0.0427
r_{min} (10^{-4}pc)	1.1967	0.4024	1.0826
$_{min}$ (R_s)	730	3460	1372
$kT_{\rm BB}$ (eV)	100^{+1}_{-1}	100^{+2}_{-2}	100^{+1}_{-1}
Norm$_{\rm BB}$ (10^{-04})	$1.50^{+0.02}_{-0.02}$	$1.11^{+0.25}_{-0.22}$	$0.85^{+0.01}_{-0.01}$
Fe Kα LE (keV)	$6.40^{+0.02}_{-0.03}$	$6.36^{+0.04}_{-0.05}$	$6.35^{+0.02}_{-0.02}$
EW (eV)	101^{+16}_{-15}	82^{+22}_{-20}	95^{+29}_{-32}
Norm (10^{-5})	$1.97^{+0.32}_{-0.29}$	$1.58^{+0.42}_{-0.38}$	$1.35^{+0.23}_{-0.23}$
Abund	$1.87^{+0.18}_{-0.16}$	f	f
Abund$_{\rm Fe}$	$2.39^{+0.22}_{-0.21}$	f	f
Γ	$2.05^{+0.003}_{-0.003}$	$2.10^{+0.005}_{-0.005}$	$2.05^{+0.005}_{-0.005}$
Norm$_{\rm PL}$ (10^{-03})	$7.82^{+0.02}_{-0.02}$	$8.34^{+0.03}_{-0.03}$	$5.43^{+0.01}_{-0.01}$

f represents the parameter fixed at corresponding value at the pre-flare phase.

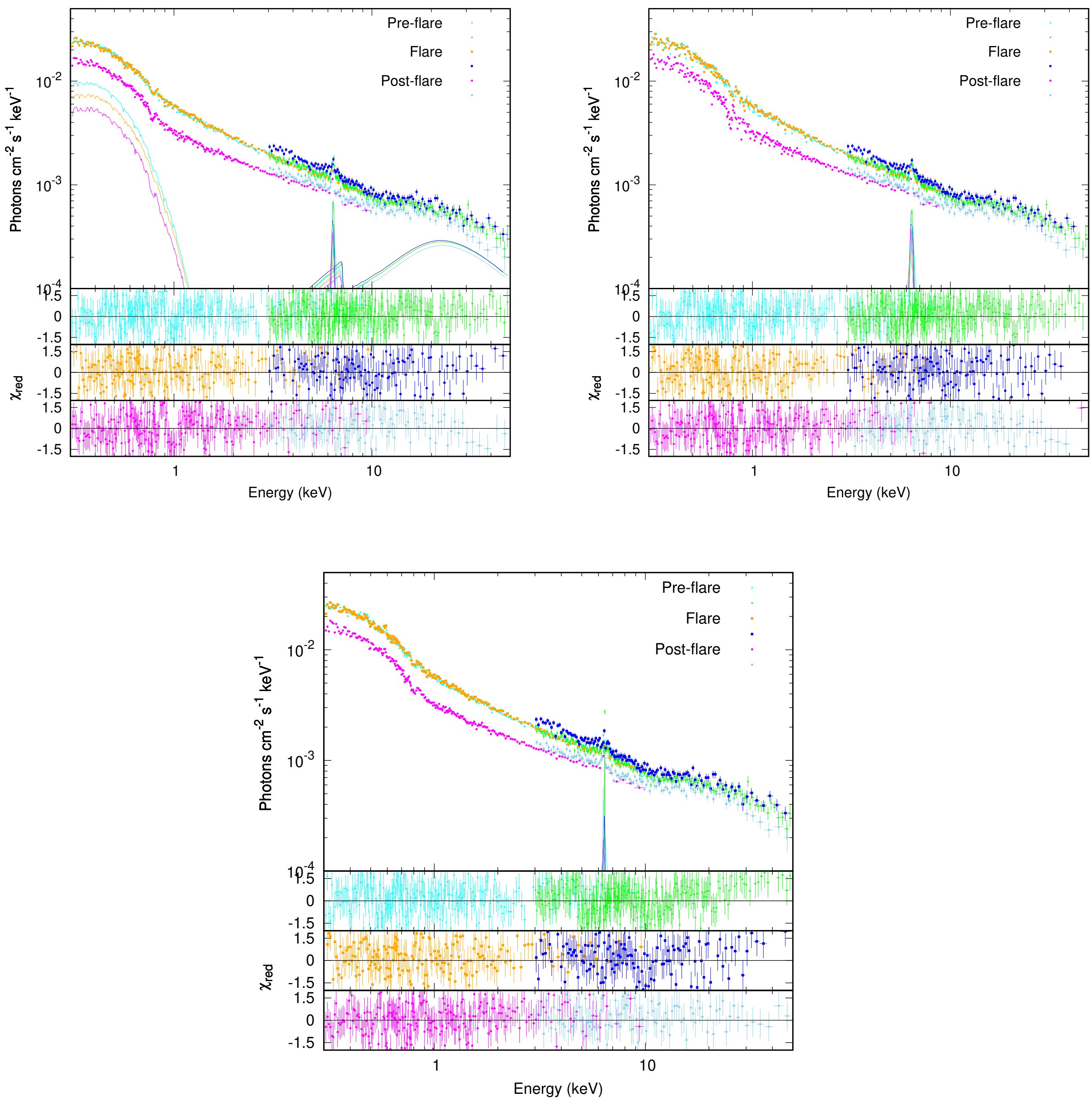

Figure 5.8: The $0.3 - 50$ keV *XMM-Newton* + *NuSTAR* spectra fitted with the Model-1 (top left panel), Model-2 (top right panel), and Model-3 (bottom panel) for the pre-flare, flare, post-flare phases. Corresponding residuals for the pre-flare, flare, post-flare phases are shown in three sub-panels of each figure. The cyan, orange and magenta points represent the *XMM-Newton* data for the pre-flare, flare, post-flare phases, respectively. The green, blue and turquoise points represent the *NuSTAR* data for the pre-flare, flare, post-flare phases, respectively.

Table 5.4: The best fitted parameters obtained after fitting $0.3 - 50$ keV time-resolved spectra simultaneously using XMM-Newton and NuSTAR observations with phenomenological model `compPS`.

Parameters	Pre-flare segment	Flare segment	Post-flare segment
$N_{\rm H,1}$ (10^{22} cm^{-2})	$8.22^{+0.25}_{-0.87}$	$7.55^{+1.17}_{-1.47}$	$5.64^{+0.36}_{-0.26}$
$\log \xi_1$	$1.93^{+0.09}_{-0.02}$	$1.89^{+0.07}_{-0.04}$	$1.80^{+0.02}_{-0.06}$
Cov Frac1	$0.35^{+0.01}_{-0.02}$	$0.28^{+0.07}_{-0.05}$	$0.45^{+0.03}_{-0.02}$
z2	$-0.26^{+0.007}_{-0.009}$	$-0.26^{+0.02}_{-0.02}$	$-0.21^{+0.006}_{-0.004}$
$N_{\rm H,2}$ (10^{22} cm^{-2})	$0.47^{+0.43}_{-0.08}$	$1.37^{+2.02}_{-0.76}$	$1.24^{+0.32}_{-0.54}$
$\log \xi_2$	$2.15^{+0.08}_{-0.06}$	$2.14^{+0.13}_{-0.09}$	$2.04^{+0.08}_{-0.05}$
Cov Frac2	> 0.63	> 0.47	$0.71^{+0.16}_{-0.06}$
z1	$0.001^{+0.01}_{-0.008}$	$0.009^{+0.02}_{-0.01}$	$0.04^{+0.01}_{-0.005}$
Fe Kα LE (keV)	$6.40^{+0.02}_{-0.03}$	$6.37^{+0.04}_{-0.05}$	$6.35^{+0.02}_{-0.02}$
σ (eV)	97^{+55}_{-49}	115^{+88}_{-58}	70^{+38}_{-41}
EW (eV)	125^{+18}_{-17}	101^{+25}_{-22}	118^{+19}_{-18}
Norm (10^{-05})	$2.38^{+0.35}_{-0.33}$	$1.82^{+0.44}_{-0.39}$	$1.56^{+0.24}_{-0.23}$
$kT_{\rm e}$ (keV)	182^{+24}_{-23}	184^{+28}_{-26}	228^{+52}_{-15}
$kT_{\rm bb}$ (eV)	19^{+3}_{-3}	19^{+5}_{-4}	16^{+4}_{-3}
τ_y	$0.37^{+0.02}_{-0.02}$	$0.36^{+0.03}_{-0.03}$	$0.31^{+0.02}_{-0.01}$
relrefl	$2.19^{+0.16}_{-0.16}$	$2.10^{+0.21}_{-0.23}$	$2.58^{+0.29}_{-0.46}$
Abund	$4.68^{+0.47}_{-0.41}$	f	f
Abund$_{\rm Fe}$	$2.25^{+0.29}_{-0.30}$	f	f

f represents the parameter fixed at corresponding value at the pre-flare phase.

in the inner regions of the accretion disk due to strong gravity of the central black hole. We used the `relxilllpion` variant of the `relxill` model to describe the soft X-ray excess. The `relxill` model computes the continuum emission and its reflection from the accretion disk that includes the reprocessing of the continuum photons in the disk. The blurring of the emission lines due to relativistic motion of the inner disk in the soft X-ray gives the smooth curvature which appears as soft X-ray excess. This model is parameterized by the inclination angle, inner radius, reflection fraction, ionization parameter ($\log\xi$) with constant ionization throughout the disk. The `relxilllpion` model allows the ionization of the disk to vary with radius and this variation is approximated by power-law.

The composite model in `XSPEC` reads as

$$\texttt{constant} \times \texttt{tbabs} \times \texttt{zxipcf} \times \texttt{zxipcf} \times (\texttt{relxilllpion})$$

While fitting the data with this model, we tied the iron abundance across the three intervals. The Eddington ratio for this source is calculated to be ~ 0.01 for black hole mass $1.73 \times 10^6 \mathrm{M}_\odot$ and bolometric luminosity $\sim 2.3 \times 10^{42}$ erg s^{-1}. The cutoff energy is kept fixed at 370 keV as earlier. We required two absorbers to fit the residuals in the soft X-ray range (< 2 keV) of the spectra. Initially, we varied the value of inner disk radius ($\mathrm{R_{in}}$), ionization parameter ($\log\xi$) and found fairly unchanged parameter values. Therefore, we tied these parameters for all three segments. The height of the corona from the disk increased to $12.18^{+0.98}_{-0.92}$ R_g accompanied by reduction in the reflection fraction during the flare. After the flare, the coronal height decreased with the highest reflection fraction among the three phases.

5.4 Discussion

In this work, we explored the changes in the spectral and timing properties of NGC 4051 during the pre-flare, flare and post-flare phases using the data obtained from the *XMM-Newton* and *NuSTAR* observations in November 2018. We explored the accretion properties, accretion mechanism and the corona structural changes of the source in detail using various phenomenological and physical models. The results obtained from our work are described here.

Table 5.5: The best fitted parameters obtained after fitting $0.3-50$ keV time-resolved spectra simultaneously using *XMM-Newton* and *NuSTAR* observations with physical model `relxilllpion`.

Parameters	Pre-flare segment	Flare segment	Post-flare segment
$N_{\rm H,1}$ (10^{22} cm^{-2})	$21.04^{+4.79}_{-2.39}$	$46.46^{+4.89}_{-4.09}$	$47.59^{+6.93}_{-9.00}$
$\log\xi_1$	$1.92^{+0.08}_{-0.07}$	$2.00^{+0.03}_{-0.03}$	$1.77^{+0.23}_{-0.30}$
Cov. Frac1	$0.27^{+0.02}_{-0.02}$	$0.30^{+0.01}_{-0.01}$	$0.30^{+0.01}_{-0.01}$
z1	$-0.33^{+0.01}_{-0.02}$	$-0.31^{+0.03}_{-0.02}$	$-0.36^{+.02}_{-0.03}$
$N_{\rm H,2}$ (10^{22} cm^{-2})	$3.98^{+0.59}_{-0.59}$	$5.44^{+0.39}_{-0.47}$	$1.07^{+0.11}_{-0.30}$
$\log\xi_2$	$1.91^{+0.09}_{-0.06}$	$1.98^{+0.08}_{-0.11}$	$1.90^{+0.04}_{-0.07}$
Cov Frac1	$0.28^{+0.03}_{-0.02}$	$0.35^{+0.02}_{-0.03}$	$0.45^{+0.01}_{-0.01}$
z2	$-0.01^{+0.02}_{-0.01}$	$-0.01^{+0.01}_{-0.02}$	$0.001^{+0.007}_{-0.008}$
h	$9.61^{+1.38}_{-1.68}$	$12.18^{+0.98}_{-0.92}$	$7.36^{+1.51}_{-0.98}$
a	> 0.85	f	f
$R_{\rm in}$	< 2.52	f	f
$\log\xi_1$	$3.10^{+0.05}_{-0.06}$	f	f
Γ	$2.16^{+0.007}_{-0.008}$	$2.18^{+0.009}_{-0.009}$	$2.15^{+0.009}_{-0.007}$
Abund$_{Fe}$	$1.02^{+0.16}_{-0.04}$	f	f
Reflfrac	$2.00^{+0.06}_{-0.06}$	$1.42^{+0.05}_{-0.05}$	$2.12^{+0.07}_{-0.06}$
Ionization index	$1.07^{+0.08}_{-0.05}$	$1.15^{+0.09}_{-0.09}$	$1.03^{+0.05}_{-0.05}$
Norm$_{\rm PL}$ (10^{-04})	$1.79^{+0.71}_{-0.72}$	$1.91^{+0.06}_{-0.05}$	$1.73^{+0.19}_{-0.18}$

f represents the parameter fixed at corresponding value at the pre-flare phase.

Table 5.6: Fluxes and Luminosities

Parameters	Pre-flare segment	Flare segment	Post-flare segment
$F^{\rm BB}_{0.3-2\ \rm keV}(10^{-12})\star$	7.65 ± 0.08	5.88 ± 0.09	4.54 ± 0.05
$F^{\rm PL}_{2-10\ \rm keV}(10^{-11})\star$	1.77 ± 0.01	1.82 ± 0.01	1.26 ± 0.06
$L_{0.1-200}\ (10^{41})\bullet$	8.55 ± 0.03	9.20 ± 0.03	6.04 ± 0.02
$L_{\rm ion}\ (10^{41})\bullet$	5.85 ± 0.02	6.18 ± 0.02	4.04 ± 0.01
$L_{2-10\ \rm keV}\ (10^{41})\bullet$	2.06 ± 0.004	2.39 ± 0.005	1.5 ± 0.003
$\lambda_{\rm Edd}$	0.014 ± 0.001	0.016 ± 0.001	0.011 ± 0.001
l	$9.12^{+0.02}_{-0.03}$	$9.82^{+0.02}_{-0.05}$	$6.44^{+0.03}_{-0.02}$
θ	$0.356^{+0.05}_{-0.04}$	$0.36^{+0.06}_{-0.06}$	$0.446^{+0.10}_{-0.03}$

$\star$ in units of ergs $\rm s^{-1}\ cm^{-2}$
$\bullet$ in units of erg $\rm s^{-1}$

5.4.1 Black Hole spin

The spin of the black hole is estimated self-consistently from the X-ray reflection models. In the present work, the spin parameter was linked while fitting spectra of three segments simultaneously. From the relativistic reflection model `relxilllpion`, we found that the black hole is rapidly spinning with the spin parameter $a > 0.85$, while keeping the values of the inner radius and spin parameter tied for three time intervals.

5.4.2 Location of the absorbers

While fitting the spectra from the simultaneous observations of NGC 4051 with *XMM-Newton* and *NuSTAR*, we required two absorbers to get rid of the residuals below 2 keV in all the spectral models used in this work. We took into account absorption with partially ionized and partially covered absorber models `zxipcf`. The properties of these absorbers are listed in Tables 5.3, 5.4, & 5.5. The ionization parameter of an absorber is defined as $\xi = L_{\rm ion}/nr^2$ (Tarter et al., 1969), where $L_{\rm ion}$, n and r are the unabsorbed ionizing luminosity of the emitting source, number density and radial location of the absorber from the central source, respectively. The absorption from the excited states or absorption variability can be used to determine the limits of r using the definition of ξ. It is possible to estimate the upper limit of the radial distance based on the assumption that the thickness of the absorber can not exceed its location from the SMBH (Ebrero et al., 2011; Crenshaw & Kraemer, 2012);

$$r \leq r_{\max} = \frac{L_{\rm ion}}{N_{\rm H}\xi}$$

where, $N_{\rm H}$ is the column density of the absorber.

A lower limit on the location of the outflow can be calculated as

$$r \geq r_{\min} = \frac{2GM_{\rm BH}}{\nu^2}$$

Another way of calculating the lower limit is by considering the light travel time $D = \Delta t \times c$ during the observation if the absorber does not seem to be variable. We used the values from the `zcutoffpl` model to estimate the radial location of both the absorbers. The ionizing luminosity of this source has been calculated for three intervals by considering the power law component in the 0.3-50 keV range (see Table 5.6). The locations of the absorber 1 and absorber 2 are estimated and listed in Table 5.3 separately for three time intervals. These values of locations and redshift are consistent with the WAs and UFOs found in the studies of type 1 Seyfert galaxies (Tombesi et al., 2012; Tombesi et al., 2013).

We have also calculated the marginal posterior distributions for the absorber parameters to check the spectral fitting degeneracy between them. To search through the parameter space, we used the Markov Chain Monte Carlo (MCMC) sampling procedure. We used Goodman & Weare, 2010 algorithm implemented in `XSPEC` to determine the chain. We considered 20 walkers with a total chain length of 200000 and burnt the initial 20000 steps. The one-dimensional (1D) and two-dimensional (2D) distributions are shown in Figure 5.9.

5.4.3 Properties of corona

The X-ray emitting corona is characterized by the optical depth (τ), hot electron plasma temperature ($\mathrm{kT_e}$) and the X-ray continuum photon index (Γ). As the power-law with high energy cut-off continuum model gives information only on the photon-index, we utilized the `compPS` model, which considers $\mathrm{kT_e}$, Compton y parameter and inner disk temperature ($kT_{\rm bb}$) as free parameters. We find that the temperature of the corona increased after the flare subsided and the source went into the low flux state. During the flare, when flux was high, the slope of the spectrum became steep. This softening of the X-ray continuum with high flux is consistent with the "softer when brighter" nature observed in many AGNs (Connolly

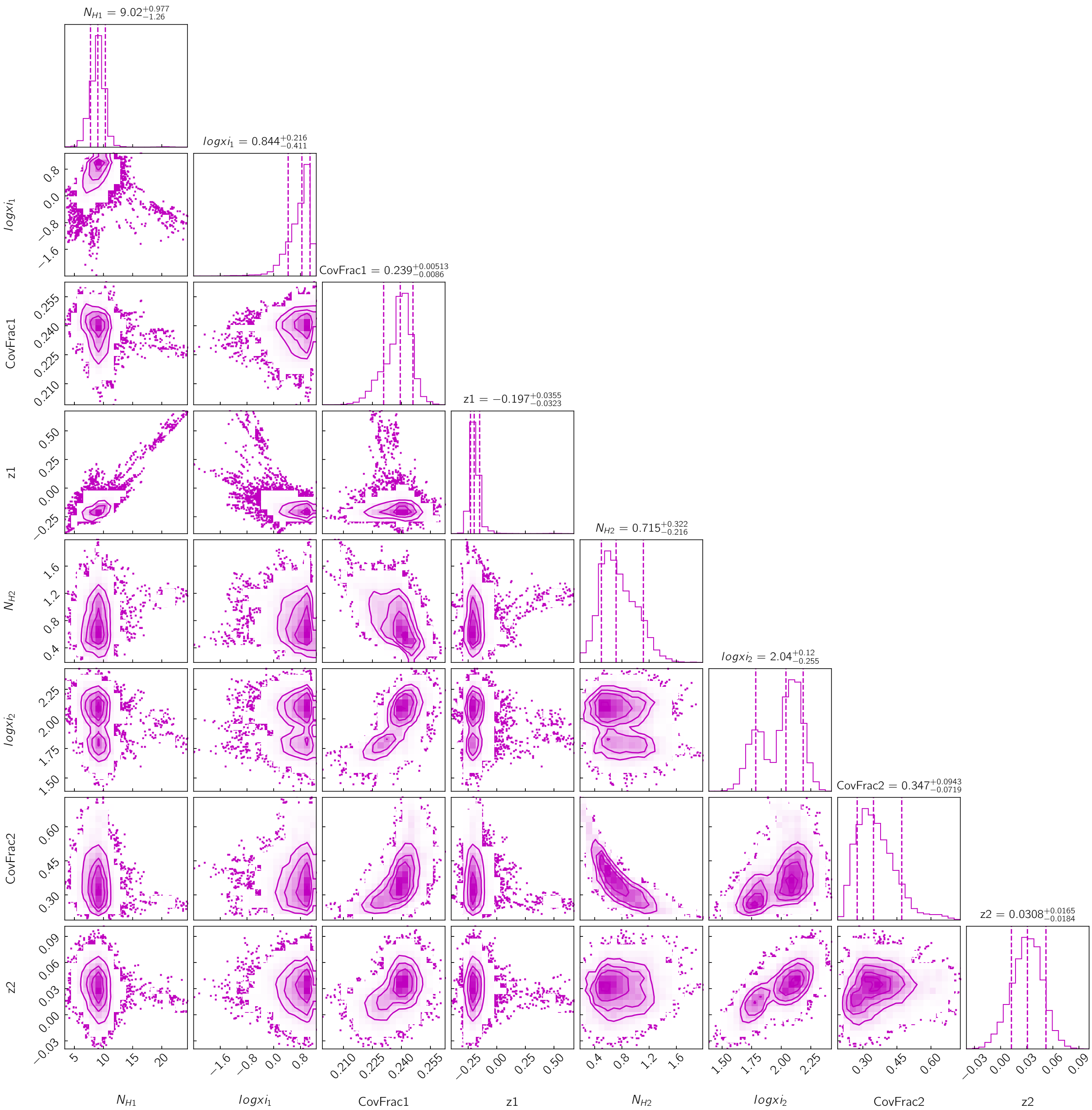

Figure 5.9: The 1D and 2D posterior distribution curves resulted from the MCMC analysis of the ionization parameter ($log\xi$), covering factor, and redshift (z) of the two absorbers. The vertical lines in the 1D distribution show 16%, 50%, and 90% quantiles. CORNER.PY (Foreman-Mackey, 2016) was used to plot the distributions.

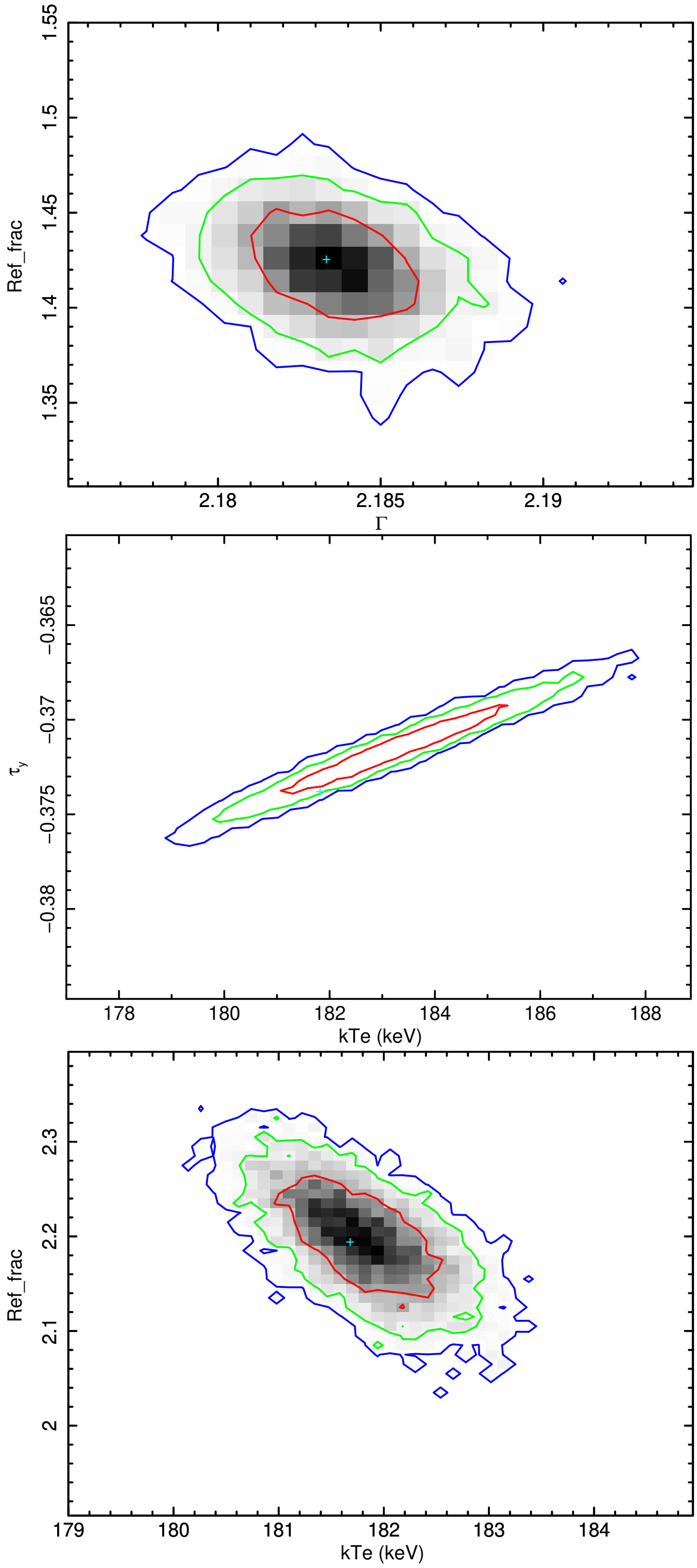

Figure 5.10: Contour plots resulted from the MCMC analysis of the `relxilllpion`, `compPS` models for the reflection fraction vs Γ (top panel), Compton y-parameter (τ_y) vs $\mathrm{kT_e}$ (middle panel) and reflection fraction vs $\mathrm{kT_e}$ (bottom panel).

et al., 2016). The less energetic seed photons from the accretion disk get Comptonized in the corona, producing X-ray emission. In the present work, it is found that the coronal temperature increased after the flare. An increase in temperature of the corona after the flare can be interpreted as due to the injection of fewer seed photons into the corona resulting in the reduction of the Compton cooling rate. Considering the magnitude of the observed flare and the duration of the observation, it is highly unlikely that there could be any significant variation in the accretion rate (see $\lambda_{\rm Edd}$ values from Table 5.6). Moreover, the flux of the soft X-ray excess ($0.3 - 2$ keV range) does not show any clear correlation with the photon index (see Table 5.6). This indicates that the change in the spectral state during the flaring phase is inherent to the corona instead of the variations in the seed photons. In an AGN, the corona is likely to be powered by the small-scale magnetic flux tubes associated with the orbiting plasma in the accretion disk Yuan et al. (2019). Any change in the magnetic field can cause a change in the location and geometry of the corona, which in turn can result in the coronal temperature variation. Recently, Wilkins et al. (2022) studied a similar kind of X-ray flaring event in NLS1 galaxy IZw1. They found that the temperature was higher in the pre-flare phase and decreased during the flare, probably due to the expansion of the corona accompanied by softening of the spectrum. After the flare, the temperature again started to increase with the hardening of the continuum spectrum. In NGC 4051, we found that the coronal temperature increased after the flare and the spectrum became harder. In this case, the corona perhaps started inflating in the pre-flare phase and reached a maximum during the flare. After the flare, it again contracted, followed by an increase in temperature.

In the present work, the coronal temperature was found to be high (average value of $\sim$198 keV). This is likely the reason we could not constrain the cut-off energy for this source. From the best fitted values of the coronal temperature (kT_e) and Compton y-parameter (y) (although these two parameters are degenerate as shown in the middle contour plot of Figure 5.10), the value of optical depth ($\tau = \frac{\tau_y}{4T_e/m_ec^2}$) is calculated as 0.26 ± 0.04, 0.25 ± 0.04, 0.17 ± 0.03 in the pre-flare, flare and post-flare phases, respectively. These values of τ are consistent with the mean value obtained for a sample of 838 Swift/BAT AGNs (Ricci et al., 2018). The coronal temperature carries important information on the state of the X-ray emitting plasma. The position of the AGN in the compactness-temperature ($\theta - l$ plane) space provides an insight to the dominant process in the corona (Fabian et al., 2015). In the corona of an AGN, the most significant processes are inverse Compton scattering, bremsstrahlung and pair production. Among these, the dominant process is the one for which the cooling time is shortest. The Comptonization process dominates when $l > 3\alpha_f \theta^{-1/2}$, where $\alpha_{\rm f}$ and θ are the fine structure constant and coronal temperature normalized to the electron rest energy, respectively. The electron-proton coupling dominates when $3\alpha_{\rm f}\theta < l < 0.04\theta^{-3/2}$ while for $0.04\theta^{-3/2} < l < 80\theta^{-3/2}$, the electron-electron coupling becomes prominent. There is a regime in the $\theta - l$ plane where the pair production process becomes the runaway process that depends on the corona shape and on the radiation mechanism. Stern et al. (1995) computed the position of these pair runaway lines for a slab corona. Svensson (1984) calculated this regime for isolated clouds and gave the condition for its occurrence when $l \sim 10\theta^{5/2}e^{1/\theta}$. The compactness parameter is defined as,

$$l = \frac{L}{R}\frac{\sigma_T}{m_e c^3}$$

where L, R, σ_T, m_e and c are the luminosity, radius of the corona, the Thomson cross-section, mass of the electron and speed of light, respectively. We estimated this parameter for NGC 4051 considering power-law continuum luminosity extrapolated to the $0.1-200$ keV band in three intervals and radius as 10 R_g (for standard sources, (Fabian et al., 2015)). The l and θ values are given in Table 5.6 and plotted in Figure 5.11. NGC 4051 is found to be located at the edge of the pair runaway region corresponding to the slab corona. This suggests that the process is mostly dominated by pair production and annihilation. In a compact corona ($l > 1$) when the photons are highly energetic, the photon-photon collision generates an electron-positron pair. If the temperature reaches $\sim$1 MeV, the pair production process becomes significant, thereby soaking energy and limiting further rise in temperature.

5.4.4 Soft X-ray excess and reflection

The soft X-ray excess above the continuum is very often seen in AGNs. This component is prominent in the NLS1s. However, the origin of the soft X-ray excess is still part of the discourse. There are various models in the literature that take account of the origin of this component. The Comptonization of the photons in an optically thick and warm corona in the inner part of the disc is one explanation (Done et al., 2012) for the origin of the soft excess. Another scenario is the one in which the photons from the hot corona ($\sim$100 keV) get reflected from the relativistically moving inner accretion disc and give rise to the soft excess (Fabian et al., 2002; Ross & Fabian, 2005; Pal et al., 2016). In the ionized absorption model, the photons are absorbed by the high-velocity winds originating from the accretion disc and

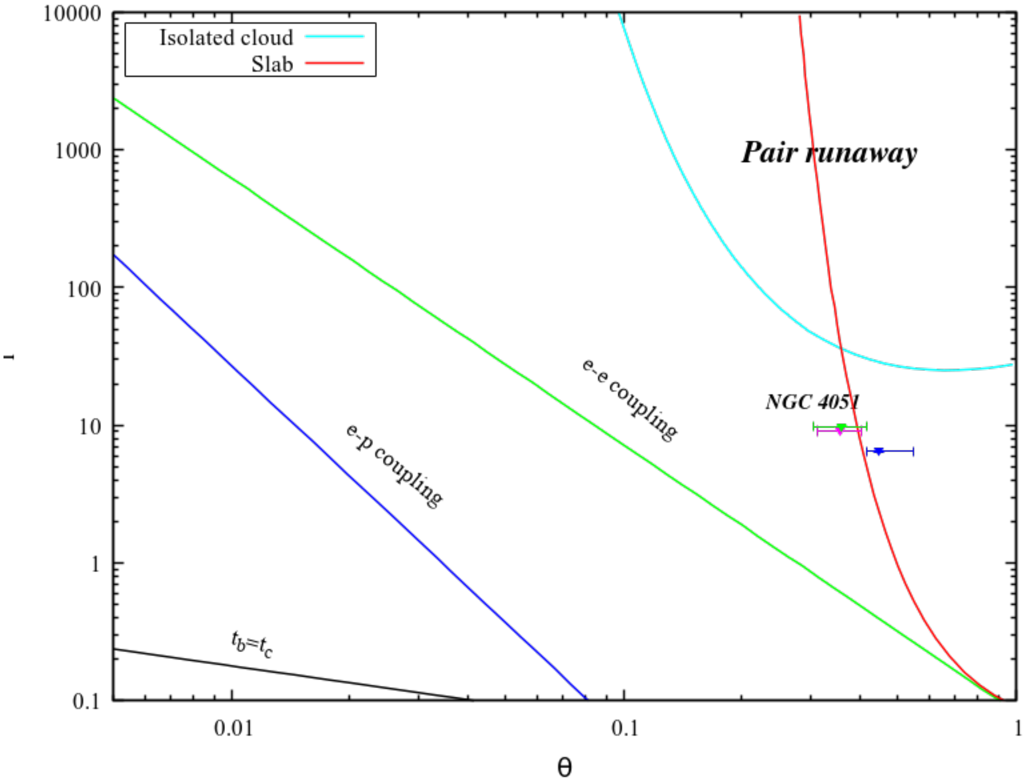

Figure 5.11: Theoretical compactness-temperature diagram is shown. The green line represents the region below which the electron-electron coupling time scale is shorter than the Compton cooling time while the region below the blue line, the electron-proton coupling time is shorter. Bremsstrahlung is dominant in the region below the black line. The region beyond the cyan and red curves represents where pair run-away process occur for for isolated cloud (Svensson, 1984) and slab geometry (Stern et al., 1995). The green, magenta and blue points are drawn for pre-flare, flare and post-flare phase positions of NGC 4051, respectively.

re-emitted (Gierliński & Done, 2004).

In our analysis, we initially used the `zbbody` model to fit the soft X-ray excess. We found the blackbody temperature (kT_{BB}) to be $\sim$ 100 eV which was almost constant throughout the observation. This non-variation or minimal variation of the soft excess temperature is expected, as suggested by earlier studies (Gierliński & Done, 2004; Ricci et al., 2017). We calculated the unabsorbed flux of the blackbody component for the soft excess and found it to be unaffected during the flare and decreasing with time.

From the `relxilllpion` model, we found that during the flare, the reflection fraction decreased to 1.42 from 2.00 in the pre-flare phase and again increased to 2.09 in the post-flare phase (bottom panel of Figure 5.13). Similar trend was also observed from the `compPS` model. The change in the reflection component can be seen in Figure 5.12 where the ratio between the 3-50 keV spectrum from the *NuSTAR* observation and the best-fitted power-law is plotted. The reflection fraction is the ratio of reflected emission from the disc and direct emission from the corona. From our analysis, we found this factor to be greater than unity, which means the source is reflection dominated. The gravitational bending causes the X-rays to be concentrated towards the accretion disc resulting in a high reflection fraction (Miniutti & Fabian, 2004). As we mentioned above, NGC 4051 hosts a highly spinning black hole. Therefore, the effect of light bending causing a high reflection fraction is expected. In the simple lamppost geometry scenario, the compact corona is located above the central black hole. The drop of reflection fraction during the flare can be explained in terms of the coronal height from the accretion disc. We found that the coronal height increased, i.e., the corona moved away from the accretion disc during the flare when the reflection fraction was lowest (second and bottom panels of Figure 5.13). After the flare, coronal height decreased and the reflection fraction increased again. Another possibility of the drop in the reflection during the flare and enhancement after the flare could be due to the change in the inner accretion disc radius (De Marco et al., 2021). As mentioned before, we did not find any significant change in the inner radius during three phases. Over-ionization could be another reason for the drop of the reflection during the flare. However, the ionization parameter was invariable during the observation and was fixed for the final fitting. Therefore, the motion of the corona from the accretion disc seems to be the most plausible explanation for the variable reflection fraction.

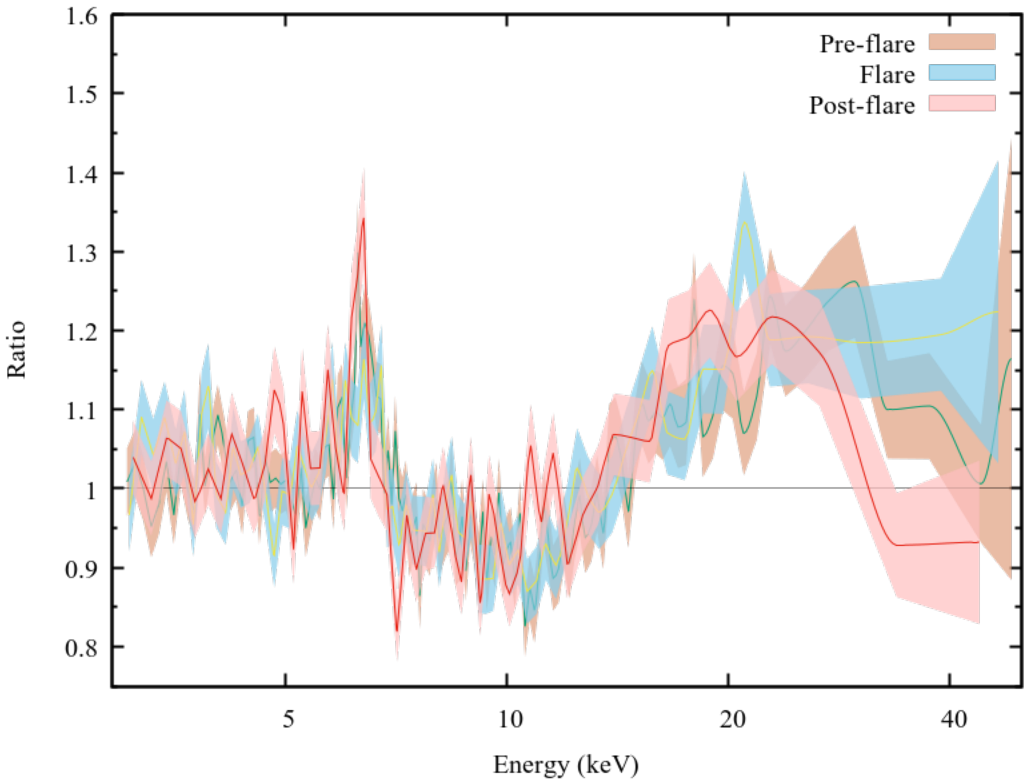

Figure 5.12: The ratio of the $3-50$ keV spectrum from *NuSTAR* observation and the best fitted power-law model is shown. The varying strength of the reflection component above 10 keV is evident for all three phases of the observation.

5.5 Summary & Conclusions

A detailed broadband X-ray spectral and timing analysis of a minor flaring event in the NLS1 galaxy NGC 4051 during 4-11 November 2018 has been performed using simultaneous observations with *NuSTAR* and *XMM-Newton* observatories. While analysing the data, we divided the total exposure into pre-flare, flare and post-flare segments and carried out timing and spectral studies. Following are the main results and conclusions of our study.

- NGC 4051 showed a rapid variability in the $3-50$ keV energy band of *NuSTAR*, where the count rate increased by a factor of $\sim$2.5, followed by a decrease to the pre-flare level within a day. The X-ray variability spectrum of the source showed a trend where variability is higher in soft bands, i.e., soft excess or ionized absorbers.

- From the spectral analysis in $3-50$ keV range, we found that the spectral slope changes during the observation period. During the flare, the $0.3-50$ keV spectrum was softest.

- During the X-ray flare, the reflection fraction is estimated to be the lowest which is consistent with the increase in coronal height. After the flare, the coronal height reaches at its lowest during the observation with the increase in the reflection fraction.

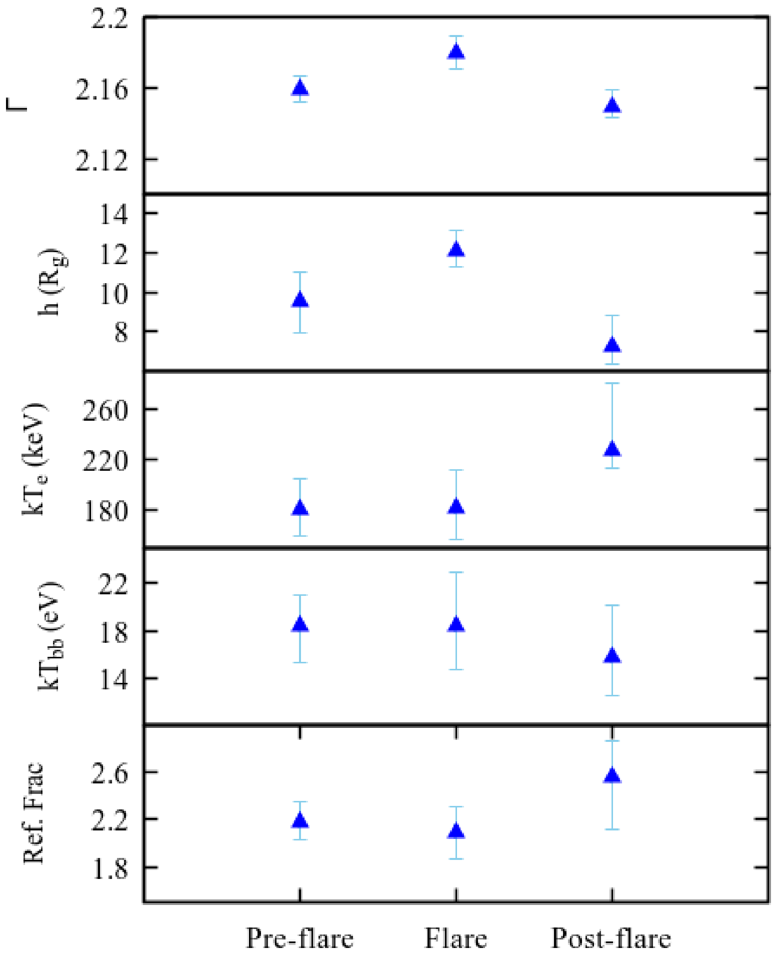

Figure 5.13: Variation of the best fit parameters are shown for three segments. The photon-index (Γ), coronal height (h) and ref.frac (R) are obtained from the `relxilllpion` model while coronal temperature (kT_e) and inner disc temperature (kT_{bb}) has been taken from the `compPS` model.

- We find that the temperature of the corona increased significantly after the flare (see Figure 5.13) from 184^{+26}_{-28} to 228^{+15}_{-52} keV. This re-heating of the corona is consistent with the hardening of the spectra after flare subsides.

- In this source, we found signatures of warm absorbers and ultra-fast outflows.

- NGC 4051 hosts a rapidly spinning black hole with spin parameter $a > 0.85$.

- NGC 4051 is positioned in the compactness-temperature plane at a region between the electron-electron coupling and the pair runaway line for a slab corona. This implies that the dominant process in the corona is pair production.

- Rapid spectral variabilities in NGC 4051 or similar type of NLS1s could be due to the change in the coronal geometry and/or location, which in turn produces small scale flares. Due to the short time scale of these flares, their origin in the corona is likely to be associated with ejection of the magnetic field.

Chapter 6

Concluding remarks and Future prospects

This chapter summarizes the main results of the thesis. Along with the summary, possible future work is discussed that can be carried out to understand different kinds of variability properties of different components in the AGNs. The primary findings of this thesis work are presented below.

6.1 Summary & Conclusion

In **Chapter 3**, a detailed timing and spectral analysis of multi-wavelength observations of a Seyfert galaxy Mrk 509 is presented to study the variability properties of the source in the optical/UV and X-ray bands and correlation between them. The long term simultaneous observations in multi-wavebands from the Swift observatory, spanning from 2006 to 2019, have been utilized to perform the analysis. In the beginning, we started the spectral analysis by fitting the average X-ray spectrum over the entire duration of observations that shows a strong soft X-ray excess above the power law continuum. We find two thermal components with temperatures of $\sim$120 eV and $\sim$460 eV that can accurately represent this soft X-ray excess. The warm Comptonizing zone is likely the one where the warm thermal component is coming from. From the timing studies, we found that the increasing wavelength resulted in a decrease in fractional variability amplitude with the exception that the hard X-ray emission is less variable. The strength of correlation among emission in the UV and optical bands was stronger than that found between the emission in the UV and X-ray bands. All these results indicate that the emitting region of hard X-ray and UV/optical emission may be distinct or partly interacting. While calculating the time lag between the UVW2 and other UV/optical and X-ray bands, a large excess was found in the U band and X-ray bands. The U band excess supposedly comes from the contribution of diffused emission from the BLRs. After filtering the light curves for slow variations and omitting the X-ray lags, the lag spectrum can be described approximately by the 4/3 rule for the standard accretion disc. All of these findings imply that the real disc is complicated and that the UV emission is probably processed further to produce X-ray and optical emission in the accretion disc.

Chapter 4 presents the spectral and timing properties of an AGN NGC 1566 during an X-ray outburst event in June 2018 when the X-ray flux of the source increased up to ∼25-30 times in comparison to its quiescence state. A detailed spectral and timing analysis was performed using semi-simultaneous pointed observations from *XMM-Newton*, *NuSTAR*, and *Swift* observatories in pre-outburst, outburst and post-outburst epochs. The broadband spectra in 0.5–70 keV range were fitted with various phenomenological and physical models. The spectra show a strong soft X-ray excess during the outburst, while it was feeble before and after. Since soft excess produces the majority of ionizing flux required to generate the broad optical lines, so the broad line occurred during the outburst the resulting in changing-look event. The origin of the soft excess emission is complex and found to be emitted from the warm Comptonizing region in the inner part of the accretion disc. Using the results obtained from this work, we find that the increase in the accretion rate, which could be due to the disc instability is responsible for the sudden rise in the luminosity and rule out the possibility of a tidal-disruption event (TDE). This result is corroborated by the 'q'-shape of the hardness-intensity plot that is the typical characteristic of outbursts in black hole binary systems. From this analysis, we find that NGC 1566 has a low-spinning supermassive black hole at the centre with spin parameter $a^* \sim 0.2$. We also considered a scenario in which the core of this AGN could be a merging supermassive black hole. This scenario could explain the recurrent outburst.

In **Chapter 5**, the findings on the investigation of the cause of a small flaring event in the narrow line Seyfert 1 (NLS1) galaxy NGC 4051 is presented. The flaring event was caught in a ∼300 ks long *NuSTAR* observation of the AGN. The event lasted for a duration of ∼100 ks. Though the AGN was also observed with *XMM-Newton* for a shorter exposure compared to the *NuSTAR* observation, the flaring event was partially caught in its rising phase. To investigate the timing and spectral properties of the AGN during the flaring event, the *NuSTAR* observation and the overlapping *XMM-Newton* exposure were segregated into pre-flare, flare and post-flare segments. We found that during the flare, the *NuSTAR* count rate peaked at 2.5 times the mean count rate before the flare. We explored the variation of X-ray emission in three phases using various phenomenological and physical models. The 0.3-50 keV X-ray spectrum of the source can be described by a composite model consisting of a primary continuum, reprocessed emission, warm absorber and ultra-fast outflows. From spectral analysis, we found that the reflection fraction drops significantly during the flare, accompanied by the increase in the coronal height to $\sim$12.2 R_g from $\sim$9.6 R_g (during the pre-flare phase) above the disc. The spectrum became softer during the flare showing the "softer when brighter" nature of the source. After the flare is over, the coronal height drops to $\sim$7.4 R_g and the corona heats up to the temperature of $\sim$228 keV. This indicates that there could be inflation of corona during the flare. We did not find any significant change in the inner accretion disc or the seed photon temperature during the observation. These results suggest that the flaring event occurred due to the change in the coronal properties rather than any notable change in the accretion disc.

6.2 Future work

6.2.1 X-ray/UV/Optical/IR variability of the bare AGN UGC 6728

In Chapter 3, a detailed cross-correlation study and lag spectrum of a Seyfert galaxy Mrk 509 (with the mass of the central black hole $M_{BH} \sim 10^8$ $M_\odot$) is presented using a long *Swift*XRT/UVOT monitoring campaign. As the time delay $\tau \propto M_{BH}^{2/3}$, therefore, the AGNs with lower black hole mass such as UGC 6728 ($M_{BH} = 7.1 \pm 4.0 \times 10^5 M_\odot$; Bentz et al., 2016) give us an opportunity to demonstrate similar kind of study within a few days of observation. We proposed multi-wavelength observations of UGC 6728 with *AstroSat*. The proposal was accepted for observing time with *AstroSat*, and data are available with us. The primary objectives of the proposal are as follows.

Lag spectrum- We aim to perform an intense cross-correlation and reverberation mapping analysis between emission in the UV/optical and X-ray bands using the *AstroSat* observation. We will use all the light curves with available UVIT filters and X-ray light curves in the soft band, e.g. below 2 keV as seen by SXT and hard band > 10 keV using LAXPC. Such correlation studies have never been done before for this AGN.

Connection between UV, soft excess, hard X-ray and thermal Comptonization-

We will attempt to establish a correlation study between the UV, soft excess and hard X-ray bands based on broadband spectroscopy. We will be able to study both the primary power-law generated through Comptonization and reflection components based on their variability.

6.2.2 Radio emission from NLS1

Seyfert galaxies are one of the classes of Active Galactic Nuclei (AGNs), which are usually radio-quiet and show prominent features like soft X-ray excess below 2 keV, Iron lines in 6-7 keV range, and Compton hump above 10 keV in their spectra. These are further classified as type 1 and 2 on the basis of their optical spectra and orientation. There is another subcategory, such as Narrow-Line Seyfert 1 (NLS1) galaxies, which show extreme properties in the AGN parameter space. This subclass was first identified by Osterbrock & Pogge, 1985 and named as 'NLS1' by Gaskell, 1985. The classification criteria used to define NLS1 are small width of the broad line < 2000 km/s in optical spectra as compared to the regular Seyfert 1, the ratio $[\mathrm{OIII}]/\mathrm{H}_\beta < 3$, and presence of strong Fe II emission lines. The extreme properties of NLS1s include the near Eddington accretion rate with a lower bound of the black hole mass range of AGNs. Because of their extreme properties, the NLS1s provide us with important insights into the physics of the AGNs. The majority of the NLS1 population is radio-quiet, but there is a small fraction (7%; Komossa et al., 2006) which are radio-loud and highly variable in radio emission, along with γ-ray emission. The radio-loudness of an AGN is commonly quantified by the radio-index, R which is the ratio of the radio flux at 6 cm over the optical flux at 4400Å. The AGNs with $R > 10$ are usually referred to as radio-loud. These intriguing objects are considered to probe the formation of jets at the near-Eddington rate and low black hole mass, unlike the blazars or radio galaxies.

The understanding of launching powerful radio jets in radio-loud AGNs is still not complete. The role of the accretion disk and black hole spin in the formation and collimation of jets is an open question. Recent studies show that the hot corona, which is responsible for the strong X-ray emission in the AGNs, may be powered by failed jets (Yuan et al., 2019). This needs explanation on the factors that decide the failed or successful launching of jets. Unlike blazars, the NLS1 shows a strong thermal component originating from the accretion disk along with a non-thermal component from the jets. As the NLS1 possesses a unique position in the parameter space (Figure 6.1), these are ideal laboratories to disentangle these key questions in the field of accretion physics.

There are dozens of NLS1 sources which are radio-loud; e.g. RX J1633+4179, PKS0558–504,

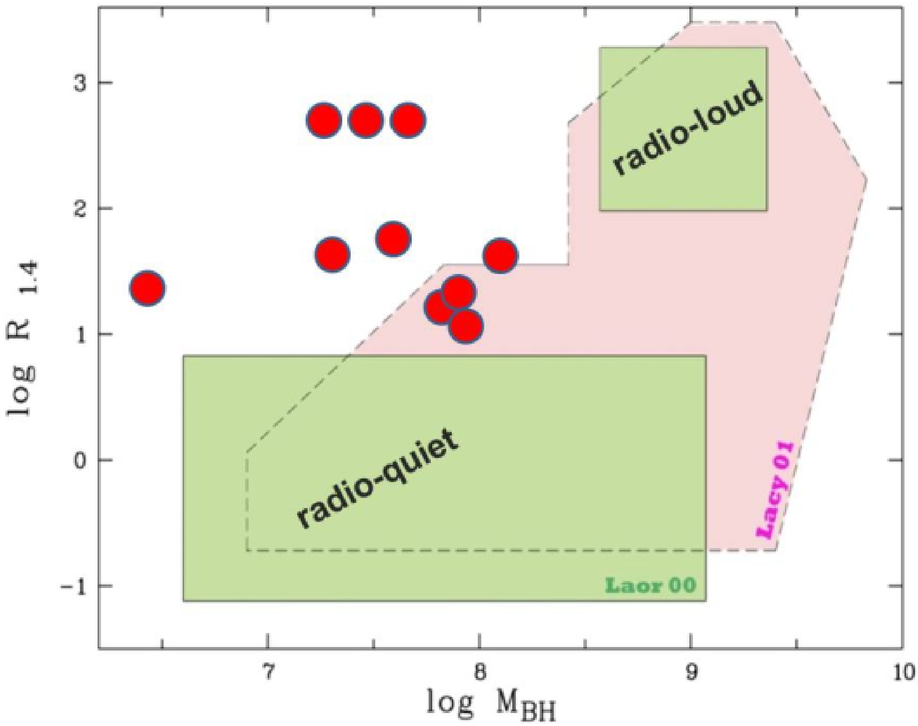

Figure 6.1: Distribution of NLS1 galaxies (red bullets) in radio-loudness vs SMBH mass diagram. Image credit: Komossa et al., 2006

RXJ0134–4258, SDSSJ094857.3+002225, and SDSSJ172206.03+565451.6. We have selected one, NLS1 RX J1633+4179, as the first source for the research objectives. This radio-loud NLS1 galaxy is located at a redshift z=0.116 with radio-loudness parameter $R_5 = f(5GHz)/f(4400) > 100$. Its relativistic radio-jet is pointed almost towards our line-of-sight with an inclination angle 10 degrees (Yuan et al., 2008) like blazars. This source is known to show an ultra-soft X-ray excess which is modelled by thermal emission from the accretion disk with the disk blackbody temperature of ∼32 eV. Interestingly, this temperature is lower than that usually found in the radio-quiet NLS1s and follows the standard accretion disk (Mallick et al., 2016). Using XMM-Newton observations, Mallick et al. (2016) showed that the temperature of ultra-soft X-ray excess is ∼40 eV. The UV part of the spectrum was fitted with a power-law of photon index ∼3.25, which is comparable to the typical value of photon index in FSRQs. This indicates that the UV emission is not entirely emitted from the disk and has some contribution from other parts, likely from the radio jet. The first result on the ultra-soft X-ray excess implies that the nature of the accretion disk in radio-loud NLS1s is somewhat different from that in the radio-quiet sources. In this regard, there must be some connection between the accretion disk and jet formation. The second one, the UV enhancement, is explained as the high energy tail of synchrotron emission from the radio jet. One possibility to confirm this is to get the correlation between the IR and UV emission as in both the bands, the contribution comes from synchrotron emission as well as an accretion disk. The variability time scale in different energy bands depends on various physical mechanisms such as X-ray reprocessing, Comptonization and absorption along the line-of-sight. Therefore, the correlation and lag studies between X-ray and UV/optical/IR bands is one of the tools to diagnose the origin of emissions in different energies. Since the time lag $\tau \propto M_{BH}^{2/3}$, this source, harbouring a low mass black hole ($\sim 3 \times 10^6\ M_\odot$; Yuan et al., 2010) can be studied for a few days of observation from any X-ray observatory. Following are the main research objectives on this topic:

To check the IR, optical/UV, and X-ray variabilities and correlation between them- In the previous studies of this source (Mallick et al., 2016), it has been found that the soft energy flux (0.3-1 keV range) is not correlated with the hard energy flux (1-10 keV range). This means that the cause of variability of soft and hard X-ray photons is different. Also, the fractional variability amplitude of the hard band ($17.9 \pm 1.4\%$) is greater than that in the soft band ($9.6 \pm 1.7\%$). This may be due to the intrinsic variable nature of the primary continuum instead of absorption. This can be confirmed from the correlation studies in the soft band (0.3-1 keV), the intermediate band (1-10 keV) and the hard band (above 10 keV) by using broadband X-ray observation. As mentioned previously, the origin of UV excess is associated with the jets, which should be in synchronization with the IR emission from the jet. Simultaneous observations in UV and IR/optical bands would help to verify the origin of the UV emission. Therefore, my main objective is to perform cross-correlation and reverberation mapping studies between the IR/UV/optical and X-ray energy bands. This task has not been performed in the previous studies for this source. This can shed light on whether the UV emission is entirely disk emission or reprocessed emission from soft X-ray photons.

To understand the jet-corona coupling- In Seyfert 1 AGNs, the origin of soft excess is debatable. However, in RX J1633+4719, this component is described as direct thermal emission from the disk. With reference to the cold Comptonization model, this is the indication of the lack of Comptonization region that is supposed to be responsible for the soft excess. This implies that in radio-quiet AGNs, the Comptonization region may be formed by aborted jets whose kinetic energy is converted into internal energy to heat the electrons and form the Comptonization region. This is analogous to the soft/hard states in the black hole X-ray binaries with relatively weak corona and can be correlated to the formation of jets at the cost of suppression of corona. The absence of reflection components like iron line also supports the lack of a strong hot Comptonization medium, which is essential in the reflection model. Therefore, this object and similar types of radio-loud NLS1s with high radio-loudness parameters are important to disentangle the enigma of the formation of jet and its connection with the corona. This can be fulfilled by the broad-band spectral analysis of the source at different epochs.

Dedicated simultaneous multi-wavelength observation campaigns with the next generation X-ray telescopes will be able to reveal the actual nature of the sources in near future. Already existing X-ray observatories such as NuSTAR, XMM-Newton and Chandra along with various radio telescopes like GMRT, LOFAR, VLA, MeerKAT, SKA, EHT hold the potential to deepen our understanding on the extreme environment near the black holes.

Bibliography

Akiyama, K., Alberdi, A., Alef, W., et al. 2019, First M87 event horizon telescope results. IV. Imaging the central supermassive black hole, The Astrophysical Journal Letters, 875, L4

Alexander, T. 1997, Is AGN Variability Correlated with Other AGN Properties? ZDCF Analysis of Small Samples of Sparse Light Curves, ed. D. Maoz, A. Sternberg, & E. M. Leibowitz, Vol. 218, 163

Alloin, D., Pelat, D., Phillips, M., & Whittle, M. 1985, Recent spectral variations in the active nucleus of NGC 1566., ApJ, 288, 205

Alloin, D., Pelat, D., Phillips, M. M., Fosbury, R. A. E., & Freeman, K. 1986, Recurrent Outbursts in the Broad-Line Region of NGC 1566, ApJ, 308, 23

Amaro-Seoane, P., Brem, P., & Cuadra, J. 2013, Tidal Disruptions in Circumbinary Disks. I. Star Formation, Dynamics, and Binary Evolution, ApJ, 764, 14

Antonucci, R. 1993, Unified models for active galactic nuclei and quasars., ARA&A, 31, 473

Antonucci, R. R. J. & Miller, J. S. 1985, Spectropolarimetry and the nature of NGC 1068., ApJ, 297, 621

Aretxaga, I., Joguet, B., Kunth, D., Melnick, J., & Terlevich, R. J. 1999, Seyfert 1 Mutation of the Classical Seyfert 2 Nucleus NGC 7582, ApJ, 519, L123

Arévalo, P., Uttley, P., Kaspi, S., et al. 2008, Correlated X-ray/optical variability in the quasar MR2251-178, MNRAS, 389, 1479

Arnaud, K. A. 1996, in Astronomical Society of the Pacific Conference Series, Vol. 101, Astronomical Data Analysis Software and Systems V, ed. G. H. Jacoby & J. Barnes, 17

Arnaud, K. A., Branduardi-Raymont, G., Culhane, J. L., et al. 1985, EXOSAT observations of a strong soft X-ray excess in MKN 841., MNRAS, 217, 105

Arévalo, P., Uttley, P., Lira, P., et al. 2009, Correlation and time delays of the X-ray and optical emission of the Seyfert Galaxy NGC 3783, Monthly Notices of the Royal Astronomical Society, 397, 2004

Avni, Y. 1976, Energy spectra of X-ray clusters of galaxies., ApJ, 210, 642

Baloković, M., Brightman, M., Harrison, F. A., et al. 2018, New Spectral Model for Constraining Torus Covering Factors from Broadband X-Ray Spectra of Active Galactic Nuclei, ApJ, 854, 42

Barthelmy, S. D., Barbier, L. M., Cummings, J. R., et al. 2005, The Burst Alert Telescope (BAT) on the SWIFT Midex Mission, Space Sci. Rev., 120, 143

Bennett, C. L., Halpern, M., Hinshaw, G., et al. 2003, First-Year Wilkinson Microwave Anisotropy Probe (WMAP) Observations: Preliminary Maps and Basic Results, ApJS, 148, 1

Bentz, M. C., Batiste, M., Seals, J., et al. 2016, A Low-mass Black Hole in the Nearby Seyfert Galaxy UGC 06728, ApJ, 831, 2

Bentz, M. C., Denney, K. D., Cackett, E. M., et al. 2007, NGC 5548 in a Low-Luminosity State: Implications for the Broad-Line Region, ApJ, 662, 205

Bentz, M. C., Walsh, J. L., Barth, A. J., et al. 2009, The Lick AGN Monitoring Project: Broad-line Region Radii and Black Hole Masses from Reverberation Mapping of Hβ, ApJ, 705, 199

Bianchi, S., Guainazzi, M., Matt, G., Fonseca Bonilla, N., & Ponti, G. 2009a, CAIXA: a catalogue of AGN in the XMM-Newton archive. I. Spectral analysis, A&A, 495, 421

Bianchi, S., Panessa, F., Barcons, X., et al. 2012, Simultaneous X-ray and optical observations of true type 2 Seyfert galaxies, Monthly Notices of the Royal Astronomical Society, 426, 3225

Bianchi, S., Piconcelli, E., Chiaberge, M., et al. 2009b, How Complex is the Obscuration in Active Galactic Nuclei? New Clues from the Suzaku Monitoring of the X-Ray Absorbers in NGC 7582, ApJ, 695, 781

Blandford, R. D. & McKee, C. F. 1982, Reverberation mapping of the emission line regions of Seyfert galaxies and quasars., ApJ, 255, 419

Blustin, A. J., Page, M. J., Fuerst, S. V., Branduardi-Raymont, G., & Ashton, C. E. 2005, The nature and origin of Seyfert warm absorbers, A&A, 431, 111

Bondi, H. 1952, On spherically symmetrical accretion, MNRAS, 112, 195

Braito, V., Ballo, L., Reeves, J. N., et al. 2013, Decoupling absorption and continuum variability in the Seyfert 2 NGC 4507, MNRAS, 428, 2516

Braito, V., Reeves, J. N., Dewangan, G. C., et al. 2007, Relativistic Iron K Emission and Absorption in the Seyfert 1.9 Galaxy MCG -5-23-16, ApJ, 670, 978

Brandt, W. N., Mathur, S., & Elvis, M. 1997, A comparison of the hard ASCA spectral slopes of broad- and narrow-line Seyfert 1 galaxies, MNRAS, 285, L25

Breedt, E., McHardy, I. M., Arévalo, P., et al. 2010, Twelve years of X-ray and optical variability in the Seyfert galaxy NGC 4051, MNRAS, 403, 605

Buisson, D. J. K., Lohfink, A. M., Alston, W. N., & Fabian, A. C. 2016, Ultraviolet and X-ray variability of active galactic nuclei with Swift, Monthly Notices of the Royal Astronomical Society, 464, 3194

Burrows, D. N., Hill, J. E., Nousek, J. A., et al. 2005, The Swift X-Ray Telescope, Space Sci. Rev., 120, 165

Cackett, E. M., Chiang, C.-Y., McHardy, I., et al. 2018, Accretion Disk Reverberation with-Hubble Space TelescopeObservations of NGC 4593: Evidence for Diffuse Continuum Lags, The Astrophysical Journal, 857, 53

Cackett, E. M., Horne, K., & Winkler, H. 2007, Testing thermal reprocessing in active galactic nuclei accretion discs, MNRAS, 380, 669

Cappi, M., Tombesi, F., Bianchi, S., et al. 2009, X-ray evidence for a mildly relativistic and variable outflow in the luminous Seyfert 1 galaxy Mrk 509, A&A, 504, 401

Chatterjee, A., Chakrabarti, S. K., Ghosh, H., & Garain, S. K. 2018, Images and spectra of time-dependent two-component advective flow in presence of outflows, MNRAS, 478, 3356

Chen, X., Madau, P., Sesana, A., & Liu, F. K. 2009, Enhanced Tidal Disruption Rates from Massive Black Hole Binaries, ApJ, 697, L149

Churazov, E., Gilfanov, M., & Revnivtsev, M. 2001, Soft state of Cygnus X-1: stable disc and unstable corona, MNRAS, 321, 759

Cleveland, W. S. & Devlin, S. J. 1988, Locally Weighted Regression: An Approach to Regression Analysis by Local Fitting, Journal of the American Statistical Association, 83, 596

Cohen, R. D., Rudy, R. J., Puetter, R. C., Ake, T. B., & Foltz, C. B. 1986, Variability of Markarian 1018: Seyfert 1.9 to Seyfert 1, ApJ, 311, 135

Collier, S., Horne, K., Wanders, I., & Peterson, B. M. 1999, A new direct method for measuring the Hubble constant from reverberating accretion discs in active galaxies, MNRAS, 302, L24

Collier, S. J., Horne, K., Kaspi, S., et al. 1998, Steps toward Determination of the Size and Structure of the Broad-Line Region in Active Galactic Nuclei. XIV. Intensive Optical Spectrophotometric Observations of NGC 7469, ApJ, 500, 162

Connolly, S. D., McHardy, I. M., Skipper, C. J., & Emmanoulopoulos, D. 2016, Long-term X-ray spectral variability in AGN from the Palomar sample observed by Swift, MNRAS, 459, 3963

Crenshaw, D. M. & Kraemer, S. B. 2012, Feedback from Mass Outflows in Nearby Active Galactic Nuclei. I. Ultraviolet and X-Ray Absorbers, ApJ, 753, 75

Cutri, R. M., Mainzer, A. K., Dyk, S. D. V., & Jiang, N. 2018, NEOWISE Mid-Infrared Observations of the Outburst in the Nucleus of NGC 1566, The Astronomer's Telegram, 11913, 1

Czerny, B. 2006, in Astronomical Society of the Pacific Conference Series, Vol. 360, AGN Variability from X-Rays to Radio Waves, ed. C. M. Gaskell, I. M. McHardy, B. M. Peterson, & S. G. Sergeev, 265

da Silva, P., Steiner, J. E., & Menezes, R. B. 2017, NGC 1566: analysis of the nuclear region from optical and near-infrared Integral Field Unit spectroscopy, MNRAS, 470, 3850

Dai, X., Kochanek, C. S., Chartas, G., et al. 2009, The sizes of the X-ray and optical emission regions of RXJ 1131-1231, The Astrophysical Journal, 709, 278

Dai, X., Stanek, K. Z., Kochanek, C. S., Shappee, B. J., & ASAS-SN Collaboration. 2018, ASAS-SN Light Curve Reveals Dramatic Variability of Seyfert 1.5 AGN in NGC 1566, The Astronomer's Telegram, 11893, 1

Dauser, T., Garcia, J., Parker, M. L., Fabian, A. C., & Wilms, J. 2014, The role of the reflection fraction in constraining black hole spin., MNRAS, 444, L100

Dauser, T., García, J., Walton, D. J., et al. 2016, Normalizing a relativistic model of X-ray reflection. Definition of the reflection fraction and its implementation in relxill, A&A, 590, A76

Dauser, T., Wilms, J., Reynolds, C. S., & Brenneman, L. W. 2010, Broad emission lines for a negatively spinning black hole, MNRAS, 409, 1534

De Marco, B., Zdziarski, A. A., Ponti, G., et al. 2021, The inner flow geometry in MAXI J1820+070 during hard and hard-intermediate states, A&A, 654, A14

de Vaucouleurs, G. 1973, Southern Galaxies.VI. Luminosity Distribution in the Seyfert Galaxy NGC 1566, ApJ, 181, 31

de Vaucouleurs, G. & de Vaucouleurs, A. 1961, Classification and radial velocities of bright southern galaxies., MNRAS, 68, 69

Denney, K. D., De Rosa, G., Croxall, K., et al. 2014, The Typecasting of Active Galactic Nuclei: Mrk 590 no Longer Fits the Role, ApJ, 796, 134

Denney, K. D., Watson, L. C., Peterson, B. M., et al. 2009, A Revised Broad-line Region Radius and Black Hole Mass for the Narrow-line Seyfert 1 NGC 4051, ApJ, 702, 1353

Done, C., Davis, S. W., Jin, C., Blaes, O., & Ward, M. 2012, Intrinsic disc emission and the soft X-ray excess in active galactic nuclei, MNRAS, 420, 1848

Done, C., Gierliński, M., & Kubota, A. 2007, Modelling the behaviour of accretion flows in X-ray binaries. Everything you always wanted to know about accretion but were afraid to ask, A&A Rev., 15, 1

Done, C. & Krolik, J. H. 1996, Kinematics of the Broad Emission Line Region in NGC 5548, ApJ, 463, 144

Ducci, L., Siegert, T., Diehl, R., et al. 2018, INTEGRAL detection of hard X-ray emission from NGC 1566, The Astronomer's Telegram, 11754, 1

Ebrero, Kriss, G. A., Kaastra, J. S., et al. 2011, Multiwavelength campaign on Mrk 509 - V. Chandra-LETGS observation of the ionized absorber, A&A, 534, A40

Edelson, R., Gelbord, J., Cackett, E., et al. 2019, The First Swift Intensive AGN Accretion Disk Reverberation Mapping Survey, The Astrophysical Journal, 870, 123

Edelson, R., Gelbord, J. M., Horne, K., et al. 2015, Space Telescope and Optical Reverberation Mapping Project. II. Swift and HST Reverberation Mapping of the Accretion Disk of NGC 5548, ApJ, 806, 129

Edelson, R., Griffiths, G., Markowitz, A., et al. 2001, High Temporal Resolution XMM-Newton Monitoring of PKS 2155-304, ApJ, 554, 274

Edelson, R. & Malkan, M. 2012, Reliable Identifications of Active Galactic Nuclei from the WISE, 2MASS, and ROSAT All-Sky Surveys, ApJ, 751, 52

Edelson, R., Turner, T. J., Pounds, K., et al. 2002, X-Ray Spectral Variability and Rapid Variability of the Soft X-Ray Spectrum Seyfert 1 Galaxies Arakelian 564 and Ton S180, ApJ, 568, 610

Edelson, R. et al. 2017, Swift monitoring of NGC 4151: Evidence for a Second X-ray/UV Reprocessing, Astrophys. J., 840, 41

Edelson, R. A., Alexander, T., Crenshaw, D. M., et al. 1996, Multiwavelength Observations of Short-Timescale Variability in NGC 4151. IV. Analysis of Multiwavelength Continuum Variability, ApJ, 470, 364

Edge, D. O., Shakeshaft, J. R., McAdam, W. B., Baldwin, J. E., & Archer, S. 1959, A survey of radio sources at a frequency of 159 Mc/s., MmRAS, 68, 37

Elitzur, M. 2012, On the Unification of Active Galactic Nuclei, ApJ, 747, L33

Elitzur, M., Ho, L. C., & Trump, J. R. 2014, Evolution of broad-line emission from active galactic nuclei, MNRAS, 438, 3340

Elvis, M., Risaliti, G., Nicastro, F., et al. 2004, An Unveiling Event in the Type 2 Active Galactic Nucleus NGC 4388:A Challenge for a Parsec-Scale Absorber, ApJ, 615, L25

Eracleous, M. & Halpern, J. P. 2001, NGC 3065: A Certified LINER with Broad, Variable Balmer Lines, ApJ, 554, 240

Eracleous, M., Livio, M., Halpern, J. P., & Storchi-Bergmann, T. 1995, Elliptical Accretion Disks in Active Galactic Nuclei, ApJ, 438, 610

Evans, P. A., Beardmore, A. P., Page, K. L., et al. 2009, Methods and results of an automatic analysis of a complete sample of Swift-XRT observations of GRBs, MNRAS, 397, 1177

Evans, P. A., Beardmore, A. P., Page, K. L., et al. 2007, An online repository of Swift/XRT light curves of γ-ray bursts, A&A, 469, 379

Event Horizon Telescope Collaboration, Akiyama, K., Alberdi, A., et al. 2022, First Sagittarius A* Event Horizon Telescope Results. I. The Shadow of the Supermassive Black Hole in the Center of the Milky Way, ApJ, 930, L12

Event Horizon Telescope Collaboration, Akiyama, K., Alberdi, A., et al. 2019, First M87 Event Horizon Telescope Results. I. The Shadow of the Supermassive Black Hole, ApJ, 875, L1

Ezhikode, S. H., Gandhi, P., Done, C., et al. 2017, Determining the torus covering factors for a sample of type 1 AGN in the local Universe, MNRAS, 472, 3492

Fabian, A. C. 1994, Hot Plasmas and the Generation of Gamma Rays, ApJS, 92, 555

Fabian, A. C., Ballantyne, D. R., Merloni, A., et al. 2002, How the X-ray spectrum of a narrow-line Seyfert 1 galaxy may be reflection-dominated, MNRAS, 331, L35

Fabian, A. C., Iwasawa, K., Reynolds, C. S., & Young, A. J. 2000, Broad Iron Lines in Active Galactic Nuclei, PASP, 112, 1145

Fabian, A. C., Lohfink, A., Kara, E., et al. 2015, Properties of AGN coronae in the NuSTAR era, MNRAS, 451, 4375

Fabian, A. C. & Miniutti, G. 2005, in Kerr Fest: Black Holes in Astrophysics, General Relativity and Quantum Gravity

Fabian, A. C., Miniutti, G., Gallo, L., et al. 2004, X-ray reflection in the narrow-line Seyfert 1 galaxy 1H 0707–495, Monthly Notices of the Royal Astronomical Society, 353, 1071

Fabian, A. C., Zoghbi, A., Ross, R. R., et al. 2009, Broad line emission from iron K- and L-shell transitions in the active galaxy 1H0707-495, Nature, 459, 540

Fabian, A. C., Zoghbi, A., Wilkins, D., et al. 2012, 1H 0707-495 in 2011: an X-ray source within a gravitational radius of the event horizon, MNRAS, 419, 116

Fanaroff, B. L. & Riley, J. M. 1974, The morphology of extragalactic radio sources of high and low luminosity, MNRAS, 167, 31P

Fath, E. A. 1909, The spectra of some spiral nebulae and globular star clusters, Lick Observatory Bulletin, 149, 71

Fausnaugh, M. M., Denney, K. D., Barth, A. J., et al. 2016, Space Telescope and Optical Reverberation Mapping Project. III. Optical Continuum Emission and Broadband Time Delays in NGC 5548, ApJ, 821, 56

Ferrigno, C., Siegert, T., Sanchez-Fernandez, C., et al. 2018, Swift follow-up observations determine enhanced nuclear activity from NGC 1566, The Astronomer's Telegram, 11783, 1

Foreman-Mackey, D. 2016, corner.py: Scatterplot matrices in Python, The Journal of Open Source Software, 1, 24

Gabriel, C., Denby, M., Fyfe, D. J., et al. 2004, in Astronomical Society of the Pacific Conference Series, Vol. 314, Astronomical Data Analysis Software and Systems (ADASS) XIII, ed. F. Ochsenbein, M. G. Allen, & D. Egret, 759

García, J., Dauser, T., Lohfink, A., et al. 2014, Improved Reflection Models of Black Hole Accretion Disks: Treating the Angular Distribution of X-Rays, ApJ, 782, 76

García, J., Dauser, T., Reynolds, C. S., et al. 2013, X-Ray Reflected Spectra from Accretion Disk Models. III. A Complete Grid of Ionized Reflection Calculations, ApJ, 768, 146

García, J. & Kallman, T. R. 2010, X-ray Reflected Spectra from Accretion Disk Models. I. Constant Density Atmospheres, ApJ, 718, 695

García, J. A., Kara, E., Walton, D., et al. 2019, Implications of the Warm Corona and Relativistic Reflection Models for the Soft Excess in Mrk 509, ApJ, 871, 88

Gardner, E. & Done, C. 2017, The origin of the UV/optical lags in NGC 5548, Monthly Notices of the Royal Astronomical Society, 470, 3591

Gaskell, C. M. 1985, Observational evidence for the radiative acceleration of broad-line clouds in Seyfert 1 galaxies and quasars., ApJ, 291, 112

Gaskell, C. M. & Peterson, B. M. 1987, The Accuracy of Cross-Correlation Estimates of Quasar Emission-Line Region Sizes, ApJS, 65, 1

Gehrels, N., Chincarini, G., Giommi, P., et al. 2004, The Swift Gamma-Ray Burst Mission, ApJ, 611, 1005

George, I. M. & Fabian, A. C. 1991, X-ray reflection from cold matter in Active Galactic Nuclei and X-ray binaries., MNRAS, 249, 352

Ghisellini, G. 2013, Radiative Processes in High Energy Astrophysics, Vol. 873

Ghisellini, G., Haardt, F., & Fabian, A. C. 1993, On re-acceleration, pairs and the high-energy spectrum of AGN and galactic black hole candidates., MNRAS, 263, L9

Ghisellini, G., Haardt, F., & Matt, G. 1994, The contribution of the obscuring torus to the X-ray spectrum of Seyfert galaxies: a test for the unification model., MNRAS, 267, 743

Ghosh, R. & Laha, S. 2020, A broad-band X-ray spectral study of the Seyfert 1 galaxy ESO 141-G055 with XMM-Newton and NuSTAR, MNRAS, 497, 4213

Gierliński, M. & Done, C. 2004, Is the soft excess in active galactic nuclei real?, MNRAS, 349, L7

Gliozzi, M., Papadakis, I. E., Sambruna, R. M., & Eracleous, M. 2004, in AAS/High Energy Astrophysics Division, Vol. 8, AAS/High Energy Astrophysics Division #8, 04.02

Goodman, J. & Weare, J. 2010, Ensemble samplers with affine invariance, Communications in Applied Mathematics and Computational Science, 5, 65

Greenstein, J. L. 1963, Red-Shift of the Unusual Radio Source: 3C 48, Nature, 197, 1041

Grupe, D., Komossa, S., & Schartel, N. 2018a, Swift observations in all filters of the Seyfert galaxy NGC 1566 in outburst, The Astronomer's Telegram, 11903, 1

Grupe, D., Mikula, R., Komossa, S., et al. 2019, Swift catches the changing-look AGN NGC 1566 in an X-ray outburst again, The Astronomer's Telegram, 12826, 1

Grupe, D., Mikula, R., Komossa, S., et al. 2018b, Rebrightening of the changing look Seyfert galaxy NGC 1566, The Astronomer's Telegram, 12314, 1

Guainazzi, M. 2002, The formerly X-ray reflection-dominated Seyfert 2 galaxy NGC 6300, MNRAS, 329, L13

Guainazzi, M., Mihara, T., Otani, C., & Matsuoka, M. 1996, Spectral Variability and Iron Line Emission in the ASCA Observations of the Seyfert 1 Galaxy NGC 4051, PASJ, 48, 781

Guainazzi, M., Risaliti, G., Awaki, H., et al. 2016, The nature of the torus in the heavily obscured AGN Markarian 3: an X-ray study, MNRAS, 460, 1954

Haardt, F. & Maraschi, L. 1991, A Two-Phase Model for the X-Ray Emission from Seyfert Galaxies, ApJ, 380, L51

Haardt, F. & Maraschi, L. 1993, X-Ray Spectra from Two-Phase Accretion Disks, ApJ, 413, 507

Haardt, F., Maraschi, L., & Ghisellini, G. 1994, A Model for the X-Ray and Ultraviolet Emission from Seyfert Galaxies and Galactic Black Holes, ApJ, 432, L95

Harrison, F. A., Craig, W. W., Christensen, F. E., et al. 2013, The Nuclear Spectroscopic Telescope Array (NuSTAR) High-energy X-Ray Mission, ApJ, 770, 103

Hayasaki, K. & Loeb, A. 2016, Detection of Gravitational Wave Emission by Supermassive Black Hole Binaries Through Tidal Disruption Flares, Scientific Reports, 6, 35629

Hayasaki, K., Mineshige, S., & Sudou, H. 2007, Binary Black Hole Accretion Flows in Merged Galactic Nuclei, PASJ, 59, 427

Hernández Santisteban, J. V., Edelson, R., Horne, K., et al. 2020, Intensive disc-reverberation mapping of Fairall 9: first year of Swift and LCO monitoring, Monthly Notices of the Royal Astronomical Society, 498, 5399

HI4PI Collaboration, Ben Bekhti, N., Flöer, L., et al. 2016, HI4PI: A full-sky H I survey based on EBHIS and GASS, A&A, 594, A116

Hill, J. E., Burrows, D. N., Nousek, J. A., et al. 2004, in Society of Photo-Optical Instrumentation Engineers (SPIE) Conference Series, Vol. 5165, Proc. SPIE, ed. K. A. Flanagan & O. H. W. Siegmund, 217–231

Homan, J., Wijnands, R., van der Klis, M., et al. 2001, Correlated X-Ray Spectral and Timing Behavior of the Black Hole Candidate XTE J1550-564: A New Interpretation of Black Hole States, ApJS, 132, 377

Huchra, J., Latham, D. W., da Costa, L. N., Pellegrini, P. S., & Willmer, C. N. A. 1993, The Morphological Catalogue of Galaxies Equatorial Survey, AJ, 105, 1637

Ilić, D., Popović, L. Č., Ciroi, S., La Mura, G., & Rafanelli, P. 2010, in Journal of Physics Conference Series, Vol. 257, Journal of Physics Conference Series, 012034

Jana, A., Chatterjee, A., Kumari, N., et al. 2020, Probing the nuclear and circumnuclear properties of NGC 6300 using X-ray observations, MNRAS, 499, 5396

Jana, A., Kumari, N., Nandi, P., et al. 2021, Broad-band X-ray observations of the 2018 outburst of the changing-look active galactic nucleus NGC 1566, MNRAS, 507, 687

Jansen, F., Lumb, D., Altieri, B., et al. 2001, XMM-Newton observatory. I. The spacecraft and operations, A&A, 365, L1

Kaastra, Detmers, R. G., Mehdipour, M., et al. 2012, Multiwavelength campaign on Mrk 509 - VIII. Location of the X-ray absorber, A&A, 539, A117

Kaspi, S., Smith, P. S., Netzer, H., et al. 2000, Reverberation Measurements for 17 Quasars and the Size-Mass-Luminosity Relations in Active Galactic Nuclei, ApJ, 533, 631

Kaufman, J., Blaes, O. M., & Hirose, S. 2017, The contribution of bulk Comptonization to the soft X-ray excess in AGN, MNRAS, 467, 1734

Kelly, B. C., Bechtold, J., & Siemiginowska, A. 2009, Are the variations in quasar optical flux driven by thermal fluctuations ?, The Astrophysical Journal, 698, 895

Kembhavi, A. K. & Narlikar, J. V. 1999, Quasars and Active Galactic Nuclei: An Introduction (Cambridge University Press)

Kishimoto, M., Hönig, S. F., Antonucci, R., et al. 2013, Evidence for a Receding Dust Sublimation Region around a Supermassive Black Hole, ApJ, 775, L36

Komossa, S. 2015, Tidal disruption of stars by supermassive black holes: Status of observations, Journal of High Energy Astrophysics, 7, 148

Komossa, S. 2017, Tidal disruption of stars by super-massive black holes—XMM-Newton highlights and the next decade, Astronomische Nachrichten, 338, 256

Komossa, S., Halpern, J., Schartel, N., et al. 2004, A Huge Drop in the X-Ray Luminosity of the Nonactive Galaxy RX J1242.6-1119A, and the First Postflare Spectrum: Testing the Tidal Disruption Scenario, ApJ, 603, L17

Komossa, S., Voges, W., Xu, D., et al. 2006, Radio-loud Narrow-Line Type 1 Quasars, The Astronomical Journal, 132, 531

Koratkar, A. & Blaes, O. 1999, The Ultraviolet and Optical Continuum Emission in Active Galactic Nuclei: The Status of Accretion Disks, PASP, 111, 1

Korista, K. T. & Goad, M. R. 2001, The Variable Diffuse Continuum Emission of Broad-Line Clouds, ApJ, 553, 695

Korista, K. T. & Goad, M. R. 2004, What the Optical Recombination Lines Can Tell Us about the Broad-Line Regions of Active Galactic Nuclei, ApJ, 606, 749

Korista, K. T. & Goad, M. R. 2019, Quantifying the impact of variable BLR diffuse continuum contributions on measured continuum interband delays, Monthly Notices of the Royal Astronomical Society, 489, 5284

Kormendy, J. & Richstone, D. 1995, Inward Bound—The Search For Supermassive Black Holes In Galactic Nuclei, ARA&A, 33, 581

Koss, M., Trakhtenbrot, B., Ricci, C., et al. 2017, BAT AGN Spectroscopic Survey. I. Spectral Measurements, Derived Quantities, and AGN Demographics, ApJ, 850, 74

Krolik, J. H. 1999, Active galactic nuclei : from the central black hole to the galactic environment

Krolik, J. H. & Begelman, M. C. 1988, Molecular Tori in Seyfert Galaxies: Feeding the Monster and Hiding It, ApJ, 329, 702

Krolik, J. H., Horne, K., Kallman, T. R., et al. 1991, Ultraviolet Variability of NGC 5548: Dynamics of the Continuum Production Region and Geometry of the Broad-Line Region, ApJ, 371, 541

Krolik, J. H. & Kriss, G. A. 2001, Warm Absorbers in Active Galactic Nuclei: A Multitemperature Wind, ApJ, 561, 684

Krongold, Y., Nicastro, F., Brickhouse, N. S., et al. 2003, Toward a Self-Consistent Model of the Ionized Absorber in NGC 3783, ApJ, 597, 832

Kubota, A. & Done, C. 2018, A physical model of the broad-band continuum of AGN and its implications for the UV/X relation and optical variability, MNRAS, 480, 1247

Kuin, P., Bozzo, E., Ferrigno, C., et al. 2018, Swift/UVOT observation of the enhanced nuclear activity from NGC 1566, The Astronomer's Telegram, 11786, 1

Kumari, N., Pal, M., Naik, S., et al. 2021, Complex optical/UV and X-ray variability in Seyfert 1 galaxy Mrk 509, PASA, 38, e042

Laha, S., Reynolds, C. S., Reeves, J., et al. 2021, Ionized outflows from active galactic nuclei as the essential elements of feedback, Nature Astronomy, 5, 13

Lamer, G., McHardy, I. M., Uttley, P., & Jahoda, K. 2003, X-ray spectral variability of the Seyfert galaxy NGC 4051, MNRAS, 338, 323

Lawrence, A. 2018, Quasar viscosity crisis, Nature Astronomy, 2, 102

Lawther, D., Goad, M. R., Korista, K. T., Ulrich, O., & Vestergaard, M. 2018, Quantifying the diffuse continuum contribution of BLR Clouds to AGN Continuum Inter-band Delays, Monthly Notices of the Royal Astronomical Society, 481, 533

Leighly, K. M. 1999, A Comprehensive Spectral and Variability Study of Narrow-Line Seyfert 1 Galaxies Observed by ASCA. II. Spectral Analysis and Correlations, ApJS, 125, 317

Li, G., Naoz, S., Kocsis, B., & Loeb, A. 2015, Implications of the eccentric Kozai-Lidov mechanism for stars surrounding supermassive black hole binaries, MNRAS, 451, 1341

Lyubarskii, Y. E. 1997, Flicker noise in accretion discs, MNRAS, 292, 679

MacLeod, C. L., Ross, N. P., Lawrence, A., et al. 2016, A systematic search for changing-look quasars in SDSS, MNRAS, 457, 389

Magdziarz, P. & Zdziarski, A. A. 1995, Angle-dependent Compton reflection of X-rays and gamma-rays, MNRAS, 273, 837

Makishima, K., Kubota, A., Mizuno, T., et al. 2000, The Nature of Ultraluminous Compact X-Ray Sources in Nearby Spiral Galaxies, ApJ, 535, 632

Mallick, L., Dewangan, G. C., Gandhi, P., Misra, R., & Kembhavi, A. K. 2016, Accretion disc–corona and jet emission from the radio-loud narrow-line Seyfert 1 galaxy RX J1633.3+4719, Monthly Notices of the Royal Astronomical Society, 460, 1705

Maoz, D., Markowitz, A., Edelson, R., & Nandra, K. 2002, X-Ray versus Optical Variations in the Seyfert 1 Nucleus NGC 3516: A Puzzling Disconnectedness, The Astronomical Journal, 124, 1988

Marinucci, A., Bianchi, S., Matt, G., et al. 2016, NuSTAR catches the unveiling nucleus of NGC 1068, MNRAS, 456, L94

Marshall, K., Ryle, W. T., & Miller, H. R. 2008, Correlated X-Ray and Optical Variability in Markarian 509, ApJ, 677, 880

Matt, G., Fabian, A. C., & Reynolds, C. S. 1997, Geometrical and chemical dependence of K-shell X-ray features, MNRAS, 289, 175

Matt, G., Guainazzi, M., & Maiolino, R. 2003, Changing look: from Compton-thick to Compton-thin, or the rebirth of fossil active galactic nuclei, MNRAS, 342, 422

Matt, G., Perola, G. C., & Piro, L. 1991, The iron line and high energy bump as X-ray signatures of cold matter in Seyfert 1 galaxies., A&A, 247, 25

McHardy, I. M., Cameron, D. T., Dwelly, T., et al. 2014, Swift monitoring of NGC 5548: X-ray reprocessing and short-term UV/optical variability, Monthly Notices of the Royal Astronomical Society, 444, 1469

McHardy, I. M., Connolly, S. D., Horne, K., et al. 2018, X-ray/UV/optical variability of NGC 4593 with Swift: reprocessing of X-rays by an extended reprocessor, Monthly Notices of the Royal Astronomical Society, 480, 2881

McHardy, I. M., Connolly, S. D., Peterson, B. M., et al. 2016, The origin of UV-optical variability in AGN and test of disc models: XMM-Newton and ground-based observations of NGC 4395, Astronomische Nachrichten, 337, 500

McHardy, I. M., Papadakis, I. E., Uttley, P., Page, M. J., & Mason, K. O. 2004, Combined long and short time-scale X-ray variability of NGC 4051 with RXTE and XMM-Newton, MNRAS, 348, 783

McKernan, B., Yaqoob, T., & Reynolds, C. S. 2007, A soft X-ray study of type I active galactic nuclei observed with Chandra high-energy transmission grating spectrometer, MNRAS, 379, 1359

Mehdipour, M., Branduardi-Raymont, G., Kaastra, J. S., et al. 2011, Multiwavelength campaign on Mrk 509. IV. Optical-UV-X-ray variability and the nature of the soft X-ray excess, A&A, 534, A39

Merloni, A., Dwelly, T., Salvato, M., et al. 2015, A tidal disruption flare in a massive galaxy? Implications for the fuelling mechanisms of nuclear black holes, MNRAS, 452, 69

Miniutti, G. & Fabian, A. C. 2004, A light bending model for the X-ray temporal and spectral properties of accreting black holes, MNRAS, 349, 1435

Mizumoto, M. & Ebisawa, K. 2016, Nature of the warm absorber outflow in NGC 4051, Monthly Notices of the Royal Astronomical Society, 466, 3259

Morgan, C. W., Kochanek, C. S., Morgan, N. D., & Falco, E. E. 2010, THE QUASAR ACCRETION DISK SIZE-BLACK HOLE MASS RELATION, The Astrophysical Journal, 712, 1129

Naik, S., Pal, M., & Kumari, N. 2019, Short-term variabilities in X-ray/Optical/UV emission from Seyfert 1 galaxy NGC 4593, Bulletin de la Societe Royale des Sciences de Liege, 88, 143

Nandi, P., Chatterjee, A., Chakrabarti, S. K., & Dutta, B. G. 2021, Long term X-Ray Observations of Seyfert 1 Galaxy Ark 120: On the origin of soft-excess, MNRAS[[arXiv]2101.08043]

Nandra, K., George, I. M., Mushotzky, R. F., Turner, T. J., & Yaqoob, T. 1997, ASCA Observations of Seyfert 1 Galaxies. I. Data Analysis, Imaging, and Timing, ApJ, 476, 70

Narayan, R. 1996, Advection-dominated Models of Luminous Accreting Black Holes, ApJ, 462, 136

Nardini, E. & Risaliti, G. 2011, The effects of X-ray absorption variability in NGC 4395, MNRAS, 417, 2571

Nenkova, M., Sirocky, M. M., Ivezić, Ž., & Elitzur, M. 2008a, AGN Dusty Tori. I. Handling of Clumpy Media, ApJ, 685, 147

Nenkova, M., Sirocky, M. M., Nikutta, R., Ivezić, Ž., & Elitzur, M. 2008b, AGN Dusty Tori. II. Observational Implications of Clumpiness, ApJ, 685, 160

Netzer, H. 2015, Revisiting the Unified Model of Active Galactic Nuclei, ARA&A, 53, 365

Nicastro, F. 2000, Broad Emission Line Regions in Active Galactic Nuclei: The Link with the Accretion Power, ApJ, 530, L65

Niedźwiecki, A., Szanecki, M., & Zdziarski, A. A. 2019, Improved spectral models for relativistic reflection, MNRAS, 485, 2942

Niedźwiecki, A., Zdziarski, A. A., & Szanecki, M. 2016, On the Lamppost Model of Accreting Black Holes, ApJ, 821, L1

Noda, H. & Done, C. 2018, Explaining changing-look AGN with state transition triggered by rapid mass accretion rate drop, MNRAS, 480, 3898

Noda, H., Makishima, K., Nakazawa, K., & Yamada, S. 2013, A Suzaku discovery of a slowly varying hard X-ray continuum from the type I Seyfert galaxy NGC 3516, The Astrophysical Journal, 771, 100

Noda, H., Makishima, K., Yamada, S., et al. 2011, Suzaku Studies of Wide-Band Spectral Variability of the Bright Type I Seyfert Galaxy Markarian 509, Publications of the Astronomical Society of Japan, 63, S925

Noda, H., Minezaki, T., Watanabe, M., et al. 2016, X-ray and optical correlation of type I Seyfert NGC 3516 studied with Suzaku and Japanese ground-based telescopes, The Astrophysical Journal, 828, 78

Ochmann, M. W., Kollatschny, W., & Zetzl, M. 2020, Spectral changes and BLR kinematics of eruptive changing-look AGN, Contributions of the Astronomical Observatory Skalnate Pleso, 50, 318

Oknyansky, V. L., Gaskell, C. M., Huseynov, N. A., et al. 2017, The curtain remains open: NGC 2617 continues in a high state, MNRAS, 467, 1496

Oknyansky, V. L., Lipunov, V. M., Gorbovskoy, E. S., et al. 2018, New changing look case in NGC 1566, The Astronomer's Telegram, 11915, 1

Oknyansky, V. L., Winkler, H., Tsygankov, S. S., et al. 2020, The post-maximum behaviour of the changing-look Seyfert galaxy NGC 1566, MNRAS, 498, 718

Oknyansky, V. L., Winkler, H., Tsygankov, S. S., et al. 2019, New changing look case in NGC 1566, MNRAS, 483, 558

Osterbrock, D. E. 1981, Seyfert galaxies with weak broad H alpha emission lines, ApJ, 249, 462

Osterbrock, D. E. & Pogge, R. W. 1985, The spectra of narrow-line Seyfert 1 galaxies., ApJ, 297, 166

Padovani, P., Alexander, D. M., Assef, R. J., et al. 2017, Active galactic nuclei: what's in a name?, A&A Rev., 25, 2

Pahari, M., McHardy, I. M., Vincentelli, F., et al. 2020, Evidence for variability time-scale-dependent UV/X-ray delay in Seyfert 1 AGN NGC 7469, Monthly Notices of the Royal Astronomical Society, 494, 4057

Pal, M., Dewangan, G. C., Connolly, S. D., & Misra, R. 2016, Correlated X-ray/ultraviolet/optical variability and the nature of accretion disc in the bare Seyfert 1 galaxy Fairall 9, Monthly Notices of the Royal Astronomical Society, 466, 1777

Pal, M., Dewangan, G. C., Kembhavi, A. K., Misra, R., & Naik, S. 2018, Complex optical/UV and X-ray variability of the Seyfert 1 galaxy 1H 0419-577, MNRAS, 473, 3584

Pal, M., Dewangan, G. C., Misra, R., & Pawar, P. K. 2016, X-ray/UV variability and the origin of soft X-ray excess emission from II Zw 177, MNRAS, 457, 875

Pal, M. & Naik, S. 2017, Correlated X-ray/UV/optical emission and short-term variability in a Seyfert 1 galaxy NGC 4593, Monthly Notices of the Royal Astronomical Society, 474, 5351

Papadakis, I. E. & Lawrence, A. 1993, Improved Methods for Power Spectrum Modelling of Red Noise, MNRAS, 261, 612

Papadakis, I. E., Nandra, K., & Kazanas, D. 2001, Frequency-dependent Time Lags in the X-Ray Emission of the Seyfert Galaxy NGC 7469, ApJ, 554, L133

Parker, M. L., Schartel, N., Grupe, D., et al. 2019, X-ray spectra reveal the reawakening of the repeat changing-look AGN NGC 1566, MNRAS, 483, L88

Pastoriza, M. & Gerola, H. 1970, Spectral Variation in the Seyfert Galaxy NGC 1566, Astrophys. Lett., 6, 155

Peters, P. C. 1964, Gravitational Radiation and the Motion of Two Point Masses, Physical Review, 136, 1224

Peterson, B. M. 1997, An Introduction to Active Galactic Nuclei (Cambridge University Press)

Peterson, B. M. 2006, in Physics of Active Galactic Nuclei at all Scales, ed. D. Alloin, Vol. 693, 77

Peterson, B. M. 2014, Measuring the Masses of Supermassive Black Holes, Space Sci. Rev., 183, 253

Peterson, B. M., Ferrarese, L., Gilbert, K. M., et al. 2004, Central Masses and Broad-Line Region Sizes of Active Galactic Nuclei. II. A Homogeneous Analysis of a Large Reverberation-Mapping Database, The Astrophysical Journal, 613, 682

Peterson, B. M., Wanders, I., Horne, K., et al. 1998, On Uncertainties in Cross-Correlation Lags and the Reality of Wavelength-dependent Continuum Lags in Active Galactic Nuclei, PASP, 110, 660

Petrucci, P. O., Paltani, S., Malzac, J., et al. 2013, Multiwavelength campaign on Mrk 509. XII. Broad band spectral analysis, A&A, 549, A73

Piconcelli, E., Bianchi, S., Guainazzi, M., Fiore, F., & Chiaberge, M. 2007, XMM-Newton broad-band observations of NGC 7582: N{H} variations and fading out of the active nucleus, A&A, 466, 855

Ponti, G., Miniutti, G., Cappi, M., et al. 2006, XMM-Newton study of the complex and variable spectrum of NGC 4051, MNRAS, 368, 903

Poole, T. S., Breeveld, A. A., Page, M. J., et al. 2007, Photometric calibration of the Swift ultraviolet/optical telescope, Monthly Notices of the Royal Astronomical Society, 383, 627

Pounds, K. A., Reeves, J. N., King, A. R., & Page, K. L. 2004, Exploring the complex X-ray spectrum of NGC 4051, Monthly Notices of the Royal Astronomical Society, 350, 10

Poutanen, J. & Svensson, R. 1996, The Two-Phase Pair Corona Model for Active Galactic Nuclei and X-Ray Binaries: How to Obtain Exact Solutions, ApJ, 470, 249

Qiao, C.-K., Wei, J.-W., & Chen, L. 2021, An Overview of the Compton Scattering Calculation, Crystals, 11

Quintana, H., Kaufmann, P., & Sasic, J. L. 1975, Activity of the nucleus of the southern Seyfert galaxy NGC 1566, MNRAS, 173, 57P

Raban, D., Jaffe, W., Röttgering, H., Meisenheimer, K., & Tristram, K. R. W. 2009, Resolving the obscuring torus in NGC 1068 with the power of infrared interferometry: revealing the inner funnel of dust, MNRAS, 394, 1325

Rees, M. J. 1988, Tidal disruption of stars by black holes of 10^6-10^8 solar masses in nearby galaxies, Nature, 333, 523

Reeves, J., Done, C., Pounds, K., et al. 2008, On why the iron K-shell absorption in AGN is not a signature of the local warm/hot intergalactic medium, MNRAS, 385, L108

Remillard, R. A. & McClintock, J. E. 2006, X-Ray Properties of Black-Hole Binaries, ARA&A, 44, 49

Reynolds, C. S. & Nowak, M. A. 2003, Fluorescent iron lines as a probe of astrophysical black hole systems, Phys. Rep., 377, 389

Ricci, C., Bauer, F. E., Arevalo, P., et al. 2016, IC 751: A New Changing Look AGN Discovered by NuSTAR, ApJ, 820, 5

Ricci, C., Ho, L. C., Fabian, A. C., et al. 2018, BAT AGN Spectroscopic Survey - XII. The relation between coronal properties of active galactic nuclei and the Eddington ratio, MNRAS, 480, 1819

Ricci, C., Kara, E., Loewenstein, M., et al. 2020, The Destruction and Recreation of the X-Ray Corona in a Changing-look Active Galactic Nucleus, ApJ, 898, L1

Ricci, C., Loewenstein, M., Kara, E., et al. 2021, The 450 Day X-Ray Monitoring of the Changing-look AGN 1ES 1927+654, ApJS, 255, 7

Ricci, C., Trakhtenbrot, B., Koss, M. J., et al. 2017, BAT AGN Spectroscopic Survey. V. X-Ray Properties of the Swift/BAT 70-month AGN Catalog, ApJS, 233, 17

Ricci, C., Walter, R., Courvoisier, T. J. L., & Paltani, S. 2011, Reflection in Seyfert galaxies and the unified model of AGN, A&A, 532, A102

Risaliti, G., Elvis, M., Bianchi, S., & Matt, G. 2010, Chandra monitoring of UGC 4203: the structure of the X-ray absorber, MNRAS, 406, L20

Risaliti, G., Elvis, M., Fabbiano, G., et al. 2007, Occultation Measurement of the Size of the X-Ray-emitting Region in the Active Galactic Nucleus of NGC 1365, ApJ, 659, L111

Risaliti, G., Elvis, M., & Nicastro, F. 2002, Ubiquitous Variability of X-Ray-absorbing Column Densities in Seyfert 2 Galaxies, ApJ, 571, 234

Risaliti, G., Nardini, E., Elvis, M., Brenneman, L., & Salvati, M. 2011, Probing general relativistic effects during active galactic nuclei X-ray eclipses, MNRAS, 417, 178

Romano, P., Campana, S., Chincarini, G., et al. 2006, Panchromatic study of GRB 060124: from precursor to afterglow, A&A, 456, 917

Roming, P. W. A., Kennedy, T. E., Mason, K. O., et al. 2005, The Swift Ultra-Violet/Optical Telescope, Space Science Reviews, 120, 95

Ross, R. R. & Fabian, A. C. 2005, A comprehensive range of X-ray ionized-reflection models, MNRAS, 358, 211

Runnoe, J. C., Cales, S., Ruan, J. J., et al. 2016, Now you see it, now you don't: the disappearing central engine of the quasar J1011+5442, MNRAS, 455, 1691

Rybicki, G. B. & Lightman, A. P. 1979, Radiative processes in astrophysics

Saxton, R., Komossa, S., Auchettl, K., & Jonker, P. G. 2020, X-Ray Properties of TDEs, Space Sci. Rev., 216, 85

Schurch, N. J., Done, C., & Proga, D. 2009, The Impact of Accretion Disk Winds on the X-Ray Spectra of Active Galactic Nuclei. II. Xscort + Hydrodynamic Simulations, ApJ, 694, 1

Seifina, Chekhtman, Alexandre, & Titarchuk, Lev. 2018, NGC 4051: Black hole mass and photon index-mass accretion rate correlation, A&A, 613, A48

Seyfert, C. K. 1943, Nuclear Emission in Spiral Nebulae., ApJ, 97, 28

Shakura, N. I. & Sunyaev, R. A. 1973a, Black holes in binary systems. Observational appearance., A&A, 24, 337

Shakura, N. I. & Sunyaev, R. A. 1973b, Reprint of 1973A&A....24..337S. Black holes in binary systems. Observational appearance., A&A, 500, 33

Shappee, B. J., Prieto, J. L., Grupe, D., et al. 2014, The Man behind the Curtain: X-Rays Drive the UV through NIR Variability in the 2013 Active Galactic Nucleus Outburst in NGC 2617, ApJ, 788, 48

Shemmer, O., Brandt, W. N., Netzer, H., Maiolino, R., & Kaspi, S. 2008, The Hard X-Ray Spectrum as a Probe for Black Hole Growth in Radio-Quiet Active Galactic Nuclei, The Astrophysical Journal, 682, 81

Shemmer, O., Uttley, P., Netzer, H., & McHardy, I. M. 2003, Complex optical-X-ray correlations in the narrow-line Seyfert 1 galaxy NGC 4051, MNRAS, 343, 1341

Sheng, Z., Wang, T., Jiang, N., et al. 2017, Mid-infrared Variability of Changing-look AGNs, ApJ, 846, L7

Shields, G. A. 1999, A Brief History of Active Galactic Nuclei, PASP, 111, 661

Shobbrook, R. R. 1966, Southern groups and clusters of galaxies. III, Distances of some southern galaxies, MNRAS, 131, 365

Shuder, J. M. & Osterbrock, D. E. 1981, Empirical results from a study of active galactic nuclei., ApJ, 250, 55

Sikora, M., Stawarz, Ł., & Lasota, J.-P. 2007, Radio Loudness of Active Galactic Nuclei: Observational Facts and Theoretical Implications, ApJ, 658, 815

Singh, K. P., Garmire, G. P., & Nousek, J. 1985, Observations of Soft X-Ray Spectra from a Seyfert 1 and a Narrow Emission-Line Galaxy, ApJ, 297, 633

Starkey, D., Horne, K., Fausnaugh, M. M., et al. 2017, Space telescope and optical reverberation mapping project.VI. Reverberating disk models for NGC 5548, The Astrophysical Journal, 835, 65

Steenbrugge, Kaastra, J. S., Detmers, R. G., et al. 2011, Multiwavelength campaign on Mrk 509 - VII. Relative abundances of the warm absorber, A&A, 534, A42

Stern, B. E., Poutanen, J., Svensson, R., Sikora, M., & Begelman, M. C. 1995, On the Geometry of the X-Ray–Emitting Region in Seyfert Galaxies, ApJ, 449, L13

Stone, N. C., Vasiliev, E., Kesden, M., et al. 2020, Rates of Stellar Tidal Disruption, Space Sci. Rev., 216, 35

Strüder, L., Briel, U., Dennerl, K., et al. 2001, The European Photon Imaging Camera on XMM-Newton: The pn-CCD camera, A&A, 365, L18

Suganuma, M., Yoshii, Y., Kobayashi, Y., et al. 2006, Reverberation Measurements of the Inner Radius of the Dust Torus in Nearby Seyfert 1 Galaxies, ApJ, 639, 46

Sunyaev, R. A. & Titarchuk, L. G. 1980, Comptonization of X-rays in plasma clouds. Typical radiation spectra., A&A, 500, 167

Svensson, R. 1984, Steady mildly relativistic thermal plasmas - Processes and properties, MNRAS, 209, 175

Tadhunter, C. 2008, An introduction to active galactic nuclei: Classification and unification, New A Rev., 52, 227

Tarter, C. B., Tucker, W. H., & Salpeter, E. E. 1969, The Interaction of X-Ray Sources with Optically Thin Environments, ApJ, 156, 943

Taylor, R. D., Uttley, P., & McHardy, I. M. 2003, The nature of X-ray spectral variability in Seyfert galaxies, Monthly Notices of the Royal Astronomical Society, 342, L31

Tombesi, F., Cappi, M., Reeves, J. N., & Braito, V. 2012, Evidence for ultrafast outflows in radio-quiet AGNs - III. Location and energetics, MNRAS, 422, L1

Tombesi, F., Cappi, M., Reeves, J. N., et al. 2013, Unification of X-ray winds in Seyfert galaxies: from ultra-fast outflows to warm absorbers, Monthly Notices of the Royal Astronomical Society, 430, 1102

Tristram, K. R. W., Burtscher, L., Jaffe, W., et al. 2014, The dusty torus in the Circinus galaxy: a dense disk and the torus funnel, A&A, 563, A82

Troyer, J., Starkey, D., Cackett, E. M., et al. 2016, Correlated X-ray/ultraviolet/optical variability in NGC 6814, MNRAS, 456, 4040

Turner, M. J. L., Abbey, A., Arnaud, M., et al. 2001, The European Photon Imaging Camera on XMM-Newton: The MOS cameras, A&A, 365, L27

Turner, T. J., Reeves, J. N., Kraemer, S. B., & Miller, L. 2008, Tracing a disk wind in NGC 3516, A&A, 483, 161

Urry, M. 2003, in Astronomical Society of the Pacific Conference Series, Vol. 290, Active Galactic Nuclei: From Central Engine to Host Galaxy, ed. S. Collin, F. Combes, & I. Shlosman, 3

Uttley, P., Edelson, R., McHardy, I. M., Peterson, B. M., & Markowitz, A. 2003, Correlated Long-Term Optical and X-Ray Variations in NGC 5548, The Astrophysical Journal, 584, L53

Vasudevan, R. V. & Fabian, A. C. 2009, Simultaneous X-ray/optical/UV snapshots of active galactic nuclei from XMM-Newton: spectral energy distributions for the reverberation mapped sample, MNRAS, 392, 1124

Vaughan, S., Edelson, R., Warwick, R. S., & Uttley, P. 2003, On characterizing the variability properties of X-ray light curves from active galaxies, MNRAS, 345, 1271

Vaughan, S., Reeves, J., Warwick, R., & Edelson, R. 1999, X-ray spectral complexity in narrow-line Seyfert 1 galaxies, Monthly Notices of the Royal Astronomical Society, 309, 113

Verner, D. A., Ferland, G. J., Korista, K. T., & Yakovlev, D. G. 1996, Atomic Data for Astrophysics. II. New Analytic FITS for Photoionization Cross Sections of Atoms and Ions, ApJ, 465, 487

Wada, K. 2012, Radiation-driven Fountain and Origin of Torus around Active Galactic Nuclei, ApJ, 758, 66

Walton, D. J., Nardini, E., Fabian, A. C., Gallo, L. C., & Reis, R. C. 2013, Suzaku observations of 'bare' active galactic nuclei, MNRAS, 428, 2901

Wang, T., Brinkmann, W., & Bergeron, J. 1996, X-ray properties of active galactic nuclei with optical FeII emission., A&A, 309, 81

Welsh, W. F. 1999, On the Reliability of Cross-Correlation Function Lag Determinations in Active Galactic Nuclei, PASP, 111, 1347

Wheaton, W. A., Dunklee, A. L., Jacobsen, A. S., et al. 1995, Multiparameter Linear Least-Squares Fitting to Poisson Data One Count at a Time, ApJ, 438, 322

Wilkins, D. R. & Fabian, A. C. 2011, Determination of the X-ray reflection emissivity profile of 1H 0707-495, MNRAS, 414, 1269

Wilkins, D. R., Gallo, L. C., Costantini, E., Brandt, W. N., & Blandford, R. D. 2022, Acceleration and cooling of the corona during X-ray flares from the Seyfert galaxy IZw1, Monthly Notices of the Royal Astronomical Society, 512, 761

Wilms, J., Allen, A., & McCray, R. 2000, On the Absorption of X-Rays in the Interstellar Medium, ApJ, 542, 914

Winkler, H. 1992, Variability studies of Seyfert galaxies - II. Spectroscopy., MNRAS, 257, 677

Winter, L. M., Mushotzky, R. F., Reynolds, C. S., & Tueller, J. 2009, X-Ray Spectral Properties of the BAT AGN Sample, ApJ, 690, 1322

Wolf, J., Nandra, K., Salvato, M., et al. 2021, First constraints on the AGN X-ray luminosity function at z 6 from an eROSITA-detected quasar, A&A, 647, A5

Woo, J.-H. & Urry, C. M. 2002, Active Galactic Nucleus Black Hole Masses and Bolometric Luminosities, ApJ, 579, 530

Wu, X.-B. & Liu, F. K. 2004, Black Hole Mass and Accretion Rate of Active Galactic Nuclei with Double-peaked Broad Emission Lines, ApJ, 614, 91

Wu, Y.-J., Wang, J.-X., Cai, Z.-Y., et al. 2020, More than softer-when-brighter: The X-ray powerlaw spectral variability in NGC 4051, Science China Physics, Mechanics, and Astronomy, 63, 129512

Yaqoob, T., Tatum, M. M., Scholtes, A., Gottlieb, A., & Turner, T. J. 2015, A Compton-thin solution for the Suzaku X-ray spectrum of the Seyfert 2 galaxy Mkn 3, MNRAS, 454, 973

Yuan, W., Liu, B., Zhou, H., & Wang, T. 2010, X-ray observational signature of a black hole accretion disk in an active galactic nucleus RX J1633+ 4718, The Astrophysical Journal, 723, 508

Yuan, W., Zhou, H., Komossa, S., et al. 2008, A population of radio-loud narrow-line Seyfert 1 galaxies with blazar-like properties?, The Astrophysical Journal, 685, 801

Yuan, Y., Spitkovsky, A., Blandford, R. D., & Wilkins, D. R. 2019, Black hole magnetosphere with small-scale flux tubes - II. Stability and dynamics, MNRAS, 487, 4114

Zdziarski, A. A., Johnson, W. N., & Magdziarz, P. 1996, Broad-band γ-ray and X-ray spectra of NGC 4151 and their implications for physical processes and geometry., MNRAS, 283, 193

Zdziarski, A. A., Lubiński, P., & Smith, D. A. 1999, Correlation between Compton reflection and X-ray slope in Seyferts and X-ray binaries, MNRAS, 303, L11

Zhu, S. F., Brandt, W. N., Luo, B., et al. 2020, The L_X-L_{uv}-L_{radio} relation and corona-disc-jet connection in optically selected radio-loud quasars, MNRAS, 496, 245

Zimmer, F., Schmidt, R. W., & Wambsganss, J. 2011, X-ray microlensing in the quadruply lensed quasar Q2237+0305, MNRAS, 413, 1099

Zu, Y., Kochanek, C. S., Kozłowski, S., & Udalski, A. 2013, Is quasar optical variability a damped random walk, The Astrophysical Journal, 765, 106

Zu, Y., Kochanek, C. S., & Peterson, B. M. 2011, An alternative approach to measuring reverberation lags in active galactic nuclei, The Astrophysical Journal, 735, 80

Życki, P. T., Done, C., & Smith, D. A. 1999, The 1989 May outburst of the soft X-ray transient GS 2023+338 (V404 Cyg), MNRAS, 309, 561